Center for Quantum Devices

UNIVERSITY OF COPENHAGEN

YSR States in Double Quantum Dots

- Transport and Bound State Dynamics -

by

Gorm Ole Steffensen

Ph.D Thesis
October 1, 2021

Condensed Matter Theory
Niels Bohr Institute
Faculty of Science
University of Copenhagen

Supervisor:
Jens Paaske

Assessment Committee:
Karsten Flensberg
Felix Von Oppen
Ramón Aguado

This thesis has been submitted to the PhD School ofThe Faculty of Science, University of Copenhagen

ABSTRACT

Joining a bulk superconductor with a spin-1/2 impurity realizes a microscopic model embodying the rich competition between magnetism and superconductivity, and leads to the formation of an isolated subgap bound state named the Yu-Shiba-Rusinov (YSR) state. The large tunability of semiconductor-superconductor hybrid devices, specifically InAs nanowires with epitaxial aluminium, allows for the creation of a double quantum dot geometry directly coupled to two superconducting leads, known as a S-DQD-S junction. When occupied by an odd number of electrons, each of these quantum dots host a single spin-1/2 degree of freedom enabling us to investigate the interaction between two YSR subgap states under tunable conditions. The electronic transport in the S-DQD-S junction combines aspects of single quasiparticle and cooper-pair tunnelling, leading to detailed maps of differential conductance. Understanding these maps is not only a necessary requirement to characterize devices, but also reveals information about the non-equilibrium properties of the isolated quantum levels themselves.

In this thesis we characterize and calculate transport in the S-DQD-S junction. This provides us with a window into the complicated dynamics of the two-impurity YSR state, and the various competitions at play. Using these tools we are able to classify charge diagrams of the double quantum dot by measurements of noise-dominated supercurrent, and by following the changes in these diagrams we realize the fully screened two-impurity YSR groundstate. Finite bias spectroscopy of YSR states is investigated using Keldysh Floquet Green's functions capturing multiple Andreev reflections (MAR) to all orders. In this framework, we highlight the important roles of relaxation and poisoning in regard to subgap state transport, which are tested in measurements of direct transport between two opposing subgap states, where additional relaxation channels from MAR can be tuned on and off on demand.

DANSK RESUMÉ

Ved at koble et superledende materiale til en spin 1/2 urenhed opnås en mikroskopisk model som indkapsler den rige konkurrence mellem magnetisme og superlednng, og leder til formationen af en isoleret bunden tilstand kaldet Yu-Shiba-Rusinov tilstanden. Den store grad af tunings frihed der er til stede i halvleder-superleder hybrid enheder, specifikt i InAs nanotråde med epitaxial aluminium, tillader skabelsen af en dobbelt kvanteprik geometri direkte koblet til to superledende ledninger, kendt som en S-DQD-S kontakt. Hvis en af disse kvanteprikker er besat af et ulige antal elektroner vil de indeholde en fri spin 1/2 frihedsgrad, hvilket tillader os at undersøge vekselvirkningerne mellem to YSR tilstande under tunbare forhold. Ladningstransporten i S-DQD-S kontakten kombinerer aspekter af enkelt kvasipartikel og cooper-par transport, hvilket leder til detaljeret grafer af differential konduktans. Forståelsen af disse grafer er ikke blot et nødvendigt krav for at kunne karakterisere enhederne, men afsløre også information om uligevægtsegenskaberne af de isolerede kvante niveauer.

I denne afhandling karakteriserer og udregner vi transporten i S-DQD-S kontakten. Dette giver os et vindue til den komplicerede dynamik af to-urenheds YSR tilstanden, og de mange konkurrerende kræfter der er i spil. Ved brug af disse redskaber kan vi klassificere dobbelt kvanteprikkens ladnings diagrammer ved at måle støj-domineret superstrøm, og ved at følge ændringerne i disse diagrammer opnår vi den fuldt afskærmede to-urenheds YSR tilstand. Endelig bias spektroskopi af YSR tilstande undersøges ved brug af Keldysh Floquet Greens funktioner, som fanger effekten af gentagende Andreev reflektioner (MAR) til alle ordner. I denne ramme fremhæver vi den vigtige rolle spillet af relaksation og forgiftning, i forhold til transport i tilstande under gabbet, hvilket vi tester i målinger af direkte transport mellem modstående tilstande under gabbet, hvor yderlige relaksations kanaler fra MAR kan blive tændt og slukket på kommando.

ACKNOWLEDGEMENTS

To start of I would like to express my deepest gratitude to my supervisor **Jens Paaske**, who have not only facilitated this Ph.D project but have also shown me the joy of working in close collaboration with experimentalists. You are not only a great *connoisseur* of articles and books, but also a fantastic mentor able to handle both the ups and downs of academic work. My gratitude also extends to **Kasper**, **Jesper**, **Juan Carlos**, and **Alexandros**, at the experimental side of Qdev, for the joyful collaboration over the years. Your amazing patience towards a naive theorist such as I have been crucial for my growth.

Next, the value of the Condensed Matter Theory group's social life cannot be understated. The halls of either Rockefeller, Vibenhus, or occupied NBB have been filled with both hearty laughter and discussion. Here special thanks goes to the lunchclub, may it be reborn, and **Morten Munk**, **Hano**, **Ida**, and **Andrea** for great company and support during my stay in the group.

For bringing me outside of the confinements of home, I would like to thank **Václav Janiš** and **Tomáš Novotný** for a great stay in Prague, and **Alfredo Levy Yeyati** for the short visit in Madrid (damm the Corona). Both visits where greatly inspiring and showed me how many facets CMT can have. A special thanks also goes to **Peter Zalom** for your immediate openness and friendliness.

A round of applause goes to **Ida**, **Hano**, **Andrea**, and **Cliff** for both correcting and providing feedback on the thesis. Im sure that the finished product is happier for it, and I will get you a beer at the airport.

Having spent close to a decade at the Niels Bohr Institute, it would almost constitute treachery not to mention the fantastic passion and openness that is the heart of student life here. From tutoring, to the Revy, to ølkrokket in the fields and long evenings at Cafeen?, this truly is a special place to have studied.

Last but not least, I would like to thank **Ida Holk** for your incredible patience with me during this marathon of a writing process, and for being there for me no matter the weather. It cannot be priced.

PREFACE AND PUBLICATIONS

This thesis focuses on the theoretical study of transport in semiconductor-superconductor hybrid devices on which double quantum dots are formed. The interactions between superconductors and quantum dots leads to the formation of YSR states, which are measured both by zero-bias supercurrent and finite bias spectroscopy. This thesis provides the necessary tools to interpret and fit these measurements to simple transport models. This thesis resulted in the five following articles which we present and discuss in the main text:

[1] J. C. Estrada Saldaña, A. Vekris, G. O. Steffensen, R. Žitko, P. Krogstrup, J. Paaske, K. Grove-Rasmussen, and J. Nygård, "Supercurrent in a Double Quantum Dot", Phys. Rev. Lett. 121, 257701 (2018)

[2] J. C. Estrada Saldaña, A. Vekris, R. Žitko, G. O. Steffensen, P. Krogstrup, J. Paaske, K. Grove-Rasmussen, and J. Nygård, "Two-Impurity Yu-Shiba-Rusinov States in Coupled Quantum Dots", Phys. Rev. B 102, 195143 (2020)

[3] G. O. Steffensen, J. C. Estrada Saldaña, A. Vekris, P. Krogstrup, K. Grove-Rasmussen, J. Nygård, A. L. Yeyati, and J. Paaske, "Direct Transport between Superconducting Subgap States in a Double Quantum Dot", arXiv:2105.06815 (2021) - Submitted to PRL

[4] D. Bouman, R. J. J. van Gulik, G. O. Steffensen, D. Pataki, P. Boross, P. Krogstrup, J. Nygård, J. Paaske, A. Pályi, A. Geresdi, "Triplet-blockaded Josephson supercurrent in double quantum dots", Phys. Rev. B 102, 220505(R) (2020)

[5] D. Chatzopoulos, D. Cho, K. M. Bastiaan, G. O. Steffensen, D. Bouwmeester, A. Akbari, G. Gu, J. Paaske, B. M. Andersen, M. P. Allan, "Spatially dispersing Yu-Shiba-Rusinov states in the unconventional superconductor $FeTe_{0.55}Se_{0.45}$", Nature Communications volume 12, Article number: 298 (2021)

CONTENTS

THESIS

1 INTRODUCTION

In the 1930s and 40s the consolidation of modern quantum mechanics changed the face of condensed matter theory by providing the microscopic framework necessary to understand the bulk properties of materials. The following decade saw the development of hallmark theories such as Landau Fermi liquid theory (1957), explaining the emergence of simple quasiparticles from strongly interacting systems, in addition to Ginzburg-Landau (1950), and Barden-Cooper-Schrieffer (BCS, 1956) theory, which finally captured the microscopic mechanism behind the elusive superconducting phase. In spite of these successes, the quantum entities themselves (quasiparticles, cooper-pairs, etc.) remained largely elusive revealing only their presence through ensemble averages and bulk properties.

Driven by the semiconductor industries remarkable technological advances, the last 40 years have seen significant developments in both fabrication and control of nanoscale circuitry and devices. Due to size quantization, devices on this scale clearly exhibit isolated quantum states, which can be continuously tuned and controlled by capacitively coupled gates. These technologies have allowed scientist to peek behind the curtain of bulk properties, and observe the underlying quantum phenomena in isolated form. One example is the *quantum dot*, realized when charge confinement in three dimensions creates a potential dip of size comparable to the electron wavelength, effectively forming a quantum well. The quantized states formed by these wells mimics the orbitals of single atoms, and quantum dots are therefore often described as artificial atoms [6]. If a dot is occupied by an odd number of electrons, one spin-1/2 degree of freedom is left unpaired, and the dot behaves as a single magnetic impurity. Furthermore, since the dot occupation can be controlled by gates the magnetic behaviour can be turned on-and-off on demand by experimentalist. This ability has been used to study the famous *Kondo effect* [7], a significant milestone in our understanding of the low-bias resistivity of metals and the origin of heavy fermion materials, and characterized by the logarithmic divergence of perturbative approaches [8]. For a single impurity the Kondo effect describes the screening of a magnetic doublet state into a singlet state by exchange interactions with a metallic lead. In spectroscopic

measurements this screening leads to the formation of a zero-bias conductance peak [9], whose peak-to-width ratio contains detailed information about couplings and scalings. Using this platform a large number of experiments have been performed, for example *Potok et al* [10] who realized the predicted [11] non-fermi liquid groundstate of the overscreened Kondo impurity; a strong test of the underlying foundations of condensed matter theory.

In addition to these studies of fundamental physics, the isolated quantum levels of nanoscale devices are also promising in the field of quantum computing where they can be utilized as *qubits*. A fruitful avenue in this field has been the study of nanoscale superconducting devices, which due to the presence of a superconducting gap preserves fermionic parity at low temperatures. Also, the macroscopic nature of the superconducting groundstate allows single quantum states (e.g. in nanoscale Josephson junctions or cooper-pair boxes) to easily couple to the supercurrent and flux states of quantized circuits - a useful property for creating entangled states between multiple qubits. This is exploited in the *transmon* qubit [12] utilized in Google's Sycamore computer which achieved *quantum supremacy* in 2019 [13]. This progress illustrates how the realm of quasiparticles in condensed matter systems, once hidden, has moved from an area of fundamental science to potential application within the span of a single generation.

In this thesis we study transport in hybrid semiconductor-superconductor devices hosting quantum dots. The interplay of dot coulomb interaction and quasiparticles in the superconductor leads to the formation of a single subgap state, known either as a *Yu-Shiba-Rusinov* (YSR) or *Andreev** boundstate. Due to its isolation inside the gap and coupling to superconducting parameters such as phase, this state constitutes a promising platform for both investigating fundamental physics and for developing quantum technology. In the next sections we introduce the YSR state in greater detail, and illustrate how it is formed in quantum dots coupled to superconductors.

1.1 THE CLASSICAL YSR BOUNDSTATE

Conventional superconductivity originates from the low temperature condensation of cooper-pairs, composed of two time-reversed electrons, into a phase coherent collective groundstate. BCS theory captures this effect via a mean-field parameter $\Delta = |\Delta|e^{i\phi}$

* Originally the name was used for boundstates formed at superconducting interfaces and single channel Josephson junctions due to resonant Andreev reflections. Today, it is often used as a catch-all term for any subgap boundstate in superconductors originating from any impurity or spatial variation.

consisting of a quasiparticle gap $|\Delta|$ and a phase parameter ϕ conjugate to electron charge. In this description the minimal Hamiltonian of a bulk superconductor is given by,

$$H_S = \sum_{k,\sigma} \xi_k c^\dagger_{k\sigma} c_{k\sigma} + \sum_k \left(\Delta c^\dagger_{k\uparrow} c^\dagger_{-k\downarrow} + \Delta^* c_{-k\downarrow} c_{k\uparrow} \right), \tag{1.1}$$

with $c_{k\sigma}$ denoting electron annihilation with momentum k relative to Fermi momentum k_F, and σ denoting spin degree of freedom†. Almost from its conception, it was well known that superconductivity interacts strongly with magnetism, exemplified by the expulsion of magnetic fields by the Meissner effect and the breakdown of the superconducting phase at a critical field strength, B_c. In the 1960s, inspired by the Kondo effect, it was discovered by Yu, Shiba, and Rusinov [14–16] that the pair-breaking effect of a single magnetic impurity in a superconductor leads to the formation of an isolated quasiparticle state inside of the gap, which at finite impurity concentrations forms a subgap band [17]. This result was obtained using a Kondo model,

$$H_K = \sum_{\sigma\sigma'} J c^\dagger_\sigma \mathbf{S} \cdot \boldsymbol{\tau}_{\sigma\sigma'} c_{\sigma'} \tag{1.2}$$

where impurity spin $\mathbf{S}$ is exchange coupled ($J > 0$) to the electronic spin by $\boldsymbol{\tau}_{\sigma\sigma'}$, which denotes a vector of pauli matrices. $c_\sigma = \sum_k c_{k\sigma}$ is local electron annihilation operators at $r = 0$. In the limit of a classical spin $|S| \to \infty$, $J \to 0$ with $J|S| \to const$, the Hamiltonian $H_S + H_K$ is analytically tractable, and for a single impurity one obtains a subgap resonance with the energy dispersion [14–16],

$$E_0 = |\Delta| \frac{1 - \alpha^2}{1 + \alpha^2}, \tag{1.3}$$

shown in fig.1.1, and characterized by the effective coupling $\alpha = \pi \nu_F |S| J$ where ν_F is the superconductors normal-state density of states. Uncoupled ($\alpha = 0$), the system is in a tensor product state of the spin, $|\Uparrow\rangle$, and BCS groundstate, which we collectively denote $|\Uparrow, 0_{qp}\rangle$ with second index indicating number of excited quasiparticles. As α increases an excited state with a single quasiparticle $|\Uparrow, \downarrow_{qp}\rangle$, starting from $|\Delta|$, moves inside of the gap due to the gain in energy from magnetic exchange, thereby removing the sharp BCS peak at $|\Delta|$. For $\alpha > 1$ this gain in energy is larger than the cost of a quasiparticle, and the groundstate transitions into a singlet state $|\Uparrow, \downarrow_{qp}\rangle$, where a screening quasiparticle is bound to the spin. Although state $|\Uparrow, 0_{qp}\rangle$ and $|\Uparrow, \downarrow_{qp}\rangle$ have different fermion parity, they are both singlet states as Kramers degeneracy is broken by the classical spina acting as a local magnetic field. For an impurity pointing in the z-direction the screening Bogoliubov quasiparticle is a superposition of electron

† Throughout this thesis when σ is used as a subscript or in summation assume $\sigma \in \{\uparrow, \downarrow\}$

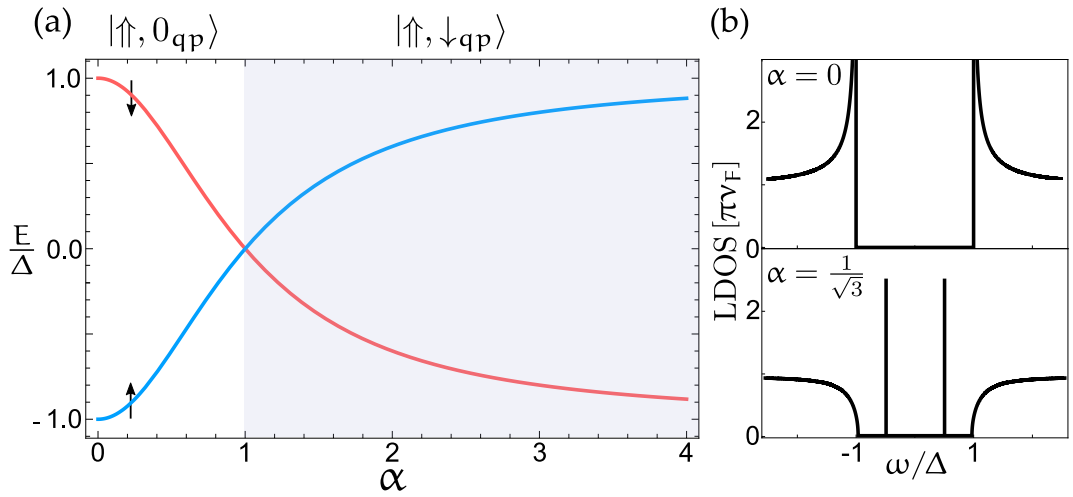

Figure 1.1: (a) Dispersion of a classical spin YSR state, eq.(1.3), with $\alpha = \pi\nu_F JS$. The excitation is between the unscreened $|\Uparrow, 0_{qp}\rangle$ and the screened $|\Uparrow, \downarrow_{qp}\rangle$ state with overlay denoting groundstate; white for $|\Uparrow, 0_{qp}\rangle$ and grey for $|\Uparrow, \downarrow_{qp}\rangle$. The red (blue) line shows an excitation from the groundstate by the addition or removal of a spin-up (spin-down) electron; addition for $E > 0$ and removal for $E < 0$. (b) Local density of state (LDOS) for no magnetic coupling ($\alpha = 0$) and finite coupling ($\alpha = 1/\sqrt{3}$). Peaks indicate delta function weights, and the gap is given by $\text{LDOS} = -\pi\nu_F \,\text{Im}\left[\frac{|\omega|\sqrt{\Delta^2-\omega^2}}{E_0^2-\omega^2}\right]$.

spin-down and hole spin-up. Consequently, transitions $|\Uparrow, 0_{qp}\rangle \leftrightarrow |\Uparrow, \downarrow_{qp}\rangle$ can be done either by the addition or removal of an electron. In the semiconductor picture this is depicted as two peaks, at $\pm E_0$, representing the two ways excitations can occur, although only a single subgap excitation is present inside of the gap. This classical spin description can be seen as an approximation of an underlying quantum spin, with $|S|$ finite, valid for large-spin impurities in materials containing magnetic anisotropy locking the spin's direction.

1.2 YSR STATES IN QUANTUM DOTS

A quantum dot is a small region where charge confinement leads to the formation of effectively zero-dimensional localized electron states. A single level on a quantum dot is described by the Hamiltonian,

$$H_D = \epsilon_d \sum_\sigma n_\sigma + U n_\uparrow n_\downarrow, \tag{1.4}$$

here $n_\sigma = d_\sigma^\dagger d_\sigma$ is the occupation operator of the level, U is the coulomb charging energy and is commonly determined from capacitive couplings $U \sim 2e/C$. ϵ_d is a

quadratic term controlling level occupation, and proportional to gate voltage $\epsilon_d \propto -V_g$. The Hilbert space of H_D consist of four states: $|0\rangle$, $|\sigma\rangle$ and $|2\rangle$ with $\sigma \in \{\uparrow, \downarrow\}$, and corresponding energies $E_0 = U/2 + \xi_d$, $E_\sigma = 0$, and $E_2 = U/2 - \xi_d$ with $\xi_d = -\epsilon_d - U/2$. As gate ($\xi_d$) is increased, the dot groundstate changes from $|0\rangle \to |\sigma\rangle \to |2\rangle$ with excitations forming a diamond pattern, whose width and height is determined by U. If charging U is the largest energy scale, compared to lead coupling, temperature and fluctuations, the dot is said to be *coulomb blockaded* [18]. This means that at the center of coulomb diamonds charge fluctuations only occur virtually, which in turn severely reduces the electron transport that can pass through the dot, limiting it to quantum tunnelling, and hence the blockade.

The full Hamiltonian of a dot tunnel coupled to a superconductor is $H = H_D + H_S + H_T$ with,

$$H_T = t_d \sum_\sigma c_\sigma^\dagger d_\sigma + h.c, \tag{1.5}$$

known as the superconducting Anderson model. Interactions in this system is determined by the competition of three energy scales: U, Δ and effective coupling $\Gamma = \pi \nu_F |t_d|^2$. This seemingly simple system hosts a variety complicated physics stemming from the interacting term U. Before we discuss various limits and theoretical models that exist, we next introduce a phenomenological way to understand the emergence of YSR subgap states. This phenomenological picture is supported by the zero-bandwidth (ZBW) limit, in which the superconductor is replaced by a single quasiparticle at energy Δ [19–21].

In the limit $U \gg \Delta$ required for YSR physics, in addition to $U \gg \Gamma$, the quantum dot is effectively coulomb blockaded. Deep inside a coulomb diamond, e.g. $\xi_d \approx 0$, the nearest bare dot excitations cost $E_{ex} \approx U/2$, meaning that the lowest lying excitation is a quasiparticle at Δ. In the vicinity of dot groundstate transitions, i.e. $\xi_d \approx \pm U/2$, the coulomb diamond lines move inside of the gap. Due to tunnelling H_T, these lines anti-cross with the gap at $E_{ex} \approx \Delta$ as the excited dot states can hybridize with quasiparticle states. This leads to the appearance of delocalized excited states, such as $a|\sigma, 0_{qp}\rangle + b|0, \sigma_{qp}\rangle$ for groundstate $|0, 0_{qp}\rangle$, with entrances referring to electron and quasiparticle number respectively. Since Bogoliubov quasiparticles only conserve electron parity (odd or even), and not electron number, dot occupation stops being a good quantum number. Instead, we use the total fermion parity of H as our quantum number, and due to Kramers degeneracy odd parity is a doublet state ($\mathcal{D}$), while even is a singlet ($\mathcal{S}$). As a consequence, only a single $\mathcal{S} \leftrightarrow \mathcal{D}$ excitation line is present inside of the gap as depicted in fig. 1.2. When this line crosses zero it signals a groundstate transition between the even and odd parity state.

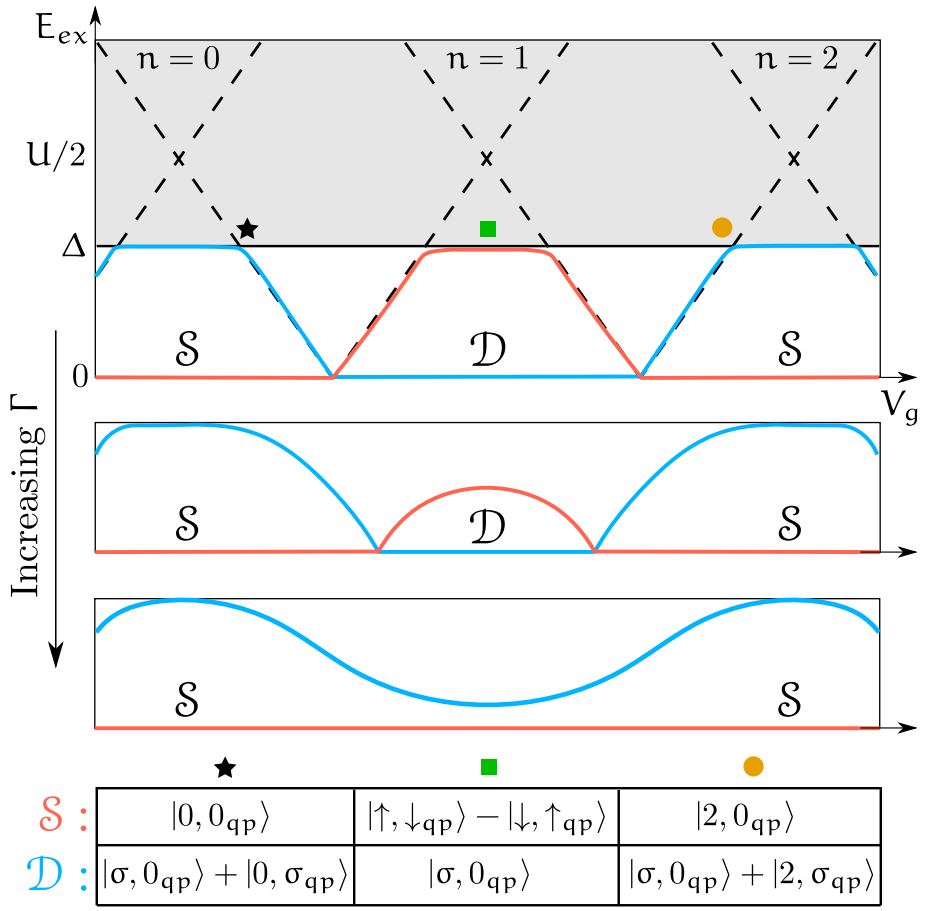

Figure 1.2: Schematic of the dot-superconductor excitations as a function of gate V_g with n (in the top) denoting bare dot occupation inside coulomb diamonds, and symbols referencing the bottom table. Dashed lines indicates excitations of the uncoupled dot, and the grey overlay shows the gap. The red and blue subgap line shows the even and odd parity state respectively, with $\mathcal{S}$ and $\mathcal{D}$ indicating current groundstate. Plots below illustrates the effect of increasing coupling on subgap spectrum. Bottom table schematically shows the composition of states $\mathcal{S}$ and $\mathcal{D}$ at gates indicated by symbols.

Importantly, at the center of the odd coulomb diamond ($\xi_d \approx 0$), the even parity excited state is composed of a single electron and quasiparticle $|\sigma, \sigma'_{qp}\rangle$, both carrying a spin-1/2 degree of freedom. Due to tunnelling the $|\uparrow, \downarrow_{qp}\rangle$ and $|\downarrow, \uparrow_{qp}\rangle$ combinations are coupled to the higher energy $|0, 0_{qp}\rangle$ and $|2, 0_{qp}\rangle$ states, facilitating magnetic exchange through virtual transitions. This is captured by the *Schrieffer-Wolff transformation* [22–24], which maps the Anderson model into a Kondo exchange model,

$$H_D + H_T \xrightarrow{S.W} H_K, \tag{1.6}$$

valid at the center of the odd $n = 1$ diamond for $U \gg \Gamma \gg \Delta$, and with $\alpha = \pi \nu_F J \propto \Gamma/U$. This mapping connects quantum dots to magnetic impurities, but in contrast to the

classical spin presented in the previous section, the resulting impurity consists of the dot electrons spin-1/2 degree of freedom. Phenomenologically, the effect of this quantum spin is similar to the classical spin; the even parity state, with an excited quasiparticle at energy Δ forms an exchange bond with the dot electron,

$$|S\rangle \approx \frac{1}{\sqrt{2}} \left(|\uparrow, \downarrow_{qp}\rangle - |\downarrow, \uparrow_{qp}\rangle \right) \tag{1.7}$$

lowering the state's energy and moving it inside of the gap. As Γ increases, the energy won by exchange increases correspondingly, moving the state further into the gap. At a critical $\Gamma \sim U$ this gain in energy is larger than Δ, and the groundstate transitions from an odd spin-1/2 state into a non-magnetic screened singlet state, which we recognize as the YSR state. The effect of increasing Γ on the exchange singlet state is depicted in fig. 1.2. Although this picture is fairly simple, calculations are complex and no tractable analytical solution exists for a spin-1/2 impurity. Theoretically, this complexity stems from higher order spin correlations, appearing first at third order (J^3) in perturbative expansions, containing logarithmic terms $\log(D/\Delta)$, where D denotes bandwidth and Δ provides a low energy cutoff. These terms are a characteristic feature of the Kondo problem [8], where in the case of a normal lead the low energy scale is typically temperature T, yielding logarithmic terms $\log(D/T)$ instead. Going beyond our phenomenological picture from the ZBW model, and by drawing inspiration from the *Yosida anzats* [25], these higher order terms appear due to interactions of the dot-spin with multiple quasiparticles at various frequencies, resulting in a complicated exchange singlet state,

$$\begin{aligned} |\uparrow, \downarrow_{qp}\rangle = &\int_{\Delta}^{D} d\omega_1 a(\omega_1) |\uparrow, \downarrow_{\omega_1}\rangle + \int_{\Delta}^{D} d\omega_1 d\omega_2 d\omega_3 b(\omega_1, \omega_2, \omega_3) |\uparrow, \downarrow_{\omega_1} \uparrow_{\omega_2} \downarrow_{\omega_3}\rangle \\ &+ \mathcal{O}(5qp) \end{aligned} \tag{1.8}$$

with frequencies denoting quasiparticle energies restricted by bandwidth D, and prefactors $a(\omega_1)$ and $b(\omega_1, \omega_2, \omega_3)$ denoting the spectral weight at each frequency. These prefactors can be obtained self-consistently through the Schrödinger equation up to a sufficient order of J, which at J^3 shows the aforementioned logarithmic terms in D [24, 26]. The appearance of these terms signals that a renormalization procedure of higher order terms is required to obtain a tractable model. The resulting energy scale T_K, denoting a Kondo temperature, fully characterizes the system insofar $U \gg \Gamma$, effectively removing the dependence of other scales in the problem, e.g. Γ, D, U. At the particle-hole symmetric point ($\varepsilon_d = 0$), the doublet groundstate switches to a screened singlet state at $T_K \approx 0.3\Delta$ [27]. Although, T_K better characterize transitions, throughout the thesis, we typically use Γ instead of T_K to address screening. This is motivated by

the low level approximations we apply, which do not display the logarithmic terms, and consequently does not yield a reasonable T_K.

The study of these interactions and the various limits of Δ, Γ and U is a rich field in its own right, with a number of competing approaches, most of which requires numerics. Next follows a short discussion of these approaches: The *numerical renormalization group* (NRG), based on Wilson's logarithmic discretization[28], can be generalized to the superconducting case [29] and reliably captures all parameter limits [30], but requires substantial numerical effort. Of particular interest is that this approach can describe the $T_K \gg \Delta$ limit where Kondo correlations dominate, and a resonant peak forms around the gap [30, 31], which evolves into the normal Kondo resonance as $\Delta \to 0$. In the YSR limit $T_K \gtrsim \Delta$ a number of numerically simpler approaches, including self-consistent spin-polarizing [20, 32] and spin-conserving [33, 34] Hartree-Fock mean-field theories, functional renormalization group [35, 36], and slave-boson expansion [37], has been used to investigate various properties of S-QD-S devices and related transport. Additionally, the limit of $\Delta \gg U, \Gamma$ known as the atomic limit, have also been investigated [38] and is analytically solvable for $\Delta \to \infty$. Here, instead of hybridizing with quasiparticles, the dot becomes proximitized by the superconductor, and the lowest subgap singlet state ($\mathcal{S}$) is at odd occupancy composed of a superposition of dot states, $|S\rangle = \frac{1}{\sqrt{2}}(|0\rangle - |2\rangle)$, which smoothly evolves into the YSR state as Δ decreases. Comparisons of these approaches can be found in Refs.[33, 36, 39].

1.3 EXPERIMENTAL REALIZATION OF YSR STATES

In order to investigate YSR states one requires a setup in which they not only appear, but where they also can be measured. This is commonly done by transport measurements, where the YSR state is contacted by a probe through which current can run. As the capabilities to create nanoscale devices evolved, two main routes to investigate YSR states have appeared: Using scanning tunnelling microscopy (STM) to probe magnetic impurities placed on superconducting substrates, or by contacting quantum dots to a source and drain lead. In STM setups YSR states from magnetic impurities have been measured by metallic tips [40–44], superconducting tips [45–50], and recently a tip hosting another YSR state [51]. In these setups the magnetic adatoms often host a complex orbital texture [52, 53], resulting in large spin degrees of freedom, which due to magnetic anisotropy typically can be modelled as classical spins. The advantage of these setups, compared to quantum dots, is the high resolution across large bias ranges [45], the ability to easily compare measurements of the impurity to the bare

substrate (by moving the tip), and the fine control of tip height enabling measurements across many magnitudes of tunnel coupling [46, 51].

In systems hosting YSR states from quantum dots one lead is necessarily superconducting, while the other lead, typically coupled weekly to simplify interactions, can be either metallic (S-QD-N) or superconducting (S-QD-S). Quantum dots have in these setups typically been formed on carbon nanotubes or nanowires placed, capacitively coupled to bottom gates with which a dot geometry is tuned, although examples of YSR in self-assembled dots [54] and gated molecules [55, 56] also exists. On these setups, both the S-QD-N geometry [54, 57–63], and the S-QD-S geometry [55, 56, 64–74] have been extensively explored through bias spectroscopy. The typical features from such measurements are very similar to STM, with two subgap conductance peaks located at bias $eV = \pm E_0$ in the S-QD-N geometry, and at $eV = \pm(E_0 + \Delta_R)$ in S-QD-S, where Δ_R is the gap of the probing superconductor. These conductance peaks stem from transport processes, which become available when the probes electron (hole) density of states is aligned with YSR states hole (electron) peak, as depicted in figs. 1.3 (a, b). Examples of YSR state bias spectroscopy in a S-QD-N and S-QD-S geometry is shown in figs.1.3 (c-e), and the observed gate dependence can be compared to sketches in fig. 1.2. The advantages of quantum dot setups compared to STM are: the easy gating of ξ_d controlling dot occupancy over many orbitals as shown in fig. 1.3, the large tuneability of couplings as the geometry can be tuned by gate [58, 62, 75], the certainty from coulomb blockade that the free spin is spin-1/2, and the ease at which YSR junctions can be integrated into larger circuitry as the system is fabricated on chip. An example of larger circuitry includes SQUID interferometers, enabling the measurement of a YSR state's full current phase relation (CPR) [67, 76–78], which have revealed the predicted π phase ($I = I_c \sin(\phi + \pi)$) at odd dot occupation, heralded by negative supercurrent for $\phi \in \{0, \pi\}$ [39], and the elusive ϕ_0 phase ($I = I_c \sin(\phi + \phi_0)$) [79]. In summary, these rich studies of YSR states in both STM and quantum dot junctions have allowed tuning, manipulation and measurements of single subgap states across a large parameter space.

Next, we focus on YSR states in other setups and highlight potential uses and issues. A number of nanowires show signatures of YSR states originating from, often unintentional, dots. This commonly occurs if a section of wire is strongly depleted by a gate, thereby close to pinch-off, and may depend on the length of the wire [80]. This has been observed in *gatemons* [81], where sharp resonances are measured close to depletion [82].

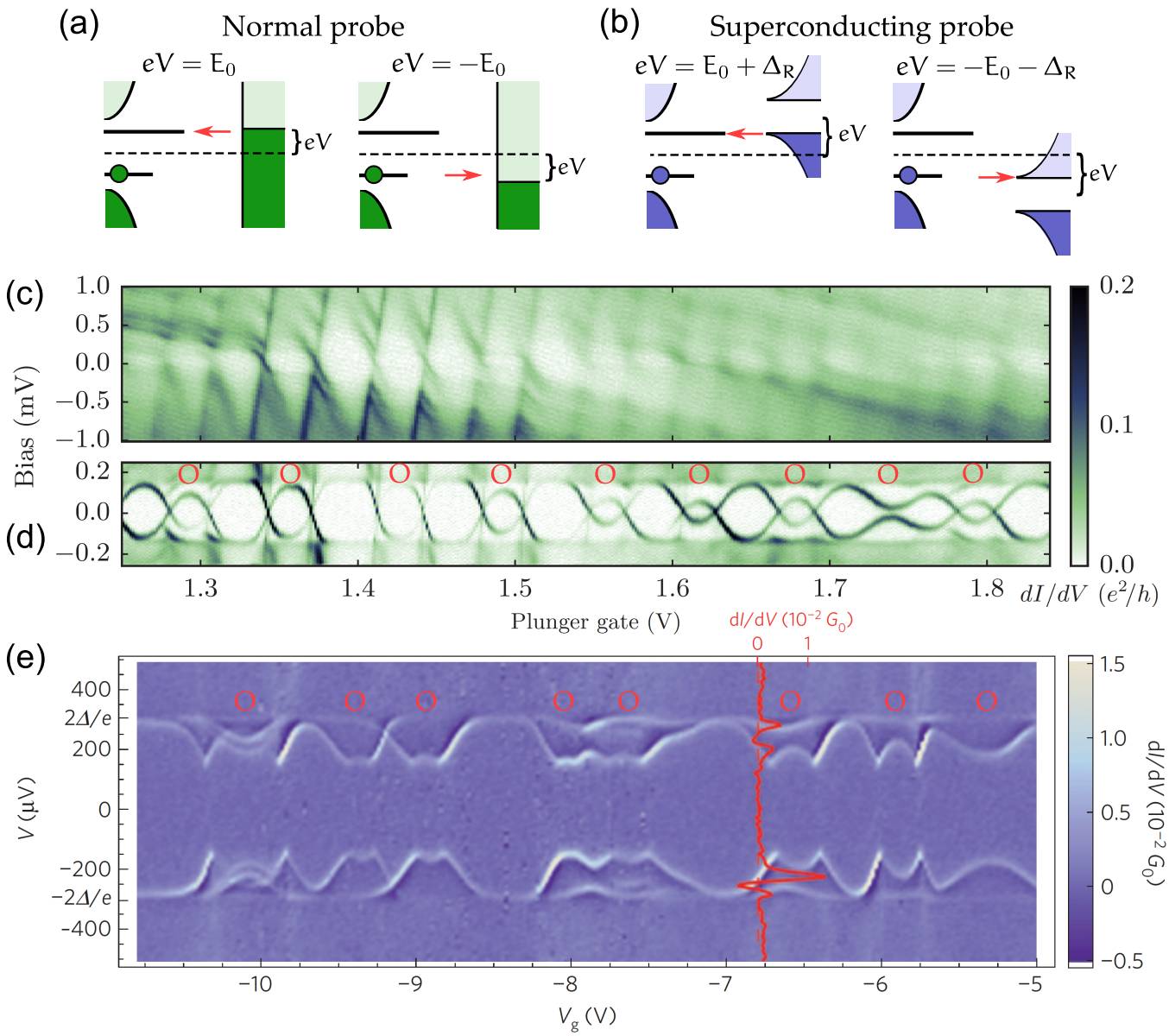

Figure 1.3: Schematics of transport at threshold bias eV involving a YSR state for a normal lead (a), and a superconducting lead (b). Colors relate to (c, d, e), with dark tones indicating filled states and light tones empty states. (c, d) Differential conductance as a function of gate in a S-QD-N setup with (c) and without (d) an applied 150 mT magnetic field to drive the S lead normal. Heavily broadened coulomb diamond in (c) correspond to odd subgap states deep in the gap in (d), corresponding to large coupling Γ. Red rings indicate position of odd occupation diamonds. (e) Differential conductance as a function of gate in a S-QD-S setup. Features are similar to (d), but displaced from zero by Δ_R due to processes (b). Red inset shows a conductance linecut, while red rings indicate odd occupation diamonds. Rings are not as evenly spaced as in (d), due to the multiorbital nature of the carbon nanotube measured in (e), compared to the InAs nanowire measured in (c, d). Figures (c, d) are adapted from Ref. [75] while (e) is adapted from Ref. [67].

As stated in Ref. [82] the presence of a dot is not necessarily detrimental; the proximity of a resonance renders the critical current I_c, characterizing the Josephson energy, E_J, highly tuneable, and can be tuned almost to a perfectly transmitting single channel. In addition to uses as tuneable Josephson junctions in superconducting quantum electrodynamics (QED), the YSR subgap states themselves also constitute a quantum degree of freedom [83]. This can be utilized in Andreev spin qubit designs [84], or by photons coupling to the YSR's CPR [85] in QED circuits, as done for quantum point contact (QPC) experiments in e.g. Ref. [86]. Additionally, the InAs nanowires on which YSR states have been studied are very similar to devices built with topological superconductivity in mind, where experimental signatures of *Majorana boundstates* are sought [87]. Consequently, measurements of zero-bias conductance peaks can also be attributed to topologically trivial Andreev states (see review Ref.[88]), where e.g. YSR states can lead to 'robust' zero-bias peaks [89]. As dots form both unintentionally and intentionally, when used as probes [87, 90], on superconducting nanowires it is important to be able to identify transport features stemming from YSR states. Accounting for these observations further research into the formation, measurement and characterization of YSR states in quantum dots is of great value to the expanding field of nanowire semiconductor-superconductor qubits.

1.4 THESIS OUTLINE

In this thesis we primarily investigate transport across serially coupled double quantum dots (DQD) in superconducting junctions, i.e. S-DQD-S geometry. This geometry hosts rich competition between various tunnel couplings and as of its high tuneability, allows for measurements of many different regimes. Specifically, the presence of two superconducting leads, compared to one superconducting lead (S-DQD-N) addressed in the author's master thesis [21, 62], enables us to measure the superconducting version of the famous *two-impurity Kondo model* [8, 91], where interdot exchange interaction competes with the simultaneous screening of both dot spins. Similar to adatom chains measured with STM [92–94], predicted to host Majorana states at the boundary [95, 96], 1D quantum dot arrays also mimic Kitaev chains [97], and correspondingly can host Majorana states [98–100]. In this regard, characterizing and controlling the S-DQD-S setup is an important stepping stone for the realization of larger arrays.

This thesis is composed of five projects, all focussed on experiment, for which the author has provided theoretical support. These projects labelled 1 to 5 are all published, with the exception of no.3 currently submitted for publication in PRL. Additionally, projects 1 to 3 are all performed on a single DQD device and concordingly this thesis

will primarily focus on transport in this device. Lastly, as the bulk of this work is provided in the articles supplemental material, this thesis is written in a 'supplement first' manner with the aim of highlighting the theoretical work.

This chapter, in combination with chapter 2 presenting the DQD experiment, serves as an introduction. The following chapters 3 to 6 focus on measurements of supercurrent. In chapter 3 we derive the necessary circuit equations to fit supercurrent by an Ex-RCSJ model, from which we extract the critical current I_c. This is then compared to theory in chapter 4, where I_c is obtained from lowest order perturbation theory. We show the resulting papers of this work in chapter 5 and 6, where we succeed in fully screening the DQD.

From there we turn our attention to finite bias spectroscopy. In chapter 7 we derive the Floquet Keldysh Green's function equations required to calculate DC current at finite bias. In chapter 8 we use a spin-polarizing mean-field approximation to obtain non-interacting Green's function to use in DC calculations, and present a number of single dot results. This is used in project 3, presented in chapter 9, where direct transport between two subgap states is measured. This papers supplemental material is included in chapter 10.

Lastly, projects 4 and 5, which are performed on different experiments, are presented in chapter 11 and 12. Here we used techniques derived in the previous chapters to aid in data interpretation and fitting. Afterwards, we present the conclusion in chapter 13.

2

DOUBLE QUANTUM DOT EXPERIMENT

In this chapter we present the experiment which forms the basis of the first three projects of this thesis. In presenting this work, it should be clear that I as a theorist have not participated in either fabrication or measurement, and my contributions are limited to data interpretation, analysis and model development. Nonetheless, this experiment, and indeed this single device, takes such a central role that a proper introduction and walk-through is required. To the authors knowledge, only three other YSR experiments in the S-DQD-S geometry exists [4, 67, 101]. Of these, Ref. [67] is effectively probed as a single dot, while Ref. [101] contains a significant soft-gap obscuring features. The last device is part of this thesis, presented in chapter 11.

2.1 INTRODUCTION

The original goal of the experiment was to expand upon earlier work in which YSR screening was investigated in a double quantum dot, contacted by a normal and superconducting lead (S-DQD-N) [62], for which the author also supplied theory [21]. In that experiment, characterization was done by spectroscopy with the normal lead acting as a weakly coupled probe, revealing identifiable charge diagrams and characteristic YSR subgap states, whose dispersion followed theoretical expectations. In regard to screening the double quantum dot, this device was limited, as the single superconducting lead could only screen the nearest dot, and consequently full screening of both dot spins where unachievable.

In producing a double quantum dot contacted by two superconducting leads (S-DQD-S), the goal was to achieve full screening, and to investigate the interplay between YSR states formed on each dot. The device consist of a 110 nm diameter InAs nanowire, with 7 nm epitaxial aluminium grown *in situ* on three facets. The wire is placed on a bed of finger gates isolated by 20 nm of hafnium oxide serving as a dielectric barrier. The epitaxial aluminium is etched away above the five bottom gates, and the wire is contacted by metallic Ti/Au strips serving as source and drain. These are placed about one 1 μm from the central etched region as shown in fig. 2.1. In addition to the bottom

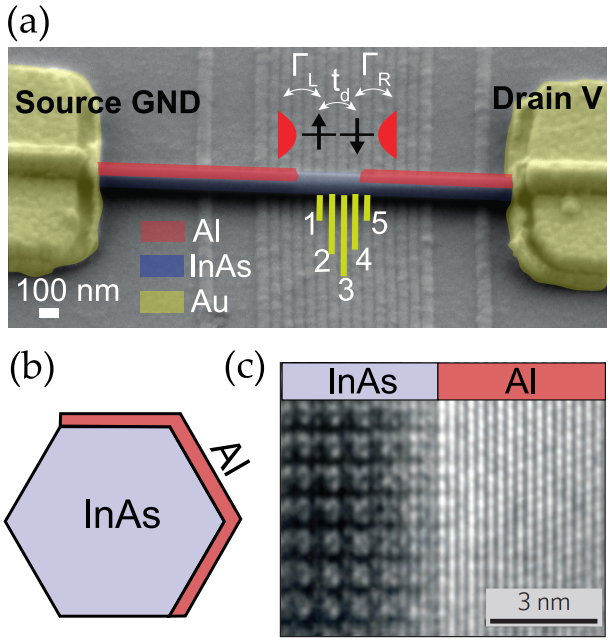

Figure 2.1: (a) False coloured scanning tunnelling micrograph of the device, with the five bottom gates used to define the double quantum dot highlighted. Schematic of the double quantum dot is shown above. (b) Schematic of the wire with 7 nm epitaxial aluminium grown on three facets. (c) High resolution transmission electron microscopy image of a similar InAs wire with epitaxial aluminium, showing the pristine interface between Al and InAs adapted from Ref.[102]

gates, the Si substrate on which the device is placed is used as a global backgate and separated by 300 nm Si oxide from the device.

By tuning the five bottom gates a double well potential can be formed, effectively behaving as a double quantum dot, with gate 2 and 4 primarily controlling dot occupancy. These two dots are tunnel coupled to the aluminium covered InAs wire on either side, acting as superconducting leads. Gates 1, 3 and 5 control left, interdot and right tunnel coupling respectively, by setting the size of the intermediate potential barrier electrons tunnel across. In this geometry one does not *a priori* know if the superconducting leads consists of the epitaxial aluminium, a region of proximitized InAs or a combination thereof. By enforcing a source-drain bias, the double quantum dot effectively serves as a junction between the two superconducting leads, thus enabling spectroscopic measurements of the S-DQD-S system. Due to low yield in fabrication the device was designed for two terminal measurements [103] instead of four terminal, making it harder to investigate the surrounding electromagnetic environment experienced by the junction.

Measurements are carried out in a $T \approx 20$ mK dilution fridge where differential conductance dI/dV is extracted through standard lock-in technique, using an AC signal of amplitude 2 μV in conjunction with a tuneable DC component V. Current, I, is measured simultaneously by a digital multimeter. On the bias-line into the dilution fridge there are filters with a total resistance $R_S = 8.24$ kΩ, which determines the load-line resistance. In this two terminal setup, voltage drop across R_S is subtracted and we define $V_{sd} = V - R_S I$ as the voltage drop across source-drain yielding the following differential conductance,

$$\frac{dI}{dV_{sd}} = \frac{dI}{dV}\left(1 - R_S \frac{dI}{dV}\right)^{-1}. \tag{2.1}$$

In this manner, current characteristics I - V_{sd} and differential conductance spectroscopy V_{sd} - dI/dV_{sd} can be performed.

2.2 DOUBLE QUANTUM DOT CHARACTERISTICS

At this day and age, double quantum dots is a well established subject and they are widely used in qubit proposals [104, 105] with particular focus on spin-qubits. In common setups, the double quantum dot is contacted by two metallic leads and characterization is done by use of charge diagrams, which consists of measuring zero-bias conductance as a function of the gates controlling dot occupations [106]. Next, we will give a short overview of this subject in relation to our specific device.

By gating a dot, electrons can be added or removed one by one each time electrostatic energy, tuned by bottom gate V_g, overcomes charging energy U. Accounting for all charging energies the Hamiltonian for a double quantum dot with N_L (N_R) orbitals on the left (right) dot can be written as,

$$H = H_D + H_T, \tag{2.2}$$

$$\begin{aligned} H_D = {} & \frac{U_L}{2}\sum_i^{N_L}\left(n_{Li} + \delta_{Li} - V_{g1}\right)^2 + \frac{U_R}{2}\sum_j^{N_R}\left(n_{Rj} + \delta_{Rj} - V_{g2}\right)^2 \\ & + U_L\sum_{i\neq j}^{N_L} n_{Li}n_{Lj} + U_R\sum_{i\neq j}^{N_R} n_{Ri}n_{Rj} + U_d\sum_{ij}^{N_L,N_R}\left(n_{Li} + \delta_{Li} - V_{g1}\right)\left(n_{Rj} + \delta_{Rj} - V_{g2}\right), \end{aligned} \tag{2.3}$$

$$H_T = \sum_{ij}^{N_L,N_R}\sum_\sigma t_{ij} d^\dagger_{Li\sigma} d_{Rj\sigma} + h.c. \tag{2.4}$$

Here the left/right charging energy $U_{L/R}$ is assumed constant across all levels, $n_{L/Ri} = \sum_\sigma n_{L/Ri\sigma}$ is the electron occupation operator for the ith level with corresponding

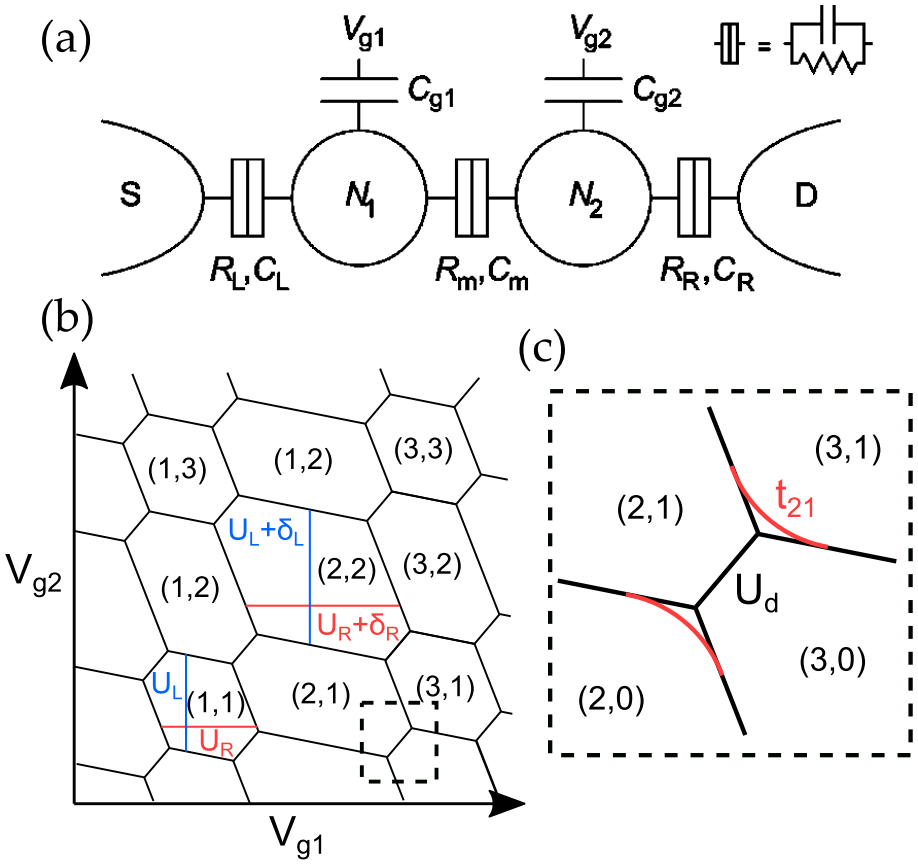

Figure 2.2: (a) Schematic of a classical double quantum dot with charging energies stemming from capacitive couplings. Taken from Ref.[106]. (b) Schematic of the charge diagram obtained from eq. (2.2). Numbers refer to groundstate electron occupation (n_L, n_R), and lines mark degeneracies between charge states at groundstate crossings. Dashed inset marks position of (c). (c) Zoom in at a triplet point with red lines indicating the effects of finite interdot tunnelling t_{ij}. (b-c) are adapted from Ref.[106]

$d_{L/Ri\sigma}$ annihilation operator, U_d is the interdot charging energy assumed constant, and $\delta_{L/Ri}$ accounts for level spacing between different electron orbitals on the left/right system. H_T introduces tunnelling between various levels on the left and right dot, with tunnel coupling t_{ij}. Written in this form, V_{g1} and V_{g2} are on the scale of $U_{L/R}$, but in experiment the actual scale of gate 2 and 4 controlling these parameters are *a priori* unknown. In the classical model [106], depicted in fig. 2.2 (a), the various charging energies can be inferred from capacitances, but in typical devices they are estimated from measurements of coulomb diamonds, as we show later.

In the range of small interdot couplings $U_d, t_{ij} \ll U_L, U_R$, each dot can independently be charged and the groundstate of eq. (2.2) can be described by number states $|n_L, n_R\rangle$ whose occupation increases with increasing gates. The occurring pattern is known as

a honeycomb diagram, shown in fig. 2.2 (b), and is characterized by charge sectors surrounded by sectors of ± 1 electron on either dot. As each level can contain two electrons, one of either spin, sectors of even n_L and/or n_R appear elongated since the sectors atop and underneath represent different levels separated by energy $\delta_{L/R}$. Each such pair of levels, centered around charge states where both n_L and n_R are odd, is known as a shell. If both dots are weakly coupled to a metallic lead resonant transport will occur at charge degeneracies, where electrons are more easily transferred. This occurs along each line of the honeycomb diagram resulting in significant zero-bias conductance around each charge sector. Especially in the vicinity of triple points, shown in fig. 2.2 (c), will transport be enhanced as both dots are close to charge degeneracies. As such, by measuring zero-bias conductance one expects to obtain a map resembling fig. 2.2 (b) showing the shell-filling of each dot.

Next, we account for the effect of finite interdot tunnel coupling t_{ij}. In the proximity of triple points interdot tunnelling allows transitions of the type $|n_L, n_R\rangle \leftrightarrow |n_L \pm 1, n_R \mp 1\rangle$, which changes the groundstate into a superposition of charge states, lowering its energy. The effect of this is the formation of anti-crosses at triple points, as depicted in fig. 2.2 (c). A major difference between sectors of total odd occupation and even occupation is the groundstates degeneracy; for odd states the groundstate is a degenerate Kramers spin doublet, while for even states where both n_L and n_R are even the groundstate is a singlet state. Lastly, at a center of a shell where n_L and n_R are both odd the groundstate becomes an exchange singlet state $|S_{ex}\rangle = \frac{1}{\sqrt{2}}(|\uparrow,\downarrow\rangle - |\downarrow,\uparrow\rangle)$ with arrows referring to spin on left/right dot in the given shell, due to the effect of exchange interactions. This exchange coupling arises from virtual transitions through states $|2,0\rangle$ and $|0,2\rangle$ by interdot tunnel coupling, and gives a splitting of scale $t_{ij}^2/U_{L/R}$ to a three times degenerate triplet state.

For our device, measurements of zero-bias conductance $G = dI/dV_{sd}(V_{sd} = 0)$ is performed across a large range of gate 2 and 4 who tune dot occupation. A wide field view is shown fig. 2.3 on a logarithmic scale. We observe a pattern resembling shell filling with three visible shells labelled X, Y and Z, showing large level spacing $\delta_{L/R}$ on the scale of $U_{L/R}$. The measured conductance is strongly enhanced in the vicinity of shell X and Y, while conductance for shell Z is fainter and particularly enhanced at the triple points. Additionally, the triple points appear closed for shell Z, in contrast to shell X and Y, which naively indicates that interdot tunnel t_Z and interdot coulomb coupling U_Z are small on scale of $U_{L/R}$ for this shell. Lastly, charge instabilities around $V_{g4} \approx -0.4$ V appear. Such switchings, due to single electron trapping, are unfortunately commonplace in nanoscale devices. The above interpretation is supported by additional measurements of coulomb diamonds, which in this device are typically on

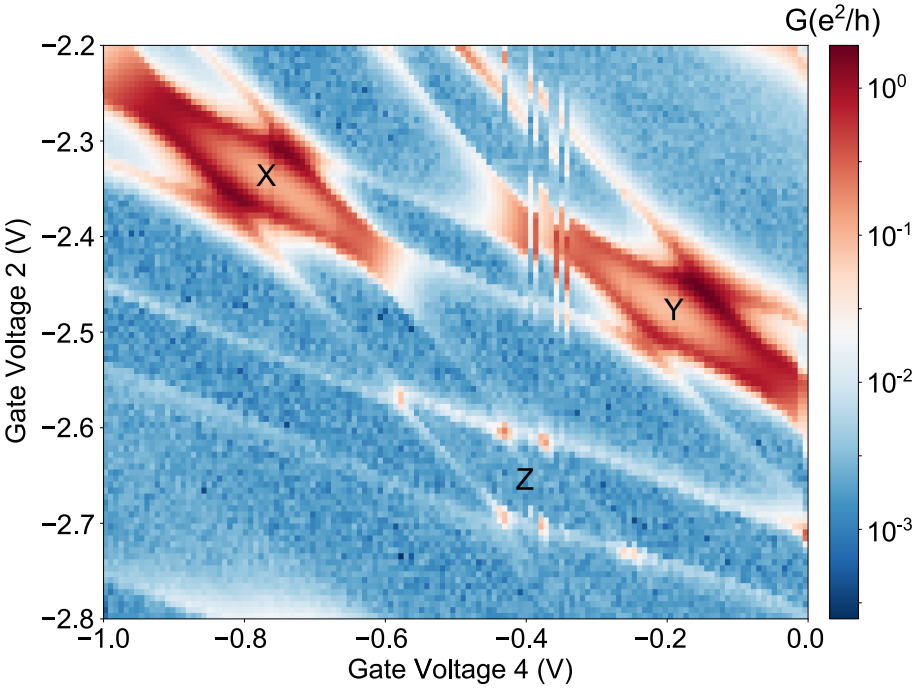

Figure 2.3: Zero-bias conductance colormap in logarithmic scale. Three identifiable shells appear, labelled X, Y and Z. Charge instabilities around $V_{g4} \approx -0.4V$ (Gate Voltage 4) are visible. For additional details and gate settings se supplement of Ref. [1].

the scale of $U \approx 2$ meV, and of a pristine superconducting gap of size $\Delta \approx 0.27$ meV (measured at a different backgate), placing us firmly in the YSR regime $\Delta \ll U_L, U_R$. These measurements can be seen in the supplement of Ref. [1] in fig. S1 and fig. S6 respectively. Lastly, although we expect InAs nanowires, including our device, to contain significant spin-orbit coupling we neglect it in modelling as we only focus on measurements with no magnetic field present. In this case, spin-orbit coupling is not expected to play a significant role, and due to Kramers degeneracy odd occupation doublet states are still degenerate, although spin is not a good quantum number [107].

At this juncture, we should remind ourselves that zero-bias conductance is measured across two superconducting leads with the double quantum dot in between, and not two metallic leads from which charge diagrams are normally obtained. This raises two major questions: what is the zero-bias signal that we measure, since normal resonant transport cannot occur between two gapped density of states, and what of the YSR screening which supposedly should occur between dot and superconducting lead? In the two following sections we will elaborate on these subjects by considering bias spectroscopy of shell X at low and high bias.

2.3 LOW-BIAS SPECTROSCOPY

In this section we explore in greater detail the zero-bias signal used to identify charge diagrams in the previous section by considering various gate linecuts through shell X at finite source-drain bias. In fig. 2.4 (a) we show zero-bias conductance for shell X but in a slightly different gating configuration*. The various charge sectors are labelled by expected left and right dot occupation for this particular shell. Panels fig. 2.4 (b-e) shows differential conductance linecuts taken across shell X with (b, c) cutting through an odd occupation sector and (d, e) through the (1,1) sector. The main contribution to zero-bias conductance is identified as a bias symmetric peak approximately 18 μV wide, which across all cuts sticks to zero. This feature is flanked by peaks of negative differential conductance (NDC) who appears to stick at $V_{SD} \approx \pm 12$ μV. Additionally, the height of the NDC peak follows monotonically the zero-bias peak. We claim that these two features stems from supercurrent with the double quantum dot operated as a Josephson junction, and is related to the cotunneling of cooper-pairs across the junction which we investigate in chapter 3 and chapter 4.

At higher bias, we see conductance features whose position varies with gate. Some of these features show subsequent NDC while others do not. A common trend is that they close in around and sometimes cross zero-bias at the same gate as extrema of the supercurrent peak occurs. These features are not easily identifiable even through we, due to their eye-like dispersion, relate them to transport involving YSR subgap states. In chapter 8 we discuss low-bias transport cycles which can yield features of this kind, but the precise identification of all features remain beyond the scope of this work.

* It is quite common for this device that gate configurations varies slightly between datasets as charge trapping effects, similar to those in shown in fig. 2.3, moves shells slightly between different scans

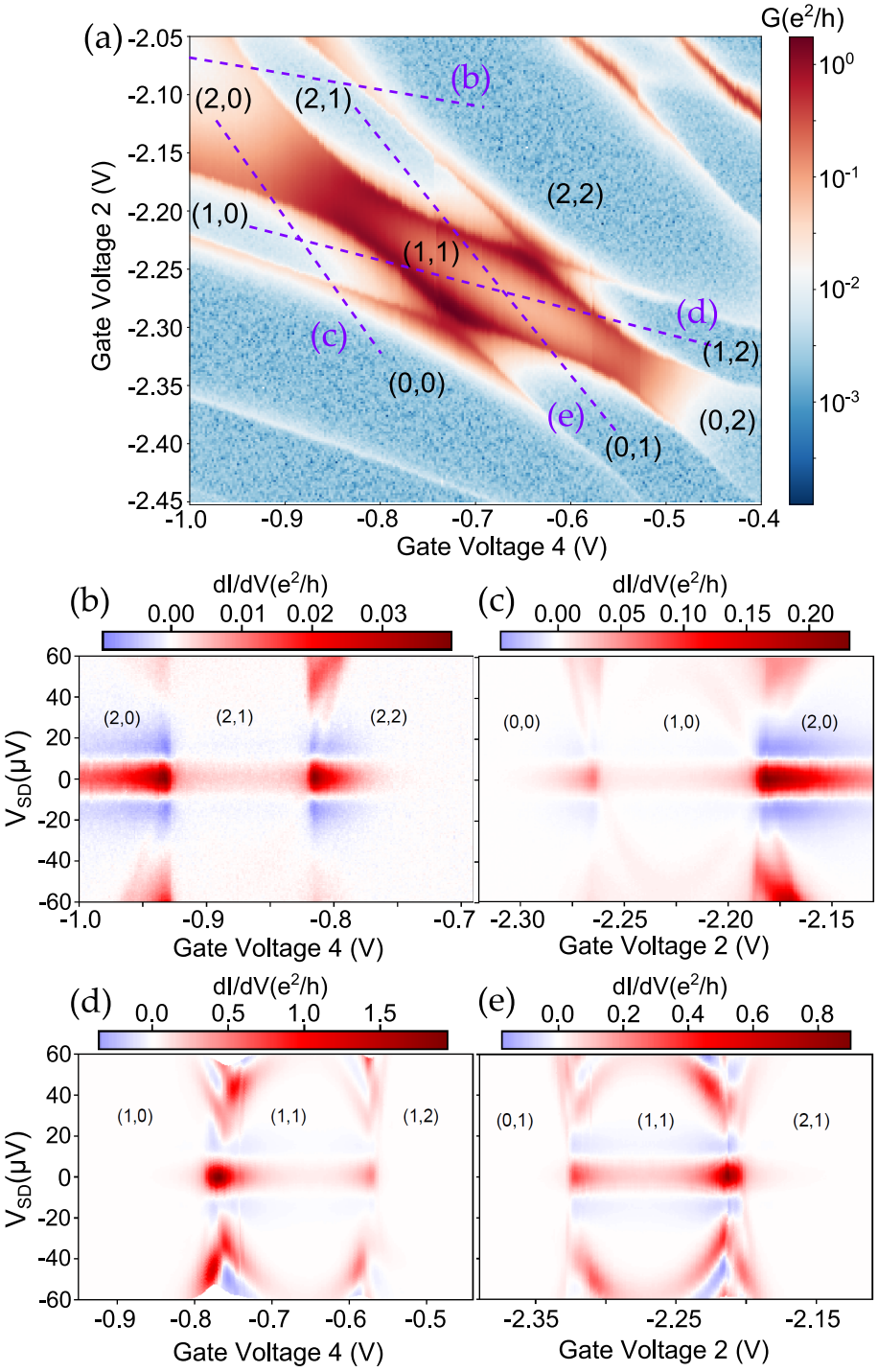

Figure 2.4: (a) Zero-bias charge diagram of shell X. Numbers (n_L, n_R) indicate expected electron occupation for each sector. Purple dashed lines show the gate tuning of linecuts (b-e). (b-e) Bias linecuts taken across (a) with (b, d) parametrized by Gate 4 and (d, e) parametrized by Gate 2. (b-e) are adopted from Ref. [103]

2.4 LARGE-BIAS SPECTROSCOPY

Next, we discuss spectroscopy of shell X with bias on the range of observed superconducting gaps. As previously stated, the original intent was to characterize the double dot using differential conductance measurements to perform subgap state spectroscopy. This turned out to be more complicated than initially expected due to three issues: (1) it is in practice hard to determine what left lead feature is probing what right lead feature, as both are expected to host subgap YSR states in addition to the weakened gap. (2) the number of scales. For shell X we expect interdot coupling t_X to be of similar scale as left and right tunnel coupling, making it hard to differentiate between dot bonding states and YSR states. (3) the observed gap is not of size $\Delta = 0.27$ meV as measured in another gate setting, but appears to be around $\Delta^* \approx 0.15$ meV for both dots. Our interpretation is that the effective InAs-Al gap is composed of a cluster of Andreev states below 0.27 meV, similar as in Ref. [73, 90], arising from the complicated interaction between InAs wire and epitaxial aluminium [108]. A schematic of the expected left and right lead density of states are shown in fig. 2.5 (a, b). Fig. 2.5 (c-f) show measurements of differential conductance along the same linecuts as in fig. 2.4. In all four cuts we observe split YSR like eye-shapes seemingly at $eV = \pm(E_s + \Delta^*)$ similar to measurements shown in fig. 1.2 (e). As stated above, we are not sure if it is a gap or subgap state probing the opposing subgap state, but the energy dispersion as a function of gate is indicative of a YSR state tuned by gate, probed by some stationary feature on the opposing lead. These YSR like conductance features show kinks in slope at the same gate voltage as extrema of supercurrent occurs. We interpret these kinks as groundstate changes between YSR singlet and doublet groundstates, similar to the single dot picture, since each dot is independently gated along the chosen cuts. The source-drain bias position of these kinks varies between cuts, making it hard to identify the probing feature.

In summary, even though the curvature and slope of the main feature supports a YSR interpretation, we have as of yet, not been able to explain these measurements with any simple model. Consequently, in our work focusing on shell X we only use these large-bias results in a supportive role, as in chapter 6, effectively abandoning the idea of spectroscopic characterization. An exception to this is shell Z, which was simpler to interpret due to the smallness of t_Z and U_Z reducing complexity. Here clear signatures of transport between opposing subgap states is identifiable, which we treat in detail in chapter 9.

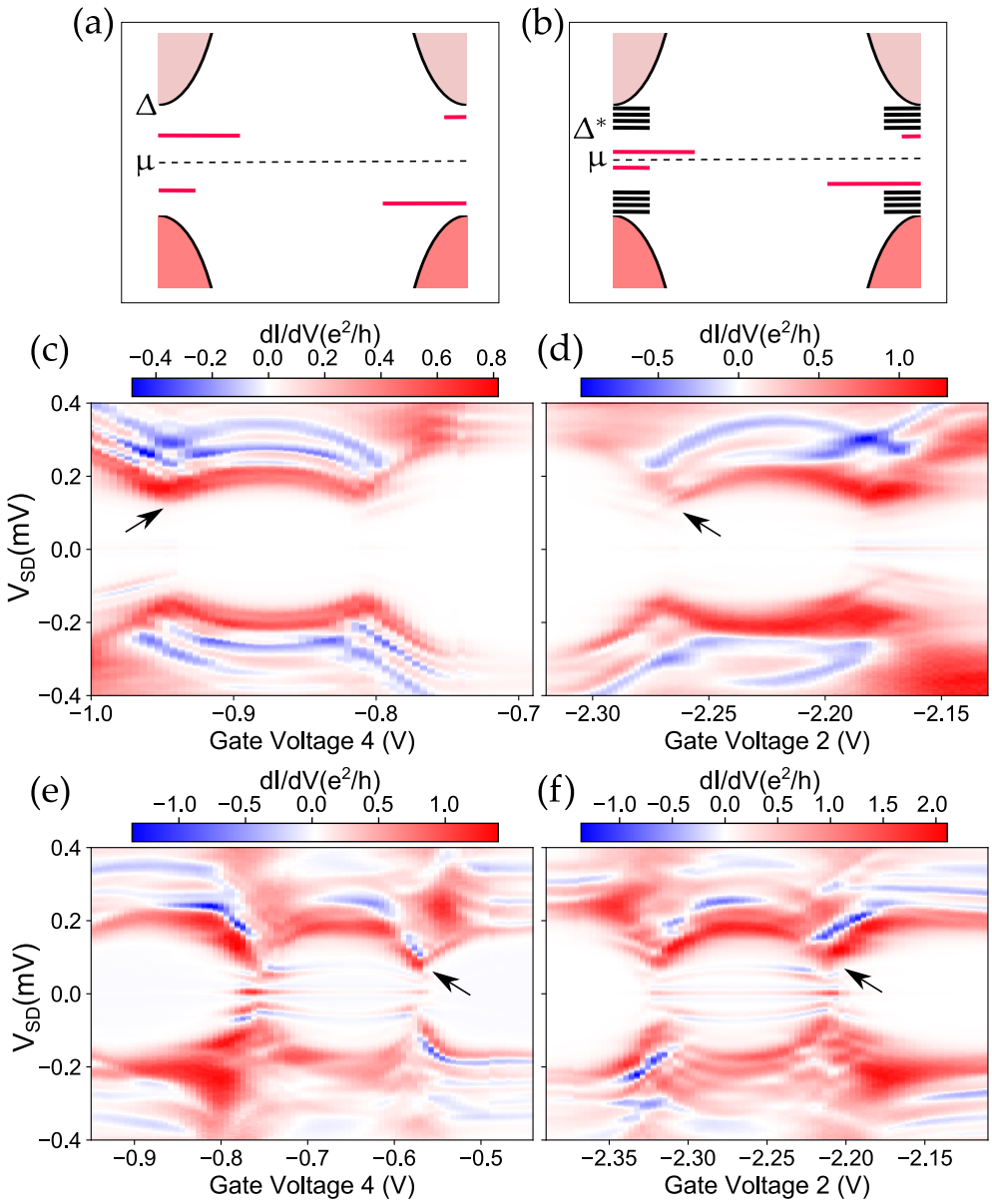

Figure 2.5: (a, b) Schematic drawing of the two opposing leads density of state, hosting subgap states coloured red. With (a) a pristine gap, and (b) a cluster of subgap states acting as a effective gap. (c-f) Bias linecuts taken across fig. 2.4 (a) with (c, e) parametrized by Gate 4 and (d, f) parametrized by Gate 2. Arrows indicate kinks in slope observed of the eye-like conductance feature.

2.5 SUMMARY AND OUTLOOK

The presented data supports that the experiment have successfully achieved a double quantum dot contacted by two superconducting leads. The strongest evidence being the zero-bias conductance map strongly resembling traditional charge diagrams with clear signatures of shell filling. Although, the original intent was to characterize the device and YSR interactions via subgap spectroscopy this turned out to be more complicated then anticipated. Nevertheless, in spectroscopy we do observe features showing characteristics of YSR states, and from the eye-like shapes we estimate that coupling to left and right lead is low to intermediate with the odd occupancy groundstates unscreened. With these considerations in mind, we decided to prioritize the study of the zero-bias supercurrent peak and utilize that to characterize the S-DQD-S device. In order to achieve this goal, we first have to find a circuit model able to explain the zero-bias signal. A major obstacle in this regard is the limited knowledge of the local electromagnetic environment, as the device was not fabricated with this kind of measurement in mind. This is the topic of the next chapter.

3

OVERDAMPED JUNCTION IN THE EX-RCSJ MODEL.

Assuming that at low bias the S-DQD-S junction, described in chapter 2, behaves as a Josephson junction with a critical current I_c, we in this chapter utilize an extended resistively and capacitively shunted junction (Ex-RCSJ) model [109–111] to characterize supercurrent measured across the junction. This model have been used to characterize similar nanoscale devices containing quantum dots yielding either *underdamped* behavior [112–114] with hysteretic $I-V$ characteristics where switching and retrapping current can be measured by repetitive bias sweeps, or *overdamped* behaviour [115, 116] with non-hysteretic $I-V$ curves accompanied by a large reduction of supercurrent due to noise. For our device no hysteretic behaviour is observed and supercurrent appears as a zero-bias conductance peak whose amplitude, but not width, varies as a function of dot gating as shown in fig. 2.4. We ascribe the varying amplitude to gate dependence of the critical current I_c which we calculate for the S-DQD-S setup in chapter 4. Lastly, on nanoscale Josephson junctions, such as ours, it is a priori hard to know the precise electromagnetic environment experienced by the junction if it is not carefully designed. This is due to unintended stray circuit elements which can be of similar (or larger) scale then junction elements. As a consequence, we do not have a detailed understanding of circuit parameters, and the goal of this section will be to obtain a minimal, realistic, and consistent model of the measured supercurrent, with circuit elements regarded as somewhat free parameters.

The measured supercurrent signal is characterized by three important properties:

- *Overdamped* - Inferred from the lack of hysteretic switching.
- *Voltage biased* - Measurements of NDC as part of the supercurrent peak necessitates voltage biasing.
- *Constant cusp voltage* - Bias width of the zero-bias signature appears constant across gate tuning even though amplitude varies.

In the following section we expand upon these properties and demonstrate how they can be obtained first within a normal RCSJ model. Afterwards, we extend the model with an additional capacitor and resistance (Ex-RCSJ) in order to realistically describe

our experimental situation. These models are to a large degree already covered in the existing literature [110, 117], and the following account is primarily focused on their application to our device. Some confusion seems to exist on the subject as we believe the Ex-RCSJ model has been applied somewhat wrongly in previous overdamped devices [115, 116], which we detail in section 3.4.

3.1 RCSJ MODEL

In the RCSJ model the junction is described as an ideal Josephson element in parallel with a capacitor C_J capturing the effect of charge build-up on either side of the junction, and a resistor R_J accounting for low-bias ($eV \ll \Delta$) quasiparticle tunnelling across the junction. In general, the resistive element R_J could have a detailed dependence on bias if e.g. it originates from multiple Andreev tunnelling [117] or subgap states mirages [73] which we detail for single dot in chapter 8. For our objectives assuming a constant R_J suffices. Lastly, a voltage drop V is enforced by a source in series with a bias-line resistance R_S. A full schematic of the circuit is shown fig. 3.1 (a).

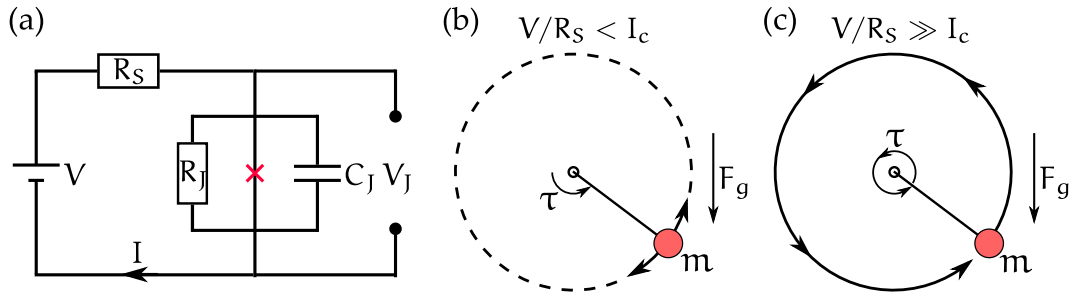

Figure 3.1: (a) Schematic of the RCSJ circuit. Red cross indicates the Josephson element. (b-c) Pendulum mapping of circuit dynamics for small bias (b) and large bias (c) compared to critical current I_c. Here $\tau = V/R_S$, $F_g = I_c$ and $m = C_J\Phi_0$ for a pendulum of unit length $l = 1$.

The Josephson element itself details the tunnelling of cooper-pairs across the junction yielding a dissipationless current I_J characterized by,

$$I_J = I_c \sin\phi \qquad \text{and} \qquad \frac{\partial\phi}{\partial t} = V_J/\Phi_0, \tag{3.1}$$

collectively known as the Josephson relations, where ϕ is the superconducting phase difference across the junction, V_J is the voltage drop across and $\Phi_0 = \hbar/2e$ the magnetic flux quantum expressed in $\hbar$. The critical current I_c is related to the co-tunnelling am-

plitude of cooper-pairs across the junction detailed in chapter 4. Applying Kirchhoff's laws to this circuit we find,

$$C_J \frac{\partial V_J}{\partial t} = V/R_S - I_c \sin\phi - V_J/\bar{R} \tag{3.2}$$

with $\bar{R} = \frac{R_S R_J}{R_S + R_J}$. For our purposes we consider V to be a applied constant and our objective is to find the solution for the canonical variables ϕ and V_J. Together with eq.(3.1) this equation maps onto a driven-damped pendulum,

$$\frac{\partial p}{\partial t} = \frac{\partial U}{\partial \phi} - \eta p, \quad \text{and} \quad p = m\frac{\partial \phi}{\partial t} \tag{3.3}$$

with angular momentum $p = C_J V_J$, angle ϕ, mass $m = C_J \Phi_0$, and potential $U = \tau\phi + F_g \cos\phi$ with gravity $F_g = I_c$ and a applied torque $\tau = V/R_S$ for a unitless pendulum length $l = 1$. Lastly, damping is provided by the friction $\eta = 1/\bar{R}\Phi_0$. From intuition, if we initialize the system at small angles $\phi \approx 0$ with an applied torque smaller than gravity $V/R_S < I_c$ we expect the pendulum to equilibrate at a fixed angle $\phi_0 = \sin^{-1}(V/R_S I_c)$ where torque cancels gravity. This constitutes the dissipationless *superconducting state* as the average 'angular momentum' $\langle V_J \rangle = 0$, while current $I_J = V/R_S$ remains finite. For torques much bigger than gravity $V/R_S \gg I_c$, we expect a rotating solution where the pendulum spins around its central axis periodically on a timescale T. If, furthermore, angular momentum is approximately constant during rotations, then phase ϕ will be evenly distributed from 0 to 2π, resulting in average zero supercurrent $\langle I_J \rangle = I_c \langle \sin\phi \rangle = 0$. This is known as the *resistive state* since a voltage drop $\langle V_J \rangle \neq 0$ have stabilized across the junction while no supercurrent runs. These two solutions, and the pendulum analogue, are shown in fig. 3.1 (b-c).

3.1.1 *Underdamped vs. overdamped behaviour*

To explore this in greater detail and investigate the effect of damping, it is useful to cast the equations in dimensionless form,

$$\frac{\partial u}{\partial \tau} = K - \sin\phi - u, \quad \text{and} \quad \frac{\partial \phi}{\partial \tau} = \frac{1}{\alpha} u, \tag{3.4}$$

with dimensionless voltage drop $u = V_J/\bar{R}I_c$, $K = V/R_S I_c$ describing the ratio of torque over gravity, and dimensionless time $\tau = \omega_{RC} t$ using the RC-frequency $\omega_{RC} = 1/\bar{R}C_J$. The ratio $\alpha = \frac{\omega_{RC}}{\omega_{RL}}$ with $\omega_{RL} = \bar{R}I_c/\Phi_0$ determines the difference in timescales at which changes of u occur compared to changes of ϕ, and is proportional to analogous friction η.

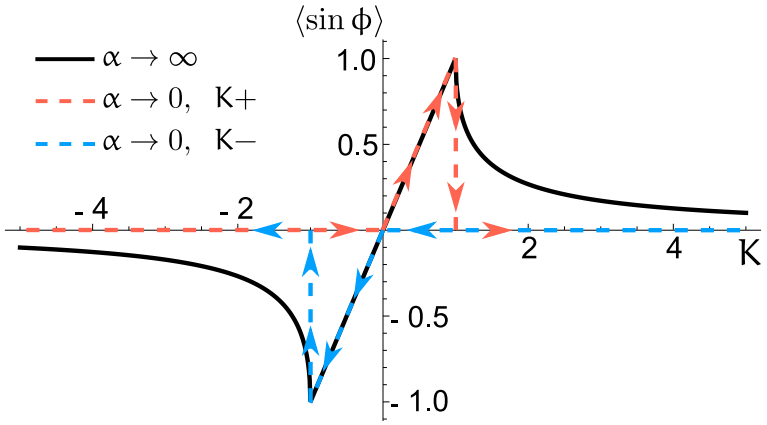

Figure 3.2: Average current through the Josephson element $\langle I_J\rangle/I_c = \langle \sin\phi\rangle$ as a function of K for different α limits. For $\alpha \to 0$ a increasing and decreasing path of K are indicated by $K\pm$

For the case $\alpha \ll 1$, which we define as the *underdamped limit*, the phase ϕ changes quickly compared to u. Considering equilibrium solutions, meaning $\frac{\partial\langle u\rangle}{\partial t} = 0$ with $\langle u\rangle$ denoting average, we find that for $|K| > 1$ only the constant $u = K$ solution is valid, as $\sin\phi$ averages to zero on the timescale u changes. For the pendulum this corresponds to a rotating solution, with many rotations occurring on the timescale angular momentum changes. For $|K| < 1$ there are two equilibrium solutions for u; one where the phase localizes $\phi = \sin^{-1} K$ with $u = 0$ and the junction is *superconducting*, and the previous solution with $u = K$. The non-uniqueness of solutions at $|K| < 1$ yields the hysteretic behaviour characteristic of underdamped junctions, which switch between a completely resistive state $u = K$ and superconducting state $u = 0$. Starting from e.g. $K < -1$ the junction is initially in a resistive state ($u = K$), and for increasing K the system tend to follow this solution until $K = 0$, where both solutions correspond to a motionless pendulum at $\phi = 0$. Increasing K slowly from this stage brings one to the phase localized superconducting state with torque balancing gravity, resulting in $u = 0$, until $K > 1$ where a switch to the resistive state must occur. This evolution means that the direction at which bias (V) is applied matters, as depicted in fig. 3.2. Accounting for finite values $\alpha \lesssim 1$ some modification to this simple picture are necessary which are detailed in Ref.[117].

For $\alpha \gg 1$, which we call the *overdamped limit*, u changes quickly on the scale at which ϕ changes. Phase ϕ can therefore be regarded as constant on the time scale u equilibrates, meaning that the only solution to $\frac{\partial u}{\partial t} = 0$ is $u = K - \sin\phi$. Inserting this into eq. (3.4) yields,

$$\frac{\partial\phi}{\partial\bar{\tau}} = K - \sin\phi, \tag{3.5}$$

with $\bar{\tau} = \tau/\alpha$. This equation has a unique solution for all K (no hysteresis) which for $|K| \leqslant 1$ is $\phi = \sin^{-1} K$, while for $|K| > 1$ we obtain a periodic solution with $T = 2\pi/\sqrt{K^2 - 1}$, and for which,

$$\langle \sin\phi \rangle = \frac{1}{T}\int_0^T \sin\phi = K - \mathrm{sgn}(K)\sqrt{K^2 - 1}, \tag{3.6}$$

Unlike the underdamped limit, the average current going through the Josephson element $\langle I \rangle = I_c \langle \sin\phi \rangle$ remains finite for $|K| > 1$. At K slightly larger than 1 the analogous pendulum is going through uneven rotations, spending more time in the vicinity of $\phi = \pi/2$ than $\phi = -\pi$ for e.g. positive K. This uneven distribution of ϕ renders $\langle \sin\phi \rangle \neq 0$ in this range, while increasing K smoothens the distribution such that $\langle \sin\phi \rangle \to 0$ as seen in fig. 3.2.

3.1.2 *current vs. voltage bias*

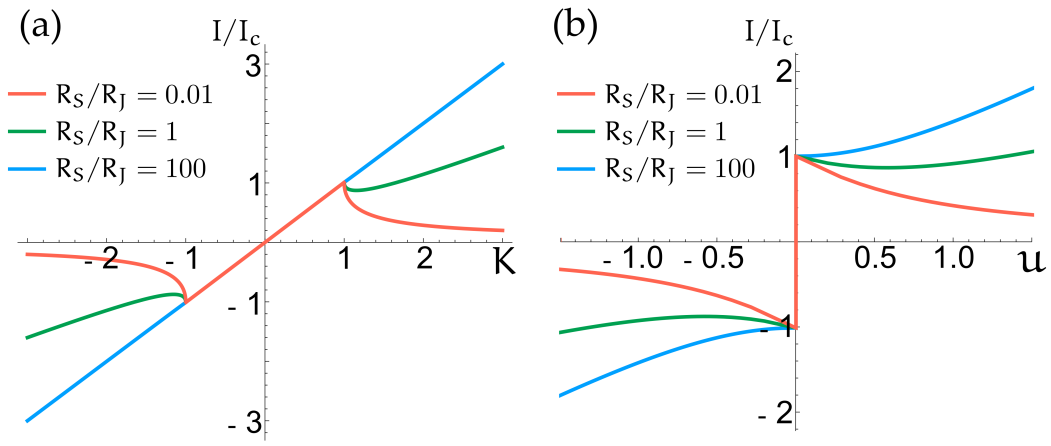

Figure 3.3: (a) Current through Josephson junction as a function of $K = V/R_S I_c$ for various rations of R_S/R_J. (b) Current through Josephson junction as a function of junction bias $u = V_J/\bar{R}I_c$ for various ratios of R_S/R_J.

The non-linearity of a Josephson junction means that multiple solutions for the current I can exist for a given bias V. Consequently, we have to specify how the junction is biased, which can be either the enforcement of a constant voltage drop V_J or

a constant current I, resulting in a *voltage biased* or *current biased* junction. Considering the full current through the junction in the overdamped limit we find,

$$I = I_c \sin\phi + C_J \frac{\partial V_J}{\partial t} + \frac{V_J}{R_J} \tag{3.7}$$

$$\Rightarrow \quad \langle I\rangle / I_c = \langle \sin\phi\rangle + \frac{\bar{R}}{R_J}\langle u\rangle = \begin{cases} K & |K| \leqslant 1. \\ K - \operatorname{sgn}(K)\frac{R_J-\bar{R}}{\bar{R}_J}\sqrt{K^2-1} & |K| > 1. \end{cases} \tag{3.8}$$

Plots of this equation are shown for varies R_J/R_S ratios in fig. 3.2 (a). For $R_S \gg R_J$ the average current passing through the junction is linearly increasing with bias $\langle I\rangle = V/R_S$ for all V, resulting in *current biasing*. This is consistent with Thévenin's theorem, and traditional bias-line analysis where the presence of a large serial resistor renders the circuit current biased. In the opposing limit $R_S \ll R_J$, the circuit is current biased for $|K| < 1$ where $\langle I\rangle = V/R_S$, since the initial resistor R_S is always larger than the zero resistance superconducting junction, but for $|K| \gg 1$ current passing through the Josephson element goes to zero and all current passes through R_J. As we assumed $R_J \gg R_S$ the system becomes effectively *voltage biased* with $V = V_J$ meaning that V controls the voltage drop across the junction.

As seen in fig. 3.2 (a, b) it is only in the regime of large R_J that decreasing current as a function of either V or V_J is possible. Meaning that the measurement of NDC in experiment requires voltage biasing. In the case of current biasing, current increases monotonically as a function of V and no NDC can appear.

3.1.3 *Critical current dependent vs. independent cusp voltage*

So far, we have obtained the requirements for an overdamped and voltage biased junction. Lastly, we need to consider the *cusp voltage* V_0 defined as the bias at which current I peaks, which in differential conductance measurements separates the positive zero-bias peak from the flanking negative differential conductance (NDC) peaks. In experiment V_0 appears constant as a function of gate, and as a consequence must be independent of I_c, as we expect I_c to be strongly gate dependent. In the previous sections, current always peaked at $K = 1$ corresponding to $V_0 = R_S I_c$, failing the requirement of constant cusp voltage. To obtain a model satisfying this constraint we have to extend our model with a stochastic voltage element $L(t)$ such that $V \to V + L(t)$ stemming from a noise source. In principle, this noise could be non-Markovian and drawn from a complicated distribution, but for our current calculations we, for

simplicity, assume white spectrum Gaussian noise (Markovian), similar to the original calculation of Ref. [118]. In general a stochastic variable can be defined by its moments,

$$\begin{aligned} \langle L(t)\rangle &= 0, \qquad & \langle L(t_1)L(t_2)\rangle &= 2\mathcal{L}\delta(t_1-t_2), \\ \langle L(t_1)L(t_2)L(t_3)L(t_4)\rangle &= & \langle L(t_1)L(t_2)\rangle\langle L(t_3)L(t_4)\rangle &+ \langle L(t_1)L(t_3)\rangle\langle L(t_2)L(t_4)\rangle \\ & & + \langle L(t_1)L(t_4)\rangle\langle L(t_2)L(t_3)\rangle, \end{aligned} \tag{3.9}$$

where the last equation displays Wick's probability theorem, allowing partitioning of all high order moments. Next, we return to our overdamped junction and add the stochastic voltage element,

$$\frac{\partial\phi}{\partial\bar{\tau}} = K + \bar{L}(\bar{\tau}) - \sin\phi \tag{3.10}$$

with dimensionless noise $\bar{L}(\bar{\tau})$ obeying $\langle \bar{L}(\bar{\tau}_1)\bar{L}(\bar{\tau}_2)\rangle = \frac{2\mathcal{L}}{I_c\Phi_0\bar{R}}\delta(\bar{\tau}_1-\bar{\tau}_2)$ in dimensionless time. Stochastic equations, such as eq. (3.10), are known as Langevin equations, and the procedure is to solve for the distribution of ϕ, which we call $P(\phi,\bar{\tau})$, for a random sample of $\bar{L}(\tau)$, as ϕ itself is a stochastic object now. In the following segment, we derive a differential equation for this distribution known as the Fokker-Planck equation. Our derivation follows Ref. [119], which has the advantage of highlighting the similarity between classical stochastic mechanics and quantum mechanics.

We start by considering a distribution of ϕ, labelled $\sigma(\phi,\bar{\tau})$, fulfilling $\int\sigma(\phi,\bar{\tau})\,d\phi = 1$, and where the dynamics at each ϕ is governed by eq.(3.10). Furthermore, we assume that a specific $\bar{L}(\bar{\tau})$ have been drawn from its distribution for each time step, which corresponds to deterministic time evolution of $\sigma(\phi,\bar{\tau})$ with $\bar{L}(\bar{\tau})$ not being a stochastic variable. Enforcing local particle conservation for each time step, meaning that changes in probability, $\sigma(\phi,\bar{\tau})$, at coordinate ϕ must be due to inflow or outflow of probability from neighbouring ϕ, yields a continuity equation,

$$0 = \frac{\partial\sigma}{\partial\bar{\tau}} + \frac{\partial}{\partial\phi}\left(\frac{\partial\phi}{\partial\bar{\tau}}\sigma\right) \quad\Rightarrow\quad \frac{\partial\sigma}{\partial\bar{\tau}} = \Omega\sigma, \tag{3.11}$$

with $\Omega(\bar{\tau}) = -\frac{\partial}{\partial\phi}\left(\frac{\partial\phi}{\partial\bar{\tau}}(\bar{\tau})\right)$ defined as an operator, where the derivative must also be applied to whatever state $\Omega(\bar{\tau})$ is applied to. From our knowledge of quantum mechanics we know that the solution to such an equation can be written in terms of a time-evolution operator, which propagates the distribution forward in time,

$$\sigma(\phi,\bar{\tau}+\Delta\bar{\tau}) = U(\bar{\tau}+\Delta\bar{\tau},\bar{\tau})\sigma(\phi,\bar{\tau}), \quad \text{with} \quad U(\bar{\tau}_1,\bar{\tau}_2) = T_{\bar{\tau}}e^{\int_{\bar{\tau}_2}^{\bar{\tau}_1}d\bar{\tau}\Omega(\bar{\tau})}. \tag{3.12}$$

By expanding the time-evolution operator, subtracting the zeroth order term and dividing by $\Delta\bar{\tau}$ one finds,

$$\frac{\sigma(\phi,\bar{\tau}+\Delta\bar{\tau})-\sigma(\phi,\bar{\tau})}{\Delta\bar{\tau}} = \frac{1}{\Delta\bar{\tau}}\left[\int_{\bar{\tau}}^{\bar{\tau}+\Delta\bar{\tau}} d\bar{\tau}_1\Omega(\bar{\tau}_1)+\int_{\bar{\tau}}^{\bar{\tau}+\Delta\bar{\tau}} d\bar{\tau}_1\int_{\bar{\tau}}^{\bar{\tau}_1} d\bar{\tau}_2\Omega(\bar{\tau}_1)\Omega(\bar{\tau}_2)+\dots\right]\sigma(\phi,\bar{\tau}). \tag{3.13}$$

The next step is a crucial one, we average over all possible configurations of $\bar{L}(\bar{\tau})$. and since the noise is Markovian it holds that $\langle\phi(\bar{\tau}_1)\frac{\partial\phi}{\partial\bar{\tau}}(\bar{\tau}_2)\rangle = \langle\phi(\bar{\tau}_1)\rangle\langle\frac{\partial\phi}{\partial\bar{\tau}}(\bar{\tau}_2)\rangle$ for $\bar{\tau}_2 \geqslant \bar{\tau}_1$ meaning that future random changes are uncorrelated of current coordinate ϕ. This renders $\sigma(\phi,\bar{\tau})$ uncorrelated of all $\Omega(\bar{\tau})$ in eq.(3.13). The distribution $\sigma(\phi,\bar{\tau})$ averaged over all configurations of $\bar{L}(\bar{\tau})$ yields the sought distribution $P(\phi,\bar{\tau}) = \langle\sigma(\phi,\bar{\tau})\rangle$. Performing the average we find,

$$\frac{P(\phi,\bar{\tau}+\Delta\bar{\tau})-P(\phi,\bar{\tau})}{\Delta\bar{\tau}} = \frac{1}{\Delta\bar{\tau}}\left[\int_{\bar{\tau}}^{\bar{\tau}+\Delta\bar{\tau}} d\bar{\tau}_1\langle\Omega(\bar{\tau}_1)\rangle+\int_{\bar{\tau}}^{\bar{\tau}+\Delta\bar{\tau}} d\bar{\tau}_1\int_{\bar{\tau}}^{\bar{\tau}_1} d\bar{\tau}_2\langle\Omega(\bar{\tau}_1)\Omega(\bar{\tau}_2)\rangle+\dots\right]P(\phi,\bar{\tau}). \tag{3.14}$$

These integrals can be solved by recalling eq. (3.9), and as only the lowest two orders scales as $\Delta\bar{\tau}$ the limit of $\Delta\bar{\tau}\to 0$ yields,

$$\frac{\partial P}{\partial\bar{\tau}}(\phi,\bar{\tau}) = \frac{\partial}{\partial\phi}\left[K-\sin\phi\right]P(\phi,\bar{\tau})+\frac{1}{A}\frac{\partial^2 P}{\partial\phi^2}(\phi,\bar{\tau}), \tag{3.15}$$

which is the Fokker-Plank equation for our system with $A = \Phi_0\bar{R}I_c/\mathcal{L}$, corresponding to inverse noise. To solve for the equilibrium distribution $P_0(\phi)$ we set the Fokker-Plank equation equal to zero, and as our problem is periodic it is convenient to express it as a fourier series,

$$x_n = \frac{1}{2\pi}\int_0^{2\pi} d\phi P_0(\phi)e^{-in\phi} \quad \text{and} \quad P_0(\phi) = \sum_{n=-\infty}^{\infty} x_n e^{in\phi}. \tag{3.16}$$

By demanding that each orthogonal component in the expansion equilibrates independently $\frac{\partial x_n}{\partial\bar{\tau}} = 0$ we obtain a recursive formula for the fourier components,

$$x_{n+1}-x_{n-1} = -2\left(\frac{n}{A}-iK\right), \tag{3.17}$$

whose solution we recognize as the complex modified Bessel function,

$$x_n = C\Theta(n)I_{n-iKA}(A)+D\Theta(-n)I_{n+iKA}(A). \tag{3.18}$$

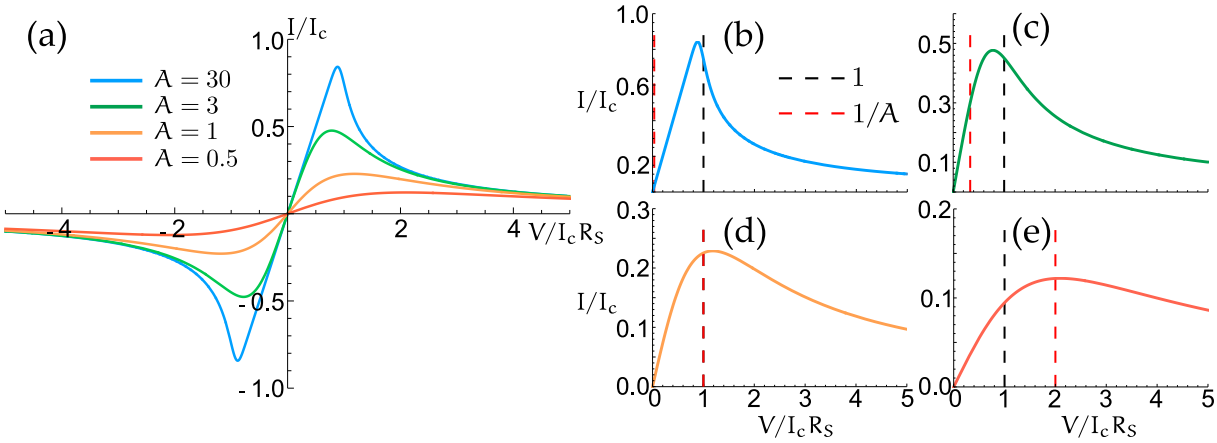

Figure 3.4: (a-e) Current through junction in the overdamped and voltage biased limit for varies A. (b-e) Black (red) dashed lines indicates the position of maximum current (V_0) in the limit of large (small) A

Lastly, to normalize the probability distribution we demand $\int_0^{2\pi} d\phi P_0(\phi) = x_0 = 1$, for which we find,

$$x_n = \Theta(n)\frac{I_{n-iKA}(A)}{I_{-iKA}(A)} + \Theta(-n)\frac{I_{n+iKA}(A)}{I_{iKA}(A)},. \tag{3.19}$$

The average equilibrium current through the Josephson element is then,

$$I_c\langle\sin\phi\rangle = I_c\frac{1}{2\pi}\int_0^{2\pi} d\phi \sin\phi P_0(\phi) = \operatorname{Im} x_1 = I_c \operatorname{Im}\frac{I_{1-iKA}(A)}{I_{-iKA}(A)}, \tag{3.20}$$

known as the Ivanchenko-Zil'berman curve [118]. These can be evaluated numerically as shown in fig. 3.4. In the limit of $A \to \infty$, corresponding to no stochastic noise, the current reduces to eq. (3.8), and as A decreases one initially observes that the cusp voltage V_0 decreases. This is due to noise-activated rotations; for $K \lesssim 1$, close to where the analogous pendulum changes from a localized to a rotating phase, noise may activate single rotations delocalizing ϕ and thus decreasing $\langle\sin\phi\rangle$. As A continues to decrease the cusp voltage starts to increase, and at $A = 1$ it becomes larger than the cusp voltage at zero noise $V_0 > R_S I_c$, and for $A \ll 1$ we find $V_0 \approx R_S I_c/A$. In the picture of the analogous pendulum, this corresponds to noise larger than gravity such that the pendulum never localizes as random forces constantly spins it, resulting in a wide ϕ distribution for all K. For $K \approx 0$ noise-activated rotations occur evenly in both directions, but as applied torque (V) increases more and more of the random rotations occur in the direction of applied torque, until $V = R_S I_c/A$ for which almost all rotations are in the same direction, and $\langle\sin\phi\rangle$ peaks. This limit can be captured by an expansion of small A in eq. (3.20) yielding [118],

$$I_c\langle\sin\phi\rangle \approx I_c\frac{1}{2}\frac{A^2K}{1+A^2K^2} \tag{3.21}$$

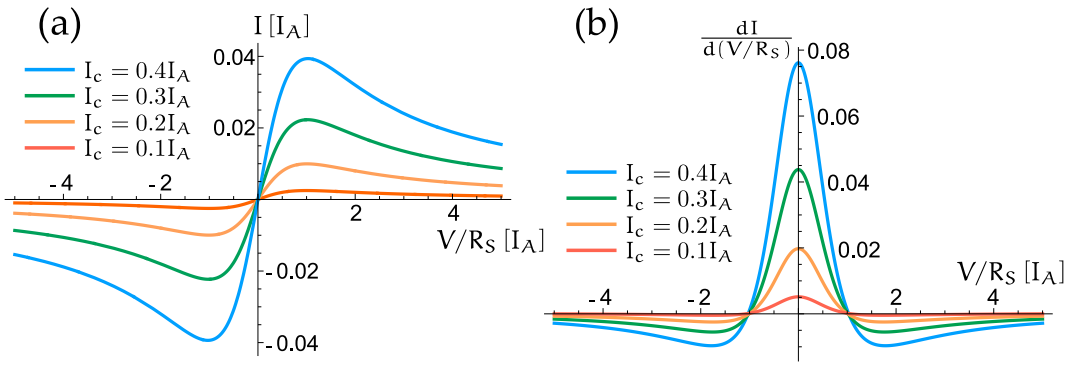

Figure 3.5: (a) Current through the junction in the overdamped and voltage biased limit for $A \ll 1$ and various I_c. Plot is in units of noise current scale $I_A = I_c/A$. (b) Differential conductance for the same limits.

This functions peaks at,

$$V_0 = \frac{R_S I_c}{A} = \frac{\mathcal{L} R_S}{\bar{R}\Phi_0} \tag{3.22}$$

with peak current,

$$I_0 = \frac{I_c A}{4} = \frac{1}{4}\frac{\bar{R} I_c^2 \Phi_0}{\mathcal{L}}. \tag{3.23}$$

In the limit of voltage biasing $R_J \gg R_S$ we find $V_0 = \mathcal{L}/\Phi_0$, which is completely independent of junction parameters R_J and I_c. Cusp voltage V_0 in this limit does therefore not depend on gate, in accordance with observed constant cusp voltage. Our third requirement is thereby satisfied in the large noise limit $A \ll 1$. In fig. 3.5 (a) we show current in the $R_J \gg R_S$ limit for various I_c showcasing the constant cusp voltage. In fig. 3.5 (b) differential conductance is shown as a function of bias, and we observe that zero-bias conductance and NDC amplitudes changes as a function I_c, while peak widths remain constant, similar to experimental data shown in fig. 2.4.

In summary, we demand of our circuit that it satisfies the following requirements within the standard RCSJ model:

- *Overdamped* - Requiring $\alpha \gg 1$.
- *Voltage biased* - Requiring $R_J \gg R_S$.
- *Constant cusp voltage* - Requiring $A \ll 1$.

Unfortunately, the standard RCSJ model is not sufficient to describe the experimental situation. The primary issue is that the junction capacitance, which by a simple parallel plate argument is estimated to be $C_J \approx 3$ aF, is so low that stray capacitances would easily overwhelm it. Inspired by previous work [112, 114, 116] our experimentalist colleagues estimate that the indirect capacitance through the Si substrate between

source and drain bonding pads is $C \approx 9$ pF. Using this value as junction capacitance C_J would for our parameters result in a underdamped junction $\alpha \ll 1$. Consequently, we have to further assume that a resistive element R exist between the bonding pads and junction to obtain a model consistent with data. This corresponds to the extended RCSJ model presented in the next section

3.2 EXTENDED RCSJ

In this section we analyse the RCSJ model extended with an additional shunt capacitor C, in series with a resistor R as shown in fig. 3.6. The junction resistance R_J is neglected as we expect low-bias quasiparticle tunnelling across a coulomb blockaded quantum dot to be severely limited, resulting in $R_J \gg R, R_S$ where it can be neglected. We ascribe the shunt capacitor C to the indirect capacitance between the two bonding pads (for further information see article 2 in chapter 6). R describes interface resistance between Ti/Au leads and the InAs nanowire, which has previously been measured to be in the order of kilo Ohms [114, 120]. The derivations in this section were originally presented in the supplement of article 2.

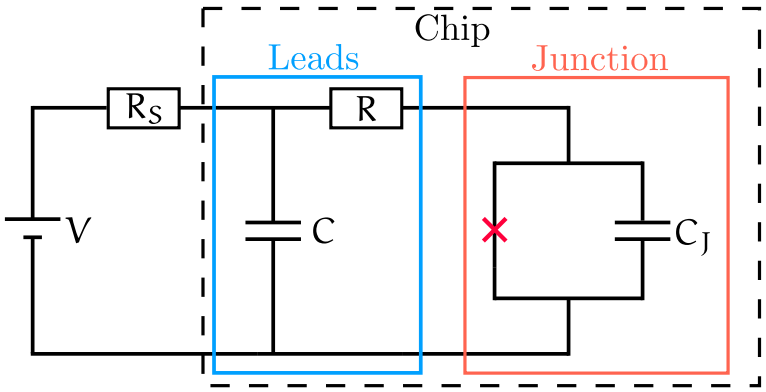

Figure 3.6: Circuit for the Extended RCSJ model. Labels 'Chip', 'Leads' and 'Junction' indicate these components position in the physical setup.

The extended RCSJ circuit was initially used to investigate nanoscale Josephson junctions [109, 110], where it allowed for overdamped solutions of junctions with miniscule capacitances [111]. As in the previous section, our goal is to find a consistent description fulfilling the requirements: overdamped, voltage biased and constant cusp voltage. In the first part of this section we will show how these limits are obtained, then we will extract junction parameters from fitting of zero-bias curves. Lastly, we will show that these extracted parameters are consistent with the initial assumptions. We name the voltage drop across shunt capacitor C, which corresponds to the voltage

drop across leads, we name V_{sd} for source-drain, and furthermore we assume that it contains a stochastic component $\bar{L}(t)$. Using Kirchhoff's laws, the Josephson relation, and some algebraic rearrangement we find the following circuit equations cast in dimensionless form,

$$\frac{du}{d\tau} = \frac{1}{\alpha}\left(\frac{V}{R_S I_c} - \sin\phi - \frac{R}{R_S}(u + L(\tau)) - \frac{1}{\alpha_0}\frac{d^2\phi}{d\tau^2}\right) \tag{3.24}$$

$$\frac{d\phi}{d\tau} = u + L(\tau) - \sin\phi - \frac{1}{\alpha_0}\frac{d^2\phi}{d\tau^2}. \tag{3.25}$$

Here $u = V_{sd}/RI_c$ denotes dimensionless voltage and we have introduced the dimensionless time $\tau = \omega_{RL}t$ with $\omega_{RL} = RI_c/\Phi_0$. The two different RC frequencies, $\omega_{RC_J} = (RC_J)^{-1}$ and $\omega_{RC} = (RC)^{-1}$, enter these equations via the ratios $\alpha_0 = \omega_{RL}/\omega_{RC} = R^2CI_c/\Phi_0$ and $\alpha_J = \omega_{RC_J}/\omega_{RL} = \Phi_0/R^2C_JI_c$ determining the different scales of time evolution. Finally, $L(\tau)$ is a dimensionless form of $\bar{L}(t)$ which is composed of Nyquist noise from the series resistor R at temperature T^*, in addition to stray voltage noise, characterized by variance $\mathcal{L}$, to account for imperfect filtering, such that $\langle L(\tau)L(\tau+\Delta\tau)\rangle = \left(\frac{2k_BT^*}{\Phi_0 I_c} + \frac{\mathcal{L}}{RI_c\Phi_0}\right)\delta(\Delta\tau)$. Noise from the bias-line resistance R_s is assumed to be excluded by the RC filters apart from the stray contribution. As $\mathcal{L}$ and T^* cannot be independently measured in this setup, we ascribe all noise to Nyquist noise of the series resistor R with an effective temperature $T = T^* + \mathcal{L}/(2Rk_B)$, which can be different from fridge temperature due to the stray noise contribution.

We furthermore narrow ourselves to the limit of $\alpha_J \gg 1$, corresponding to small junction capacitance C_J. In this limit, the terms proportional to the second derivative of phase in eq. (3.24) and eq. (3.25) can be neglected and the junction capacitance appears no more in the dynamics. For $\alpha_0 \gg 1$ source-drain bias u evolves slowly on the scale of ϕ, allowing us to solve for the distribution of ϕ while keeping u constant. Notice that this is opposite of the simple RCSJ model in the overdamped limit. There it was ϕ that evolved slowly compared to u. Solving for the ϕ-distribution using eq. (3.25) is completely equivalent to solving of eq. (3.10), and we obtain an identical solution,

$$\langle\sin\phi\rangle = \mathrm{Im}\,\frac{I_{1-iuA}(A)}{I_{-iuA}(A)} \approx \frac{1}{2}\frac{A^2u}{1+A^2u^2} \tag{3.26}$$

where noise $A = \Phi_0 I_c/k_BT$ is characterized by the effective temperature T, and we have expanded in small A necessary to achieve *constant cusp voltage*. As such, a large α_0 in combination with a large α_J leaves the junction overdamped. Having solved for the ϕ-distribution as a function of u we insert this result back into eq. (3.24), and

average to find the equilibrium distribution of $\langle u \rangle$ by enforcing $\partial\langle u \rangle/\partial\tau = 0$ which yields,

$$\frac{V}{R_s I_c} - \frac{R}{R_S}\langle u \rangle = \frac{1}{2}\frac{A^2\langle u \rangle}{1 + A^2\langle u \rangle^2}. \tag{3.27}$$

The behaviour of this equation determines if the junction is voltage or current biased dependent on the ratio R/R_S. In the limit of $R \gg R_S$ eq. (3.27) has a unique solution for u, meaning that for any applied bias V only one value of lead bias V_{sd} is possible at equilibrium - corresponding to *voltage biasing*. In the opposing regime $R \ll R_S$ a constant current is enforced instead, and for $|V|/(R_S I_c) < \max\langle \sin\phi \rangle$ three solutions of eq. (3.27) are possible allowing for switching even in the overdamped regime - corresponding to *current biasing*. These two scenarios are depicted in fig. 3.7. As the region with decreasing current corresponds to an unstable solution [109, 110], NDC cannot be observed in the current biased regime. The two other solutions are stable and metastable, both of which can be measured [109]. The threshold between current and voltage biasing is determined by the minimal slope,

$$\min \frac{\partial}{\partial\langle u \rangle}\langle \sin\phi \rangle = \frac{A^2}{16}, \tag{3.28}$$

whose size compared to R/R_S determines the type of biasing experienced by the junction as shown in fig. 3.7. Lastly, for $R/R_S \to 0$ the left hand side of eq. (3.27) is constant and does not intersect the right hand side for large bias. In realistic junctions, solutions of higher current are available at large bias, for example at $eV = 2\Delta$ with Δ denoting the gap. These are the solutions the system switches to in the limit of $R/R_S \to 0$ for large V/R_S.

At this point, we have obtained the requirements for the three conditions to be satisfied. We will now turn to fitting of zero-bias peaks and model consistency. In the extended RCSJ circuit, when equilibrium have been reached, all current passes through the Josephson element such that we can fit $I - V_{sd}$ curves to,

$$\langle I \rangle = I_c \operatorname{Im} \frac{I_{1-i\langle u \rangle A}(A)}{I_{-i\langle u \rangle A}(A)}, \tag{3.29}$$

while the V_{sd} derivative of this formula allows fitting of $dI/dV_{sd} - V_{sd}$. Fitting is done by setting $T = 80$ mK (an assumption we discuss in a bit), and by keeping R and I_c as the only free parameters. With few exceptions, as we discuss in section 4.3, we find good fits of $I - V_{sd}$ measured by multimeter, and $dI/dV_{sd} - V_{sd}$ measured by lock-in across all gate configurations of shell X, assuming constant $R \approx 3$ kΩ and with varying

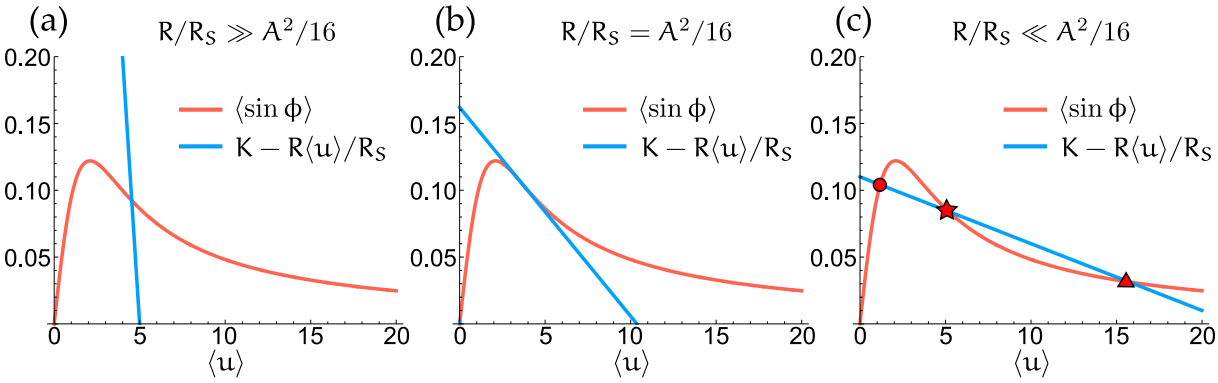

Figure 3.7: Solutions of u for eq. (3.27), visualized via intersect, plotted in the voltage biased regime (a), at the threshold (b), and in the current biased regime (c). All plots are with $A = 0.5$ and $K = V/R_S I_c$. In (c) circle indicates a metastable solution, star an unstable, and triangle a stable solution [109]

I_c. In fig. 3.8 (a) and (b) we show fits of conductance and current as a function of gate and bias. In the fitted range we find that the expansion in small A is valid, such that,

$$\langle I \rangle \approx \frac{I_c}{2} \frac{A^2 \langle u \rangle}{1 + A^2 \langle u \rangle^2}, \tag{3.30}$$

fits the zero-bias peaks. This is shown in greater detail in fig. 3.8 (c-f) where directly measured cusp current I_0 is compared to $\max\langle I \rangle = I_c A/4$, and measured zero-bias conductance G is compared to,

$$\frac{dI}{dV_{sd}}(V_{sd} = 0) = \frac{A^2}{R} = \frac{\Phi_0^2 I_c^2}{R k_B^2 T^2}. \tag{3.31}$$

Discrepancy in both cases is found to be within 10%.

From our starting point in this section, we considered the interface resistance R, junction noise characterized by T, and critical current I_c to be unknown quantities, while $C_J \approx 3$ aF and $C \approx 9$ pF where obtained from estimates. In the limit where eq. (3.30) is valid we identify the following scaling,

$$\bar{R} = R/\gamma, \quad \bar{T} = \gamma T, \quad \bar{I}_c = \sqrt{\gamma} I_c \tag{3.32}$$

which keeps eq. (3.30) and cusp voltage,

$$V_0 = \arg\max\langle I \rangle (V_{sd}) = R k_B T/\Phi_0, \tag{3.33}$$

invariant. This means that if a fit is found for any choice of R, T, and I_c then any scaling of these with γ also results in a fit. From an independent measure of thermally broadened coulomb peaks the noise temperature is determined to be $T \approx 80$ mK,

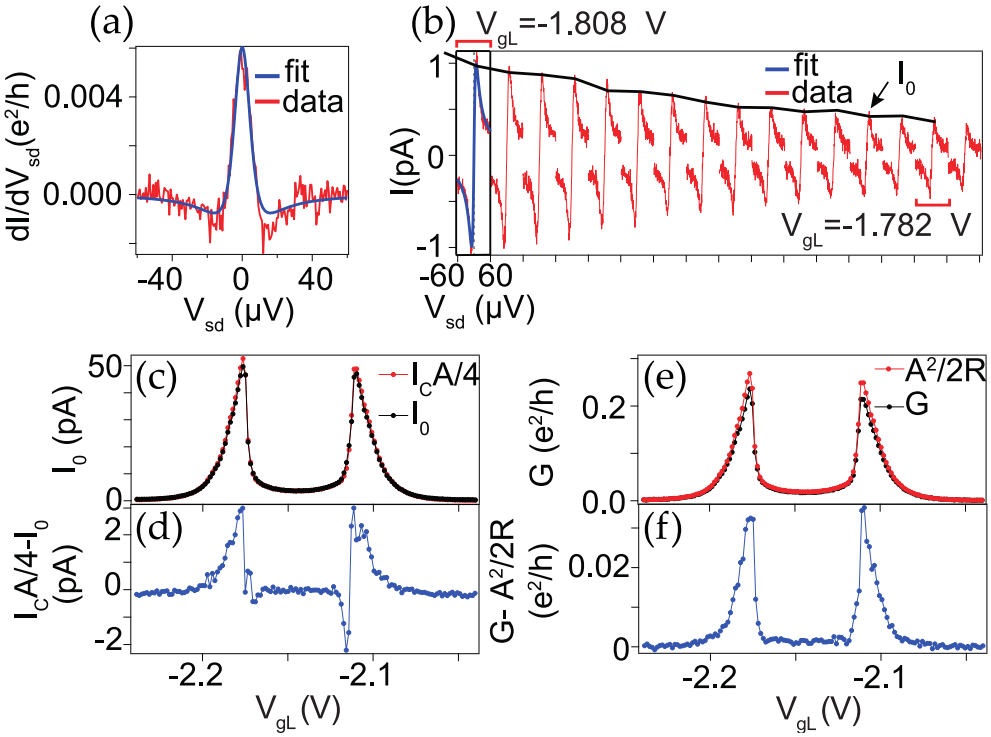

Figure 3.8: Examples of fitting. (a) $dI/dV_{sd} - V_{sd}$ trace and fit using eq. (3.29) with $T = 80$ mk at the same gate voltage as the leftmost trace in (b). (b) Examples of $I - V_{sd}$ curves as a function of gate, leftmost is superposed with eq. (3.29) using values from the fit in (a). Each curve is displaced by 120 μV and are measured from −60 to 60 μV. The black trace shows cusp current I_0 at positive bias as a function of gate. (c, e) Measured cusp current I_0, and zero-bias conductance G compared to cusp current and zero-bias conductance obtained from eq. (3.30) using I_c and A extracted from separate $dI/dV_{sd} - V_{sd}$ fits. (d, f) Difference between the curves shown in (c, e) indicating the reliability of eq. (3.30). Fits are performed by Alexandros Vekris and Juan Carlos Estrada Saldaña

which results in $R \approx 3$ kΩ. For this choice, the gate dependent critical current is fitted in the range $I_c \in [0.02, 3]$ nA resulting in $A \in [0.006, 0.9] \lesssim 1$ consistent with *constant cusp voltage* (borderline for the largest values). Using these parameters we find $\alpha_0 \in [10, 100]$ and $\alpha_J \in \left[10^4, 10^5\right]$ consistent with the junction being *overdamped*. Lastly, $R/R_s \approx 0.36$ and for the largest A we find $A^2/16 \approx 0.05$, fulfilling that the junction is *voltage biased*.

At this stage we have obtained a realistic and consistent description of the measured supercurrent peaks using a classical description of an extended RCSJ circuit, and shown the ability to fit zero-bias peaks to obtain I_c up to a global (independent of gate) scaling $\sqrt{\gamma}$, which captures our lack of knowledge of the electromagnetic environment.

Consequently, it is I_c's gate dependence and not amplitude that we can measure to a good degree of accuracy.

3.3 QUANTUM CORRECTIONS AND COULOMB BLOCKADE

In this section we discuss the validity of the classical description of phase and charge employed in the previous sections. In a fully quantum mechanical treatment, the phase difference across the junction ϕ follows an uncertainty relation $[\phi, q] = 2ie$ with the charge q building up on the junction capacitor C_J. The quantum effects of this uncertainty relation have been considered in detail for ultrasmall junctions with standard RCSJ circuits [121–124], but no full derivation accounting for quantum dots and the extended circuit, containing two capacitors C and C_J, exist to the author's knowledge. Accordingly, and accounting for our lack of knowledge of the electromagnetic environment in the present experiment, a full quantum description is beyond our scope, and using the existing literature we seek only to address the validity of our model and consider alternative explanations to data.

The importance of quantum fluctuations in the standard RCSJ circuit is determined by the four scales: Josephson energy $E_J = \Phi_0 I_c$, charging $E_c = 2e^2/C$, temperature $E_T = k_B T$ and the effective resistance $\rho = R/R_Q$ is units of the resistance quantum $R_Q = \hbar/4e^2 = 6500\ \Omega$. The classical phase diffusion description employed above is valid for $E_c \ll \rho E_T$ [122], yielding the characteristic Ivanchenko-Zil'bermann curves (eq. (3.26)) used to fit the overdamped regime. For the opposing case $E_c \gg \rho E_T$ in addition to $E_c \gg E_J$, known as the *coulomb blockaded* regime*, cooper-pairs tunnel incoherently across the junction and phase ϕ ceases to behave as a classical variable due to charge localization on the capacitor. In this regime, the tunnelling can be described using $P(E)$-theory in which the cooper-pairs tunnel across the junction at finite bias by exchanging energy with the electromagnetic environment [121, 125]. Expanding in small tunnel coupling characterized by E_J the following current is obtained,

$$\langle I \rangle = \frac{\pi e E_J^2}{\hbar} \left[P(2eV) - P(-2eV) \right], \tag{3.34}$$

with the $P(E)$ function describing environmental energy exchange,

$$P(E) = \frac{1}{2\pi\hbar} \int_{-\infty}^{\infty} dt \exp\left[J(t) + iEt/\hbar \right], \tag{3.35}$$

* In this case coulomb blockade does not refer to the quantum dots, but to the effective Josephson junction formed by the dots.

and with $J(t) = \langle [\phi(t) - \phi(0)]\, \phi(0) \rangle$ characterizing phase fluctuations, determined by the environmental impedance,

$$J(t) = 2 \int_{\infty}^{\infty} \frac{d\omega}{\omega} \frac{\mathrm{Re}\,[Z_{env}(\omega)]}{R_Q} \frac{e^{-i\omega t} - 1}{1 - e^{-\hbar\omega/k_B T}}. \tag{3.36}$$

These equations have been used to explain supercurrent in STM experiments [126, 127] yielding very similar signals to those observed in our device, including visible NDC and a constant cusp voltage under varying I_c. This similarity is clear from eq. (3.34) where the $P(E)$ function determines the width and shape of the zero-bias signal and, similar to our thermal noise, is independent of junction parameters. Another similarity is the I_c dependence, since both eq. (3.34) and eq. (3.30) scale as I_c^2. Finally, if the environmental impedance for low frequencies is small $Z_{env}(0)\rho \ll 1$ the expression eq. (3.34) actually reduces to the form of eq. (3.30) [121]. Intuitively, this coincidence occurs as both expressions describe a noise dominated regime with the width of supercurrent peak determined by the environment. If a part of this noise is due to quantum fluctuations this does not influence the shape of the peak.

To check if this is a realistic description of our device we consider the parameters extracted in the classical analysis, which yields the following hierarchy of scales,

$$E_c \ll E_J \lesssim E_T \ll E_{cj} \tag{3.37}$$

with $E_c = 2e^2/C$ and $E_{cj} = 2e^2/C_J$. The question is then; which capacitive scale determines if our system is coulomb blockaded or not? If it is C we are in the classical regime, and if C_J the coulomb blockaded regime. In the classical analysis, the dynamics became independent of C_J as $\alpha_J \gg 1$, and intuitively one would consider C to be dominant on the circuits timescales, which is also consistent with the classical description. This is in accord with Refs. [111, 115, 116] where quantum effects due to low junction capacitance was also neglected. Furthermore, similar experiments with quantum dots and the extended RCSJ circuit found underdamped behaviour [112, 114], which cannot be obtained in the coulomb blockaded regime. Finally, the quantum fluctuations are expected to mostly contribute at the frequency scale $E_{cj}/\hbar \approx 486$ THz [121] leading to a effective reduction of I_c. The size of which is determined by ρ and is negligible for $\rho \ll 1$ [122, 128]. In our device $\rho \approx 1/2$ and consequently we would expect a finite reduction to occur. For such large frequencies, however, the interface resistance R determining ρ cannot be assumed to be frequency independent due to parasitic capacitance and inductance, which is inherent in realistic resistors, but not included in our description.

In summary, an alternative explanation of our supercurrent signal could be that our junction is effectively coulomb blockaded, with cooper-pairs tunneling incoherently

across the junction. This model would probably yield fits of equal quality to our extended RCSJ model, but we find it unrealistic since it demands that the small junction capacitance C_J is the effective capacitative scale of the circuit. If the bonding pad capacitance C is assumed to be the dominant scale, then we are firmly in the classical regime in accord with our previous modelling. Lastly, not knowing the high frequency impedance of our circuit makes a reduction of measured I_c due to quantum fluctuations possible, although we expect it to be small if C_J is not an important scale.

3.4 QUALITY FACTOR Q

In a number of experiments using the extended RCSJ model to describe quantum dot Josephson junctions, the circuit have been characterized by a quality factor Q [112, 114–116]. If naively used in the same manner as the quality factor for the standard RCSJ circuit $Q = \sqrt{R^2 C I_c/\Phi_0} = 1/\sqrt{\alpha}$ (with α from section 3.1) is commonly used, wrong conclusions can be drawn. In this section, we detail how the extended RCSJ quality factor is derived and present why we think the analysis of Refs. [115, 116] is done somewhat wrongly.

Including a junction resistance R_J in parallel with the Josephson element of the circuit in fig. 4.7, and by further assuming that R_S is large such that the voltage source V in series with R_S is effectively a current source, one obtains the following circuit equation from Kirchoff's laws and the Josephson relation [112, 115],

$$I = \Phi_0 \left[C\left(1 + \frac{R}{R_J}\right) + C_J \right] \frac{\partial^2 \phi}{\partial t^2} + \left[I_c RC \cos\phi + \frac{\Phi_0}{R_J} \right] \frac{\partial \phi}{\partial t} + \Phi_0 RCC_J \frac{\partial^3 \phi}{\partial t^3} + I_c \sin\phi. \tag{3.38}$$

which is equivalent to eq. (3.24, 3.25) for $R_S \to \infty$ and $R_J \to \infty$. By further assuming that C_J is small, we neglect the third order derivative term. In the resulting equation the term in front of $\frac{\partial^2 \phi}{\partial t^2}$ controls the oscillatory motion, and the term in front of $\frac{\partial \phi}{\partial t}$ describes friction. Expanding around $\phi = 0$ yields the differential equation of a harmonic oscillator with characteristic frequency,

$$\omega_p = \sqrt{\frac{I_c}{\Phi_0}} \frac{1}{\sqrt{C_J + C\left(1 + \frac{R}{R_J}\right)}} \tag{3.39}$$

known as the plasma frequency, and for a damped oscillator the quality factor is given by $Q = I_c/\omega_p\eta$ with friction $\eta(\phi = 0) = I_c RC + \Phi_0/R_J$ yielding,

$$Q = \sqrt{\frac{\Phi_0}{I_c}} \frac{\sqrt{C_J + C\left(1 + \frac{R}{R_J}\right)}}{RC + \frac{R_J}{\Phi_0 I_c}}. \tag{3.40}$$

This Q-factor, originally derived in Ref. [129], is then used to characterize the circuit, which is overdamped for $Q \ll 1$ and underdamped for $Q \gg 1$. Next, let us relate this equation to parameters α_0 and α_J we used to characterize the circuit earlier. For $R_J \to \infty$ we can rewrite,

$$Q = \frac{1}{\sqrt{\alpha_0}}\left(1 + \frac{1}{\sqrt{\alpha_0 \alpha_J}}\right) \tag{3.41}$$

for which it is clear that our definition of overdamped $\alpha_0, \alpha_J \gg 1$ coincides with $Q \ll 1$. For $\alpha_J \sim 1$ and $\alpha_0 \gg 1$ we can obtain $Q \ll 1$, leading to some disagreement of junction behaviour, but this is simply due to the disregard of the third order derivative in our derivation of Q, corresponding to an initial assumption of $\alpha_J \gg 1$. In short, the two methods generally agree on junction behaviour.

Now we will turn to the problem. As we saw from eq. (3.27) the current biased regime is characterized by multiple solutions and branch switching even for a overdamped junction. Intuitively, this is due to the analogous pendulum's phase dependent friction,

$$\eta(\phi) = I_c RC \cos\phi + \Phi_0/R_J \tag{3.42}$$

which for large $R_J \to \infty$ can become negative, thereby enhancing instead of reducing established motion. This allows for rotating solutions of the analogous pendulum even for $Q \ll 1$, if the energy gain from negative friction at $\phi \approx \pi$ in addition to gain from torque, is sufficient to compensate for the energy loss due to large friction at $\phi \approx 0$. In Refs. [115, 116] they claim to be fully current biased, but fit measurements with the formula,

$$I(u) = \frac{I_c}{1 - R/R_J} \operatorname{Im} \frac{I_{1-iuA}(A)}{I_{-iuA}(A)} + \frac{I_c u}{R_J/R - 1}, \tag{3.43}$$

with $u = V_{sd}/RI_c$ and $A = \Phi_0 I_c/k_B T$, which is similar to eq. (3.29) in parallel with the resistor R_J. This formula assumes a single solution of u to each $I(u)$, equivalent to assuming voltage biasing. How does this effect their interpretation? If we assume both papers are correct on their assumption of current biasing ($R_S \to \infty$), then we would expect no NDC to be present as switching to a resistive state should occur when the peak of eq. (3.29) is reached, similar to Ref. [109]. In Refs. [115, 116] no NDC is observed supporting this, but is instead explained by fitting R_J at each gate, such

that the linear increasing contribution in eq. (3.43) compensates for the decreasing supercurrent at large u, thereby yielding no NDC. Even if R_J contributes to current, and is gate dependent as claimed, the fine tuning such that NDC is never observed appears artificial in light of the unexplained lack of switching. Instead, one could fit only the initial part of the curve, stopping when dI/dV appears to plateau, corresponding to where switching is expected. In this approach R_J would not be required in the fit, and one can assume $R_J \to \infty$. This approach would probably result in slightly larger fitted values of I_c for both experiments.

With these caveats, it is the author's recommendation to use α_0, α_J in addition to eq. (3.27) to determine the junctions behaviour, instead of relying solely on Q. In regard to my own work, it should be stated that in the project 1, presented in chapter 5, we also determined the junctions behaviour solely from Q, and first in project 2, presented in chapter 6, used the more rigorous analysis of section 3.2.

3.5 CONCLUSION

In this chapter we have shown that the zero-bias peaks observed throughout shell X can be explained and fitted by an extended RCSJ model, if the following requirements are fulfilled: *Overdamped dynamics*, *Voltage biased* and *Large noise compared to* I_c. For a fixed value of R and T we obtain good fits throughout shell-X varying only I_c, and we show that the obtained values are consistent with our models requirements.

Due to our lack of knowledge of the electromagnetic environment experienced by the junction, fitted I_c can be regarded as correct up to a global scaling λ which would require an independent measurement of interface resistance R or noise temperature T to fix. In addition, I_c could be somewhat reduced due to quantum phase fluctuations. Both of these reductions are independent of I_c, which we therefore know up to a global rescaling. Consequently, the scientific value of fitted I_c does not lie in its precise amplitude, but rather in its gate dependence, which we compare to theory in the next chapter.

4

SUPERCURRENT MODELLING

In this chapter we detail how the critical current I_c can be calculated for a S-DQD-S setup in the limit of low coupling to the superconducting leads. Results from this section are used to benchmark zero-bias conductance measurements shown in chapter 2. This accordance confirms that measured supercurrent indeed stems from a DQD junction, allowing us to map out charge diagrams and identify groundstates, using supercurrent as a probe. This theory, used in projects 1, 2 and 5, was originally printed in the supplement of project 1.

4.1 FOURTH ORDER PERTURBATION THEORY - SINGLE DOT

Before we move to the DQD, it is illuminating to first consider supercurrent through a single dot in a S-QD-S junction, as the derivations are largely similar. This problem is well studied in the literature for both low coupling [130, 131] and large coupling where YSR screening becomes relevant [33, 36, 39].

We begin with the Hamiltonian of a single-orbital Anderson model, describing a quantum dot locally tunnel coupled to a left and right BCS lead,

$$H = H_D + H_L + H_R + H_T \tag{4.1}$$

$$H_D = \frac{U}{2}(N - n)^2 \tag{4.2}$$

$$H_j = \sum_{k,\sigma} \xi_{kj} c^\dagger_{jk\sigma} c_{jk\sigma} + \sum_k \left(\Delta_j c^\dagger_{jk\uparrow} c^\dagger_{j-k\downarrow} + \Delta_i^* c_{j-k\downarrow} c_{jk\uparrow} \right) \tag{4.3}$$

$$H_T = \sum_{j=L,R} \sum_{k,\sigma} t_j \left(c^\dagger_{jk\sigma} d_\sigma + d^\dagger_\sigma c_{jk\sigma} \right) \tag{4.4}$$

with $N = \sum_\sigma d^\dagger_\sigma d_\sigma$ denoting total electron occupation of the quantum dot, with a local gate n controlling the groundstate occupation. Tunnel couplings t_j, for $j \in \{L, R\}$, are assumed to be real, as any phase dependence can be gauged onto the phase difference $\phi = \phi_L - \phi_R$ between the two superconductors. For simplicity we restrict ourselves to the symmetric case $\Delta = |\Delta_L| = |\Delta_R|$.

We define current as the change of electrons number on the right lead $N_{R\sigma} = \sum_k c^\dagger_{Rk\sigma} c_{Rk\sigma}$ due to tunnelling,

$$\begin{aligned} I &= i\frac{e}{\hbar}\sum_\sigma \langle [H_T, N_{R\sigma}]\rangle = \frac{2e}{\hbar}\mathrm{Im}\sum_\sigma \langle H_{TR\sigma}\rangle = \frac{2e}{\hbar}\mathrm{Im}\sum_\sigma \frac{1}{Z}\,\mathrm{Tr}\left[U(\beta,0)H_{TR\sigma}\right] \\ &= \frac{2e}{\hbar}\mathrm{Im}\sum_\sigma \frac{1}{Z}\frac{1}{\beta}\int_0^\beta d\tau\,\mathrm{Tr}\left[U(\beta,\tau)H_{TR\sigma}(\tau)U(\tau,0)\right] \end{aligned} \tag{4.5}$$

using shorthand $H_{Tj\sigma} = \sum_k t_j c^\dagger_{jk\sigma} d_\sigma$, and with time evolution operator $U(\tau,\tau') = T_\tau \exp\left(-\int_{\tau'}^{\tau} d\tau_1 H(\tau_1)\right)$ defined in imaginary time τ. Time evolution is in the Heisenberg picture such that $H_{TR\sigma}(\tau) = U(\tau,0)H_{TR\sigma}U(0,\tau)$, ensuring validity of the last line in eq. (4.5). Following Refs. [132, 133], we assume that the lead couplings t_j are small and expand the time evolution operators in them. The term that is second order in t_j does not contribute, as it describes single electron transfer for zero bias in a gapped system. Consequently, the lowest non-zero contribution is fourth order,

$$I \approx -\frac{2e}{\hbar}\frac{1}{3!}\,\mathrm{Im}\,\frac{1}{\beta}\int_0^\beta d\tau_1\,d\tau_2\,d\tau_3\,d\tau_4 \sum_\sigma \left\langle T_\tau\left(H_T(\tau_1)H_T(\tau_2)H_T(\tau_3)H_{TR\sigma}(\tau_4)\right)\right\rangle_0, \tag{4.6}$$

where $\langle ...\rangle_0$ is the statistical average in regard to H without H_T, effectively decoupling dot from leads. For this 4^{th} order contribution to be non-zero, the spin and lead indices must correspond to a cooper-pair entering the dot from the left lead and leaving into the right lead. As there are 3 ways to order lead indices and 4 ways to order spin indices to fulfil this constraint, we find

$$I = -\frac{4e}{\hbar}\,\mathrm{Im}\,\frac{1}{\beta}\int_0^\beta d\tau_1\,d\tau_2\,d\tau_3\,d\tau_4 \left\langle T_\tau\left(H^\dagger_{TL\uparrow}(\tau_1)H^\dagger_{TL\downarrow}(\tau_2)H_{TR\downarrow}(\tau_3)H_{TR\uparrow}(\tau_4)\right)\right\rangle_0, \tag{4.7}$$

with H_T indices arbitrarily placed as integrals in combination with time ordering iterates over all possible orderings, rendering any initial choice irrelevant. Using that the statistical average is in regard to a decoupled Hamiltonian, we can separate dot operators from lead operators, yielding

$$I = \frac{4e}{\hbar}t_L^2 t_R^2\,\mathrm{Im}\,\frac{1}{\beta}\int_0^\beta d\tau_1\,d\tau_2\,d\tau_3\,d\tau_4 \mathcal{F}^*_L(\tau_1-\tau_2)\mathcal{F}_R(\tau_3-\tau_4)\mathcal{B}(\tau_1,\tau_2,\tau_3,\tau_4) \tag{4.8}$$

with a sign appearing from fermion commutations. Here $\mathcal{F}_{L/R}(\tau)$ is the momentum summed anomalous Green's function of a bare superconductor derived in appendix A,

$$\mathcal{F}_j(\tau) = -\sum_k \left\langle T_\tau\left(c^\dagger_{j-k\downarrow}(\tau)c^\dagger_{jk\uparrow}(0)\right)\right\rangle_0 = -\pi\nu_j\frac{\Delta_j^*}{\beta}\sum_n \frac{e^{-i\omega_n\tau}}{\sqrt{\omega_n^2+\Delta^2}}, \tag{4.9}$$

with density of states ν_j. The object $\mathcal{B}$ contains contributions from the QD operators,

$$\mathcal{B}(\tau_1,\tau_2,\tau_3,\tau_4) = \left\langle T_\tau \left(d_\uparrow(\tau_1) d_\downarrow(\tau_2) d_\downarrow^\dagger(\tau_3) d_\uparrow^\dagger(\tau_4) \right) \right\rangle_0. \tag{4.10}$$

In eq. (4.8), the phase dependence solely resides on Δ_L and Δ_R, and by taking the imaginary part one readily arrives at $I = I_c \sin(\phi)$ with,

$$I_c = \frac{4e}{\hbar} |\Delta|^2 \Gamma_R \Gamma_L \frac{1}{\beta} \int_0^\beta d\tau_1\, d\tau_2\, d\tau_3\, d\tau_4 f^*(\tau_1-\tau_2) f(\tau_3-\tau_4) \mathcal{B}(\tau_1,\tau_2,\tau_3,\tau_4). \tag{4.11}$$

Here $\Gamma_j = \pi \nu_F |t_j|^2$ is the single electron transfer rate on side j, and

$$f(\tau) = \frac{1}{\beta} \sum_n \frac{e^{-i\omega_n \tau}}{\sqrt{\omega_n^2 + \Delta^2}} = \frac{1}{\pi} \int_\Delta^\infty d\omega \frac{n_F(-\omega) e^{-\omega|\tau|}}{\sqrt{\omega^2-\Delta^2}} - \frac{1}{\pi} \int_\Delta^\infty d\omega \frac{n_F(\omega) e^{\omega|\tau|}}{\sqrt{\omega^2-\Delta^2}}, \tag{4.12}$$

derived in appendix A. Using that the integrals in eq. (4.11) iterates through all possible operator orderings, the critical current can be rewritten as,

$$I_c = \sum_{i,j,k,l=1}^{4} I_{ijkl}, \tag{4.13}$$

where each term in the sum corresponds to a virtual tunnelling path of a cooper-pair across the junction. In this way, the critical current is the sum of all possible paths, each given by,

$$\begin{aligned} I_{ijkl} = \frac{4e}{\hbar} |\Delta|^2 \Gamma_R \Gamma_L \frac{1}{\beta} \int_0^\beta d\tau_i \int_0^{\tau_i} d\tau_j \int_0^{\tau_j} d\tau_k \int_0^{\tau_k} d\tau_l \\ \times f^*(\tau_1-\tau_2) f(\tau_3-\tau_4) \mathcal{B}_{ijkl}(\tau_1,\tau_2,\tau_3,\tau_4), \end{aligned} \tag{4.14}$$

using the following definition,

$$\mathcal{B}_{ijkl}(\tau_1,\tau_2,\tau_3,\tau_4) = \epsilon_{ijkl} \left\langle \left(d_i(\tau_i) d_j(\tau_j) d_k(\tau_k) d_l(\tau_l) \right) \right\rangle_0 \tag{4.15}$$

with $d_1(\tau_1) = d_\uparrow(\tau_1)$, $d_2(\tau_2) = d_\downarrow(\tau_2)$, $d_3(\tau_3) = d_\downarrow^\dagger(\tau_3)$ and $d_4(\tau_4) = d_\uparrow^\dagger(\tau_4)$. The four-index Levi-Civita symbol ϵ_{ijkl}, defined such that $\epsilon_{1234} = 1$, removes duplicate operators and accounts for signs from operator permutations.

To highlight the structure of the full derivation, we will now consider a specific dot groundstate $|g\rangle$ and a specific path. First, the single dot Hilbert space consists of four states: $|0\rangle$, $|\sigma\rangle$ with $\sigma \in \{\uparrow,\downarrow\}$ and $|2\rangle$ with corresponding energies $E_0 = Un^2/2$, $E_1 = U(1-n)^2/2$ and $E_2 = U(2-n)^2/2$. We choose $|g\rangle = |0\rangle$ and assume zero temperature $\beta = \infty$, with $\beta = 1/k_B T$. For this choice, the only non-zero ijkl orderings in eq. (4.15) are the ones that start with a creation operator from the right and end

with an annihilation operator. These orderings are: 1234, 2134, 2143, 1243, 2314 and 1423. Specifying the path further, e.g. 1234, we utilize $d_i(\tau) = e^{H_D\tau} d_i e^{-H_D\tau}$ to obtain,

$$\begin{aligned}\mathcal{B}_{1234}(\tau_1,\tau_2,\tau_3,\tau_4) &= \frac{\epsilon_{1234}}{Z}\langle 0|\, U(\beta,\tau_1) d_\downarrow(\tau_1) d_\uparrow(\tau_2) d_\downarrow^\dagger(\tau_3) d_\uparrow^\dagger(\tau_4) U(\tau_4,0)\,|0\rangle \\ &= \langle 0|\, d_\uparrow d_\downarrow d_\downarrow^\dagger d_\uparrow^\dagger\,|0\rangle\, e^{E_0\tau_1} e^{-E_1(\tau_1-\tau_2)} e^{-E_2(\tau_2-\tau_3)} e^{-E_1(\tau_3-\tau_4)} e^{-E_0\tau_4} \\ &= e^{-\bar{E}_1(\tau_1-\tau_2)} e^{-\bar{E}_2(\tau_2-\tau_3)} e^{-\bar{E}_3(\tau_3-\tau_4)}.\end{aligned} \tag{4.16}$$

with $\bar{E}_j = E_j - E_0$ indicating excitation energies. Inserting this into eq. (4.14) together with eq. (4.12), where we disregard the term proportional to $n_F(\omega)e^{\omega|\tau|}$ as $\beta \to \infty$, we find,

$$\begin{aligned}I_{1234} &= \frac{4e}{\pi^2\hbar}\Delta^2\Gamma_R\Gamma_L \int_\Delta^\infty \frac{d\omega_1}{\sqrt{\omega_1^2-\Delta^2}} \int_\Delta^\infty \frac{d\omega_2}{\sqrt{\omega_2^2-\Delta^2}} \frac{1}{\beta} \int_0^\beta d\tau_1 \int_0^{\tau_1} d\tau_2 \int_0^{\tau_2} d\tau_3 \int_0^{\tau_3} d\tau_4 \\ &\qquad \times \mathcal{B}_{1234}(\tau_1,\tau_2,\tau_3,\tau_4) e^{-\omega_1(\tau_1-\tau_2)} e^{-\omega_2(\tau_3-\tau_4)} \\ &= \frac{4e}{\pi^2\hbar}\Delta^2\Gamma_R\Gamma_L \int_\Delta^\infty \frac{d\omega_1}{\sqrt{\omega_1^2-\Delta^2}} \int_\Delta^\infty \frac{d\omega_2}{\sqrt{\omega_2^2-\Delta^2}} \frac{1}{\bar{E}_1+\omega_1} \frac{1}{\bar{E}_1+\omega_2} \frac{1}{\bar{E}_2},\end{aligned} \tag{4.17}$$

which constitutes the end result. This procedure must then be repeated for all other orderings. In general, considering all cooper-pair paths in eq. (4.14) for arbitrary groundstates, we find three distinct contributions to I_c, each characterized by a dimensionless integral determined by the time ordering,

$$\begin{aligned}Q_i(\bar{E}_n,\bar{E}_m,\bar{E}_l) &= \int_1^\infty \int_1^\infty \frac{d\omega_1\, d\omega_2}{\sqrt{\omega_1^2-1}\sqrt{\omega_2^2-1}} \\ &\times \begin{cases} \dfrac{1}{(\bar{E}_n/\Delta+\omega_1)(\bar{E}_l/\Delta+\omega_2)(\bar{E}_m/\Delta)} & i=1. \\ \dfrac{1}{(\bar{E}_n/\Delta+\omega_1)(\bar{E}_l/\Delta+\omega_1)(\bar{E}_m/\Delta+\omega_1+\omega_2)} & i=2. \\ \dfrac{1}{(\bar{E}_n/\Delta+\omega_1)(\bar{E}_l/\Delta+\omega_2)(\bar{E}_m/\Delta+\omega_1+\omega_2)} & i=3. \end{cases}\end{aligned} \tag{4.18}$$

To identify which integral is associated with which ordering, one uses symmetries. Starting from ordering 1234, identified as Q_1, we from spin symmetry find that replacing $1 \leftrightarrow 2$ and $3 \leftrightarrow 4$ yields 4 identical terms in time structure, therefore also Q_1, satisfying $I_{1234} = I_{2134} = I_{2143} = I_{1243}$ for $|g\rangle = |0\rangle$. Lastly, due to the time symmetry, $f(\tau) = f(-\tau)$, the full replacement $1 \to 3$, $3 \to 1$, $2 \to 4$, and $4 \to 2$ is of a similar time structure, which in total yields 8 orderings associated with Q_1. This last reordering constitutes a particle-hole transformation, and resulting paths are zero for $|g\rangle = |0\rangle$,

since they all start with the removal on an electron, $d_\sigma|0\rangle = 0$. We also identified 2314 as a contribution to the groundstate $|0\rangle$, and by evaluating eq. (4.14) we find that it is associated with Q_3. Using the same symmetry arguments we identify 8 orderings of similar time structure, of which 1423 is another resulting in $I_{2314} = I_{1423}$ for groundstate $|0\rangle$, all associated with Q_3. Lastly, the ordering 2341 constitutes a third branch with 8 identical partners from symmetries associated with Q_2. All orderings of this last type are zero for the groundstate $|0\rangle$, but contributes to e.g. $|g\rangle = |\sigma\rangle$. The number of permutations of the four operators in $\mathcal{B}$ is in total 24, and as we have now identified 3 time structures, each associated with 8 orderings, all permutations are covered.

Intuitively, orderings associated with Q_1 describes cotunnelling processes that add or subtract a whole cooper-pair at a time to the dot. Q_3 describes processes that virtually split the cooper-pair, moving one electron across at a time. Finally, Q_2 describes processes that both split the cooper-pair and transfer two electrons in one step. The different processes are depicted in fig. 4.1. For general $\bar{E}_n$, $\bar{E}_m$, and $\bar{E}_l$ only Q_1 is analytically solvable,

$$Q_1(\bar{E}_n, \bar{E}_m, \bar{E}_l) = \frac{\Delta}{\bar{E}_m} \frac{\arccos(\bar{E}_n/\Delta)}{\sqrt{1-\bar{E}_n^2/\Delta^2}} \frac{\arccos(\bar{E}_l/\Delta)}{\sqrt{1-\bar{E}_l^2/\Delta^2}} \tag{4.19}$$

while Q_3 is only analytically tractable for $\bar{E}_n = \bar{E}_l$ and $\bar{E}_m = 0$ [132]. Our general practice throughout this section will be to solve Q_2 and Q_3 numerically.

In terms of these Q_i integrals the critical current $I_c(g)$, with g denoting groundstate, can be expressed as,

$$I_c(0) = \frac{4e\Gamma_L\Gamma_R}{\pi^2\hbar\Delta}\left[4Q_1(\bar{E}_1, \bar{E}_2, \bar{E}_1) + 2Q_3(\bar{E}_1, \bar{E}_0, \bar{E}_1)\right] \tag{4.20}$$

$$I_c(\sigma) = -\frac{4e\Gamma_L\Gamma_R}{\pi^2\hbar\Delta}\left[2Q_2(\bar{E}_2, \bar{E}_1, \bar{E}_0) + 2Q_2(\bar{E}_0, \bar{E}_1, \bar{E}_2) + Q_3(\bar{E}_2, \bar{E}_1, \bar{E}_2) + Q_3(\bar{E}_0, \bar{E}_1, \bar{E}_0)\right]$$

$$I_c(2) = \frac{4e\Gamma_L\Gamma_R}{\pi^2\hbar\Delta}\left[4Q_1(\bar{E}_1, \bar{E}_0, \bar{E}_1) + 2Q_3(\bar{E}_1, \bar{E}_2, \bar{E}_1)\right]$$

As all Q_i integrals are positive functions these expressions show that the odd groundstate $|\sigma\rangle$ always yields a negative I_c, while the even groundstates $|0\rangle$ or $|2\rangle$ yield a positive I_c. In the literature the negative sign is conventionally recast into a phase factor, $I = -|I_c|\sin(\phi) = |I_c|\sin(\phi + \pi)$, and the supercurrent is said to be in the π-phase. Correspondingly, if I_c is positive the supercurrent is in the 0-phase. In calculations, the sign of a given cooper-pair path is purely determined by operator ordering in eq. (4.15), and to illustrate this further we focus on an odd groundstate $|\uparrow\rangle$, and a path

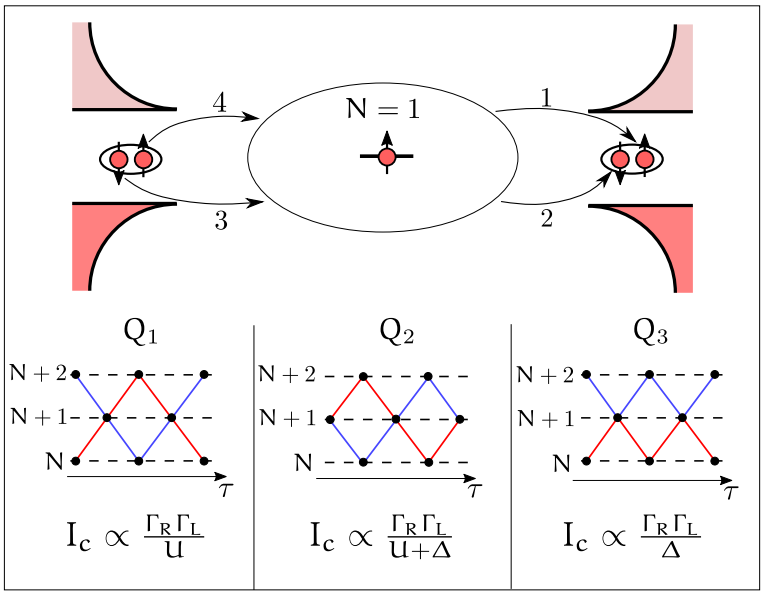

Figure 4.1: Illustration of the four processes transporting a cooper pair across the QD, depicted in the $|\uparrow\rangle$ groundstate. Numbers $1-4$ on the arrows relate to operators in I_{ijkl}. Q_1, Q_2, and Q_3 label the paths that lead to a respective integral in eq. (4.18). The red and blue paths depict the number of electrons N on the QD as a function of virtual time in the tunnelling process. Red lines relate to paths that start with the addition of an electron, while blue lines are paths starting with removal. These are related to each other by particle-hole symmetry. Expressions in the bottom indicate the scale of the Q_i contributions to I_c, in the vicinity of a groundstate transition.

e.g. 4231 associated with a Q_3 process. Disregarding the time-dependence in eq. (4.15), which yields the Q_2 integral, we are left with,

$$\epsilon_{4231} \langle\uparrow| d_4 d_2 d_3 d_1 |\uparrow\rangle = -\langle\uparrow| d^\dagger_\downarrow d_\downarrow d^\dagger_\downarrow d_\uparrow |\uparrow\rangle = -1, \tag{4.21}$$

and the sign is negative. This procedure is performed for each path, in total yielding eq. (4.20), and can be related to drawings as in Ref. [131]. An interesting question is if the detailed structure, with all contribution of equal sign for a given groundstate in eq. (4.15), is a protected attribute or merely coincidental. This we explore further in subsection 4.2.1 in relation to the double quantum dot.

Another interesting feature is that eq.(4.20), which describes lowest order tunnelling, does not diverge at dot phase transitions, dissimilar to normal state tunnelling. For a dot coupled to two metallic leads one commonly separates cotunnelling, which is a low order contributions, from resonant tunnelling which dominates in the vicinity of groundstate transitions. For resonant tunnelling all orders of couplings $t_{L/R}$ need to be included in the summation [18]. This failure of cotunnelling is commonly heralded by divergences at groundstate transitions. In the superconducting case these divergences

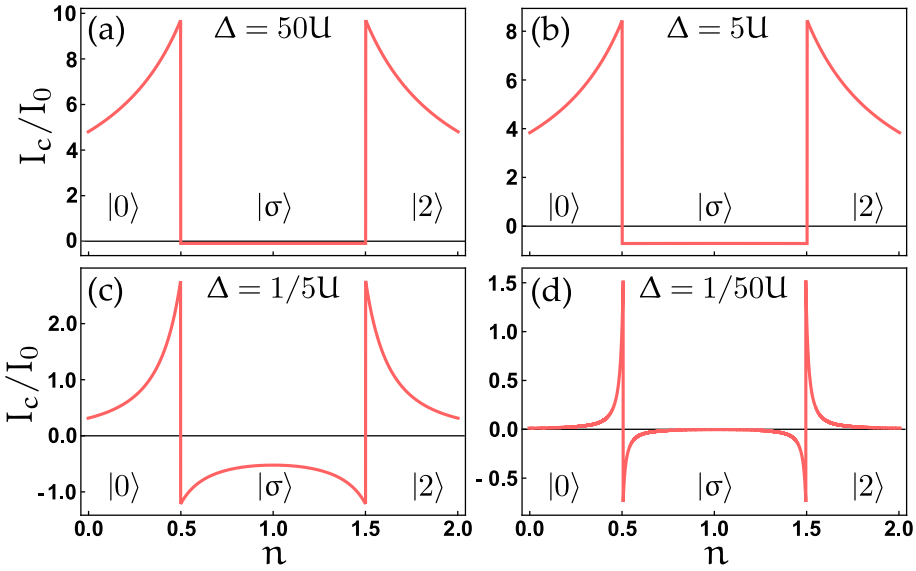

Figure 4.2: Critical current for various U, Δ ratios as a function of dot tuning n calculated with eq. (4.20). Current is given in units of $I_0 = \frac{4e\Gamma_L\Gamma_R}{\pi^2\hbar}\left(\frac{1}{U}+\frac{1}{\Delta}\right)$ such that it scales with U for large Δ and vice versa. Kets in the bottom indicates groundstate for a given gate.

does not appear since both energy scales U and Δ are present. Even at groundstate transitions, where all dot excitations cost zero energy $\bar{E} = 0_+$, e.g. $Q_3(0_+, 0, 0_+)$, the current is not divergent since $Q_3(0_+, 0, 0_+) \approx 0.674$, and consequently I_c scales as $1/\Delta$ for these processes. The energy cost Δ is associated to the virtual steps where a cooper-pair is split, leaving a virtual quasiparticle in the superconductor at energy $E_{qp} \geqslant \Delta$. Only $Q_1(E_n, E_m, E_l)$ can diverge for $E_m = 0$, but from the path associated with this process we see that state m has ±2 electrons compared to the groundstate, and consequently $E_m \geqslant U$. The process Q_2 requires both the splitting of a cooper-pair, at cost Δ, and the transition through states separated by two electrons, at cost U, and does therefore not diverge either. From these arguments we see that higher order processes, i.e. $t_L^4 t_R^2$, scales either as $\Gamma_{L/R}/U$ or $\Gamma_{L/R}/\Delta$, and so for $U, \Delta \gg \Gamma_L, \Gamma_R$ we expect 4^{th} order perturbation to be a valid approximation of I_c for all gates n.

In fig. 4.2 we show I_c for various ratios of U and Δ. The limit of $\Delta \gg U$, in which Q_1 is the main contributor to I_c, is characterized by a lack of supercurrent in the odd parity sector and broad peaks in the even $N = 0, 2$ sectors. In the opposing limit $\Delta \ll U$ only Q_3 contributes and the odd sector shows negative I_c peaks, half the amplitude of the even sector peaks, close to groundstate transition. These limits can be readily understood in terms of eq. (4.20). In the first limit, one cannot add or subtract two electrons from the odd groundstate as $N = -1$ and $N = 3$ are not part of the Hilbert space, hence I_c for an odd groundstate is zero. In the opposite limit, the factor of two difference between odd and even peaks is simply due to the number of paths; in even

sectors one can either start by adding or removing a spin up or down electron, while in the odd sector only a single spin can be added or removed. In the intermediate regime $\Delta \approx U$, process Q_2 begins to contribute and is largest at the odd sector center at $N = 1$. This concludes our derivations for the single QD. In the following section we expand this approach to the DQD and find that the results can in large parts be understood in terms of single QD processes.

4.2 FOURTH ORDER PERTURBATION THEORY - DOUBLE DOT

In this section we detail how the critical current I_c can be obtained for a serial DQD situated between two superconductors using perturbation theory. Similar to a single QD the validity of this expansion relies on $\Gamma_L, \Gamma_R \ll U_{L/R}, |\Delta_{L/R}|$ for which YSR screening is weak and the DQD charge diagram resembles a honeycomb. This weak coupling regime have been investigated in Ref. [134] using a Green's function approach. For stronger lead couplings, where screening occurs, the S-DQD-S junction has been investigated using NRG [135], FRG [136], the tractable $\Delta \to \infty$ limit [137], and with self-consistent mean-field [138]. Our model should therefore be thought of as a weak coupling baseline, on which we can gain some intuition on various parameter limits. We start by assuming that the DQD can be described as two serially coupled Anderson orbitals,

$$H = H_D + H_L + H_T + H_T, \tag{4.22}$$

$$H_D = \sum_{j=L,R} \frac{U_j}{2} \left(N_j - n_j\right)^2 + U_{LR}(N_L - n_L)(N_R - n_R) + t_d \sum_\sigma \left(d^\dagger_{L\sigma} d_{R\sigma} + d^\dagger_{R\sigma} d_{L\sigma}\right), \tag{4.23}$$

$$H_j = \sum_{k,\sigma} \xi_j c^\dagger_{jk\sigma} c_{jk\sigma} + \sum_k \left(\Delta_j c^\dagger_{jk\uparrow} c^\dagger_{j-k\downarrow} + \Delta_j^* c_{j-k\downarrow} c_{jk\uparrow}\right), \tag{4.24}$$

$$H_T = \sum_{k,\sigma} \sum_{j=L,R} t_j \left(c^\dagger_{jk\sigma} d_{j\sigma} + d^\dagger_{j\sigma} c_{jk\sigma}\right). \tag{4.25}$$

Here $N_j = \sum_\sigma d^\dagger_{j\sigma} d_{j\sigma}$ denotes the electron occupation operator for dot $j \in \{L, R\}$, while local gates n_j are used to tune individual dot occupations. The U_{LR} interaction accounts for interdot charging where electrons on one QD capacitively feels the charge of electrons on the second. Similar to the single QD case, all tunnel couplings are chosen real. Completely analogous to the single dot case, we define current as the rate

of electrons running from the right dot to the right lead and expand the time evolution operator to second order in both t_L and t_R yielding,

$$I \approx -\frac{4e}{\hbar}\,\mathrm{Im}\,\frac{1}{\beta}\int_0^\beta d\tau_1\,d\tau_2\,d\tau_3\,d\tau_4 \Big\langle T_{fi}\left(H^\dagger_{TL\uparrow}(\tau_1)H^\dagger_{TL\downarrow}(\tau_2)H_{TR\downarrow}(\tau_3)H_{TR\uparrow}(\tau_4)\right)\Big\rangle_0, \quad (4.26)$$

with $H_{Tj\sigma} = t_j c^\dagger_{jk\sigma} d_{j\sigma}$. Sorting operators and taking the imaginary part yields,

$$I_c = \sum_{ijkl} I_{ijkl} = \frac{4e}{\hbar}\,|\Delta|^2\,\Gamma_R\Gamma_L \sum_{ijkl}\frac{1}{\beta}\int_0^\beta d\tau_i \int_0^{\tau_i} d\tau_j \int_0^{\tau_j} d\tau_k \int_0^{\tau_k} d\tau_l \quad (4.27)$$
$$\times\, f^*(\tau_1-\tau_2)f(\tau_3-\tau_4)\mathcal{B}_{ijkl}(\tau_1,\tau_2,\tau_3,\tau_4)$$

with the only difference, compared to the single QD derivation, appearing in $\mathcal{B}_{ijkl}$ now defined for the uncoupled DQD Hamiltonian,

$$\mathcal{B}_{ijkl}(\tau_1,\tau_2,\tau_3,\tau_4) = \epsilon_{ijkl}\Big\langle \left(d_i(\tau_i)d_j(\tau_j)d_k(\tau_k)d_l(\tau_l)\right)\Big\rangle_0, \quad (4.28)$$

with $d_1(\tau_1) = d_{R\uparrow}(\tau_1)$, $d_2(\tau_2) = d_{R\downarrow}(\tau_2)$, $d_3(\tau_3) = d^\dagger_{L\downarrow}(\tau_3)$ and $d_4(\tau_4) = d^\dagger_{L\uparrow}(\tau_4)$. The complexity of a DQD compared to a single QD stems from the large Hilbert space $4^2 = 16$ and the interdot tunnel coupling t_d in H_D, which renders eigenstates of H_D into superpositions of left and right number states, thereby delocalizing electrons across the two dots. Consider, as an example a gate region where $|\uparrow,0\rangle$ is almost degenerate with $|0,\uparrow\rangle$, with left and right position indicating left and right dot. Due to t_d these two states hybridize into,

$$E_B = A\,|\uparrow,0\rangle - B\,|0,\uparrow\rangle, \quad \text{and} \quad E_{aB} = B\,|\uparrow,0\rangle + A\,|0,\uparrow\rangle, \quad (4.29)$$

with label B for bonding and aB for anti-bonding and $E_B < E_{ab}$. Similar processes occur for other states fulfilling $|N_L, N_R\rangle = |N_L \pm 1, N_R \mp 1\rangle$, with largest complexity in the $N_L + N_R = 2$ sector of the Hilbert space, spanned by 4 states, where e.g. exchange singlet formation occurs. We can tackle this large Hilbert space by two different strategies. Strategy one is to expand in t_d in a pertubative manner, similar to t_L and t_R, generating higher order contributions than the three Q_i integrals in eq. (4.18). Strategy two is to utilize the diagonal basis of H_D, which is obtained numerically, and recast d_i operators in this basis.

In the following, we pursue the second strategy, while in subsection 4.2.1 we present an important result on the sign of I_c, derived using the first strategy. In the charge basis, DQD states can be written as $|n\rangle = \left|N_{L\uparrow}, N_{L\downarrow}, N_{R\uparrow}, N_{R\downarrow}\right\rangle$ yielding a 16×16 dimensional Hilbert space. In this basis,

$$d_i(\tau) = \sum_{n,m=1}^{16} e^{H_D\tau}\,|n\rangle\,\langle n|\,d_i\,|m\rangle\,\langle m|\,e^{-H_D\tau} = \sum_{n,m=1}^{16} e^{H_D\tau}\,|n\rangle\,M_{i,nm}\,\langle m|\,e^{-H_D\tau}, \quad (4.30)$$

where $M_{i,nm} = \langle n| d_i |m\rangle$ is the matrix representation of operator d_i. In the charge basis M_i contains only off-diagonal elements of value ± 1 (minus sign from fermionic commutations), connecting subspaces that are ± 1 dot electron apart. The next step is to perform a unitary transformation of M_i into the diagonal basis of H_D yielding $\bar{M}_i = AM_iA^\dagger$, where A diagonalizes H_D with corresponding energies E_i. Inserting unities into eq. (4.28) we find,

$$\mathcal{B}_{ijkl} = \epsilon_{ijkl} \sum_{n,m,p=1}^{16} \bar{M}_{i,gn}\bar{M}_{j,nm}\bar{M}_{k,mp}\bar{M}_{l,pg} e^{-\bar{E}_n(\tau_i-\tau_j)} e^{-\bar{E}_m(\tau_j-\tau_k)} e^{-\bar{E}_p(\tau_k-\tau_l)} \tag{4.31}$$

with $\bar{E}_i = E_i - E_g$ and g referring to the groundstate of H_D, since U diagonalize time evolution operators as well. In this expression all time dependence resides on the exponential function in an identical manner to the single QD. As such, solving the integrals in eq. (4.27) will yield the same Q_i integrals (eq. (4.18)), but with excitation energies from the DQD eigenstates which are tied together with $\bar{M}_i$ matrix indices describing a specific path through the 16×16 dimensional Hilbert space. As an example let us again consider the $ijkl$ ordering 1234 which describes the addition and subsequent removal of a full cooper-pair from the DQD for the empty groundstate $|N = 0\rangle$, with $N = N_L + N_R$, which is an eigenstate of H_D. This ordering of imaginary time is associated with the Q_1 integral, and we find,

$$I_{1234} = \frac{4e\Gamma_L\Gamma_R}{\pi^2\hbar\Delta} \sum_{n,p\in N=1} \sum_{m\in N=2} \bar{M}_{1,0n}\bar{M}_{2,nm}\bar{M}_{3,mp}\bar{M}_{4,p0} Q_1(\bar{E}_n, \bar{E}_m, \bar{E}_p). \tag{4.32}$$

This equation details how the addition of an electron to the $|N = 0\rangle$ groundstate takes the system to the delocalized bonding and anti-bonding $|N = 1\rangle$ subspace, and the further addition of an electron brings the system to the strongly hybridized $|N = 2\rangle$ subspace with four available states. Lastly, the removal of two electrons brings the system back to the $|N = 0\rangle$ groundstate, again through $|N = 1\rangle$. Each transition is determined by a $\bar{M}_i$ entry which describes the overlap between local charge addition d_i and delocalized states, while the Q_i integral captures tunnelling denominators of virtually passed states. In this manner, all contributions are generally of the form,

$$I_{ijkl} = \frac{4e\Gamma_L\Gamma_R}{\pi^2\hbar\Delta}\epsilon_{ijkl} \sum_{n,m,p}^{16} \bar{M}_{i,gn}\bar{M}_{j,nm}\bar{M}_{k,mp}\bar{M}_{l,pg} Q_i(\bar{E}_n, \bar{E}_m, \bar{E}_p). \tag{4.33}$$

with index i denoting the given Q_i integral of a specific $ijkl$ ordering, which we identified for all orderings in section 4.1. To numerically compute I_c for the DQD we diagonalize H_D to obtain A for each gate tuning n_R, n_R. Using this A we find all $\bar{M}_i$

matrices and sum all operator orderings $I_c = \sum_{i,j,k,l=1}^{4} I_{ijkl}$, solving the appropriate Q_i integrals numerically with eigenenergies of H_D as arguments.

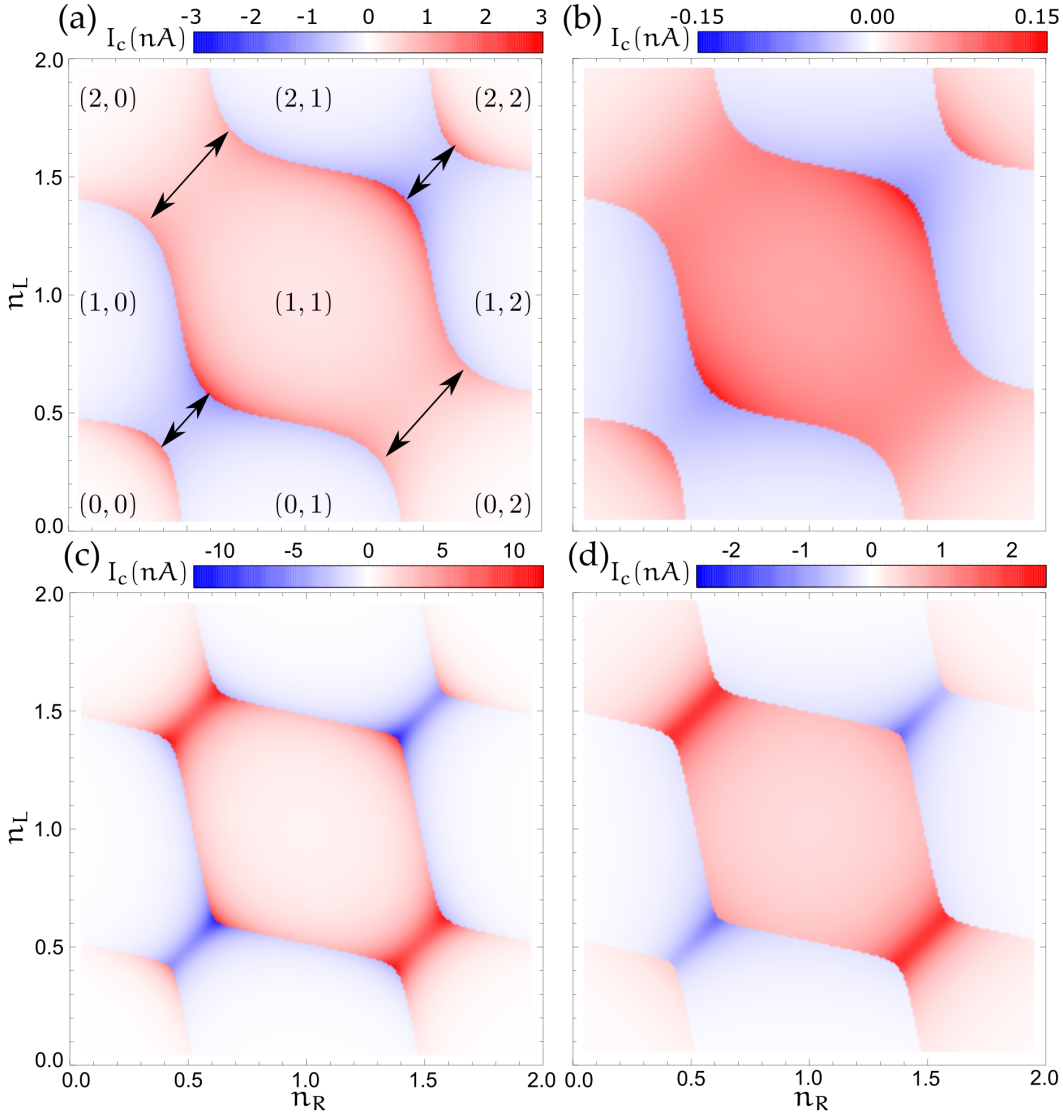

Figure 4.3: Critical current I_c as a function of gate tunings showing the full DQD charge diagram. Parentheses indicate charge sectors in (N_L, N_R) notation. Black arrows indicate openings of the charge sectors due to left-right hybridization from interdot tunneling t_d or charging U_{LR}. For all plots $U_L = U_R = 2$ meV. $\Delta = 0.25$ meV for (a, c) and $\Delta = 1$ eV for (b, d). For (a, b) $\Gamma_L = \Gamma_R = 0.08$ meV, $t_d = 0.3$ meV, $U_{LR} = 0.0$ and for (c, d) $\Gamma_L = \Gamma_R = 0.48$ meV, $t_d = 0.05$ meV, $U_{LR} = 0.4$ meV. The I_c scale, difference of one order of magnitude between (a, c) and (b, d), corresponds to the scale between U and Δ.

In fig. 4.3 we show results of this calculation done in the experimentally relevant regime $U_L, U_R \gg \Delta_L, \Delta_R$ in (a, c), and the opposite regime, for context, in (b, d).

Similarly to single dot results, I_c is largest close to parity transitions, and odd states are found to have negative I_c (π-phase), which for (a, c) is approximately half the amplitude of positive I_c peaks close to a parity transition. In the $\Delta \gg U_L, U_R$ regime, the critical current does not vanish for odd groundstates unlike the single dot results. This is due to Q_1 processes, which are the only non-zero contributions for $\Delta \to \infty$, being available for odd states in the DQD, as a cooper-pair can be added to the $N_L + N_R = 1$ or removed from the $N_L + N_R = 3$ sector if t_d is of similar scale as $U_{L/R}$, allowing electrons to easily delocalize across the dots. Considering the full charge diagram, we find for all cases that the critical current is enhanced in the proximity of the central $N_L = N_R = 1$ sector. This is due to the large number of available cotunnelling processes, since both cooper-pair paths that add and subtract electrons are simultaneously available. In the vicinity of quadruple points, indicated by black arrows in fig. 4.3, single dot states hybridize into bonding states, creating gaps in the charge diagram between states that fulfil $|N_L, N_R\rangle = |N_L \pm 1, N_R \mp 1\rangle$. In these regions the critical current is enhanced as single electrons are easily transferred from the left to right QD. This enhancing is particularly prominent for $t_d \ll U_L, U_R$, shown in fig. 4.3 (c, d), where hybridization is limited to a small region. The parameters in fig. 4.3 are chosen as to yield honeycomb diagrams resembling measured charge diagrams, which we show alongside linecuts in section 4.3.

As an outlook, it should be appreciated that the above calculations of 4^{th} order critical current can be generalized to any diagonalizable system, including one with interactions. One could for example imagine chains of N sites, potentially multiorbibtal, with superconducting leads connected to sites n and m. Lowest order critical current is then given by eq. (4.27) with the simple replacement of lead index L and R with n and m. In the diagonal basis one finds the overlap between adding electrons on site n and removing them on site m, yielding contributions of the form of eq. (4.33). Time structure simply results in the Q_a integrals, no matter the object in between.

4.2.1 *Sign of the critical current*

For the single quantum dot, the number of paths a cooper-pair could take was small enough that we could directly compute the sign of each path. We found that all contributions to I_c for a given groundstate have the same sign; negative (π) for odd parity groundstates and positive (0) for even. In this subsection we investigate the sign of contributions to I_c for the double quantum dot. Utilizing eq. (4.33) it turns out that paths of both negative and positive sign contributes to I_c simultaneously within a given groundstate, even if we account for signs stemming from $\bar{M}_i$ matrices

containing information about operator permutations. However, in our calculations shown in fig. 4.3, we observe that an odd parity groundstate is linked to negative I_c, and even groundstates to positive I_c, just like the single dot. This raises the question; is the sign of I_c guaranteed by the fermionic parity of the groundstate, or are our results merely coincidental, and does there exists parameters ranges where the sign of I_c switches within a parity sector? This we investigate following the strategy of expanding time evolution operators in eq. (4.27) to N'th order in H_D instead of using the diagonal basis. We then consider generic terms in this expansion with the intent of showing that all contributions have the same sign. Derivations in this approach are not necessarily hard, but are notationally very cumbersome for the general case. The full derivation is shown in appendix B, and was originally presented in the supplement of project 4 seen in chapter 11. Here we merely sketch the underlying principles and provide some intuition for the main result.

The main idea is that by using a spin-sorted basis representation, i.e. $|N=4\rangle = d^\dagger_{\uparrow L} d^\dagger_{\uparrow R} d^\dagger_{\downarrow L} d^\dagger_{\downarrow R} |0\rangle$, spin-up operators can be sorted from spin-down operators in regards to eq. (4.28) which determines the sign. Disregarding time dependence, which only contributes to positive denominators from tunnelling, the remaining operators can be spin sorted,

$$\mathcal{B}_{ijkl} = \mathcal{B}_{\uparrow i'j'} \mathcal{B}_{\downarrow i''j''}, \tag{4.34}$$

with $i'j'$ referring to the order of spin-up operators, and $i''j''$ to the order of spin down, i.e. $\mathcal{B}_{4213} = \mathcal{B}_{\uparrow 41}\mathcal{B}_{\downarrow 23}$. The isolated spin objects are given by,

$$\mathcal{B}_{\sigma ij} = \epsilon_{ij} \langle g_\sigma | (H_{D\sigma})^{N_\sigma} d_i (H_{D\sigma})^{M_\sigma} d_j (H_{D\sigma})^{L_\sigma} | g_\sigma \rangle , \tag{4.35}$$

with $H_{D\sigma} = t_d d^\dagger_{L\sigma} d_{R\sigma} + h.c.$ originating from the expansion of time evolution operators, Levi-Civita symbols $\epsilon_{14} = \epsilon_{23} = 1$, and integers fulfilling $\sum_\sigma (N_\sigma + M_\sigma + L_\sigma) = N$ specifying which N'th order term in the expansion we are currently considering. The groundstate is for simplicity assumed to be in a tensor product state $|g\rangle = |g_\uparrow\rangle \otimes |g_\downarrow\rangle$, allowing us to separate it. This cannot be done in general for a delocalized groundstate of H_D, i.e. bonding and anti-bonding states. In appendix B we include such groundstates into the formalism as well. In these expressions all denominators, time dependence etc., relating to the amplitude of the term, but not the sign, have been disregarded. The main result is that the sign of all non-zero $\mathcal{B}_{\sigma ij}$ terms is the same to all orders N of the expansion for a given groundstate, regardless of operator ordering which only affects the amplitude. This sign can be uniquely specified by the number of same spins that a constituent electron of the cooper-pair crosses in tunnelling from left to right. If all contributions to I_c have the same sign, given by the spin-up sign multiplied by the spin-down sign in eq. (4.34), then it follows that this is also the

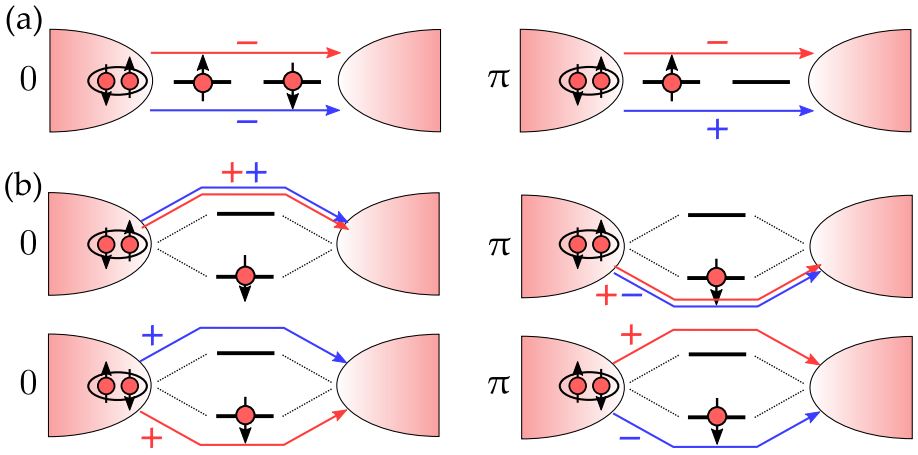

Figure 4.4: (a) Sketches of the paths each constituent electron of the cooper-pair takes across a DQD junction. Red line indicates the path of a spin-up electron, and blue of a spin-down. Coloured ± highlight the signs obtained by counting the number of crossings of electron with same spin on a given path. Label to the left indicates if the contribution in total is π or 0. (b) Sketches of the paths across a parallel DQD for a specific groundstate with a spin-down electron in the lowest orbital. Colours and signs are similar to (a).

sign of I_c, no matter the amplitude of each contribution. In fig. 4.4 we show how this result can be used to find the sign of I_c, and thereby the phase (0 or π), for different groundstates.

Applying these rules to a serial DQD junction, it is clear that the sign of I_c is fully determined by the groundstate parity, since all electrons on the dots are crossed, and consequently $\text{sign}(I_c) = (-1)^N$ with total DQD occupation N. In systems where constituent electrons can take multiple paths, i.e. parallel dots or a single multiorbital dot, contributions to I_c can be both negative and positive, and all paths need to summed with corresponding amplitudes to obtain the sign of I_c. However, these rules can still be applied to infer the signs of specific paths as shown Ref. [133] and in fig. 4.4 (b).

For the serial DQD setup the guarantee of the sign of I_c from the groundstate remains valid if one includes either spin-orbit coupling or a Zeeman term from magnetic field in the Hamiltonian. If both are present simultaneously, and are not parallel, then higher order contributions to I_c of different sign emerges, and the sign is only guaranteed to lowest order in interdot coupling. Lastly, these results and the derivations shown in appendix B appears, from the structure of the derivation, to be generalizable to larger chains than the DQD, e.g. three, four or N serial dots, although it is currently only a speculation.

4.3 DATA AND THEORY COMPARISON

In this section we compare critical current I_c obtained from 4^{th}-order perturbation theory with fitted values from shell X presented in chapter 2. The goal of this comparison is to yield credence to the DQD interpretation of the zero-bias conductance measurements, confirming that supercurrent can be used to map out DQD charge diagrams in a S-DQD-S setup. Throughout this section we use $U_L = U_R = 2$ meV and the pristine gap estimate $\Delta_L = \Delta_R = 0.25$ meV, alongside $R = 3$ kΩ and $T = 80$ mK for supercurrent fits using results of chapter 3. This parameter set places us in the range where Q_3 contributions to I_c dominate and constituent electrons of the cooper-pairs are primarily transferred sequentially across the DQD.

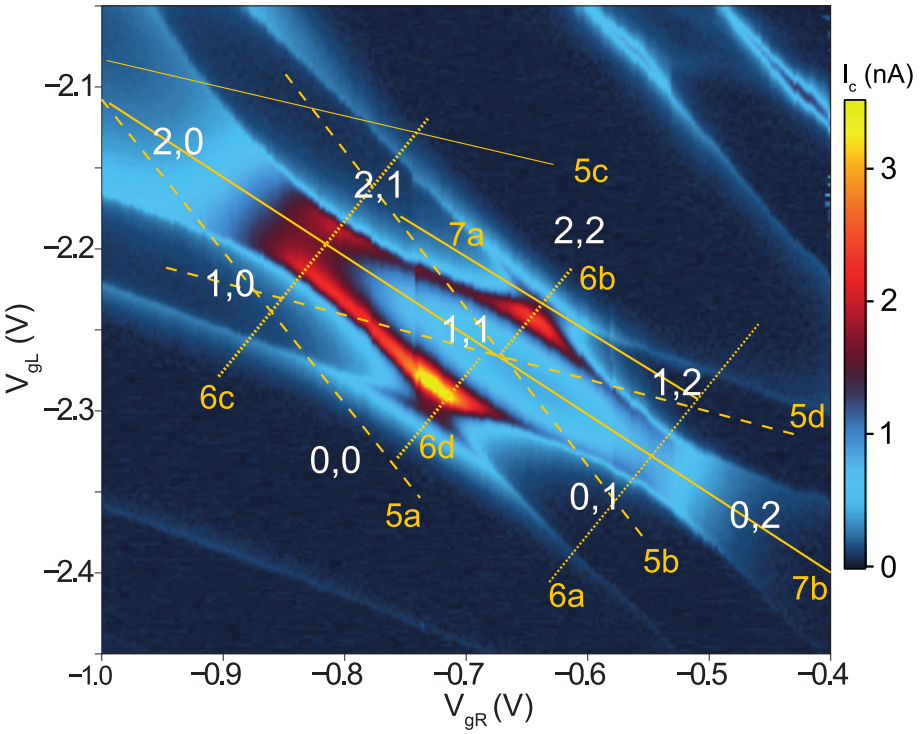

Figure 4.5: Charge stability diagram as a function of plunger gate voltages in the same gate setting as fig. 2.4, with critical current obtained from eq. (3.31) using $R = 3$ kΩ and $T = 80$ mK. Effective charge numbers N_L, N_R determined from the shell-filling pattern are indicated by white numbers for each sector. Lines on the diagram indicate linecuts shown in subsequent figures.

In fig. 4.5 we show a charge diagram of critical current estimates, obtained using a rewriting of eq. (3.31),

$$I_c = \sqrt{\frac{RG(k_B T)^2}{\Phi_0^2}}, \tag{4.36}$$

with $G = dI/dV_{sd}(V_{sd} = 0)$ valid in the noise-dominated regime. Considering the size of triple point openings between the $(1,0)$ and $(2,1)$ sector compared to the opening between $(1,1)$ and $(0,0)$, we find that the measured charge diagram mostly resembles the large t_d and small U_d, case shown in fig. 4.5. For simplicity we choose $U_{LR} = 0$ and $t_d = 0.3$ meV corresponding to fig. 4.5 (a) which approximately matches the shape of fig. 4.6. We acknowledge that finite U_{LR} may be present in experiment and contribute to triple point opening, and consequently we may overestimate t_d in our choice of parameters. Lastly, we choose $\Gamma_L, \Gamma_R = 0.08$ meV to match the amplitude of I_c. In practice they could be asymmetric $\Gamma_L \neq \Gamma_R$, but since they only appear as a global scale in eq. (4.28) we cannot observe this asymmetry in the range where 4^{th}-order perturbation theory remains valid. Moreover, if I_c is globally scaled by $\bar{I}_c = \sqrt{\lambda} I_c$ due to insufficient knowledge of the electromagnetic environment, as in section 3.2, we can adjust this by changing Γ_L and Γ_R accordingly, revealing that we cannot reliably extract $\Gamma_{L/R}$.

From fig. 4.6 to fig. 4.8 we show comparisons between fitted and calculated I_c along linecuts of fig. 4.5. In all experimental plots we show zero-bias peaks as a function of source-drain bias V_{sd} in colour density plots, with an I_c overlay obtained by fitting the zero-bias peak with the Ivanchenko-Zil'bermann equation eq. 3.29. At some gates the white line is dashed; this marks points where the fit is somewhat unreliable due to other low-bias features moving into or across the supercurrent peak. By fitting a linear resistive element R_J in conjunction to I_c, we could possibly have accounted for these features as linear corrections to the supercurrent peak similar to Ref. [115]. In the end, we deemed it more important to keep the fits simple with only one free parameter I_c. In each column, only one I_c theory plot is shown since symmetrical parameters, $U_L = U_R$ and $\Delta_L = \Delta_R$, in addition to particle-hole symmetry $I_c(n_L, n_R) = I_c(2 - n_L, 2 - n_R)$, make the shown theory plot correspond to both experimental cuts in a given column. In theory plots, we show the magnitude, $|I_c|$, as this is what we can estimate from fits, but we plot positive values (0) red and negative values (π) blue to indicate the phase. The groundstate at a given gating is determined from the charge diagram, and is labeled by $GS(n_L, n_R)$ with GS=S, D for singlet and doublet, respectively. 0 and π labels, shown on experimental plots, mark the inferred phase, although it cannot be independently measured in this setup. In chapter 11 we analyse a S-DQD-S system in a SQUID geometry where the full current phase relation (CPR) is available. Here a similar charge diagram is obtained with 0 and π phase at even and odd electron parities as expected, validating the allocation of 0 and π in this experiment.

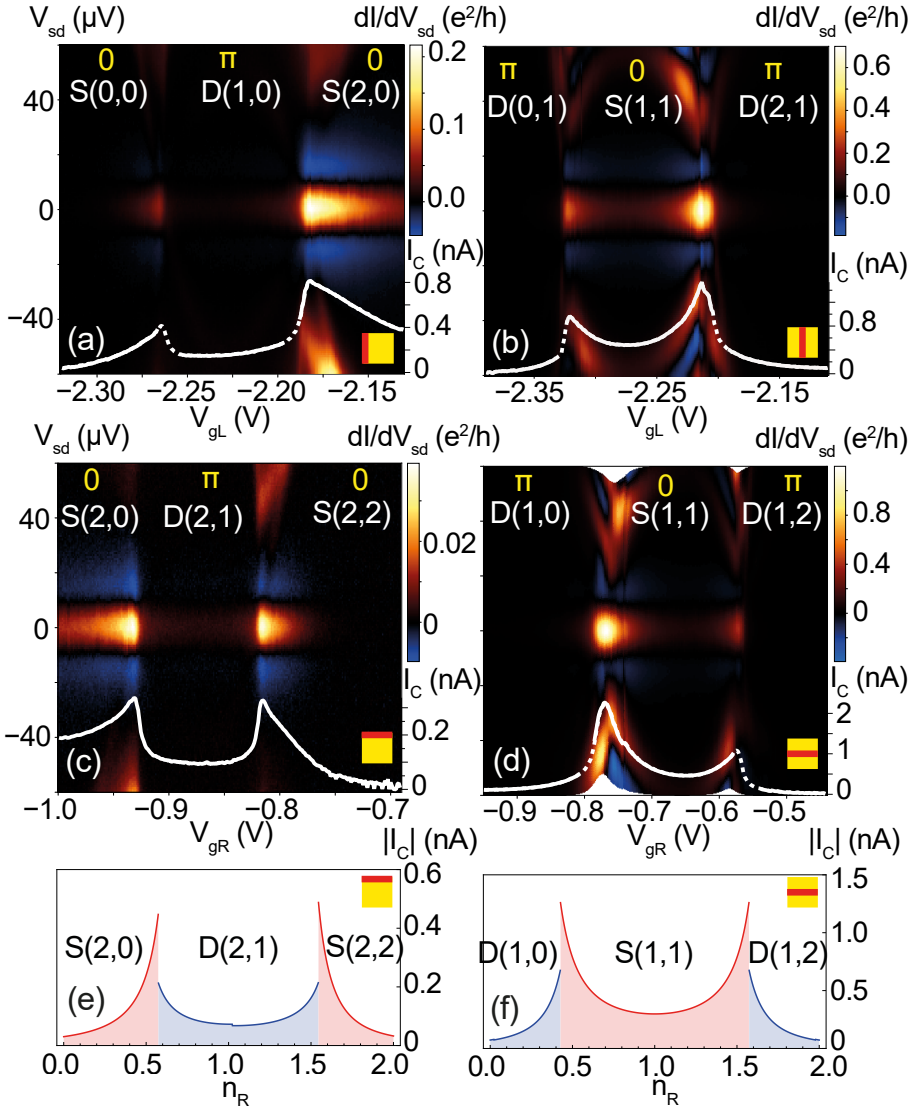

Figure 4.6: (a-d) Linecuts along the dashed lines in fig. 4.5 for fixed N_R (a, b) and for fixed N_L (c, d). *Overlays*. Fitted I_c (white curve). The notation used to name each sector is $GS(N_L, N_R)$, where GS=D, S represents groundstate of the sector. (e, f) Linecuts of $|I_c|$ calculated by 4^{th} order perturbation theory along gate trajectories of n_R. Red (blue) color indicates that I_c is positive (negative). Linecut trajectories are symbolically indicated on each panel by yellow overlays.

In fig. 4.6 (a, c, e) cuts along the edge of the charging diagram are shown. Here supercurrent is expected to resemble the single dot curves shown in fig. 4.3, since the occupation of one dot is kept fixed in a singlet state, acting as a non-interacting barrier, while the other is tuned. This is supported by (a, c) where doublet I_c is approximately half the size of the neighbouring singlet sector. The marked gate asymmetry observed in (a) between $S(0,0)$ and $S(2,0)$ is not observed in theory, and highlights a general

trend in data where I_c increases towards the top-left corner of the charging diagram in fig. 4.5. This could be explained by intergate capacitive couplings, in which the tuning of one gate influences the other gates, e.g. those that control tunnel barrier height. In this manner t_d, Γ_L, and Γ_R could all weakly depend on V_{gL} and V_{gR}. As a matter of fact, when we in chapter 6 consider YSR screening we find that in order to explain the data, Γ_R must increase as a function of V_{gL}. At this stage, we choose not to include this effect in modelling, focusing on simplicity in fitting instead.

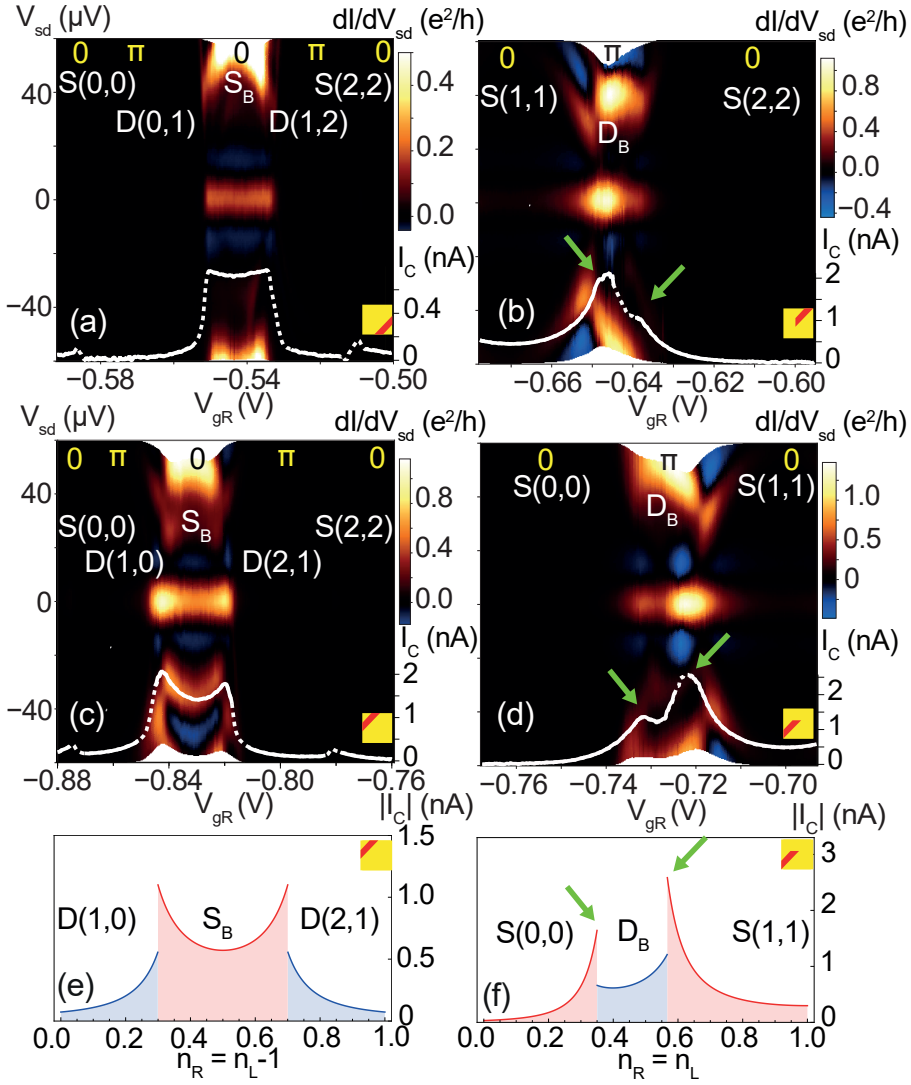

Figure 4.7: (a-d) Linecuts along the dotted lines in fig. 4.5 through triple points showing bonding groundstates (a, c) S_B and (b, d) D_B. *Overlays*. Fitted I_c (white line). (e, f) Linecuts of calculated $|I_c|$ through (e) S_B and (f) D_B ground states, done by 4^{th} order perturbation theory. Red (blue) accounts for positive (negative) I_c. Note that linecut (c) covers two additional charge sectors outside the range of the theory cut (e). Linecut trajectories are symbolically indicated on each panel by yellow overlays.

In fig. 4.7 we show cuts that go through the triple points of the charging diagram, where I_c is expected to be largest and the formation of bonding and anti-bonding states is expected. These states are labelled S_B and D_B depending of their degeneracy. In fig. 4.7 (b, d, f) we observe two I_c peaks on either side of the triple point opening highlighting this formation. In experiments the size of the D_B opening appears smaller than in theory. This could be due to effects of Γ_L or Γ_R which, if slightly larger than the validity of 4^{th}-order perturbation, would somewhat close the doublet sectors as we discuss later in chapter 6.

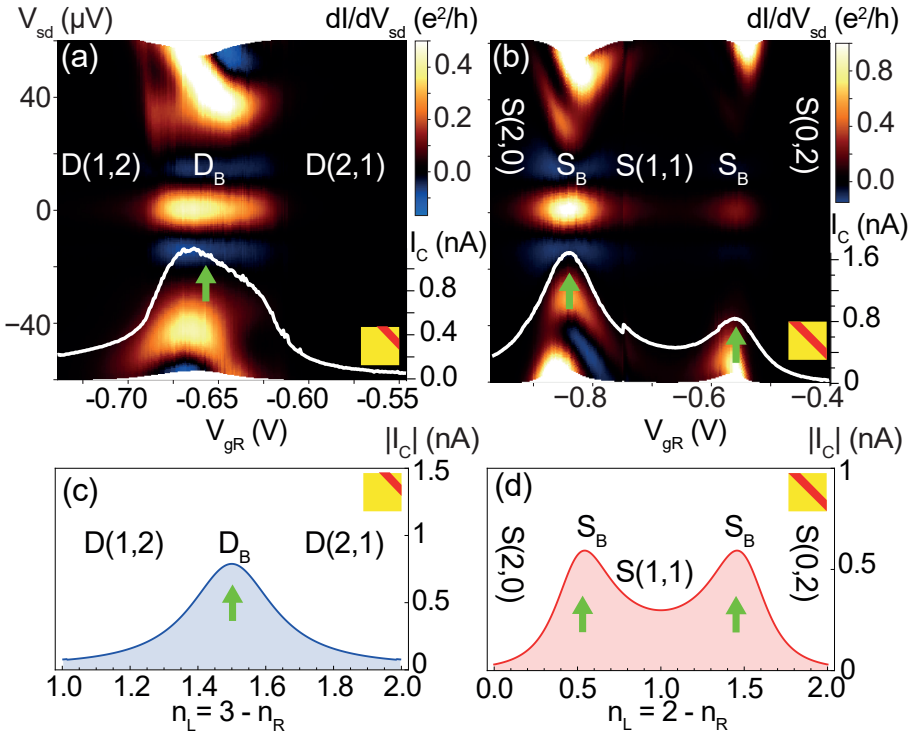

Figure 4.8: (a, b) Detuning linecuts across the triple points following the continuous lines in fig. 4.5. *Overlays*. Fitted I_c (white line). Note that the groundstate, either doublet or singlet, does not change in these linecuts. (c, d) $|I_c|$ traces calculated by 4^{th} order perturbation theory. Red (blue) accounts for positive (negative) I_c. Green arrows indicate zero-detuning points. Linecut trajectories are symbolically indicated on each panel by yellow overlays.

That the formation of bonding states has indeed taken place is highlighted in fig. 4.8 where diagonal cuts are shown keeping $N_R + N_R$ = constant. Here we observe no discontinuity between charge sectors, as we saw in other cuts, but instead smooth evolution of I_c peaking at triple points.

This demonstration constitutes the proof that in S-DQD-S devices, supercurrent can be used as a probe to obtain charge diagrams in a similar fashion to how resonant tunnel current is used in N-DQD-N devices. For small couplings, such that

no screening is present, the observed critical current pattern is nicely predicted by 4^{th} order perturbation theory. In the following sections we will show results from a zero-bandwidth approximation of theoretical interest, and use this to investigate the supercurrent in the vicinity of groundstate transitions.

4.4 ZERO-BANDWIDTH MODELLING OF CRITICAL CURRENT

As has been demonstrated [19–21, 62, 139], a zero-bandwidth (ZBW) approximation for the BCS leads reproduces the correlations leading to YSR bound states very well, and compares even quantitatively, using a sufficient choice of zero-bandwidth model parameters t_L, t_R, with results of numerical renormalization group (NRG). Here we explore the possibility of utilizing the ZBW approximation to calculate critical current I_c, and compare it to results of 4^{th} order perturbation theory. This approach provides a computationally easy way of assessing the effects of both finite temperature and finite (non-infinitesimal) couplings Γ_L, Γ_R on the I_c profiles, which we use to support 4^{th} order perturbation theory.

The basic principle of the ZBW approximation is to replace the superconducting leads by a single quasiparticle with energy $\pm|\Delta|$, equivalent to the following modification of the left and right BCS Hamiltonian,

$$H_{j,BCS} \approx H_{j,ZBW} = \left(\Delta_j c^\dagger_{j\uparrow} c^\dagger_{j\downarrow} + \Delta^*_j c_{j\downarrow} c_{j\uparrow}\right). \tag{4.37}$$

This reduces the Hilbert space of eq. (4.22) to $4^4 = 256$ states, which can be handled numerically by exact diagonalization. By calculating the free energy using eigenvalues E_i of the ZBW Hamiltonian,

$$F(\phi) = -k_B T \log \sum_i e^{-E_i(\phi)/k_B T}, \tag{4.38}$$

we can express the equilibrium supercurrent as,

$$I(\phi) = \frac{2e}{\hbar} \partial_\phi F(\phi), \tag{4.39}$$

where $\phi = \phi_L - \phi_R$ denotes phase difference. At zero temperature the free energy depends only on the groundstate and the supercurrent simplifies,

$$I(\phi) = \frac{2e}{\hbar} \partial_\phi E_g(\phi), \tag{4.40}$$

with groundstate energy E_g. For small tunnelling rate $\Gamma_L, \Gamma_R \ll |\Delta|, U_L, U_R$ and zero temperature, this numerical procedure confirms the sinusoidal current-phase relation

$I = I_c \sin\phi$, obtained from 4^{th} order perturbation theory. An issue regarding the ZBW approximation is the lack of a density of states ν_F which constitutes a important energy scale in the full BCS description. Consequently, the coupling rate $\Gamma_{L/R}$, which determines the amplitude of I_c and screening at higher coupling, is ill defined. To find a similar energy scale we perform a 4^{th} order expansion for the zero-bandwidth model as well. The imaginary time anomalous Green's function for the ZBW model is given by,

$$\mathcal{F}_j(\tau) = \frac{e^{i\phi_j}}{\beta} \sum_{i\omega_n} \frac{\Delta}{\omega_n^2 + \Delta^2} \tag{4.41}$$

$$= \frac{e^{i\phi_j}}{2} \left(n_F(-\Delta) e^{-\Delta|\tau|} - \frac{1}{2} n_F(\Delta) e^{\Delta|\tau|} \right), \tag{4.42}$$

with $j \in \{L, R\}$ as shown in appendix A. Performing the same steps as in the previous sections, the critical current $I_c = \sum_{ijkl} I_{ijkl}$ consist of terms,

$$I_{ijkl} = \frac{e t_L^2 t_R^2}{\hbar \Delta^3} \sum_{nmp} \bar{M}_{i,gn} \bar{M}_{j,nm} \bar{M}_{k,mp} \bar{M}_{l,pg} Q_{a,ZBW}(\bar{E}_n, \bar{E}_m, \bar{E}_p), \tag{4.43}$$

using the same definitions as in eq. (4.33), with the notable exception of Q-integrals which for ZBW reduce to simple denominators,

$$Q_{i,ZBW}(n, m, l) = \begin{cases} \dfrac{1}{(\epsilon_n/\Delta + 1)(\epsilon_l/\Delta + 1)(\epsilon_m/\Delta)}, & i = 1, \\ \dfrac{1}{(\epsilon_n/\Delta + 1)(\epsilon_l/\Delta + 1)(\epsilon_m/\Delta + 2)}, & i = 2, \\ \dfrac{1}{(\epsilon_n/\Delta + 1)(\epsilon_l/\Delta + 1)(\epsilon_m/\Delta + 2)}, & i = 3. \end{cases} \tag{4.44}$$

Comparing this expression for supercurrent with eq. (4.33) we obtain the same prefactor if we define $\Gamma_{j,ZBW} = \pi t_j^2/2\Delta$ corresponding to $\nu_{F,ZBW} = 1/2\Delta$.

Next, we compare I_c obtained from ZBW diagonalization (eq. (4.40)) with $T = 0$ and $\phi = 0$, with results of 4^{th} order perturbation theory for both ZBW and BCS leads using the experimental relevant parameters. This comparison is shown in fig. 4.9 where we find that for our couplings, $\Gamma_L = \Gamma_R = 0.08$ meV$< U, \Delta$, the exact ZBW calculation matches with ZBW 4^{th} order perturbation, except for slight deviations close to groundstate transitions. Comparing ZBW to 4^{th} order perturbation with BCS leads, we find that deviations are limited to a global factor of two between the models. Comparing fig. 4.9 with fig. 4.3 no notable differences are apparent, apart from the factor of two in scale.

As we also show later in chapter 6, the ZBW approximation, with minor deviations, captures the YSR screening occurring at higher coupling [139]. Correspondingly, the

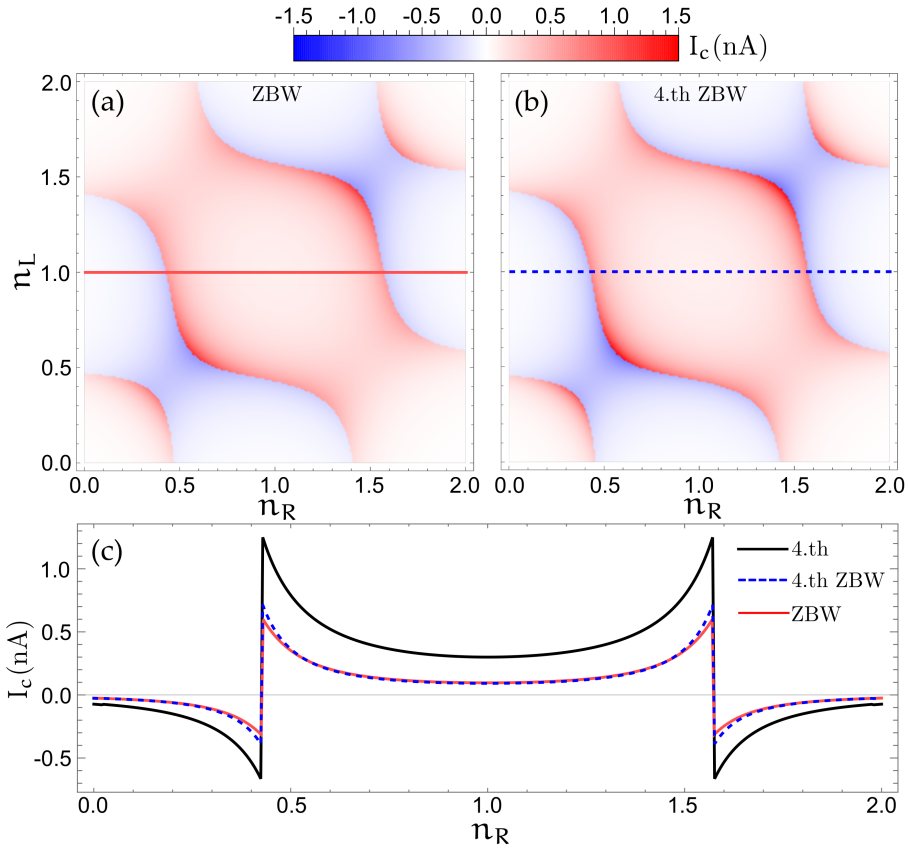

Figure 4.9: (a) and (b) I_c charge diagrams computed using eq. (4.40) and eq. (4.43) evaluated at $\phi = 0$. With experimentally fitted parameters: $U_1 = U_2 = 2$ meV, $\Delta = 0.25$ meV, $t_d = 0.3$ meV, $U_{12} = 0$ meV, $\Gamma_L = \Gamma_R = 0.08$ meV, $T = 0$. (c) shows three linecuts of I_c through the stability diagrams corresponding to the respective lines in panels (a, b) and a corresponding line in fig. 4.3 (a).

parameters obtained by fitting data to lowest order in Γ_L, Γ_R yields no significant screening, supporting that 4^{th} order expansion remains valid for fitted parameters. This shows that our fitting in section 4.3 is self-consistent with the approximations made. In our paper we also compare to results from NRG, in the supplement yielding the same result [1].

4.4.1 *Groundstate transitions*

In the above analysis the phase of the junction was always either 0 or π which we obtained from 4^{th} order perturbation or from ZBW evaluated at $\phi = 0$. From the literature [20, 33, 35, 140, 141] it is well known that the full current phase relation (CPR) is not necessarily $0 - \pi$, with deviations being especially pronounced in the

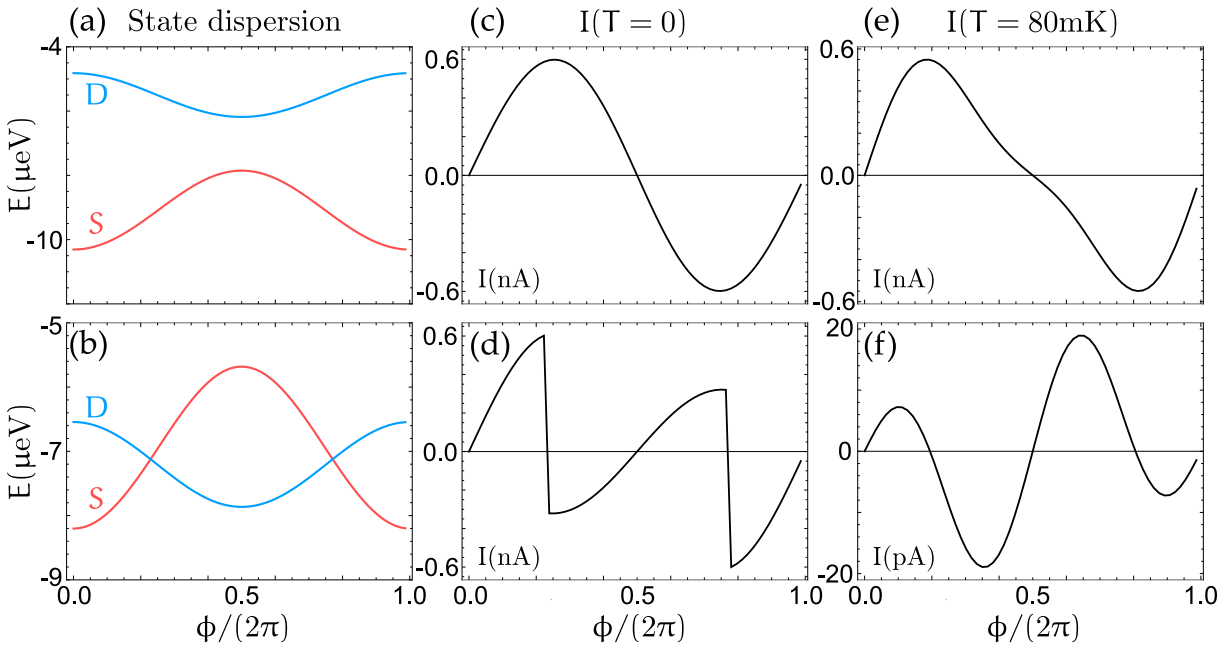

Figure 4.10: (a, b) Examples of groundstate and exited state phase dispersion obtained from exact diagonalization of a DQD ZBW model. Singlet and doublet are marked by S and D respectively. (c-d) Current phase relation (CPR) for $T = 0$ using eq. (4.40). (e, f) CPR calculated at large temperature $k_B T > E_S(\phi), E_D(\phi)$ using eq. (4.39). Top row is calculated with $N_L = 0.43$ and bottom with $N_L = 0.427$, both with $N_R = 1$. This corresponds to the transition shown in fig. 4.9 (c)

vicinity of groundstate transitions. The origin of these deviations are simple; as a function of phase an excited state may move down in energy and cross the groundstate which for $T = 0$ leads to a discontinuity in the CPR as seen from eq. (4.40) and illustrated in fig. 4.10.

From modelling with fitted parameters we find that CPR remains sinusoidal ($0 - \pi$) for the majority of the charge diagram. This is supported by the fitted critical current range $I_c \in [0.02, 3]$ nA corresponding to a phase dispersion of the groundstate through eq. (4.40) on the scale of $E_J = \hbar I_c/2e \sim \mu$eV, much smaller than $\Delta_{L/R}$ and $U_{L/R}$ whose scale determines level separation across the charge diagram. Only close to groundstate transitions, which in experiment and modelling is heralded by discontinuities of I_c, does non-sinusoidal behaviour appear. In fig. 4.10 (a, b) we show the ϕ-dependent dispersion close to a groundstate transition between a singlet and doublet state. In (b) the crossings of these states creates a discontinuity in the $T = 0$ current phase relation (CPR) shown in (d).

For small but finite temperatures the discontinuities, shown in fig. 4.10 (d), smoothens as the groundstate becomes a thermal mixture of S and D close to the level cross-

ing. Next, we investigate the dynamics when temperature is the largest scale in the problem. Consider that only two states are at low energy; a singlet with dispersion $E_S(\phi) = A\cos(\phi)$ and a doublet with $E_D(\phi) = -B\cos(\phi) - E_0$ with E_0 characterizing the energy separation between the two states, which is tuned by gate across the transition, while amplitude A and B remain approximately constant. From the free energy we find,

$$I(\phi) = -\frac{2e}{\hbar}\partial_\phi F(\phi) = \frac{2e}{\hbar}\frac{Ae^{-A\beta\cos\phi} - 2Be^{B\beta\cos(\phi)+E_0\beta}}{e^{-A\beta\cos\phi} + 2e^{B\beta\cos(\phi)+E_0\beta}}\sin\phi, \tag{4.45}$$

where the factor 2 is due to doublet states degeneracy and $\beta = 1/k_BT$. To simplify, we absorb the factor 2 in the energy separation $\bar{E}_0 = E_0 + \log(2)/\beta$ and rewrite it as an asymmetric $C = (B-A)/2$ and a symmetric $D = (A+B)/2$ part yielding,

$$I(\phi) = \frac{2e}{\hbar}\left[C + D\tanh\left(D\beta\cos\phi + \beta\bar{E}_0/2\right)\right]\sin\phi. \tag{4.46}$$

By expanding in $D\beta, \beta E_0 \ll 1$, corresponding to the large temperature limit, we find,

$$I(\phi) = \frac{2e}{\hbar}\left[(C + D\beta\bar{E}_0/2)\sin\phi + \frac{1}{2}D^2\beta\sin(2\phi)\right] + \mathcal{O}(\beta^2). \tag{4.47}$$

In this limit where temperature is much larger than level separation E_0 and phase dispersions A and B, the CPR is composed of a normal sinusoidal Josephson component and a higher order $\sin(2\phi)$ term. For most gates only the sinusoidal term is visible as the higher order term is suppressed $D\beta$, but in the vicinity of groundstate transitions the prefactor $C + D\beta\bar{E}_0/2$ crosses zero and the $\sin(2\phi)$ term dominates. This evolution is shown in fig 4.10 (f) where current is sharply reduced at the transition and the CPR includes a large $\sin(2\phi)$ component. A similar $\sin(2\phi)$ term was measured at 0-π boundaries in Refs. [78, 142] where they had access to phase tuning utilizing a SQUID setup. The calculation above shows that such 2ϕ terms have a humble origin, and are quite general in the large temperature limit.

In relation to our experiment, temperature is the dominant scale $k_BT > E_J$ and the $\sin(2\phi)$ feature is observed at groundstate transitions which we show in fig. 4.11. Defining critical current as the largest possible supercurrent $I_c = \max_\phi |I(\phi)|$ we observe a rapid drop between each groundstate transition, associated with π periodic $\sin(2\phi)$ terms which we focus on in (d). Using the nomenclature of Ref. [140] and following (d) from left to right (increasing $n_R = n_L$), a sinusoidal 0-phase develops through an intermediate non-sinusoidal 0′-phase to a π-periodic relation right at the dip minimum. A further increase in gate voltage takes the junction through a non-sinusoidal π'-phase and finally into the sinusoidal π-phase in the rightmost panel. If I_c and/or T is increased then the size of the non-sinusoidal drops would increase following the above analysis. In Ref. [115] the $I-V$ characteristic was calculated for

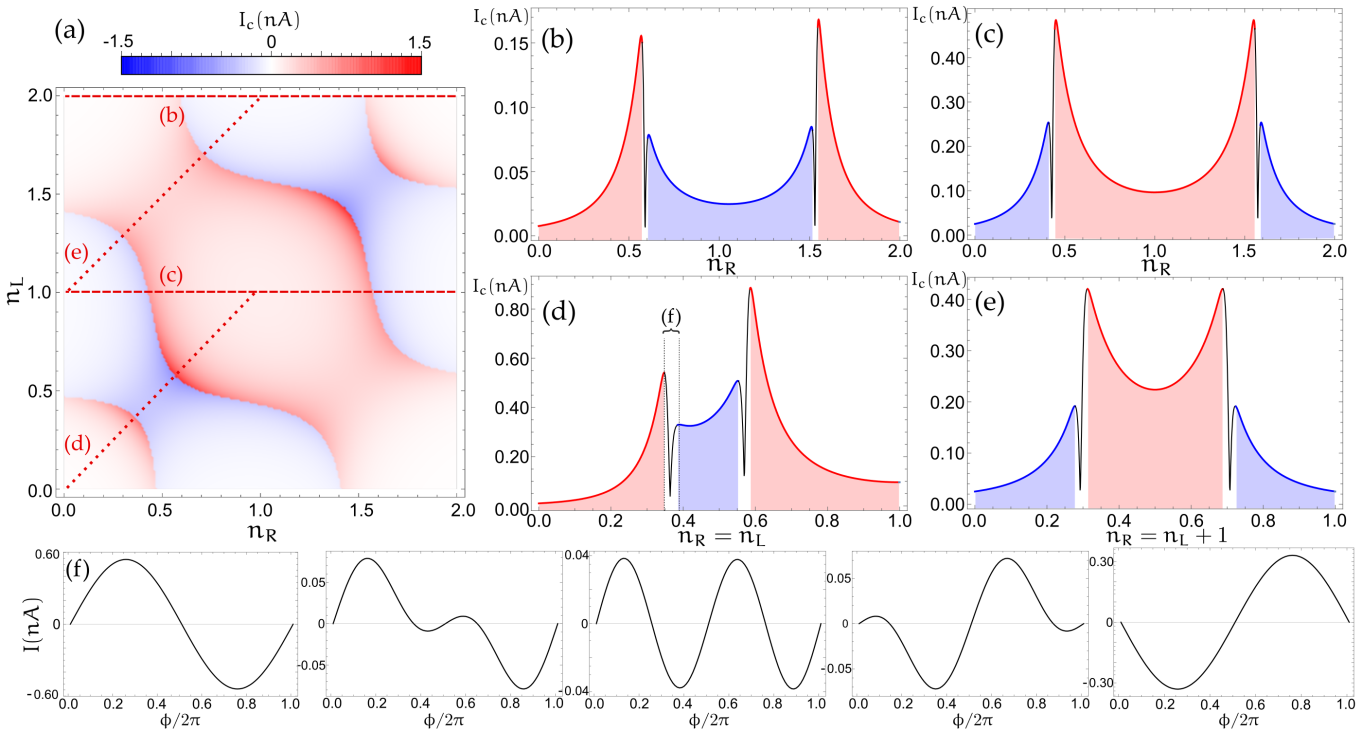

Figure 4.11: (a) Same charge diagram as in fig. 4.9 (a) with lines indicating cuts shown in (b-e). (b-e) $I_c = \max_\phi |I(\phi)|$ calculated using ZBW at finite temperature $T = 80$ mK and using parameters from the fit. The interval shown in (d) indicates the range of gate for which CPR on (f) are provided. Red and blue indicates areas with 0 and π CPR while whites indicates non-sinusoidal. Panels (f) show the current-phase relations obtained at the corresponding gate (from left to right) $n_L = n_R = [0.348, 0.363, 0.364, 0.365, 0.39]$, calculated with ZBW using the same parameters as in (b-e).

a non-sinusoidal CPR, similar to ours, in the vicinity of groundstate transitions and found only small deviations from the RCSJ result. Therefore, we should in principle be able to measure the intermediate I_c dips between 0 and π sectors. We attribute the lack of such dips in data to finite resolution, since dips are very narrow in our parameter range.

In closing, we should remark that eq.(4.39, 4.40) both assume adiabatic phase evolution at which thermal equilibration occurs for each ϕ in the CPR, which may not be realistic. Consider the states phase dispersions shown in fig. 4.10. If change of ϕ occurs rapidly compared to the time at which a subgap state equilibrates then the effective CPR is determined by the CPR of the initial state. This means that the timescales of the RCSJ circuit, which determines the timescale at which ϕ changes, should be compared with the relaxation rate of the subgap state, which determines how quickly a thermal state is reached. This scale can be small for subgap states due

to protection from the gap as we address in chapter 8. This effect could also explain the lack of I_c dips in our experiment.

4.5 CONCLUSION

In this chapter we obtained the critical current I_c to lowest order for both a single QD and DQD Josephson junction. Unlike the normal state where resonant transport to all orders have to be included, all cooper-pairs cross the junction by cotunnelling in the case of dots with superconducting leads. Consequently, lowest order perturbation in tunnel coupling shows no divergences as a function of gate and reasonably describes I_c for the full charge diagram. Similarly to the single dot, the DQD shows 0 and π phases determined by even and odd parity of the groundstate. Using these results we demonstrated the ability to identify DQD charge diagrams from zero-bias measurements of supercurrent resulting in the paper presented in chapter 5. We additionally used this methodology to investigate DQD screening in chapter 6, and CPR of a S-DQD-S device in a SQUID setup in chapter 11 where the 0 and π phase can be affirmed. Lastly, we explored the use of ZBW approximations to calculate I_c and found that by choosing $\Gamma_{i,ZBW} = \pi t_i^2/2\Delta_i$ a good match between ZBW and 4^{th} order perturbation theory was obtained, apart from a factor two global scaling. Using the ZBW approximation we investigated the CPR at groundstate transitions. Deviations from a sinusoidal CPR was for our parameters limited to a small gate range, in concord with the lack of I_c dips in measurements.

5

PROJECT 1

In this chapter we present the published version of project 1 [1], where we show that a S-DQD-S junction can be characterized by measurements of supercurrent. This allows us to identify charge sectors, and from them infer the groundstate. In addition to chapter 3 and chapter 4, which constitute my contributions to this project, NRG calculations where provided by Rok Žitko. These calculations supports the validity of 4^{th} order perturbation theory, and can be found in the supplement of Ref. [1]. Most figures, methods and conclusions have already been covered in the preceding chapter 4, and the included paper is primarily for the reader interested in further details.

Supercurrent in a Double Quantum Dot

J. C. Estrada Saldaña,[1] A. Vekris,[1] G. Steffensen,[1] R. Žitko,[2,3] P. Krogstrup,[1,4] J. Paaske,[1]
K. Grove-Rasmussen,[1] and J. Nygård[1,*]
[1]Center for Quantum Devices, Niels Bohr Institute, University of Copenhagen, 2100 Copenhagen, Denmark
[2]Jožef Stefan Institute, Jamova 39, SI-1000 Ljubljana, Slovenia
[3]Faculty of Mathematics and Physics, University of Ljubljana, Jadranska 19, SI-1000 Ljubljana, Slovenia
[4]Microsoft Quantum Materials Lab Copenhagen, Niels Bohr Institute, University of Copenhagen, 2100 Copenhagen, Denmark

(Received 22 August 2018; published 20 December 2018)

We demonstrate the Josephson effect in a serial double quantum dot defined in a nanowire with epitaxial superconducting leads. The supercurrent stability diagram adopts a honeycomb pattern. We observe sharp discontinuities in the magnitude of the critical current, I_c, as a function of dot occupation, related to doublet to singlet ground state transitions. Detuning of the energy levels offers a tuning knob for I_c, which attains a maximum at zero detuning. The consistency between experiment and theory indicates that our device is a faithful realization of the two-impurity Anderson model.

DOI: 10.1103/PhysRevLett.121.257701

Recent progress in the microfabrication of hybrid semiconductor-superconductor one-dimensional heterostructures has resulted in Josephson junctions with controlled ground states [1–3]. This control is achieved by confining electrons in a quantum dot (QD) in the semiconductor weak link. In a weakly coupled QD, the number of electrons, N, is known precisely thanks to the charging energy, U, and it is conveniently controlled by a gate voltage. A singly occupied dot shifts the phase difference between the superconducting leads by π, which corresponds to a doublet ground state. When N changes in an even-odd-even fashion, an alternating $0-\pi-0$ pattern in the phase of the supercurrent is expected. This has been experimentally observed in single QDs [4–10].

A serial double quantum dot (DQD) Josephson junction offers greater freedom in the control of the ground state of the system. DQD levels, as opposed to multilevel single dots [4,10–13], have the advantage of individual gate control of the parameters of each dot level [14–18]. The subgap states of a DQD attached to two superconducting leads have been previously investigated, but the soft gap of the device resulted in an effectively S-DQD-N system (N stands for a normal metal, and S for a superconducting lead), and a supercurrent has not been reported [14]. Subgap states have also been described in a purposely engineered S-DQD-N device, in a regime with stronger coupling to the S lead, which could then screen the spin of the dots [15]. Chains of dots in series coupled by superconductors can be mapped to the Hamiltonian of a topological superconductor, which constitutes an additional motivation for investigating this type of devices [19,20].

In this Letter, we demonstrate for the first time a gate-controlled S-DQD-S Josephson junction, and focus on a regime of weak coupling to the two S leads. We find discontinuities in the critical current which depend on the total number of electrons in the dots. Their line shape, characterized by asymmetries and changes in magnitude, allows us to identify them as $0 \to \pi$ phase transitions corresponding to singlet to doublet ground state changes, as previously done for single QDs [4–6,8,10,21]. Whenever an odd (even) total number of electrons is present in the highest-lying levels of each dot, the DQD ground state is a doublet (singlet). Additionally, we find a modulation of I_c through orbital detuning, with maximal I_c at maximal orbital hybridization. The changes in the ground state are corroborated by crossings of subgap states. We model our findings using the two-impurity serial Anderson model.

Our device is depicted in Figs. 1(a) and 1(b). A 110 nm-diameter InAs nanowire with an *in situ* grown epitaxial 7 nm Al shell [22], covering three of its facets, was first deterministically placed over a bed of finger gates insulated by a 20 nm layer of hafnium oxide dielectric. By selectively etching the Al shell over five of these gates, we obtained a 350 nm section of bare InAs nanowire. Afterwards, we contacted the ends of the wire with two Ti/Au strips, each at a distance roughly 1 μm away from the bare wire. Additionally, we used as a global backgate the highly doped Si substrate with a 300 nm Si oxide on which the device was fabricated.

Two QDs in series were defined in the bare wire through gate tuning, and were proximitized by the sections of the wire with superconducting Al. A scheme of this S-DQD-S system and its energetics are portrayed in Figs. 1(c) and 1(d), respectively. All differential conductance measurements were done in a dilution cryostat at 15 mK, using a standard lock-in technique with an AC excitation of 2 μV at a frequency of 116.81 Hz.

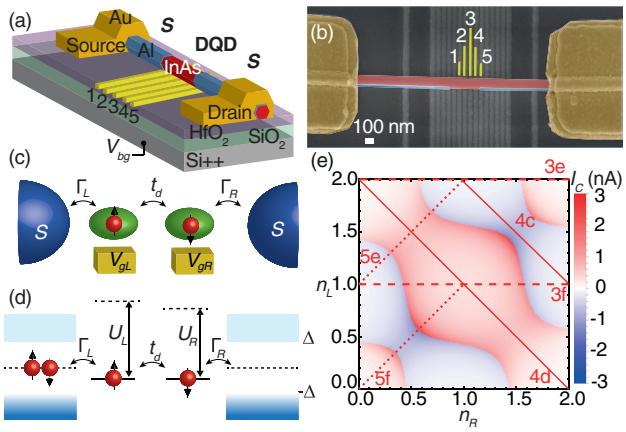

FIG. 1. (a) Schematics of the device. Gates numbered 1 to 5 were used to electrostatically define two quantum dots in the channel of the bare InAs nanowire. A backgate voltage, V_{bg}, was used for further fine-tuning of the coupling of the dots. (b) Scanning-electron micrograph of the measured device. Au contacts, epitaxial Al leads, and InAs nanowire are colored in yellow, blue, and red, respectively. (c) Schematics of two quantum dots in series, whose energy level is tuned by the voltage on gates V_{gL} and V_{gR} (for left and right dot), which in our device correspond to gates 2 and 4. (d) Energy diagram of the system, consisting of two single levels in series with energy levels ϵ_L and ϵ_R, coupled to the closest superconducting lead with tunneling rates Γ_L and Γ_R, respectively, and with interdot coupling t_d. The charging energies, $U_L \approx 1.85$ meV and $U_R \approx 1.62$ meV, are much larger than the superconducting gap, $\Delta = 0.265$ meV. The large level spacings, $\Delta E_L \approx 1.64$ meV and $\Delta E_R \approx 1.76$ meV, of the order of U_L and U_R, respectively, make the single-level approximation valid. (e) Charge stability diagram $I_c(n_L, n_R)$ calculated through fourth order perturbation theory [23], where n_L and n_R represent the gate-induced charges in the left and right dots, respectively.

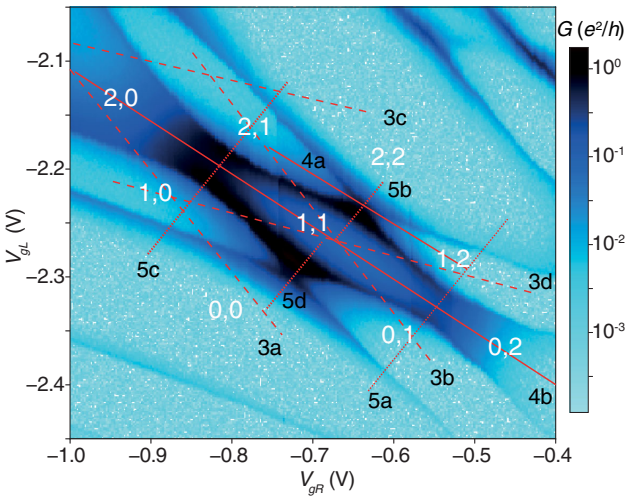

FIG. 2. Charge stability diagram as a function of plunger gate voltages. Effective charge numbers N_L, N_R determined from the shell-filling pattern (see Ref. [26]) are indicated for each sector. Lines on the diagram indicate line cuts shown in subsequent figures. The gate range in the two axes has been adjusted so distances amount to approximately equal energies. $T = 15$ mK, $V_{sd} = 0$, $V_{g1} = -9.2$ V, $V_{g3} = -9.3$ V, $V_{g5} = -0.25$ V, and $V_{bg} = 10.4$ V.

Figure 2 shows a color map of the zero-bias linear conductance (G) of the device as a function of the left and right plunger gates, V_{gL} and V_{gR}, reminiscent of the *honeycomb* charge stability diagram of normal-state DQDs [24]. This similarity stems from parity changes nearly matching charge degeneracies in the low-coupling regime. For clarity, only the number of electrons $N_L = 0,1,2$ and $N_R = 0,1,2$ in the highest-lying levels of each dot, left and right, respectively, are shown, as identified by the apparent shell filling pattern [25] (see Ref. [26]). Though this measurement is analogous to the stability diagram of a conventional N-DQD-N system, it is important to note that in our Josephson DQD circuit G originates from a supercurrent. Cotunneling processes that contribute to this supercurrent are more probable at charge degeneracies, and are particularly enhanced at the quadruple points where the charge states (N_L, N_R), $(N_L + 1, N_R)$, $(N_L, N_R + 1)$ and $(N_L + 1, N_R + 1)$ are degenerate in the case $U_{LR} = t_d = 0$, leading to an increase of G near these points.

The diagram is expected to show electron-hole symmetry, which results in a mirror symmetry around the negative-slope diagonal (0,2)–(2,0). Besides, for $U_L = U_R$, the diagram is also expected to show a mirror symmetry around the positive-slope diagonal (0,0)–(2,2). In Fig. 2, these symmetries are approximately respected. Minor differences include a larger conductance in the (1,1)–(2,0) degeneracy compared to the (1,1)–(0,2), and larger separation between the (1,1)–(0,0) sectors compared to (1,1)–(2,2). These asymmetries are due to cross coupling of V_{gL} with the left tunnel barrier, which is also evidenced by lower G in charge sectors at more negative V_{gL} (see Ref. [26]), and to U_L not being exactly equal to U_R. Figure 1(e) shows the calculated critical current, I_c, for the parameters of the device and fixed tunnel barrier [23], using fourth order perturbation theory in the tunnel coupling (for additional and qualitatively consistent NRG and zero-bandwidth calculations, and details of the theory, see Ref. [26]). These calculations confirm the experimental observation that I_c is largest close to degeneracy points and is especially enhanced near the quadruple points. The particle-hole symmetry of the underlying Hamiltonian is manifested in the figure through the relation $I_c(n_L, n_R) = I_c(2 - n_L, 2 - n_R)$. The sign change of I_c going from singlet to doublet sectors indicates the $0 - \pi$ transition.

In the following, we present maps of differential conductance, $dI/dV_{sd}(V_{sd})$, zoomed at low-bias within the superconducting gap, along the cuts indicated in Fig. 2. In Figs. 3(a) and 3(b), we show cuts taken at fixed N_R while varying N_L, corresponding to a variation of the left-dot energy level. In turn, cuts taken at fixed N_L while varying

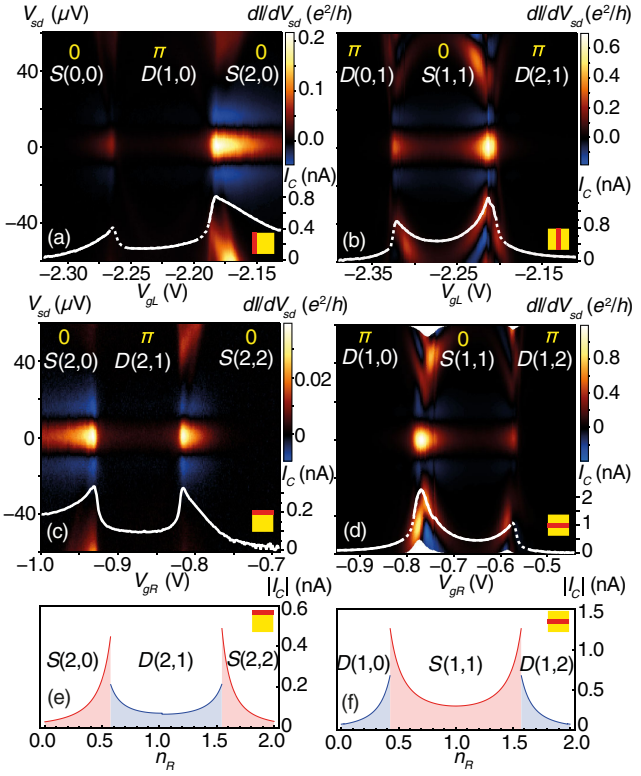

FIG. 3. (a)–(d) Line cuts along the dashed lines in Fig. 2 for fixed N_R (a) and (b) and for fixed N_L (c) and (d). *Overlays*. Fitted I_c (white curve) [52]. The notation used to name each sector is $\mathrm{GS}(N_L, N_R)$, where $\mathrm{GS} = \mathrm{D}$, S represents the ground state of the sector. (e) and (f) Line cuts of $|I_c|$ calculated by fourth order perturbation theory along trajectories in occupation number (proportional to gate voltage) given in Fig. 1(e). Red (blue) color indicates that I_c is positive (negative). Line cut trajectories in Figs. 1(e) and 2 are symbolically indicated on each panel.

N_R are shown in panels (c) and (d). Notably, a narrow zero-bias peak surrounded by negative differential conductance (NDC) traverses all four diagrams. Additional features seen here at $V_{sd} > 20\ \mu$V, also observed at larger bias between $\pm 2\Delta = 0.53$ mV, are discussed in Ref. [26].

The zero-bias peak in Figs. 3(a)–3(d) has a peculiar gate dependence, exhibiting a noticeable discontinuity in the conductance value at every parity change. It sharply drops whenever $N_L + N_R$, the total charge in the dots, is an odd number, with respect to its value at an even number.

We relate this zero-bias peak to a dissipative supercurrent. NDC comes from switching to low subgap current (see Supplemental Material [26] for an $I - V_{sd}$ curve evidencing this). Dissipation can be ascribed within the resistively and capacitively shunted junction (RCSJ) model to the overdamped nature of the junction and to the presence of thermal noise [6,7,21,53–55]. By fitting $dI/dV_{sd}(V_{sd})$ traces of Figs. 3(a)–3(d) to this model, we extract I_c as a function of the gate voltage (for details of the fit and a justification of the overdamped nature of the junction, see the Supplemental Material [26]) and plot it as overlays in the respective color maps (white curves).

The observed discontinuities in the conductance of the zero-bias peak are seen as abrupt jumps in the magnitude of the supercurrent, with peaked values at parity changes. We interpret these as $0 \to \pi$ transitions in the phase-shift ϕ_0 of the Josephson current $I = I_c \sin(\phi + \phi_0)$. These happen whenever $N_L + N_R$ changes from an even number ($\phi_0 = 0$) to an odd number ($\phi_0 = \pi$). In this regime, in which both dots are relatively decoupled from the superconducting leads, the following rule of thumb applies. When $N_L + N_R$ is even, the ground state of the DQD is a spin singlet, S, whereas when $N_L + N_R$ is odd, it changes to a doublet, D. We are able to distinguish π from 0 regions due to the small magnitude of the supercurrent within the π regions and due to the asymmetry of the I_c peaks at the parity changes. This asymmetry finds its origin in the halving of cotunneling processes in the π domain with respect to the 0 domain [56]. An example of these two observations is seen in Fig. 3(c), where I_c has a steep and asymmetric decrease (with respect to the parity-change points) towards the π sector at the charge region (2,1). We support our interpretation with line cuts taken from Fig. 1(e). Using fourth order perturbation for equal tunnelling rates to the leads, $\Gamma_0 = \Gamma_L = \Gamma_R$, we match the scale of $|I_c|$ to experiment [23] and find similar behavior in variations of gate for all line-cuts.

In the vicinity of quadruple points, single dot states hybridize into bonding and antibonding molecular orbitals [24]. We investigate the effect of interdot hybridization on I_c via detuning, by which the dot levels are pulled away from each other [14,24]. Such line cuts are shown in Figs. 4(a) and 4(b). These demonstrate that I_c (white curve) can be tuned by changing the relative detuning between the two dot levels without changing the total charge of the quantum dots. At zero detuning (green arrows), at which interdot hybridization is highest, I_c attains a local maximum. This occurs at a molecular doublet ground state D_B of the form $\alpha|D(0,1)\rangle + \beta|D(1,0)\rangle$ in Fig. 4(a), and at a molecular singlet ground state S_B of the form $\alpha|S(1,1)\rangle + \beta|S(0,2)\rangle$ in Fig. 4(b), where α and β are coefficients. I_c traces calculated by perturbation theory, shown in panels (c) and (d), are approximately consistent with the gate dependence and line shape of I_c. However, due to the aforementioned cross coupling of V_{gL} with the left tunnel barrier, the experiment does not display the exact symmetry with respect to zero detuning exhibited by the theory.

Next, we investigate the effect on I_c of driving maximally hybridized molecular orbitals (zero detuning) away from the Fermi level by taking line cuts through the quadruple points following the dotted lines in Fig. 2, so that the DQD energy levels are aligned and shifted

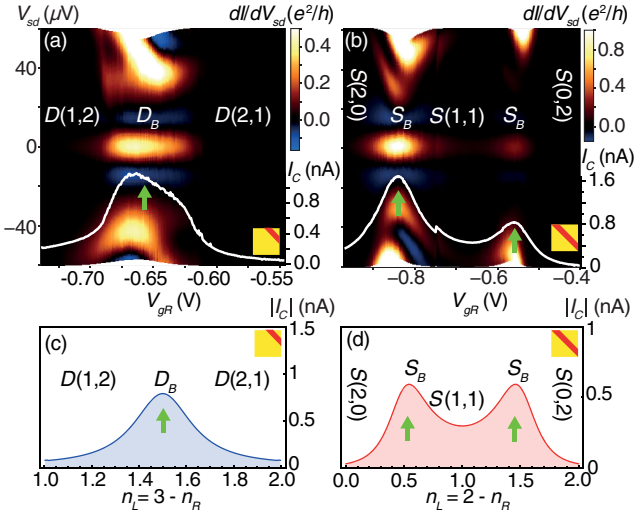

FIG. 4. (a) and (b) Detuning $\epsilon_L - \epsilon_R$ line cuts along the continuous lines in Fig. 2. *Overlays*. Fitted I_c (white line). Note that the ground state, either doublet or singlet, does not change in these line cuts. (c) and (d) $|I_c|$ traces calculated by fourth order perturbation theory. Red (blue) accounts for positive (negative) I_c. Green arrows indicate zero-detuning points.

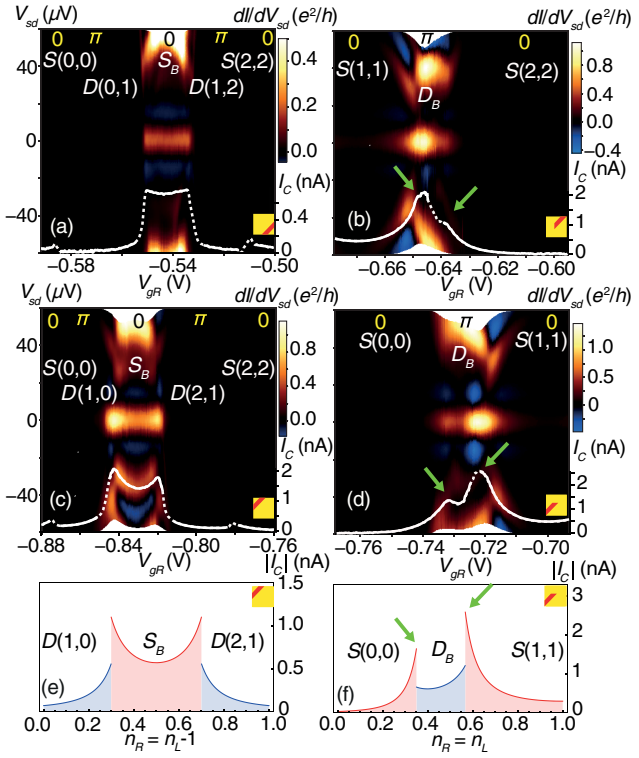

FIG. 5. (a)–(d) Line cuts along the dotted lines in Fig. 2, through (a) and (c) S_B and (b) and (d) D_B molecular ground states. The levels are aligned per (a) $\epsilon_L = \epsilon_R + U_R$, (c) $\epsilon_L + U_L = \epsilon_R$, and (b) and (d) $\epsilon_L = \epsilon_R$. The difference is due to an additional electron in one of the levels in (a) and (c). *Overlays*. Fitted I_c (white line) [52]. (e) and (f) Line cuts of calculated $|I_c|$ through (e) S_B and (f) D_B ground states, done by fourth order perturbation theory. As before, red (blue) accounts for positive (negative) I_c. Note that line cut (c) covers two additional charge sectors outside the range of the theory cut (e).

simultaneously. Such line cuts are shown in Figs. 5(a)–5(d). Consistently with our interpretation of the diagram in Fig. 2, I_c is largest at the quadruple points, and quickly decreases in the Coulomb valleys. Interestingly, I_c is symmetric with respect to the quadruple points at $V_{gR} = -0.54$ V in panel (a) and at $V_{gR} = -0.83$ V in panel (c), which correspond to line cuts through a S_B ground state, but it loses this symmetry in panels (b) and (d) with respect to $V_{gR} = -0.64$ V and $V_{gR} = -0.73$ V, respectively, which correspond to line cuts through a D_B ground state. In the two latter panels, I_c is largest at the parity changes that go towards the (1,1) sector. This happens due to a greater availability of cotunneling channels in this sector, as captured by perturbation theory [see Figs. 5(e) and 5(f)]. Asymmetric I_c peaks in panels (b) and (d) are indicated by green arrows. The observed symmetries stem from the combined effects of two types of symmetry. First, from $U_L \approx U_R$ as the system is then invariant under the transformation $(n_L, n_R) \to (n_R, n_L)$. Together with particle-hole symmetry $(n_L, n_R) \Rightarrow (2 - n_L, 2 - n_R)$ this renders $I_c(n_L, n_R) = I_c(2 - n_R, 2 - n_L)$, which corresponds to a mirror symmetry around the negative-slope diagonal (2,0)–(0,2). Line cuts (a) and (c) are perpendicular to the diagonal and are therefore symmetrical around it while (b) and (d) are taken on each side of the diagonal and are therefore images of each other.

Ground state transitions observed in I_c are consistent with crossings of Yu-Shiba-Rusinov subgap states [15,57]. These can be observed in $dI/dV_{sd}(V_{sd})$ spectroscopy at larger V_{sd} (see Ref. [26]). These states display a loop structure [58–62] and NDC [63–67] similar to those in parity-changing single dots. Interestingly, simultaneously with the maximization of I_c observed in detuning cuts in Figs. 4(a) and 4(b), the energy of the lowest pair of subgap states is minimized and displays an anticrossing consistent with an absence of parity changes.

In this Letter, we presented an experimental realization of a DQD Josephson junction, supported by the two impurity Anderson model. The stability diagram displays a honeycomb pattern. We showed that the discontinuities and gate-voltage asymmetries observed in the critical current are fully consistent with predictions of fourth-order perturbation theory. Finally, we probed molecular orbital ground states unique to the DQD system, finding a variation of I_c with detuning from the level degeneracy.

We thank A. Jellinggaard, M. C. Hels, and J. Ovesen for substrate preparation. We acknowledge financial support from the Carlsberg Foundation, the Independent Research Fund Denmark and the Danish National Research

Foundation. P. K. acknowledges support from Microsoft and the ERC starting Grant No. 716655 under the Horizon 2020 program. R. Ž. acknowledges support from the Slovenian Research Agency (ARRS) under Grants No. P1-0044 and J1-7259.

*Corresponding author.
nygard@nbi.ku.dk

[1] S. De Franceschi, L. Kouwenhoven, C. Schönenberger, and W. Wernsdorfer, Nat. Nanotechnol. **5**, 703 (2010).
[2] A. Martín-Rodero and A. Levy Yeyati, Adv. Phys. **60**, 899 (2011).
[3] V. Meden, arXiv:1810.02181.
[4] J. A. Van Dam, Y. V. Nazarov, E. P. Bakkers, S. De Franceschi, and L. P. Kouwenhoven, Nature (London) **442**, 667 (2006).
[5] J.-P. Cleuziou, W. Wernsdorfer, V. Bouchiat, T. Ondarçuhu, and M. Monthioux, Nat. Nanotechnol. **1**, 53 (2006).
[6] H. I. Jørgensen, T. Novotný, K. Grove-Rasmussen, K. Flensberg, and P. E. Lindelof, Nano Lett. **7**, 2441 (2007).
[7] A. Eichler, R. Deblock, M. Weiss, C. Karrasch, V. Meden, C. Schönenberger, and H. Bouchiat, Phys. Rev. B **79**, 161407 (2009).
[8] R. Maurand, T. Meng, E. Bonet, S. Florens, L. Marty, and W. Wernsdorfer, Phys. Rev. X **2**, 011009 (2012).
[9] R. Delagrange, D. J. Luitz, R. Weil, A. Kasumov, V. Meden, H. Bouchiat, and R. Deblock, Phys. Rev. B **91**, 241401 (2015).
[10] R. Delagrange, R. Weil, A. Kasumov, M. Ferrier, H. Bouchiat, and R. Deblock, Phys. Rev. B **93**, 195437 (2016).
[11] Y. Shimizu, H. Horii, Y. Takane, and Y. Isawa, J. Phys. Soc. Jpn. **67**, 1525 (1998).
[12] M. Lee, T. Jonckheere, and T. Martin, Phys. Rev. B **81**, 155114 (2010).
[13] C. Karrasch, S. Andergassen, and V. Meden, Phys. Rev. B **84**, 134512 (2011).
[14] Z. Su, A. B. Tacla, M. Hocevar, D. Car, S. R. Plissard, E. P. A. M. Bakkers, A. J. Daley, D. Pekker, and S. M. Frolov, Nat. Commun. **8**, 585 (2017).
[15] K. Grove-Rasmussen, G. Steffensen, A. Jellinggaard, M. Madsen, R. Žitko, J. Paaske, and J. Nygård, Nat. Commun. **9**, 2376 (2018).
[16] M.-S. Choi, C. Bruder, and D. Loss, Phys. Rev. B **62**, 13569 (2000).
[17] R. S. Deacon, A. Oiwa, J. Sailer, S. Baba, Y. Kanai, K. Shibata, K. Hirakawa, and S. Tarucha, Nat. Commun. **6**, 7446 (2015).
[18] B. Probst, F. Domínguez, A. Schroer, A. L. Yeyati, and P. Recher, Phys. Rev. B **94**, 155445 (2016).
[19] J. D. Sau and S. D. Sarma, Nat. Commun. **3**, 964 (2012).
[20] I. C. Fulga, A. Haim, A. R. Akhmerov, and Y. Oreg, New J. Phys. **15**, 045020 (2013).
[21] J. C. Estrada Saldaña, R. Žitko, J.-P. Cleuziou, E. J. H. Lee, V. Zannier, D. Ercolani, L. Sorba, R. Aguado, and S. De Franceschi, arXiv:1801.01855.
[22] P. Krogstrup, N. Ziino, W. Chang, S. Albrecht, M. Madsen, E. Johnson, J. Nygård, C. Marcus, and T. Jespersen, Nat. Mater. **14**, 400 (2015).
[23] $t_d = 0.3$ meV, $\Gamma_0 = \Gamma_L = \Gamma_R = 0.08$ meV were chosen to match the magnitude and gate dependence of I_c. For simplicity, $U_L = U_R = 2$ meV, and $\Delta = 0.25$ meV, which match closely the experimentally obtained values. For the same reason, the interdot charging energy was set to $U_{LR} = 0$.
[24] W. G. Van der Wiel, S. De Franceschi, J. M. Elzerman, T. Fujisawa, S. Tarucha, and L. P. Kouwenhoven, Rev. Mod. Phys. **75**, 1 (2002).
[25] H. I. Jørgensen, K. Grove-Rasmussen, K.-Y. Wang, A. Blackburn, K. Flensberg, P. E. Lindelof, and D. Williams, Nat. Phys. **4**, 536 (2008).
[26] See Supplemental Material at http://link.aps.org/supplemental/10.1103/PhysRevLett.121.257701 for additional data and details of the calculations and methodology, which includes Refs. [27–51].
[27] V. Ambegaokar and B. I. Halperin, Phys. Rev. Lett. **23**, 274 (1969).
[28] P. Jarillo-Herrero, J. A. Van Dam, and L. P. Kouwenhoven, Nature (London) **439**, 953 (2006).
[29] H. Nilsson, P. Samuelsson, P. Caroff, and H. Xu, Nano Lett. **12**, 228 (2012).
[30] M. Deng, S. Vaitiekėnas, E. B. Hansen, J. Danon, M. Leijnse, K. Flensberg, J. Nygård, P. Krogstrup, and C. M. Marcus, Science **354**, 1557 (2016).
[31] Y.-J. Doh, S. D. Franceschi, E. P. A. M. Bakkers, and L. P. Kouwenhoven, Nano Lett. **8**, 4098 (2008).
[32] T. Novotný, A. Rossini, and K. Flensberg, Phys. Rev. B **72**, 224502 (2005).
[33] A. Brunetti, A. Zazunov, A. Kundu, and R. Egger, Phys. Rev. B **88**, 144515 (2013).
[34] K. G. Wilson, Rev. Mod. Phys. **47**, 773 (1975).
[35] H. R. Krishna-murthy, J. W. Wilkins, and K. G. Wilson, Phys. Rev. B **21**, 1003 (1980).
[36] K. Satori, H. Shiba, O. Sakai, and Y. Shimizu, J. Phys. Soc. Jpn. **61**, 3239 (1992).
[37] O. Sakai, Y. Shimizu, H. Shiba, and K. Satori, J. Phys. Soc. Jpn. **62**, 3181 (1993).
[38] T. Yoshioka and Y. Ohashi, J. Phys. Soc. Jpn. **67**, 1332 (1998).
[39] T. Yoshioka and Y. Ohashi, J. Phys. Soc. Jpn. **69**, 1812 (2000).
[40] W. C. Oliveira and L. N. Oliveira, Phys. Rev. B **49**, 11986 (1994).
[41] K. Chen and C. Jayaprakash, Phys. Rev. B **52**, 14436 (1995).
[42] V. L. Campo and L. N. Oliveira, Phys. Rev. B **72**, 104432 (2005).
[43] R. Žitko and T. Pruschke, Phys. Rev. B **79**, 085106 (2009).
[44] R. Žitko, M. Lee, R. López, R. Aguado, and M.-S. Choi, Phys. Rev. Lett. **105**, 116803 (2010).
[45] R. Žitko, O. Bodensiek, and T. Pruschke, Phys. Rev. B **83**, 054512 (2011).
[46] R. Žitko, J. S. Lim, R. Lopez, and R. Aguado, Phys. Rev. B **91**, 045441 (2015).
[47] R. Žitko, Phys. Rev. B **91**, 165116 (2015).
[48] C. W. J. Beenakker and H. van Houten, in *Single-Electron Tunneling and Mesoscopic Devices*, edited by H. Koch and H. Lubbig (Springer, New York, 1992), pp. 175–179, also available as cond-mat/0111505.

[49] A. V. Rozhkov, D. P. Arovas, and F. Guinea, Phys. Rev. B **64**, 233301 (2001).
[50] A. V. Rozhkov and D. P. Arovas, Phys. Rev. Lett. **82**, 2788 (1999).
[51] Z. Su, A. Zarassi, J.-F. Hsu, P. San-Jose, E. Prada, R. Aguado, E. J. H. Lee, S. Gazibegovic, R. L. M. Op het Veld, D. Car *et al.*, Phys. Rev. Lett. **121**, 127705 (2018).
[52] Data points for which the fit is unreliable due to subgap states crossing zero energy at parity changes are indicated by a dotted trace. For details, see Ref. [26].
[53] Y. M. Ivanchenko and L. A. Zil'berman, Sov. Phys. JETP **28**, 1272 (1969).
[54] A. Steinbach, P. Joyez, A. Cottet, D. Esteve, M. H. Devoret, M. E. Huber, and J. M. Martinis, Phys. Rev. Lett. **87**, 137003 (2001).
[55] H. I. Jørgensen, K. Grove-Rasmussen, K. Flensberg, and P. E. Lindelof, Phys. Rev. B **79**, 155441 (2009).
[56] L. Glazman and K. Matveev, JETP Lett. **49**, 659 (1989).
[57] G. Kiršanskas, M. Goldstein, K. Flensberg, L. I. Glazman, and J. Paaske, Phys. Rev. B **92**, 235422 (2015).
[58] E. J. H. Lee, X. Jiang, M. Houzet, R. Aguado, C. M. Lieber, and S. De Franceschi, Nat. Nanotechnol. **9**, 79 (2014).
[59] A. Jellinggaard, K. Grove-Rasmussen, M. H. Madsen, and J. Nygård, Phys. Rev. B **94**, 064520 (2016).
[60] R. S. Deacon, Y. Tanaka, A. Oiwa, R. Sakano, K. Yoshida, K. Shibata, K. Hirakawa, and S. Tarucha, Phys. Rev. Lett. **104**, 076805 (2010).
[61] J.-D. Pillet, P. Joyez, R. Žitko, and M. F. Goffman, Phys. Rev. B **88**, 045101 (2013).
[62] E. J. H. Lee, X. Jiang, R. Žitko, R. Aguado, C. M. Lieber, and S. De Franceschi, Phys. Rev. B **95**, 180502 (2017).
[63] B.-K. Kim, Y.-H. Ahn, J.-J. Kim, M.-S. Choi, M.-H. Bae, K. Kang, J. S. Lim, R. López, and N. Kim, Phys. Rev. Lett. **110**, 076803 (2013).
[64] J.-D. Pillet, C. Quay, P. Morfin, C. Bena, A. Levy Yeyati, and P. Joyez, Nat. Phys. **6**, 965 (2010).
[65] K. Grove-Rasmussen, H. I. Jørgensen, B. M. Andersen, J. Paaske, T. S. Jespersen, J. Nygård, K. Flensberg, and P. E. Lindelof, Phys. Rev. B **79**, 134518 (2009).
[66] A. Eichler, M. Weiss, S. Oberholzer, C. Schönenberger, A. Levy Yeyati, J. C. Cuevas, and A. Martín-Rodero, Phys. Rev. Lett. **99**, 126602 (2007).
[67] E. J. H. Lee, X. Jiang, R. Aguado, G. Katsaros, C. M. Lieber, and S. De Franceschi, Phys. Rev. Lett. **109**, 186802 (2012).

6

PROJECT 2

In this chapter we present project 2 [2], in which the fully screened groundstate of the S-DQD-S junction is experimentally obtained. Up to now, we have established that supercurrent measurements can be utilized to characterize charge diagrams of a S-DQD-S system. Next, we use this technique to investigate how charge diagrams changes when lead couplings, characterized by Γ_L and Γ_R, are increased. Experimentally, this is done by tuning gate 1 and 5, which (mainly) control the tunnel coupling between dot and superconductor. As couplings $\Gamma_{L/R}$ increase we expect YSR screening to take effect, and since the two dots are additionally exchange coupled by a tunnel element t_d, we in this system realize the superconducting equivalent of the famous *two impurity Kondo model*. This model is integral to our understanding of heavy fermion materials [8, 91], and can exhibit exotic phenomena such as quantum criticality and non-fermi liquid behaviour [143].

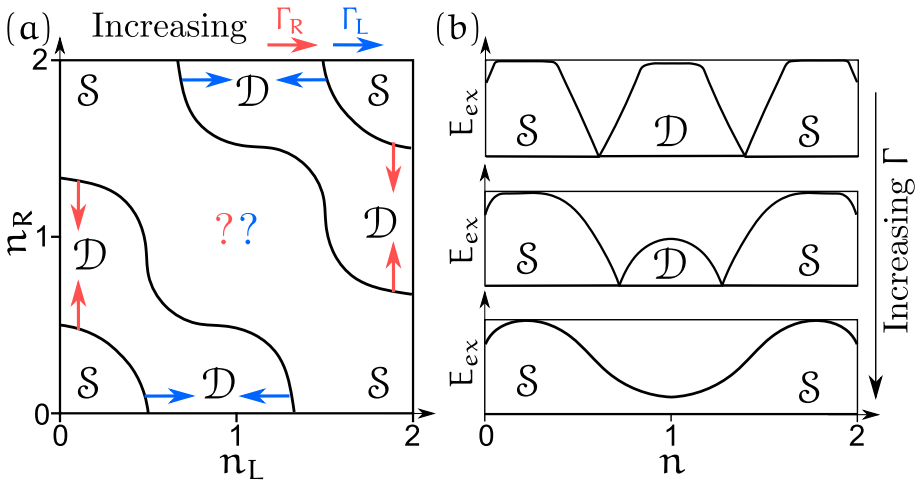

Figure 6.1: (a) A schematic of the DQD charge diagram with $\mathcal{S}$ and $\mathcal{D}$ indicating singlet or double groundstate. Red (blue) arrows indicate the expected effect of increasing Γ_R (Γ_L) inferred from our knowledge of the single impurity YSR screening shown in (b). Question marks indicates the region of highest complexity, namely the $(1,1)$ sector, where Γ_L and Γ_R competes with interdot exchange, characterized by t_d^2/U, yielding a non-trivial competition of scales.

The mapping between bulk properties and impurity model is provided by *dynamical mean-field theory* (DMFT) [144], which connects the strange properties of heavy fermion materials to simple local impurity models, such as the one we explore in this experiment. Before presenting the paper we next discuss some key concepts of S-DQD-S YSR screening, using a simple zero-bandwidth (ZBW) model which captures most of the relevant physics. A similar S-DQD-S ZBW model have been explored in Ref. [139].

Starting from the low coupling honeycomb charge diagram, shown for experiment in fig. 4.5 and from theory in fig. 4.3, we expect that increasing Γ_L and Γ_R will close the doublet sectors at occupation $(0,1)$, $(1,0)$, $(2,1)$ and $(1,2)$ in notation (N_L, N_R) as depicted in fig. 6.1 (a). These closings can be understood in terms of the single impurity YSR model, presented in the introduction and shown in fig. 6.1 (b), as along the charge diagram edges one dot is coulomb blockaded in a even sector, thereby non-interacting. This effect was also demonstrated in a S-DQD-N setup in Ref. [21, 62]. Of greatest interest is the central $(1,1)$ sector where for low Γ_L and Γ_R the groundstate is an exchange singlet state, and where the two-impurity model is realized. To investigate this region in greater detail we use the ZBW Hamiltonian,

$$
\begin{aligned}
H &= H_D + H_{ZBW} + H_T, \qquad (6.1)\\
H_D &= \sum_{j=L,R} \frac{U_j}{2}\left(N_j - n_j\right)^2 + t_d \sum_{\sigma} d^\dagger_{L\sigma} d_{R\sigma} + \text{h. c.},\\
H_T &= \sum_{j=L,R}\sum_{\sigma} t_j d^\dagger_{j\sigma} c_{j\sigma} + \text{h. c.},\\
H_{ZBW} &= \sum_{j=L,R} \Delta_j c^\dagger_{j\uparrow} c^\dagger_{j\downarrow} + \Delta^*_j c_{j\downarrow} c_{j\uparrow},
\end{aligned}
$$

defined on a Hilbert space of size $4^4 = 256$, and can therefore be numerically diagonalized. As the methodology is covered in the author's thesis [21], we will in this section only cover results related to the $(1,1)$ sector. At the center $n_L = n_R = 1$, the ZBW analysis reveals four states vying to be the groundstate, denoted by $\mathcal{S}$ or $\mathcal{D}$, for singlet or doublet, alongside two index indicating the number of screening quasiparticles. These four states are: the exchange singlet state $\mathcal{S}_{00}$, the doublet states with either the left, $\mathcal{D}_{10}$, or right, $\mathcal{D}_{01}$, dot screened, and the fully screened singlet state $\mathcal{S}_{11}$. In fig. 6.2 we depict these four states alongside a phase diagram showing the left and right dot spin-spin correlation $\langle S_1 \cdot S_2 \rangle$ as a function of Γ_L and Γ_R, obtained from ZBW with parameters: $U_L = U_R = 2$ meV, $t_d = 0.09$ meV, and $\Delta_L = \Delta_R = 0.25$ meV. We utilize the definition of the rates $\Gamma_j = 2\pi t_j^2/\Delta_j$, with $j \in \{L, R\}$, introduced in section 4.4. For the pure exchange singlet state $\mathcal{S}_{00}$ the dot spins are highly correlated yielding $\langle S_1 \cdot S_2 \rangle = -3/4$, with the minus sign indicating that the spins predominately point in

opposing directions. For $\mathcal{D}_{10}$ and $\mathcal{D}_{01}$ the dot spins are uncorrelated, as one spin is screened by a quasiparticle leaving the other dot with a free spin-1/2 degree of freedom. Similarly, the pure $\mathcal{S}_{11}$ state, with both dots screened, results in uncorrelated dot spins, as correlations with quasiparticles dominate. In the phase diagrams of fig. 6.2 (a), we see that if either Γ_L or Γ_R is increased from the weakly coupled regime one ends up with a doublet groundstate. If both couplings are increased simultaneously a smooth transition from $\mathcal{S}_{00}$ to $\mathcal{S}_{11}$ occurs, with a gradual change of $\langle S_1 \cdot S_2 \rangle$ from $-3/4$ to 0.

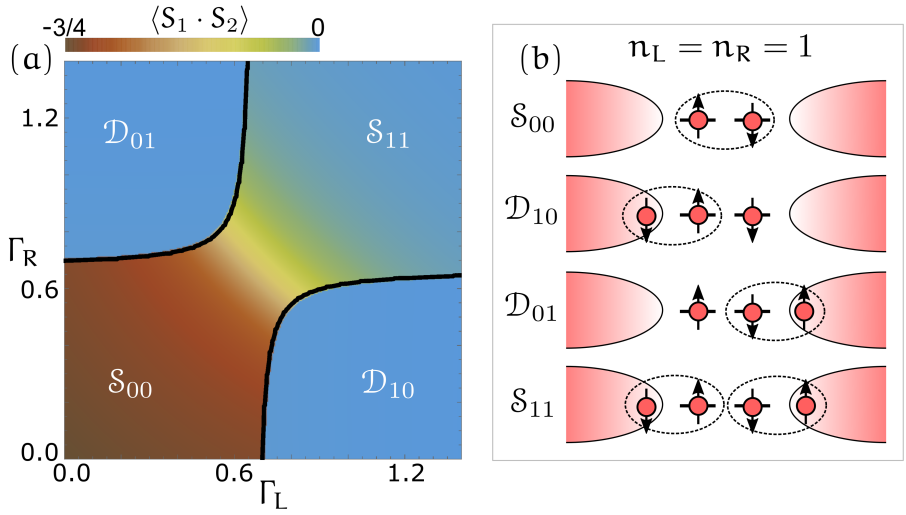

Figure 6.2: (a) Plot of dot spin-spin correlation as a function of couplings at $n_L = n_R = 1$. Black lines indicate changes of groundstate parity. (b) Schematic of the four groundstates. Dotted circles indicate strong spin correlations from exchange couplings.

This kind of gradual change, alongside the curved opening, is indicative of an anti-crossing of singlet states, with the two states hybridizing. This is further investigated in fig. 6.3 (a) where we find an anti-cross between the two singlet states, which stems from the ability of the superconducting leads to coherently add or remove a cooper-pair. As shown in fig. 6.3 (b), the tunnelling of a screening quasiparticle from left to right lead connects $\mathcal{S}_{00}$ to $\mathcal{S}_{11}$, and consequently we expect the anti-cross Hamiltonian to be of the simple form,

$$H_{00,11} = \begin{pmatrix} E_{00} & H_{hyb} \\ H_{hyb} & E_{11} \end{pmatrix}, \tag{6.2}$$

with $H_{hyb} \propto t_L t_R t_d$. To test this hypothesis we plot the minimal energy difference between the two singlet states, occurring at $E_{00} = E_{11}$, as a function of t_d in fig. 6.3 (c), and find a linear relationship with t_d. Unfortunately, this renders the superconducting

two-impurity system less interesting than the normal state version, as the aforementioned quantum criticality and breakdown of fermi-liquid behaviour originates from the crossing and competition of the exchange $\mathcal{S}_{00}$ and fully screened Kondo $\mathcal{S}_{11}$ state. In the superconducting case this quantum transition occurs in a continues manner due to the anti-cross. Nonetheless, the paper demonstrates our ability to continuously tune the double quantum dot across varies groundstates, providing control over interactions and scales, which is of potential interest for the realization of larger dot-chains on which Majoarna fermions can be obtained [98–100], or for applications in YSR (Andreev) spin-qubit designs [84, 145].

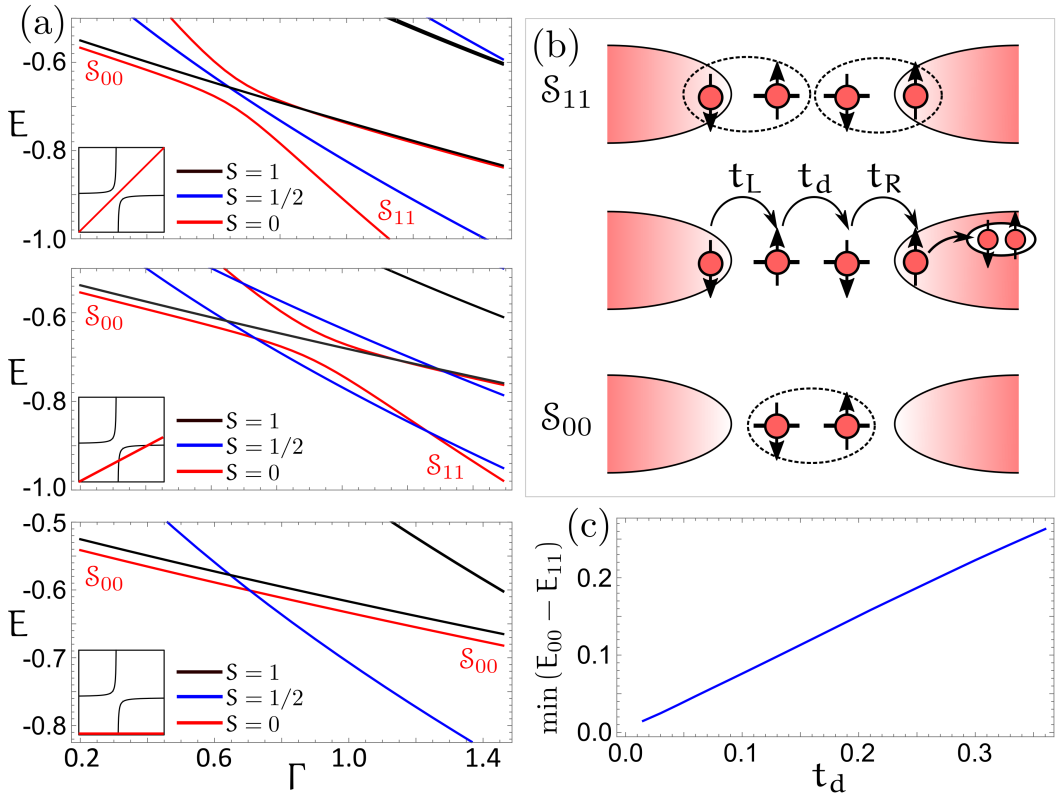

Figure 6.3: (a) Energy of the lowest lying states at $n_L = n_R = 1$ for $\Gamma = \Gamma_L = \Gamma_R$, $\Gamma = \Gamma_L = 2\Gamma_R$, and $\Gamma = \Gamma_L$ from top to bottom, with S indicating total spin. The S = 1 state is the DQD triplet state. Insets shows the respective linecut on fig. 6.2 (a). (b) Schematic of the process connecting $\mathcal{S}_{11}$ to $\mathcal{S}_{00}$. (c) Minimum energy difference as a function of $\Gamma_L = \Gamma_R$ between the lowest lying singlet states as a function of t_d.

Since most details of the experiment and measurement techniques have already been discussed in the previous chapters, we here present a quick guide to observe the main results of the two-impurity paper presented next. In fig. 4 a phase diagram, computed via NRG by Rok Žitko, is shown, which up to a scaling of $\Gamma_{L/R}$ resembles

the ZBW results. Paths on this diagram indicate tunings of gate shown in figs. 6-8, which demonstrates our ability to control the groundstate of the S-DQD-S system. In fig. 8 (c) the doubly screened S_{11} groundstate is realized. Understanding the closings of charge sectors, shown in figs. 6-8, is slightly complicated due to cross capacitive couplings between gates. By gating the left dot one also tunes Γ_R resulting in increased screening. The effect of this cross-coupling is included in a ZBW calculation, shown in figs. 14-16, which mimics the evolution of figs. 6-8.

Two-impurity Yu-Shiba-Rusinov states in coupled quantum dots

J. C. Estrada Saldaña,[1] A. Vekris,[1,2] R. Žitko,[3,4] G. Steffensen,[1] P. Krogstrup,[1,5] J. Paaske,[1] K. Grove-Rasmussen,[1] and J. Nygård[1,*]

[1]*Center for Quantum Devices, Niels Bohr Institute, University of Copenhagen, 2100 Copenhagen, Denmark*

[2]*Sino-Danish Center for Education and Research (SDC) SDC Building, Yanqihu Campus, University of Chinese Academy of Sciences, 380 Huaibeizhuang, Huairou District, 101408 Beijing, China*

[3]*Jožef Stefan Institute, Jamova 39, SI-1000 Ljubljana, Slovenia*

[4]*Faculty of Mathematics and Physics, University of Ljubljana, Jadranska 19, SI-1000 Ljubljana, Slovenia*

[5]*Microsoft Quantum Materials Lab Copenhagen, Niels Bohr Institute, University of Copenhagen, 2100 Copenhagen, Denmark*

(Received 19 September 2020; accepted 5 November 2020; published 23 November 2020)

Using double quantum dots as the weak link of a Josephson junction, we realize the superconducting analog of the celebrated two-impurity Kondo model. The device shows a cusped current-voltage characteristic, which can be modeled by an overdamped circuit relating the observed cusp current to the Josephson critical current. The gate dependence of the cusp current and of the subgap spectra are used as complementary ground-state indicators to demonstrate gate-tuned changes of the ground state from an interdot singlet to independently screened Yu-Shiba-Rusinov (YSR) singlets. In contrast to the two-impurity Kondo effect in normal-state systems, the crossover between these two singlets is heralded by quantum phase boundaries to nearby doublet YSR phases in which only a single spin is screened.

DOI: 10.1103/PhysRevB.102.195143

I. INTRODUCTION

Magnetism relies on the presence of magnetic moments and their mutual exchange interactions. At low temperatures, local moments in metals may be screened by the Kondo effect and magnetism can be disrupted. This competition was first proposed by Mott [1] as a mechanism for the vanishing of magnetism at low temperatures in the f-electron metal $CeAl_3$, and later explored by Doniach [2] within a simple one-dimensional Kondo-lattice model, from which he established a phase diagram delineating the magnetic phase as a function of the ratio between the Kondo temperature, T_K, and the interimpurity exchange. The essence of this competition was subsequently reduced to the vastly simpler two-impurity Kondo model, which exhibits an unstable fixed point separating a ground state (GS) of two local Kondo singlets from an interimpurity exchange singlet [3]. This competition remains a central ingredient in the current understanding of many heavy-fermion materials and their quantum critical properties [4–9].

In a superconductor (S), the gap around the Fermi surface terminates the Kondo screening process before its completion, but local magnetic moments may still be screened by forming local singlets with BCS quasiparticles. As demonstrated by Yu, Shiba, and Rusinov (YSR) [10–12], a local exchange coupling between a superconductor and a magnetic impurity leads to a subgap bound state. In a full quantum description, the corresponding bound state crosses zero energy and the singlet subgap state becomes the new GS at a coupling strength corresponding to $T_K \approx 0.3\Delta$, where Δ denotes the superconducting gap [13,14]. This quantum phase transition reduces the spin by $\hbar/2$, quenching a spin-1/2 altogether.

Half-filled Coulomb-blockaded quantum dots (QDs) are model magnetic impurities, and can be readily coupled to superconductors in semiconductor nanowires [15]. In Josephson junctions (JJs) hosting an impurity, the above GS transition results in a phase change from π to 0 [16–25], and constitutes a complementary experimental signature to bias spectroscopy of YSR states crossing zero energy [26–34].

In contrast to the normal-state two-impurity Kondo effect, the two-impurity YSR ground-state phase diagram depends strongly on the two different local exchange couplings and includes not only the two different singlets, but also a doublet GS in which only a single spin is screened. In a previous Letter, we used a nanowire device to demonstrate the Josephson effect in a serial double quantum dot (DQD) in the low-coupling regime, in which the interdot tunnel coupling, t_d, dominated over the dot-lead tunneling rates, Γ_L, Γ_R [23]. Here we investigate in the same device the possible GSs at stronger individual couplings to the leads. As the gate voltages controlling these couplings are tuned, the boundaries of the honeycomb charge stability diagram between GSs of different parity are erased and new two-impurity YSR GSs are accessed. This boundary deletion affects the dispersion in gate voltage of the extracted Josephson critical current, I_c, and of a closely related and directly measurable *cusp current* [35–40], as well as the dispersion of the spectral YSR resonances, which render mutually consistent GS parity information.

The article is organized in sections as follows. In Sec. II we show an overview of the DQD and its parameters. In Sec. III we introduce the method used to extract I_c. In Sec. IV we delineate the theoretical expectations for GS, I_c, and subgap spectra in the S-DQD-S system. In Sec. V we show our main

*Corresponding author: nygard@nbi.ku.dk

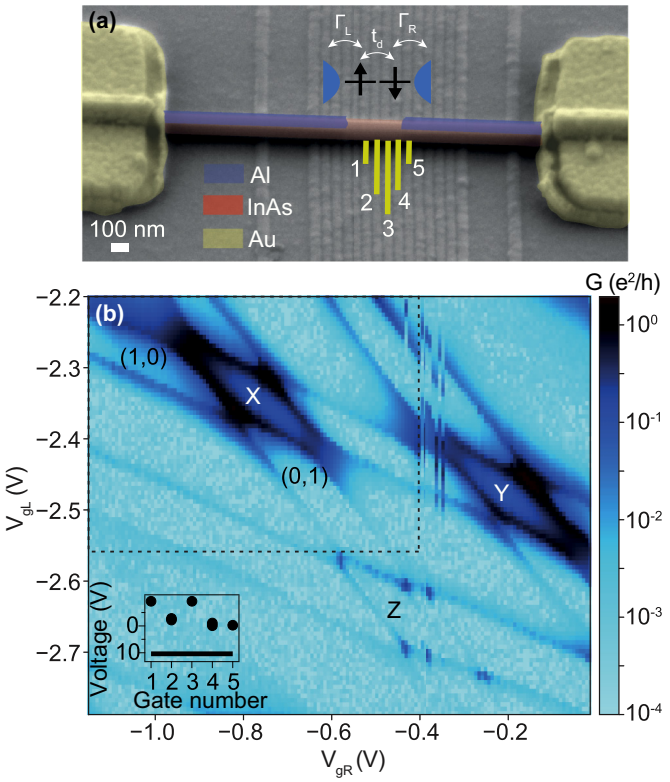

FIG. 1. (a) Scanning electron micrograph of the device, false-colored to indicate materials. Yellow lines denote local gates used. A sketch of the superconductor-double quantum dot-superconductor (S-DQD-S) system used as a two-impurity YSR model is shown in inset. (b) Zero-bias conductance, $G(V_{gL}, V_{gR})$, colormap providing an overview of the DQD shell selected for the study (X, inside the dashed line) and surrounding, less stable shells (Y and Z), which are affected by instabilities at $V_{gR} \approx -0.4$ V. The inset shows gate settings for this measurement. Dots and a line indicate local gate voltages and backgate voltage, respectively. $V_{g1} = -9.2$ V, $V_{g3} = -9.2$ V, $V_{g5} = -0.25$ V, and $V_{bg} = 10.4$ V.

experimental results, making use of the concepts introduced in Sec. IV. Finally, in Sec. VI we present our conclusions and comment on the possible applications of our findings.

II. DOUBLE QUANTUM DOT CHARACTERIZATION

The measured device [Fig. 1(a)] consists of an Al-covered InAs nanowire [41] deposited on top of narrow gates, insulated by 20 nm of hafnium oxide from the wire. Al is etched away to form a Josephson junction with a bare segment of InAs nanowire as the weak link. The device has a Si/SiO_2 substrate backgate which we operate at $V_{bg} \sim 10$ V to observe a measurable supercurrent. Gates 1, 3, and 5 are set to negative voltages to define the DQD, while gates 2 (4) are used as the plunger V_{gL} (V_{gR}) to load electrons into the left (right) QD. Slight changes in the voltage of gate 1 (5) modify Γ_L (Γ_R) of the left (right) QD to the left (right) lead. Small changes in V_{bg} also affect these tunneling rates. All measurements are done in an Oxford Triton® dilution refrigerator at $T_{fridge} \approx 20$ mK, using standard lock-in techniques with a lock-in AC excitation of 2 μV at 116.81 Hz to obtain the differential conductance, dI/dV_{sd}, superposed to a source-drain DC voltage, V_{sd}, while simultaneously recording the current, I, with a digital multimeter. The data were corrected for an offset of 3.5 pA from the current amplifier. To distinguish zero-bias from finite-bias differential conductance, we use variables G and dI/dV_{sd}, respectively.

Figure 1(b) shows a zero-bias differential conductance (G) colormap which represents a portion of the honeycomb stability diagram of the DQD in the superconducting state. Conductance lines appear at places in which the parity of the system changes, constituting a way to accurately map GS boundaries. We label charge sectors of the DQD shell selected for gate tuning (shell X) by (N_L, N_R), where N_L and N_R are the (integer) charges in the highest level of the left and right QDs, respectively. Parity lines separating doublet and singlet regions according to the total number of electrons in both QDs alternate in spacing, consistent with shell filling [23,42].

From Coulomb-diamond spectroscopy of shell X, we obtain the charging energies of the left and right QDs, $U_L \approx 1.9$ meV and $U_R \approx 1.6$ meV. From this spectroscopy, we also find that the level spacing of both QDs is equivalent to their charging energies ($\Delta E_L \approx 1.6$ meV and $\Delta E_R \approx 1.8$ meV). $\Delta = 0.27$ meV, the parent Al superconducting gap, is found from Coulomb-diamond spectroscopy in deep Coulomb blockade in an opaque regime. The fact that $U_L, U_R > \Delta$ places the system firmly in the YSR regime [43]. From the (0,2)-(1,1) anticrossing in the charge stability diagram, we estimate the interdot coupling, $t_d = 0.03-0.05$ meV and the interdot charging energy, $U_d = 0.13-0.23$ meV. Measurements of DQD and superconductor parameters are provided in Appendix A (see Figs. 9–11).

The DQD parameters Γ_L and Γ_R could not be independently measured due to the high critical field ($B_c = 2.1$ T) and high critical temperature ($T_c = 2.2$ K) of the superconducting device. We calculate in Sec. IV for our approximate DQD parameters GS boundaries set at $\Gamma_L \approx \Gamma_R \approx 0.4 < \Delta E_L, \Delta E_R$, which provide Γ_L, Γ_R sufficiently small to satisfy the single-level approximation [16]. Multilevel QD JJs show phase changes at fixed dot charge, irrespective of charge occupation [16,22], which is not observed in shells X, Y, and Z.

Near charge depletion, QDs are typically strongly confined, but also show the smallest Γ_i/U_i ratio, while a sizable Γ_i/U_i ratio for a given temperature is needed to observe a finite Josephson current [44]. This sets a narrow (ΔE_i, Γ_i, U_i) window which translates into a narrow gate range for single-level DQD JJ operation and Γ_i tuning. Outside of this window either multilevel ($\Delta E_i \ll \Gamma_i$), resonant level ($\Gamma_i \gg U_i$), or too weakly coupled regimes arise ($\Gamma_i \ll U_i$), which is why only a few shells near QD depletion could be studied here.

III. DETERMINATION OF CRITICAL AND CUSP CURRENTS

Next, we focus on the low-bias transport characteristic of the device in the superconducting state.

Initially intended for two-terminal bias spectroscopy of YSR excitations in a S-DQD-S system, for sufficiently strong t_d the device exhibits in $dI/dV_{sd} - V_{sd}$ traces a bias-symmetric, 20 μV-wide zero-bias peak flanked by negative differential conductance (NDC) dips, exemplified in Fig. 2(a). As shown in Fig. 2(b), the corresponding $I - V_{sd}$ traces have

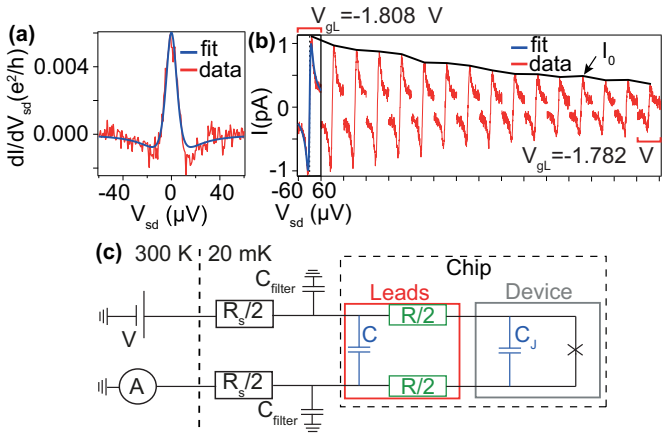

FIG. 2. (a) $dI/dV_{sd} - V_{sd}$ trace recorded at the same gate voltage as the leftmost trace in (b). (b) $I - V_{sd}$ traces taken with the gates swept along the red solid line in Fig. 8(c). Initial and final gate voltages are indicated. The traces have been shifted horizontally by 120 μV with respect to each other, and are measured from −60 to 60 μV each. Cusp current, I_0, at positive V_{sd} is plotted as a black trace to highlight its gate dependence. (c) Electrical circuit model. Details are given in the text and in Appendix B.

a finite slope between sharp cusps which occur at a current I_0. The positive V_{sd} value at which the cusps occur, $V_0 = 9.1 \pm 0.6$ μV, is gate-independent over three orders of magnitude of G and over cusp currents, I_0, ranging from 0.3 pA to 50 pA (see Fig. 12 in Appendix B). Additionally, V_0 matches the V_{sd} value of NDC dips, and I_0 shows a gate dependence similar to G [for example, compare Figs. 14(c) and 14(d) in Appendix C], indicating common origins for both phenomena.

We relate this narrow, bias-symmetric, finite-sloped $I - V_{sd}$ characteristic, which is cusped at I_0 and locked at V_0, to the supercurrent of the circuit-damped JJ formed by the S-leads and the DQD weak link, schematized in Fig. 2(c). This minimal model assumes the presence of a resistance R at the level of the leads (indicated in green) which was not designed and which was not independently measured, and which provides Johnson-Nyquist white noise at a temperature T which in principle can be larger than the temperature in the dilution refrigerator [35,45]. From its fitted value and position in the model, we speculate that R comes from the contact resistance between the nanowire and the Ti/Au leads.

In Fig. 2(c), the designed elements of the circuit at 20 mK are indicated in black. The JJ is assumed to have a current-phase relationship $I_c \sin\phi$, where the critical current, I_c, is unknown. This relationship is valid away from phase transitions [23]. Standard filtering and shielding elements include the following: (1) Two-stage low-pass RC filters with 30 kHz cutoff frequency, of total resistance $R_s/2$ per line, where $R_s = 8.24$ kΩ, and capacitance per stage $C_{filter} = 2.7$ nF. (2) Seven-stage low-pass π filters with 200 MHz cutoff frequency, positioned at 20 mK in series with the RC filters (not shown). (3) Lines to the sample are additionally attenuated at high frequency by Eccosorb® and encased by copper tape. (4) Radiation shielding is used at several stages in the dilution refrigerator, with the deepest encasing being at 20 mK at the sample level.

Nondesigned on-chip elements of known origin in the experiment are indicated in blue. Using a parallel-plate capacitor model, and from the device geometry and materials, we evaluate the junction capacitance at $C_J \approx 3$ aF, and the capacitance of the large-area bonding pads through the backgate at $C \approx 9$ pF. The latter estimation assumes that the resistance R is somewhere in the leads between the bonding pads and the device. These capacitances place the JJ in the overdamped regime, but knowledge of their values is not needed to extract I_c.

In the overdamped and voltage-biased regime this circuit gives rise to a three-parameter (I_c, R, T) voltage-current relation, as demonstrated by Ivanchenko and Zil'berman [46]. When $T > \hbar I_c/2ek_B$, corresponding to the limit of large noise amplitude [35], V_0 is I_c-independent as in the experiment and its value $V_0 = 2eRk_BT/\hbar = 10$ μV is close to the measurement. Additionally, I_c can be rescaled to I_0 and G, as shown in Fig. 13 in Appendix B, explaining their connection in the experiment.

We fit $dI/dV_{sd} - V_{sd}$ and $I - V_{sd}$ curves to obtain I_c. Since the device is measured in a two-terminal configuration, $R_s = 8.24$ kΩ is subtracted from the raw bias voltage, $V_{sd} = V - IR_s$, and raw differential conductance data, $dI/dV_{sd} = (dI/dV)/(1 - R_s dI/dV)$, before inputting them into the formula. Despite the circuit assumptions and the crudity of the model employed, the fits to the data are good for I_0 between 0.2 pA and 50 pA, and I_c ranging from 0.03 nA to 0.8 nA. Examples of the fit are shown as blue curves in Figs. 2(a) and 2(b).

The parameters $R = 3$ kΩ and $T = 80$ mK are extracted through the fitting procedure by initially keeping the parameters I_c, R, and T free. As long as $RT = 240$ kΩ mK, R and T can adopt any value and still produce a good fit to the data. A rescaling by a dimensionless number γ to R/γ and $T\gamma$ globally will merely change I_c to $\sqrt{\gamma} I_c$ without any qualitative change in its gate dependence. This is crucial for a robust interpretation of the latter, but it prevents absolute quantitative I_c assessments. Nevertheless, T is chosen from an upper-bound estimate of the electron temperature from the thermal broadening of a Coulomb peak, which also produces a reasonable I_c value, given the maximum imposed by Δ and the DQD couplings. The fitted value of R, in turn, is compatible with previous measurements of contact resistance in highly transparent nanowire junctions [47]. Once the noise RT was set, I_c was kept as the only free parameter in the fit to $V_{sd} - I$ curves at other gate voltages. Extraction of an unambiguous I_c value, impeded here by lack of measurement of R [35], should benefit from a fully designed circuit [48]. A derivation of the model and additional details are shown in Appendix B.

IV. THEORETICAL INSIGHTS

We introduce below the phase diagram of the S-DQD-S system, which distills the main consequence of the YSR spin-screening mechanism: changes in tunneling rates Γ_L and Γ_R drive GS parity transitions. We also provide calculations of the parity stability diagram, of I_c, and of the subgap dI/dV_{sd} YSR spectra, of importance to undertake the experimental results in the next section.

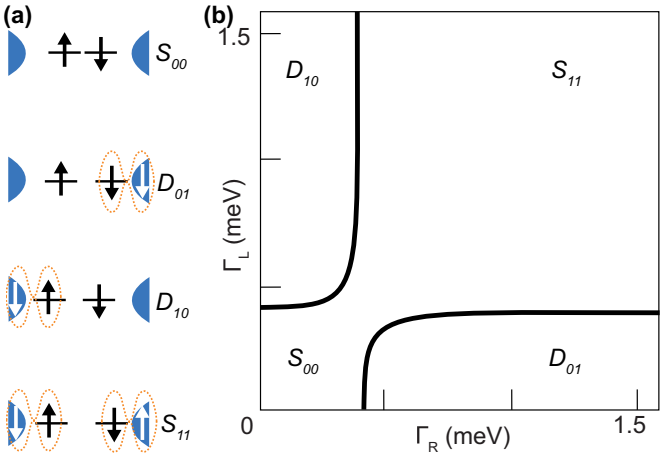

FIG. 3. (a) Schematized two-impurity YSR interaction (orange dotted line) of electron spins (black arrows) and quasiparticles (white arrows) from superconducting leads for different tunneling rates Γ_L, Γ_R. Horizontal lines indicate double quantum dot (DQD) levels. Each level contains one electron. (b) NRG calculation of the phase diagram of the two-impurity YSR S-DQD-S system for gates $n_L = n_R = 1$ corresponding to single occupancy of both dots.

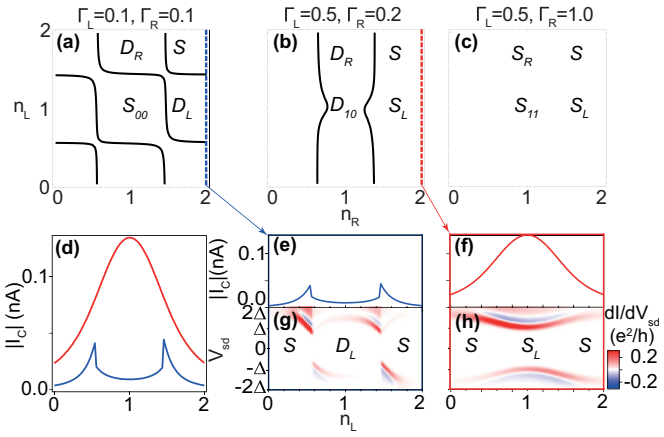

FIG. 5. NRG calculations. (a–c) Charge stability diagram with doublet-singlet GS boundaries indicated as solid black lines. (d) $|I_c|$ along respectively colored dashed lines in (a) and (b). (e, f) Comparison of the gate dependence of $|I_c|$ to (g, h) colormaps of subgap $dI/dV_{sd} - V_{sd}$ along the same gate trajectory. The colormaps are calculated by the Bardeen approach (see Appendix E).

In our GS naming convention, the parity is specified by D for doublet and S for singlet. Indexes depend on QD occupation, as follows. If the QD levels contain each one electron, we use two indexes; the first (second) denotes if the left (right) spin is screened (1) or not (0) [Fig. 3(a)]. If only one QD contains a single electron and the other is empty/full, we use a single index, L or R, to indicate if the left or right QD level is occupied [Fig. 4(a)]. Finally, if both QD levels are empty/full, we use no index. For example, in Fig. 3(a) D_{01} denotes screening of the right-QD spin for the (1,1) charge state.

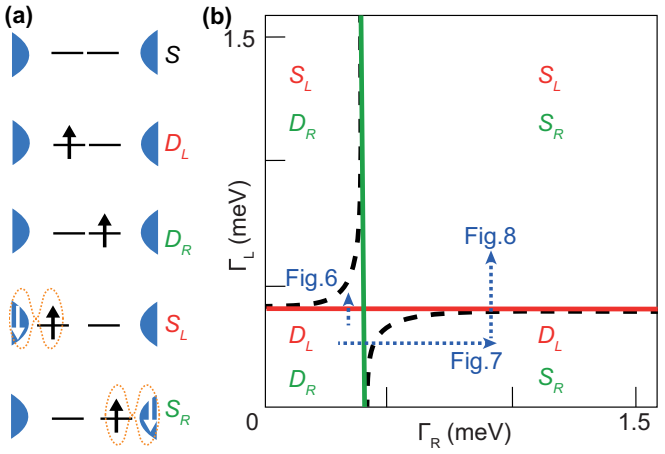

FIG. 4. (a) Schematized YSR interaction of electron spins and quasiparticles from superconducting leads for different Γ_L, Γ_R and level occupations. The bottom four cases correspond to the one-impurity YSR system. (b) NRG calculation of the phase diagram of the one-impurity YSR S-DQD-S system for single occupancy of either dot. GS boundaries for $n_L = 1, n_R = 0$ are denoted by a red solid line, while those for $n_L = 0$, $n_R = 1$ are denoted by a green solid line. Dotted blue arrows indicate qualitatively the gate-tuned Γ_L, Γ_R paths in the sequences of experimental charge stability diagrams in Figs. 6–8.

In Fig. 3(b) we show the two-impurity phase diagram of the S-DQD-S system versus Γ_L, Γ_R with dot occupations fixed at $n_L = n_R = 1$. This diagram was calculated with the Numerical Renormalization Group (NRG) technique [28,49] for $t_d = 0.1$ meV, charging energies of the QDs $U_L = U_R = 2$ meV, and $\Delta = 0.25$ meV, parameters which are used in all NRG calculations shown in this work. For simplicity, U_d was kept at zero. Black lines denote GS parity boundaries between S_{00}, S_{11} and D_{10}, D_{01}. These boundaries avoid each other due to t_d. An NRG calculation of the one-impurity phase diagram is in turn shown in Fig. 4(b). The one-impurity case corresponds to $n_L = 1$, $n_R = 0, 2$ (red) and to $n_L = 0, 2$, $n_R = 1$ (green). In contrast to two-impurity GS parity boundaries [black dashed lines overlaid from the calculation in Fig. 3(b)], one-impurity parity boundaries are straight lines.

GS parity boundaries can also be plotted as function of n_L, n_R for fixed Γ_L, Γ_R, which encourages qualitative comparison to experimental charge stability diagrams such as the one in Fig. 1(b). Three examples calculated by NRG are shown in Fig. 5. Similarly to the charge stability diagram of shell X in Fig. 1(b), the GS diagram of Fig. 5(a) exhibits all possible parity boundaries; its Γ_L, Γ_R coordinates situate it at the bottom-left corner of the two and one-impurity phase diagrams of Figs. 3(b) and 4(b). In Fig. 5(b), at stronger Γ_L, the left spin is screened and the GS changes in the (1,0) and (1,2) charge sectors from D_L to S_L, and in the (1,1) sector from S_{00} to D_{10}, deleting the horizontal parity boundaries which previously existed in Fig. 5(a) between S_{00} and D_R, and between D_L and S. In Fig. 5(c), at stronger Γ_R than in Fig. 5(b), the remaining doublet sector is screened away into a singlet, resulting in the disappearance of vertical parity boundaries.

Modifications of the GS diagram result in changes of the gate dependence of I_c and subgap YSR spectra which are also experimentally resolvable. An NRG calculation of $|I_c|$ is shown in Fig. 5(d) for an n_L trajectory which crosses two

GS parity boundaries in the case of the blue trace, and no GS parity boundaries in the case of the red one. The blue trace shows asymmetric peaks located at the two $D_L - S$ GS parity changes, whereas the red one evolves into a smooth and broad peak centered at $n_L = 1$. These are the well-known signatures of a π and a 0 QD JJ, respectively. In Figs. 5(e)–5(h) we compare the gate dependence of these traces [Figs. 5(e) and 5(f)] to a calculation of subgap dI/dV_{sd} [Figs. 5(g) and 5(h)], which is detailed in Appendix E. In Figs. 5(g) and 5(h), the calculation shows dI/dV_{sd} colormaps in which the innermost red lines appear at $eV_{sd} = \pm(\Delta + E_L)$, corresponding to quasiparticle tunneling from the gap edge of the right superconductor via the spinless right QD, to the YSR state at energy E_L in the spinful left QD, with tunneling rate $|t_d|^2$. Since BCS peaks probe subgap bound states, these peaks are followed by dips of NDC. This transport channel assumes a quasiparticle relaxation rate in the left superconductor, which is faster than the interdot tunneling rate [50]. In Fig. 5(g) the YSR dI/dV_{sd} peaks form the well-known split loop, which kinks downwards at parity changes coinciding with peaks in $|I_c|$ in Fig. 5(e). In the absence of parity changes as in Fig. 5(h), the YSR peaks evolve smoothly with minimum splitting at $n_L = 1$, which coincides with a broad peak in $|I_c|$ in Fig. 5(f).

Since the high magnetic field and/or temperature needed to drive the device into the normal state impede independent measurement of Γ_L and Γ_R, these calculations serve only as a qualitative guide for the gate-tuned behavior of experimental charge stability diagrams and of the gate dependence of I_c, I_0 and YSR excitations in the section below.

V. RESULTS

By following the deletion of parity transition lines in the charge stability diagram for DQD shell X, while knowing the departure ground states of each charge configuration (N_L, N_R) of the original diagram at weak coupling, it is possible to track GS changes of the system at stronger coupling to the leads, to which we access by changing gate voltages other than V_{gL} and V_{gR}. Before describing the data, we discuss three points not included in the NRG model above:

(1) While the model is based on a single DQD shell, the DQD device has a staircase of shells. GS changes demonstrated here for shell X are not necessarily concurrent in shells Y and Z, as is typically the case in nanowire-defined QD devices [24,29].

(2) Parity transition lines in the experimental charge stability diagram of shell X have an acute angle with respect to each other due to trivial V_{gL}, V_{gR} cross-talk [51], instead of the nearly perpendicular angle which they exhibit in the NRG calculation. While knowledge of the exact angle is not relevant, it is important to keep track of the slope of the parity transition lines of both QDs during the experiment, to avoid confusing gate-controlled parity changes with the formation of a single QD or with the introduction of a third QD, both of which should have parity transition lines of different slope. We therefore keep the same total gate variations ΔV_{gL} and ΔV_{gR} and aspect ratio in the stability diagrams of Figs. 6–8, and use red dashed lines to mark the slope of the left and right QD parity lines. These lines have the same slope in all plots, showing that the device stays as a DQD through the whole gating procedure.

(3) As discussed below, electron-hole asymmetric GS parity changes in shell X are observed for YSR screening of the right-QD spin, which can be modeled by a dependence of Γ_R on V_{gL} (see Appendix F). This cross-coupling is not unreasonable in view of the slight horizontal rightwards shift of the bottom gates in Fig. 1(a) with respect to the nanowire channel [24].

In Fig. 6(a) we show a zero-bias conductance colormap which represents the charge stability diagram of DQD shell X at slightly different gate settings than in the overview in Fig. 1(b). In these settings, the DQD has been brought to the verge of a GS transition due to YSR screening of the left-QD spin. We tune the leftmost gate of the device, V_{g1}, to gradually merge [Fig. 6(b)] and then, in combination with slight changes in V_{g3}, V_{g5} and V_{bg}, to erase [Fig. 6(c)] the parity transition lines of the stability diagram corresponding to the loading of a spin-1/2 in the left QD, consistent with an increase in Γ_L. The end result is that the singlet-doublet-singlet GS sequence $S - D_L - S$ along the solid blue line in Fig. 6(a) changes into an all-singlet sequence $S - S_L - S$ along the solid red line in Fig. 6(c).

To support our interpretation, we show in Figs. 6(d)–6(h) I_c, I_0 and subgap $I - V_{sd}$ and $dI/dV_{sd} - V_{sd}$ data taken with V_{gL} swept along these solid lines of corresponding color at different instances of the GS transition; V_{gR} is also swept to compensate for cross-capacitance. I_c and I_0 traces (in inset) in Fig. 6(d) behave similarly to NRG calculations of $|I_c|$ in Fig. 5(d). Asymmetric peaks in the blue trace come together in the intermediate green trace and merge into a single broad resonance in the red trace as the coupling Γ_L is increased by tuning the V_{g1}. The asymmetric peaks in I_c are consistent with a phase shift of $0 - \pi - 0$ added to the current-phase relationship when the GS parity changes as even-odd-even. In turn, the culminating single-broad peak is compatible with an enhanced supercurrent from screening of the spin of the left QD, as seen in earlier S-QD-S devices [17,20,27]. The absence of two asymmetric peaks in this trace is related to the even parity of the GS for all the relevant charge states.

Figures 6(e) and 6(f) compare the evolution of low-bias $I - V_{sd}$ traces in gate voltage taken along solid lines of corresponding color in Figs. 6(a) and 6(c) to Figs. 6(g) and 6(h), which show dI/dV_{sd} colormaps versus V_{gL} taken along the same respective gate trajectories, but with V_{sd} swept along a larger bias window within $\pm 2\Delta$, so as to capture the behavior of YSR subgap dI/dV_{sd} peaks. In Fig. 6(g) the lowest-lying, gapped peaks exhibit a small split-loop structure with kinks at -3.05 V and -3.1 V, which align in gate voltage to peaks in I_0 in the $I - V_{sd}$ traces from Fig. 6(e), as predicted by our NRG calculations above, and as previously observed in S-QD-S Josephson junctions [27]. The kinks vanish in Fig. 6(h), indicating absence of parity changes. Instead, the peaks exhibit a smooth point of inflexion at $V_{gL} = -3.43$ V, which aligns with a broad resonance in the V_{gL} dependence of I_0 in the $I - V_{sd}$ traces from Fig. 6(f).

As in our simple model in Figs. 5(e) and 5(f), the lowest-lying peaks appear split in bias voltage by a gapped region [26,28–30,52,53], are followed by NDC [27,54–58], and ascribe to the expected shape in gate voltage [26,28,34,59].

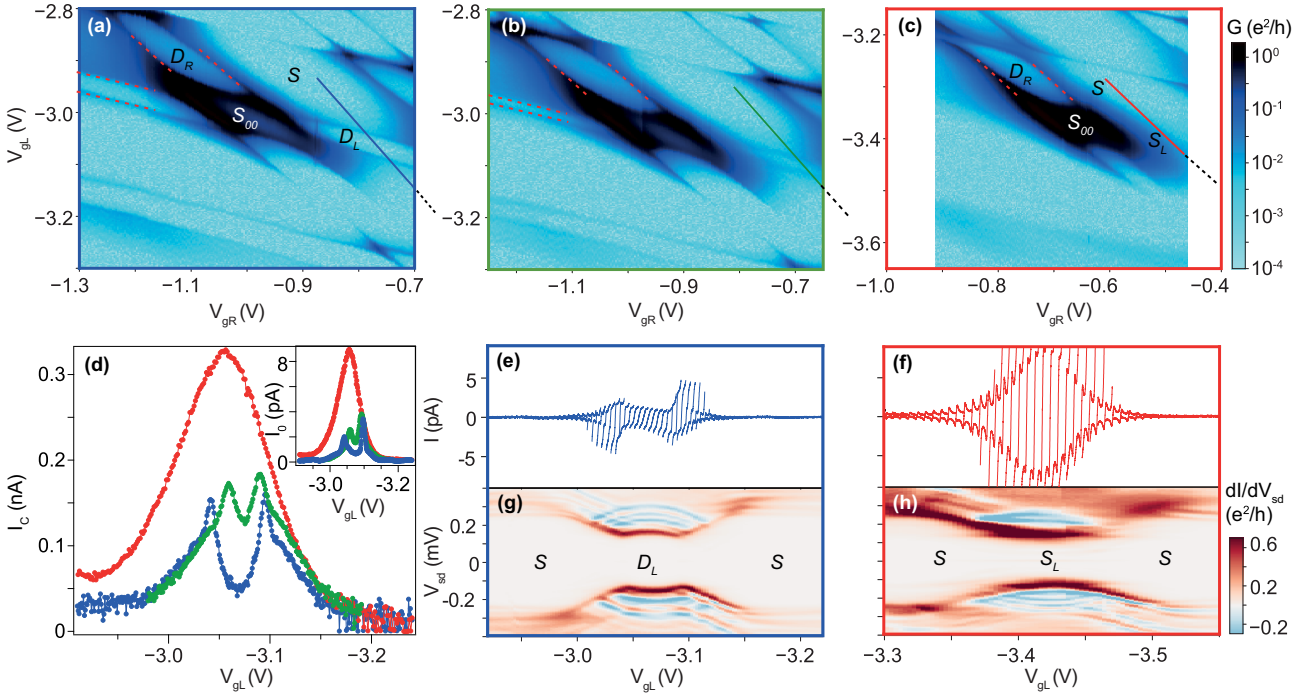

FIG. 6. (a–c) $G(V_{gL}, V_{gR})$ colormaps taken with V_{g1} set to (b) -9.2 V, (c) -9 V, and (d) -8.95 V. In (a) and (b), other gates are set to $V_{g3} = -9.3$ V, $V_{g5} = -0.25$ V, and $V_{bg} = 10.4$ V. In (c), other gates are set to $V_{g3} = -9.0$ V, $V_{g5} = -0.36$ V, and $V_{bg} = 11$ V. Changes in V_{g1} by 0.2 V require compensation in V_{gR} by $\approx$0.03 V and in V_{gL} by $\approx$0.04 V to keep the charge stability diagram in frame. (d) I_c and I_0 (in inset) vs V_{gL}, with V_{gL} and V_{gR} swept along the solid lines of corresponding color in (a)–(c). A black dotted line after the solid lines in (a)–(c) indicates that the line cuts extend beyond the gate range of the colormap. The traces are horizontally shifted to match the same gate range. (e, f) Comparison of the gate dependence of $I - V_{sd}$ traces from which the I_c and I_0 data in the blue and red curves in (d) are extracted to (g, h) colormaps of subgap $dI/dV_{sd} - V_{sd}$ measured along these gate trajectories. To avoid crowding, in (e) and (f) only every fifth trace is plotted, and the traces are horizontally shifted by 65 μV with respect to each other. V_{sd} is swept between ± 60 μV in each trace.

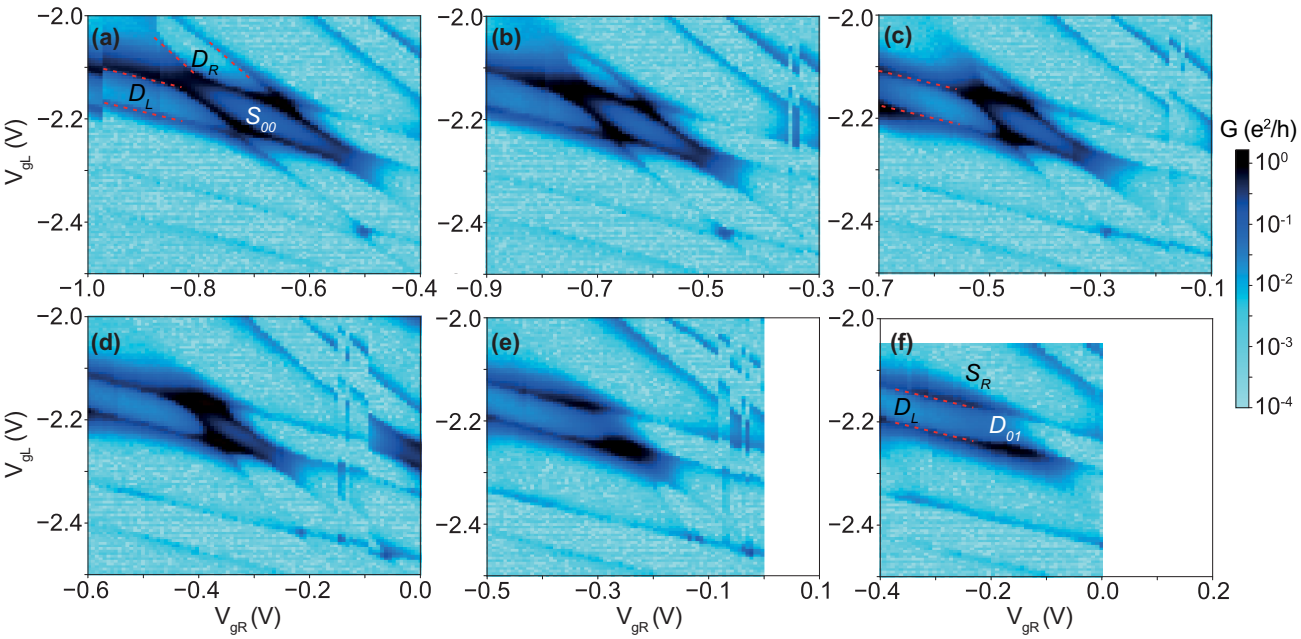

FIG. 7. Electron-hole asymmetric YSR screening. (a–f) $G(V_{gL}, V_{gR})$ colormaps with V_{g5} set at (a) -0.5 V, (b) -0.75 V, (c) -1.25 V, (d) -1.5 V, (e) -1.75 V, and (f) -2 V. Other gates are set to $V_{g1} = -9.2$ V, $V_{g3} = -9.2$ V, $V_{bg} = 10$ V. Changes in V_{g5} by -0.25 V require compensation in V_{gR} by $\approx$0.1 V, an in V_{gL} by $\approx$0.008 V to keep the charge stability diagram in frame. The sequence of parity stability diagrams serves as a prelude for Fig. 8.

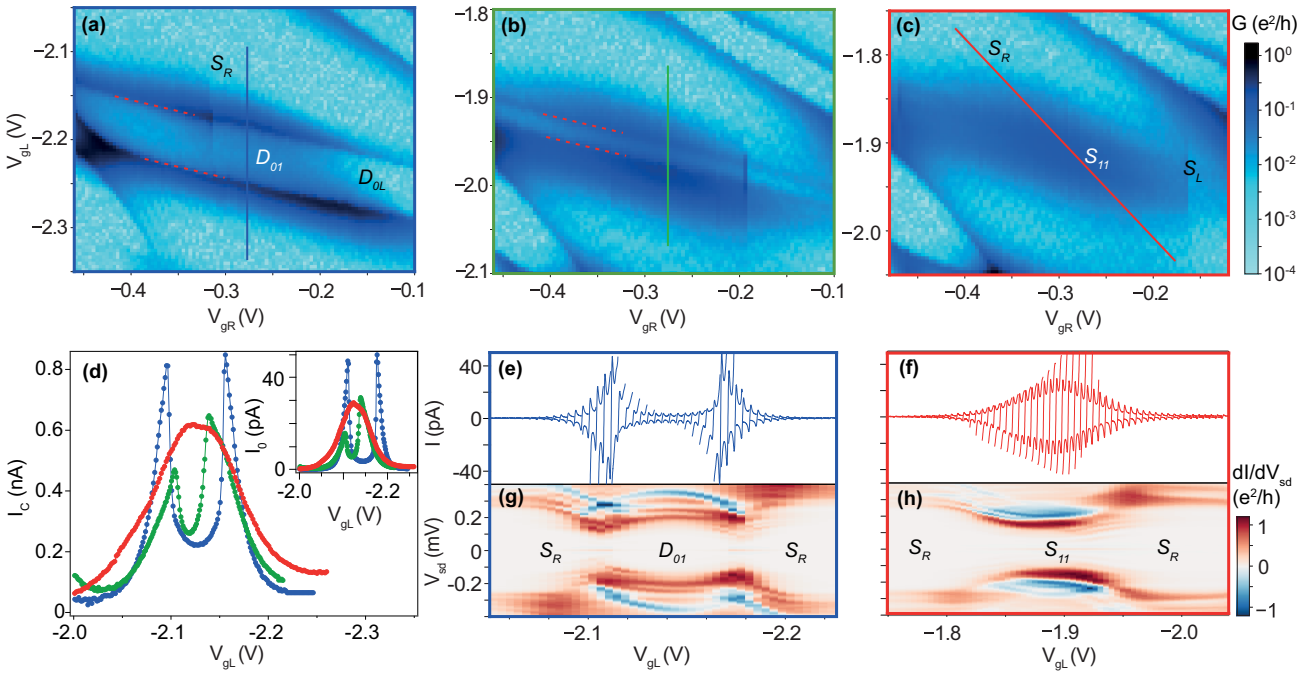

FIG. 8. (a–c) $G(V_{gL}, V_{gR})$ colormaps taken with V_{bg} set to (a) 10 V, (b) 9.74 V, and (c) 9.6 V. Other gates are set to $V_{g1} = -9.2$ V, $V_{g3} = -9.2$ V, $V_{g5} = -2$ V. Changes in V_{bg} by -0.4 V require compensation in V_{gL} by ≈ 0.3 V to keep the charge stability diagram in frame. (d) I_c and I_0 (in inset) vs V_{gL}, with V_{gL} and V_{gR} swept along the solid lines of corresponding color in (a)–(c). The traces are horizontally shifted to match the same gate range. (e, f) Comparison of the gate dependence of $I - V_{sd}$ traces from which the I_c and I_0 data in the blue and red curves in (d) are extracted to (g, h) colormaps of subgap $dI/dV_{sd} - V_{sd}$ measured along these gate trajectories. To avoid crowding, in (e) and (f) only every third trace is plotted, and the traces are horizontally shifted by 65 μV with respect to each other. V_{sd} is swept between ± 60 μV in each trace. The sequence of gate-tuned parity stability diagrams, which started in Fig. 7(a) in a honeycomb configuration, culminates here in a configuration devoid of parity lines.

However, closer inspection reveals additional complexity in the form of reduced gap values and peak replicas, which we will discuss in some detail. If the Bardeen model in Sec. IV is used to interpret the bias position of the lowest-lying gapped peak as $\Delta_R^* + E_L$, the measurements in Figs. 9(c) and 9(d) in Appendix A show that the superconducting gap is effectively reduced with respect to that of the parent Al superconductor (Δ) and that it is different for the left ($\Delta_L^* = 0.110$ meV) and right ($\Delta_R^* = 0.140$ meV) leads. By an effectively reduced gap, we mean that the gapped region in the weak tunneling regime at $V_{sd} < 2\Delta$ observed at $V_{bg} = -15$ V in Fig. 9(c) is replaced in Fig. 9(d), at the backgate voltage of operation of the device in shell X, $V_{bg} \approx 10$ V, by conductance resonances above $V_{sd} > \Delta_L^* + \Delta_R^*$. In electrostatic simulations of gating in InAs nanowire/Al hybrids, reduction of the effective induced gap in the nanowire occurred at more positive gate voltages due to weaker semiconductor/superconductor hybridization, which could explain our measurement [60].

Additionally, the colormaps display significantly less conducting, bias-symmetric replicas at $V_{sd} > \Delta_R^* + E_L$, as well as one or more faint replicas at $V_{sd} < \Delta_R^* + E_L$, the lowest of which can cross zero bias at parity crossings (see Appendix C). These replicas are often followed by NDC. In addition to replicas, on occasion a few straight horizontal lines cross the colormaps, such as in Fig. 6(h), which shows a pair of bias-symmetric lines at $V_{sd} = \Delta_R^*$. The colormaps also display additional lines with opposite curvature to that of the lowest-lying gapped peaks; a clear example of this is seen in Fig. 6(h) around $V_{gL} = -3.43$ V as split-loops terminating at the main YSR peaks. These additional lines can also exhibit replicas. The intricate replica behavior has been previously related to multiple peaks inside the superconducting gap of the hybrid nanowire-superconductor leads [61,62], to multiple Andreev reflection [63,64], quasiparticle relaxation, thermally excited transport [65–67], and/or inelastic Andreev tunneling [59]. Understanding the origin of these replicas, some of which may be visible in this work due to the unprecedented resolution of our data [the full width at half maximum of YSR peaks can be as low as 10 μV, as shown in Fig. 14(b)], is outside of the scope of this work. In what follows, we will focus only on the gate dependence of the curvature of the lowest-lying pair of gapped peaks and on its relation to I_0.

We now bring shell X back to the honeycomb regime, this time with gate settings which put it close to a GS transition due to YSR screening of the right-QD spin. Figure 7(a) shows a colormap of zero-bias conductance which represents the charge stability diagram of shell X in this regime. The sequence of colormaps in Figs. 7(a)–7(f) shows tuning of the stability diagram from the honeycomb pattern into a pattern lacking parity lines from the right QD. We interpret the change as stemming from an effective increase in Γ_R due to our tuning of the rightmost gate voltage, V_{g5}. The change is more subtle as V_{gL} also affects Γ_R, as mentioned above. Due to this, the upper section of the stability diagram transitions into a new GS faster than the lower one. We are able to model this qualitatively by introducing a linear dependence of Γ_R on n_L

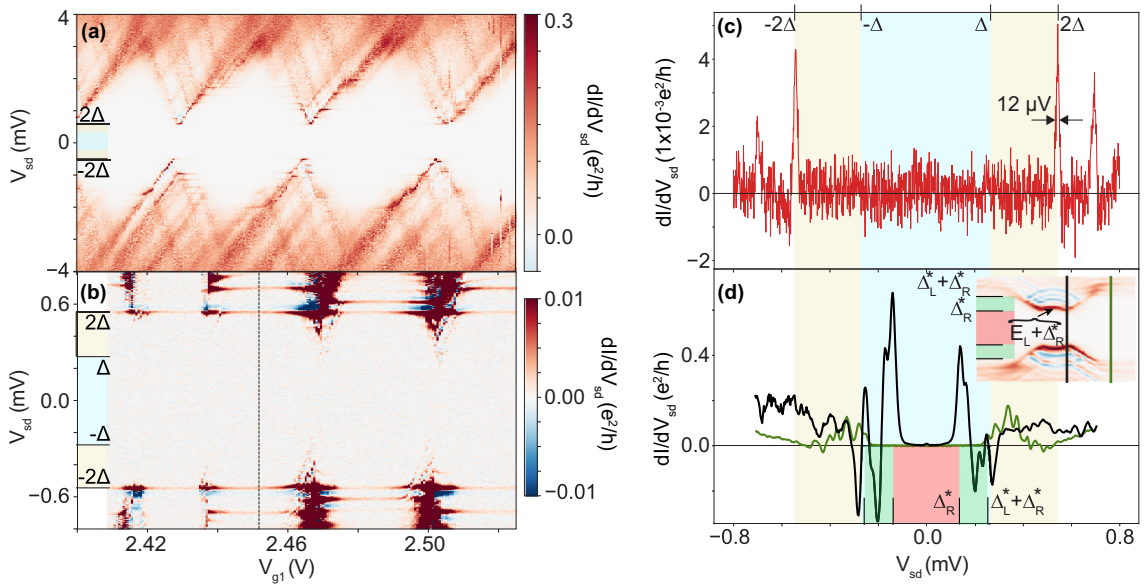

FIG. 9. (a) $dI/dV_{sd}(V_{sd}, V_{g1})$ colormap taken with other gates set at $V_{g2} = 2.25$ V, $V_{g3} = -6.5$ V, $V_{g4} = -2.16$ V, $V_{g5} = -6.5$ V, and $V_{bg} = -15$ V. (b) $dI/dV_{sd}(V_{sd}, V_{g1})$ colormap measured along the same gate trajectory as (a) and zoomed into the superconducting gap. A small gate shift occurred at $V_{g1} \approx 2.438$ V. In (a) and (b) the colorscale has been saturated to highlight faint features in the data. (c) $dI/dV_{sd}(V_{sd})$ trace obtained along the dashed line in (b). (d) $dI/dV_{sd}(V_{sd})$ traces measured along line of same color in the inset colormap, which corresponds to the same colormap as the one shown in Fig. 6(g). Only data in (d) correspond to shell X. Blue and yellow shadings separate Δ, 2Δ regions, while red and green shadings separate Δ_R^*, $\Delta_L^* + \Delta_R^*$ regions.

within a zero-bandwidth approximation of the superconducting continuum [32], as shown in Appendix F, and find that this is a faithful demonstration of a S_{00} to D_{01} GS transition in the (1,1) charge sector, and of a D_R to S_1 GS transition in the (0,1) and (2,1) charge sectors. In Appendix F, we also show that GS transitions obtained by increasing Γ_L, as those shown Fig. 6, are not significantly affected by introducing a dependence of Γ_R on n_L.

Finally, departing from the pattern in Fig. 7(f), in which the right-QD spin of DQD-shell X is screened, we demonstrate simultaneous screening of the left-QD spin, and therefore, full YSR screening of the spins of shell X. Figures 8(a)–8(c) show the step-by-step modification of this stability diagram, which contains only parity lines of the right QD in shell X in Fig. 8(a), to a diagram lacking parity lines of this shell in Fig. 8(c), which marks a D_{01} to S_{11} GS transition. In Fig. 8(c), after the GS transition occurs, the charge stability diagram of shell X shows a broad peak of conductance as the remains of the larger availability of conduction channels for Cooper pair transport in the (1,1) charge sector. The GS transition is also reflected in the gate dependence of I_c, I_0 and YSR peaks of largest conductance in Figs. 8(d)–8(h), obtained along gate paths given by solid lines of corresponding color in Figs. 8(a)–8(c), which cross the (1,1) charge sector. As in Fig. 6(d), Fig. 8(d) shows that I_c and I_0 (in inset) gradually change from a split-peak structure in the blue trace to a broad peak in the red trace. As in Figs. 6(e)–6(h), parity changes manifested in Fig. 8(g) in two kinks in the split-loop YSR structure which align to I_0 peaks in $I - V_{sd}$ traces in Fig. 8(e) are replaced by an all-singlet parity sequence, which expresses itself in the absence of kinks in Fig. 8(h), and in the smooth inflection point at $V_{gL} = -1.9$ V, which coincides in Fig. 8(f) with a broad I_0 peak in $I - V_{sd}$ traces.

From the succession of Figs. 7(a)–7(f) and Figs. 8(a)–8(c), we can see that the GS of the (1,1) charge sector, which started in Fig. 7(a) as an interdot singlet, S_{00}, has been gate-tuned in Fig. 8(c) into independently screened YSR singlets, S_{11}. This GS transition occurred through an intermediate YSR doublet phase, D_{01}, as shown in Figs. 7(f) and 8(a).

VI. CONCLUSION

In summary, we have demonstrated one- and two-impurity YSR physics in a shell of a DQD hybrid nanowire. We obtain the GS from the gate dependence of I_c, of I_0 and of YSR subgap conductance peaks, supported by the step-by-step tuning of the stability diagram to different endpoints of the phase diagrams. We find a reasonable qualitative agreement between experiment and theory. However, technical difficulties which prevent the measurement of Γ_L and Γ_R, together with cross-couplings in the device, have as a result that the S-DQD-S model cannot be quantitatively established in relation to the experiment without free fitting parameters. Quantitative comparison between experiment and theory is also complicated by lack of independent measurement of R within our model for the characteristic of the JJ circuit, which leads to extraction of I_c only up to a factor $\sqrt{\gamma} I_c$, and by the complexity of the reduced hybrid nanowire-superconductor gap, which is reflected in multiple replicas of the YSR state filling the gap between the YSR state and the parent Al superconducting gap edge.

As a spectroscopic probe of parity changes, the narrow zero-bias conductance peak of the effectively voltage-biased Josephson junction [35–40] maintains the sharpness of the relevant features in all charge, or more accurately, parity stability diagrams independently of the tunneling rates. This is

in stark contrast to the case of magnetic impurities (spinful QDs) coupled to normal metals, which broaden the conductance features at strong hybridization [68–73]. The zero-bias conductance peak also provides very direct access to I_c, just as it provides access to the local superfluid density in scanned Josephson-tunneling microscopy, which has been used recently to detect Cooper-pair density waves on surfaces of $Bi_2Sr_2CaCu_2O_{8+x}$ and $NbSe_2$ [40,74]. Unlike scanning tunneling spectroscopies of dimers of magnetic adatoms on superconducting surfaces [65,75,76], our DQD realization comprises two spin-1/2 states which are completely screened by individual superconducting channels. The Kondo-YSR analogy breaks down towards zero temperature, as confirmed by the existence of doublet domains in the phase diagram at $k_BT \ll \Delta$.

By virtue of t_d, nonmagnetic, gap-protected superpositions of the two singlet states found, the exchange singlet S_{00} and the independently screened YSR singlet S_{11}, could be prepared in future works for parameters close to the anticrossing in the phase diagram of Fig. 3 [77], with the purpose of using them as qubits [78]. In addition, the demonstrated gate control of a two-site quantum dot chain in superconducting proximity is a crucial step towards the implementation in our hybrid wires of the YSR analog of Doniach's Kondo necklace [2] and of the Kitaev chain [79–81], complementing ongoing research of emergent manifestations of topology [62,82–87].

Data availability: All data needed to evaluate the conclusions in the paper are present in the paper. Raw data used to produce the experimental figures in the paper can be found at the repository ERDA of the University of Copenhagen at [88].

ACKNOWLEDGMENTS

We thank A. Jellinggaard, M. C. Hels, and J. Ovesen for experimental assistance. The project received funding from the European Union's Horizon 2020 research and innovation program under the Marie Sklodowska-Curie Grant Agreement No. 832645. We additionally acknowledge financial support from the Carlsberg Foundation, the Independent Research Fund Denmark, QuantERA "SuperTop" (NN 127900), the Danish National Research Foundation, Villum Foundation Project No. 25310, and the Sino-Danish Center. P.K. acknowledges support from Microsoft and the ERC starting Grant No. 716655 under the Horizon 2020 program. R.Ž. acknowledges support from the Slovenian Research Agency (ARRS) under Grants No. P1-0044 and No. J1-7259.

APPENDIX A: EXTRACTION OF DQD PARAMETERS

To measure Δ, we deplete the device by setting $V_{bg} = -15\,\mathrm{V}$ (which is $\approx 25\,\mathrm{V}$ more negative than V_{bg} used in the measurements on shell X in the main text) and perform Coulomb-diamond spectroscopy as shown in Fig. 9(a). The repetitive Coulomb-blockade pattern is indicative of a multilevel QD regime. The Coulomb diamonds appear split by a forbidden bias window. Zooming in on this window, as shown in Fig. 9(b), a pair of bias-symmetric lines which cross all diamonds is identified at $eV_{sd} = \pm 2\Delta$. This feature stems from the BCS coherence peak from the left lead at energy $-\Delta$ probing the coherence peak in the right lead at energy $+\Delta$ via co-tunneling through the QDs. At parity crossings, which correspond to the apexes of split Coulomb diamonds in this opaque regime, a few pairs of bias-symmetric subgap states come down, the lowest of which reaches exactly Δ. This occurs when the coherence peak at Δ in the right lead probes a YSR excitation in the left lead which crosses zero energy at parity crossings. At $e|V_{sd}| < \Delta$, the conductance is blocked at all V_{g1} values. In Fig. 9(c) we plot a line cut at the center of one Coulomb diamond to display the position of the quasiparticle tunneling peaks at 2Δ and their extremely narrow width [66]. We measure $2\Delta = 0.54\,\mathrm{meV}$, which provides a value of Δ identical to the one obtained from S-QD-N devices made from the same batch of nanowires [34]. The position of horizontal lines outside 2Δ depends on the Coulomb diamond chosen, as can be seen in Fig. 9(b); we ascribe these lines to the probing of QD states in co-tunneling by the sharp superconducting singularities. The trace in Fig. 9(c) is compared to two traces in Fig. 9(d) displaying YSR excitations in shell X which are extracted from Fig. 6(g) to show graphically that $\Delta_R^* < \Delta$ and that $\Delta_L^* + \Delta_R^* < 2\Delta$, where Δ_L^* and Δ_R^* are the effectively reduced gaps in the left and right leads at the backgate voltage at which the device is operated, as in Sec. V. If we assign a bias position $E_L + \Delta_R^*$ to the innermost gapped YSR peaks, we measure $\Delta_R^* = 0.140\,\mathrm{meV}$ from the black trace, which is taken at a parity crossing where $E_L = 0$. In turn, we find $\Delta_L^* + \Delta_R^* = 0.250\,\mathrm{meV}$ from the green trace, which is taken in the (0,2) charge state, where E_L approaches asymptotically to Δ_L^*. From this, we deduce $\Delta_L^* = 0.110\,\mathrm{meV}$.

To measure U_L, U_R, we perform Coulomb-diamond spectroscopy on each QD in shell X as shown in Fig. 10. In spite of the larger couplings of the DQD in this regime, we observe faded Coulomb diamonds from which we can trace the actual diamonds as denoted by dashed lines. U_L, U_R correspond to the bias difference between the apex of the central Coulomb diamond and the edge of the superconducting gap at 2Δ. An indication of the order of magnitude of the tunneling rates of the DQD can be obtained from the full-width-at-half-maximum of Coulomb lines outside the gap between the pairs of arrows in Figs. 10(b) and 10(c), which is of 0.6 meV in both cases.

To estimate t_d and U_d, we use the curvature of the parity lines at the (1,1), (0,2) charge transition in the charge stability diagram of shell X. We first prolong the parity lines of the left and right QDs, as indicated by the yellow dashed lines in Fig. 11. We join their two intersections by a green line which separates the (1,1) and (0,2) charge sectors. Afterwards, by projecting the green line into the two white lines which indicate the charging energies of the QDs, we convert the gate scale of the green line into energy. The red lines along the green line indicate the distance from the curved parity lines in the colormap to each of the two intersections of the yellow dashed lines and are each equal to $2t_d$; the green line summed to the two red lines is $\sqrt{2}U_d + 4t_d$. This procedure assumes that the parity stability diagram in the superconducting state is similar to that of the normal state. In this way, we measure $t_d \approx 0.03$–$0.05\,\mathrm{meV}$ and $U_d \approx 0.13$–$0.23\,\mathrm{meV}$.

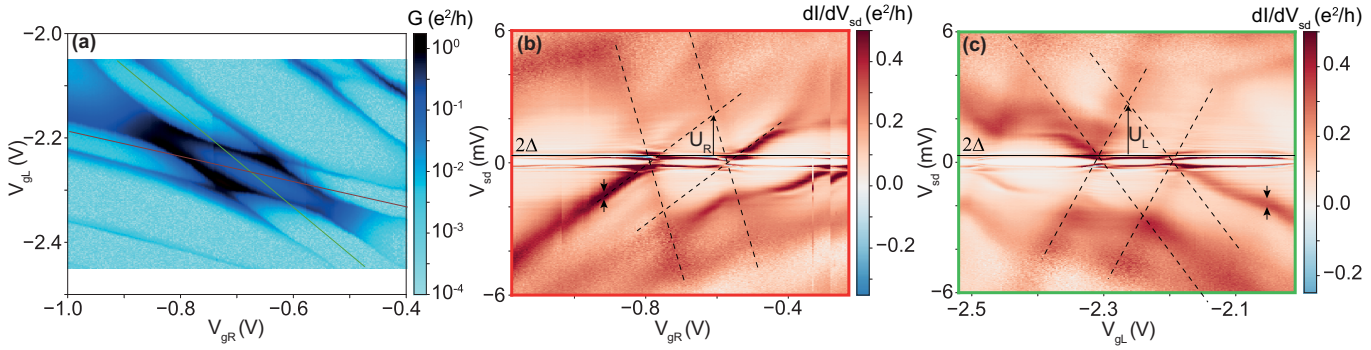

FIG. 10. (a) Colormap of zero-bias conductance, G, vs $(V_{\mathrm{gL}}, V_{\mathrm{gR}})$ for shell X measured with other gates set at $V_{\mathrm{g1}} = -9.2$ V, $V_{\mathrm{g3}} = -9.3$ V, $V_{\mathrm{g5}} = -0.25$ V, and $V_{\mathrm{bg}} = 11$ V. (b, c) Colormaps of $dI/dV_{\mathrm{sd}} - V_{\mathrm{sd}}$ vs gate voltage representing Coulomb-diamond spectroscopy of the (b) right QD, (c) left QD. Gate trajectories followed in each colormap are indicated by red and green lines in (a), respectively; however, for simplicity, only (b) V_{gR} and (c) V_{gL} gates are indicated on the horizontal axes. Dashed lines are guides to the eye to follow Coulomb diamonds. In (b) and (c), the AC lock-in excitation is set to 20 μV.

APPENDIX B: MODEL OF THE CIRCUIT

In this Appendix we elaborate on the extended RCSJ model necessary to explain the $I - V_{\mathrm{sd}}$ and $dI/dV_{\mathrm{sd}} - V_{\mathrm{sd}}$ curves observed in the experiment. The extension, compared to standard RCSJ, consists of an additional series resistance R and shunt capacitance C. This model has been applied to ultra-small Josephson junctions [89] and S-QD-S setups [19]. Disregarding C_{filter} in the circuit depicted in Fig. 2(c), Kirchhoff's laws and the Josephson relation yield two coupled Langevin equations:

$$\frac{du}{d\tau} = \frac{1}{\alpha}\left\{\frac{V}{R_s I_c} - \sin\phi - \frac{R}{R_s}[u + L(\tau)] - \frac{1}{\alpha_0}\frac{d^2\phi}{d\tau^2}\right\}, \quad \text{(B1)}$$

$$\frac{d\phi}{d\tau} = u + L(\tau) - \sin\phi - \frac{1}{\alpha_0}\frac{d^2\phi}{d\tau^2}. \quad \text{(B2)}$$

Here $u = V_{\mathrm{sd}}/RI_{\mathrm{c}}$ denotes the dimensionless voltage across the shunt capacitor C and we have introduced the dimensionless time $\tau = \omega_{RL}t$ with $\omega_{RL} = R/\mathrm{L}$, where $\mathrm{L} = \Phi/I_{\mathrm{c}}$ is the self-inductance of the Josephson junction set by the critical current, I_{c}, and $\Phi = \hbar/2e$. The two different RC frequencies, $\omega_{RC_{\mathrm{J}}} = (RC_{\mathrm{J}})^{-1}$ and $\omega_{RC} = (RC)^{-1}$, enter these equations via the dimensionless parameters $\alpha = \omega_{RL}/\omega_{RC} = R^2CI_c/\Phi$ and $\alpha_0 = \omega_{RC_{\mathrm{J}}}/\omega_{RL} = \Phi/R^2C_{\mathrm{J}}I_{\mathrm{c}}$. Finally, $L(\tau)$ is a dimensionless stochastic parameter describing white-noise voltage fluctuation of V_{sd}. $L(\tau)$ is composed of Nyquist noise from the series resistor (R) at temperature T^* and a stray voltage noise characterized by a variance, K, to account for imperfect filtering, such that $\langle L(\tau)L(\tau+\Delta\tau)\rangle = (\frac{2k_BT^*}{\Phi I_c} + \frac{K}{RI_c\Phi})\delta(\Delta\tau)$. Noise from the source resistance R_{s} is assumed to be excluded by the RC filters. As K and T^* can not be independently measured in this setup we ascribe all noise to the series resistor (R) with an effective temperature $T = T^* + K/(2Rk_B)$ which can be different from the fridge temperature.

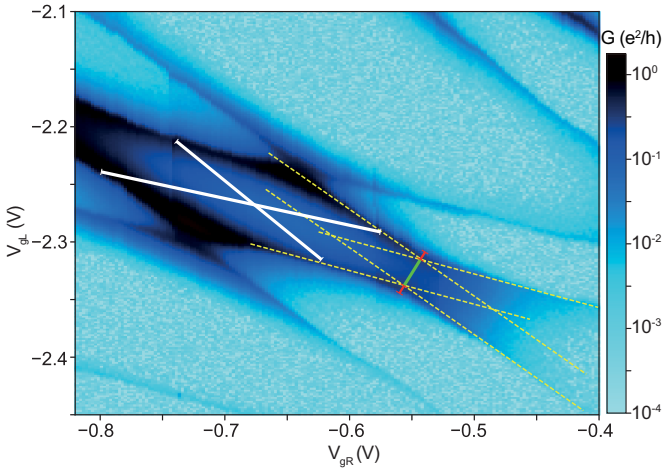

FIG. 11. Zoomed-in version of the colormap of zero-bias conductance vs $(V_{\mathrm{gL}}, V_{\mathrm{gR}})$ for shell X shown in Fig. 10. Lines are used to estimate t_{d} and U_{d} as described in Appendix A.

For $\alpha \gg 1$, u changes slowly with time, which allows us to solve for ϕ's equilibrium distribution keeping u constant. If furthermore $\alpha_0 \gg 1$, solving the stochastic equation for the ϕ distribution is equivalent to the original RCSJ problem [46] with the solution

$$\langle \sin\phi \rangle = \mathrm{Im}\,\frac{I_{1-iuA}(A)}{I_{-iuA}(A)}, \quad \text{(B3)}$$

where $A = \Phi I_{\mathrm{c}}/k_BT$ and $I_n(z)$ is a Bessel function. Inserting this solution into Eq. (B1) a constant average voltage, $\langle \dot{u} \rangle = 0$, may be enforced by satisfying the equation

$$\frac{V}{R_{\mathrm{s}}I_{\mathrm{c}}} - \frac{R}{R_{\mathrm{s}}}\langle u \rangle = \mathrm{Im}\,\frac{I_{1-i\langle u\rangle A}(A)}{I_{-i\langle u\rangle A}(A)}. \quad \text{(B4)}$$

Two limits of R/R_{s} are of interest. For small R/R_{s}, depending on I_{c} and T, this equation has three solutions for $\langle u \rangle$ arising from the nonmonotonic behavior of the right-hand side, and the setup is effectively current biased, exhibiting hysteretic $\langle I \rangle - V$ curves. For large R/R_{s}, the solution for $\langle u \rangle$ is unique and the system is effectively voltage biased and can exhibit NDC. The latter case is consistent with the experiment.

Experimental $I - \langle V_{\mathrm{sd}} \rangle$ traces can now be fitted to

$$\langle I \rangle = I_c\,\mathrm{Im}\,\frac{I_{1-i\langle u\rangle A}(A)}{I_{-i\langle u\rangle A}(A)}, \quad \text{(B5)}$$

which is identical to an earlier formula derived by Ivanchenko and Zil'berman [46], while the derivative of this formula with respect to $\langle V_{\mathrm{sd}} \rangle$ allows fitting of $dI/dV_{\mathrm{sd}} - V_{\mathrm{sd}}$ traces. In a typical Josephson junction $A \gg 1$ and the cusp voltage scale

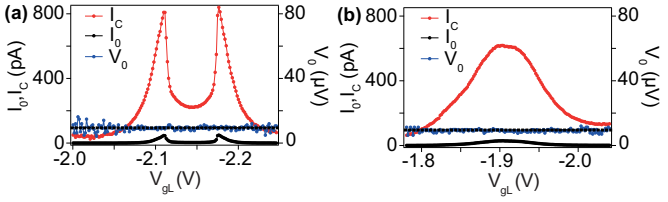

FIG. 12. (a, b) Fitted I_c, extracted cusp current, I_0 (left axes), and extracted cusp voltage, V_0 (right axes) from $I - V_{sd}$ data from Figs. 8(e) and 8(f), respectively. Data from all measured $I - V_{sd}$ traces in the gate range indicated are included, and not just every third trace. An horizontal dashed line corresponds to $V_0 = 9.1$ μV. Deviations from constant V_0 occur only for small current ($I_0 < 0.3$ pA), e.g., between $V_{gL} = -2$ and -2.05 V, where data noise prevents an accurate extraction of V_0.

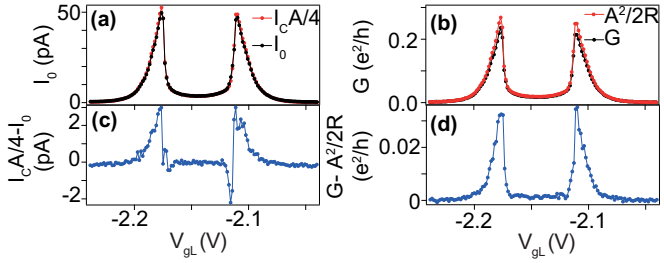

FIG. 13. (a–d) Comparison between the gate dependence of rescaled I_c and (a) measured I_0 from Fig. 14(c) and (b) G line cut through Fig. 14(d). To obtain I_0 in (a), data from all measured $I - V_{sd}$ traces corresponding to the gate trajectory in Fig. 14(c) is included, and not just every third trace. (c, d) Difference between the scaled and measured curves in (a) and (b).

is set by $V_0 \approx RI_c$. In our measurements V_0 is constant over a wide range of cusp current, I_0, as we show in Fig. 12, where extracted I_0, V_0 and fitted I_c is shown for two line cuts in the experiment.

This is consistent with the large-noise limit, $A < 1$, of Eq. (B5) where one can perform a Taylor expansion of Eq. (B5) around $A \approx 0$ to obtain [46]

$$\langle I \rangle \approx \frac{1}{2} \frac{I_c A^2 \langle u \rangle}{1 + A^2 \langle u \rangle^2}, \tag{B6}$$

from which it is clear that the cusp voltage $V_0 = \arg\max \langle I \rangle (\langle V_{sd} \rangle) = Rk_BT/\Phi$ is solely determined by noise and is independent of I_c. Cusp current,

$$I_0 = \langle I \rangle (V_0) = I_c A/4, \tag{B7}$$

and zero-bias conductance,

$$G = d\langle I \rangle / d\langle V_{sd} \rangle (0) = A^2/2R, \tag{B8}$$

can also easily be identified in this limit. We also identify a scaling γ with $\bar{R} = R/\gamma$, $\bar{T} = T\gamma$ and $\bar{I}_c = \sqrt{\gamma} I_c$ which keeps V_0 and Eq. (B6) unchanged.

If the limits above are satisfied we indeed have a model where (1) The junction is overdamped and nonhysteretic, (2) the junction is effectively voltage biased allowing measurements of NDC, and (3) the $I - V_{sd}$ curves are cusped with an I_0-independent cusp voltage V_0. We will now discuss the validity of the above limits. By fixing $T = 80$ mK, consistent fits of Eq. (B5) can be done for all gate ranges yielding a constant series resistance $R = 3$ kΩ and variable I_c in the range $I_c \sim 0.02$–3 nA which roughly corresponds to $\alpha \sim 10$–100 and $\alpha_0 \sim 10^4$–10^5 using the geometric estimates of C and C_J, consistent with our assumption that $\alpha, \alpha_0 \gg 1$. For these parameters Eq. (B4) has only one solution, consistent with the junction being voltage biased. Lastly, for these parameters $A \leqslant 1$ for the fitted range of I_c with $A \approx 1$ for the largest I_c. In Fig. 13 we compare the simple large-noise-limit expressions for I_0 and G using I_c from the fitting with measured I_0 and G and find excellent agreement with the largest discrepancies occurring for large I_c values consistent with our Taylor expansion in $A \propto I_c$.

As the above analysis is a fully classical treatment we will now discuss the impact of quantum fluctuations. The characteristic frequencies of the circuit are estimated to be $\omega_{RC} \sim 0.01$ GHz, $\omega_{RL} \sim 0.1$–10 GHz, and $\omega_{RC_J} \sim 10^5$ GHz. With $T = 80$ mK, i.e., $k_BT/\hbar \sim 10$ GHz, and $I_c = 0.02 - 3$ nA, we arrive at the following hierarchy of frequencies:

$$\omega_{RC} \ll \omega_{RL} \lesssim k_BT/\hbar \ll \omega_{RC_J} \tag{B9}$$

For these values, one may safely neglect the large capacitance, C, in the effective circuit impedance experienced by the junction

$$Z_{eff}(\omega) = [1/R + iC_J\omega + 1/(iL\omega)]^{-1}, \tag{B10}$$

and which determines the mean-squared phase fluctuations, $S_\phi = \langle (\phi - \langle \phi \rangle)^2 \rangle$, which is given by Refs. [90–92],

$$S_\phi = \int_{-\infty}^{\infty} \frac{d\omega}{\omega} \frac{\mathrm{Re}Z_{\mathrm{eff}}(\omega)}{2R_Q} \frac{1}{1 - e^{-\hbar\omega/k_BT}} \tag{B11}$$

with $R_Q = h/4e^2 \approx 6.5$ kΩ. Within a fully quantum mechanical treatment, this correlation function in turn leads to an approximately exponential reduction of the critical current [90,92]:

$$I_c^* \approx I_c \exp(-S_\phi). \tag{B12}$$

As a function of temperature, S_ϕ is roughly constant and due to quantum fluctuations for $k_BT < \hbar\omega_{RL}$. For $\hbar\omega_{RL} < k_BT$, corresponding to the parameters found above, the fluctuations are largely classical and S_ϕ increases linearly with T, consistent with the classical treatment employed above. Since k_BT is just barely larger than $\hbar\omega_{RL}$, and R just barely smaller than R_Q, a further reduction of I_c due to quantum fluctuations must be expected to reduce the actual values for I_c, which we deduce from the strictly classical analysis above and report in the figures throughout the main text. Nevertheless, the marked gate dependence of I_c remains and this is what provides the real value of the zero-bias conductance peak as a probe of YSR screening and the concomitant quantum phase transitions reported in this paper.

Summarizing the circuit analysis, the magnitudes of I_c obtained by fitting $I - V_{sd}$ and $dI/dV_{sd} - V_{sd}$ traces are expected to be slightly overestimated by leaving out quantum, and retaining only thermal fluctuations of the electromagnetic environment. Additionally, T has been fixed by an independent measurement which is only an estimate of the effective temperature experienced by the circuit. Relaxing this constraint on T, we can still obtain consistent fits utilizing a global

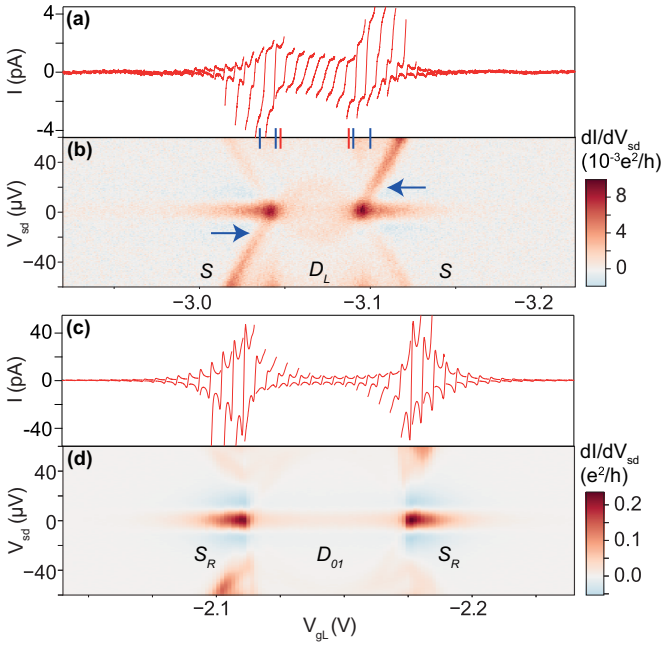

FIG. 14. (a–d) Comparison between the gate dependence of (a, c) $I - V_{\rm sd}$ traces and respective (b, d) $dI/dV_{\rm sd}$ colormaps which represent the gate dependence of the corresponding low-lying non-gapped YSR subgap states for (a, b) the $S - D_{\rm L} - S$ and (c, d) the $S_{\rm R} - D_{01} - S_{\rm R}$ GS sequences. In (a) and (c), to avoid crowding, only every seventh (every third) trace is plotted, and the traces are horizontally shifted by 65 μV with respect to each other. In each trace, $V_{\rm sd}$ is swept from -60 to 60 μV. To acquire the data sets in (a)–(d), the gates were swept along the solid lines in Fig. 6(a) for plots (a) and (b), and in Fig. 8(a) for plots (c) and (d).

scaling of R and $I_{\rm c}$. The value of these measurements therefore lies in the gate dependence of $I_{\rm c}$, not its amplitude which can include a global scaling, in good qualitative agreement with NRG calculations.

APPENDIX C: ASYMMETRIES IN CUSP CURRENT

While the model displays I_0 symmetric in $V_{\rm sd}$, in some instances the experiment fails to do so, with the discrepancy attributed to conduction through low-lying YSR subgap peaks which approach $V_{\rm sd} = 0$. In Fig. 14 we show two examples in which subgap peaks approach zero bias, and the effect which this has on the symmetry of I_0 in $V_{\rm sd}$. The extreme case when a pair of subgap peaks reaches all the way to $V_{\rm sd} = 0$ at two singlet-doublet parity crossings is shown in Fig. 14(b), and its effect on $I - V_{\rm sd}$ traces is shown in Fig. 14(a). Blue arrows indicate the subgap peak of largest conductance among the ones at positive and negative bias for a given gate voltage. To the left of state $D_{\rm L}$, this peak is at negative bias, whereas to the right it is at positive bias; i.e., the peak of largest conductance is antisymmetric with respect to the center of the state $D_{\rm L}$. Unsurprisingly, the same antisymmetry is observed for I_0, with the negative-I (positive-I) cusp occurring at larger $|I|$ than its positive-I (negative-I) counterpart to the left (right) of state $D_{\rm L}$. This occurs between the pairs of gate points marked by blue pins. This behavior contrasts with the hysteresis of underdamped Josephson junctions, where a sweep of $V_{\rm sd}$ from negative to positive values, as it is always the case in our device, would result in larger switching current for positive than negative I. Along the gate voltage delimited by the pair of red pins, the subgap states remain close to $V_{\rm sd} = 0$, affecting the positive-negative symmetry of the I cusps, which are just barely well-defined in this region. To the left and right of the parity crossings, in the S states, YSR subgap peaks are far enough away from the supercurrent zero-bias conductance peak, and $I - V_{\rm sd}$ traces are consequently fully symmetric in $V_{\rm sd}$.

Figures 14(c) and 14(d) show a different example with subgap peaks appearing near $V_{\rm sd} = 0$ in Fig. 14(d). Nevertheless, these are far enough away to not affect the cusp symmetry in the respective $I - V_{\rm sd}$ traces in Fig. 14(c).

It is natural to expect that the appearance of such additional subgap conductance channels close to zero bias affects the resistance of the junction, and therefore the effective relation between $\langle I \rangle$ and $\langle V_{\rm sd} \rangle$. The modeling of this additional complication, however, is beyond the scope of this work.

APPENDIX D: TWO-IMPURITY MODEL

We model the double quantum dot system using the following superconducting generalization of the two-impurity Anderson impurity model:

$$H = \sum_i H_{{\rm imp},i} + H_{\rm LR} + \sum_i H_{{\rm BCS},i} + \sum_i H_{{\rm hyb},i}, \qquad \text{(D1)}$$

where the impurity Hamiltonians for quantum dots $i = L$ (left) and $i = R$ (right) with on-site energies ϵ_i and electron-electron repulsion (Hubbard) parameters U_i are

$$H_{{\rm imp},i} = \frac{U_i}{2}(\hat{n}_i - n_i)^2, \qquad \text{(D2)}$$

where the impurity occupancy (charge) operators are $\hat{n}_{i,\sigma} = d^\dagger_{i,\sigma} d_{i,\sigma}$, $\hat{n}_i = \hat{n}_{i,\uparrow} + \hat{n}_{i,\downarrow}$, while $n_i = 1/2 + \epsilon_i/U_i$ is the impurity energy level ϵ_i (controlled by the corresponding gate voltage) expressed in the dimensionless units of electron number. The interdot tunneling amplitude, $t_{\rm d}$, enters through a tunneling term,

$$H_{LR} = \sum_\sigma t_{\rm d} d^\dagger_{L,\sigma} d_{R,\sigma} + {\rm H.c.}, \qquad \text{(D3)}$$

the leads are modeled using BCS Hamiltonians

$$H_{{\rm BCS},i} = \sum_{k,\sigma} \epsilon_k c^\dagger_{i,k\sigma} c_{i,k\sigma} + \sum_k \Delta c^\dagger_{i,k\uparrow} c^\dagger_{i,k\downarrow} + {\rm H.c.}, \qquad \text{(D4)}$$

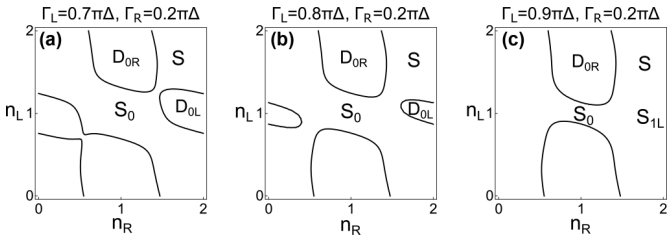

FIG. 15. Parity transition lines calculated using a ZBW approximation with a gate-dependent tunnel coupling $t_{\rm R}$. Black lines indicate changes of GS parity. Increasing $\Gamma_{\rm L}$ from (a) to (c). These figures should be qualitatively compared with Fig. 6.

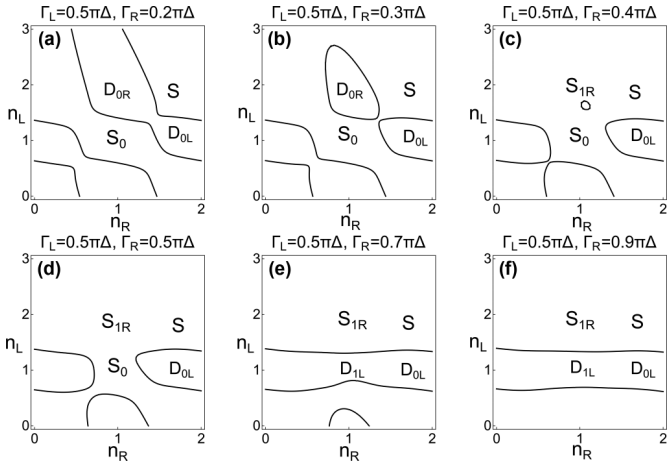

FIG. 16. Parity transition lines calculated using a ZBW approximation with a gate-dependent tunnel coupling t_R. Black lines indicate changes of GS parity. Increasing Γ_R from (a) to (f). These figures should be qualitatively compared with Fig. 7.

U_d is set to zero, and the QD-lead tunneling amplitudes, $t_{L/R}$, enter through the hybridization terms

$$H_{\mathrm{hyb},i} = t_i \sum_{k\sigma} c^\dagger_{i,k\sigma} d_{i,\sigma} + \mathrm{H.c.} \tag{D5}$$

In these expressions, $d_{i\sigma}$ are QD operators, while $c_{i,k\sigma}$ are lead operators. Finally, the tunneling rates are defined as $\Gamma_i = \pi \rho_i t_i^2$, where ρ_i is the density of states in lead i in the normal state (i.e., in the absence of superconductivity).

APPENDIX E: FINITE-BIAS CONDUCTANCE AT WEAK INTERDOT COUPLING

For weak t_d, $\mathrm{d}I/\mathrm{d}V_{sd}$ can be estimated using the tunneling (Bardeen) approach, similar to that used in the analysis of scanning tunneling microscopy (STM) experiments. We assume that the voltage drops entirely across the weak link between the two dots, and that each quantum dot is in thermodynamic equilibrium with the neighboring lead. The chemical potential shifts in the leads are $\mu_{L,R} = \pm eV_{sd}/2$, and the local spectral functions on the dots are equally shifted. The superconductors are described in the semiconductor model, neglecting all coherence effects. The current is then given by

$$I = \frac{4\pi e}{\hbar}|t_d|^2 \int_{-\infty}^{\infty} [f(\omega-\mu_L) - f(\omega-\mu_R)] \times A_L(\omega-\mu_L) A_R(\omega-\mu_R)\, d\omega, \tag{E1}$$

where $f(x) = [1+\exp(x/k_BT)]^{-1}$ is the Fermi function. At zero temperature, this becomes

$$I = \frac{4\pi e}{\hbar}|t_d|^2 \int_{-eV_{sd}/2}^{+eV_{sd}/2} A_L(\omega - eV_{sd}/2) A_R(\omega + eV_{sd}/2)\, d\omega. \tag{E2}$$

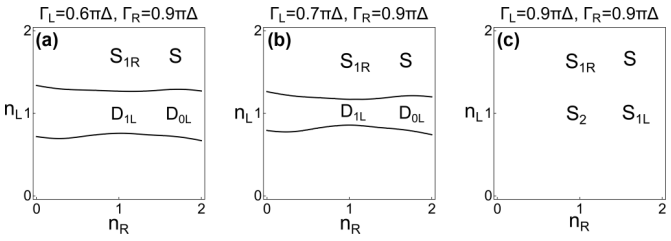

FIG. 17. Parity transition lines calculated using a ZBW approximation with a gate-dependent tunnel coupling t_R. Black lines indicate changes of GS parity. Increasing Γ_L from (a) to (c). These figures should be qualitatively compared with Fig. 8.

We computed the spectral functions $A_{L,R}(\omega)$ for the two subsystems with $t_d = 0$ using the density-matrix numerical renormalization group algorithm with discretization parameter $\Lambda = 2$, and broadened raw spectra using the broadening parameter $\alpha_b = 0.2$. After convolution of the spectral functions to obtain the current, dI/dV_{sd} was computed by taking numerical differences. This single-particle tunneling approach, valid only to second order order in t_d, neglects Andreev reflections altogether and presumes that relaxation rates of quasiparticles in the subgap states are larger than the interdot tunneling rate.

APPENDIX F: EFFECTS OF FINITE INTERDOT CHARGING ENERGY AND GATE-DEPENDENT TUNNEL COUPLING

In this section we investigate the effects of a possible influence of V_{gL} on t_R. For efficient parameter exploration, we do this using a zero-bandwidth (ZBW) approximation [32] of the superconducting leads in Eq. (D1), taking $H_{\mathrm{BCS}_i} \approx \sum_i \Delta c^\dagger_{i\uparrow} c^\dagger_{i\downarrow} + \mathrm{H.c.}$ and numerically diagonalizing the Hamiltonian. We model the tunnel couplings, t_i, as $t_L = \sqrt{2\Delta\Gamma_L/2}$ and $t_R = \sqrt{2\Delta\Gamma_R/2}(1+n_L/4)$, where t_R now depends on V_{gL} through n_L. To more realistically mimic the experimental scenario we also include an interdot Coulomb repulsion, U_d, such that $H_{\mathrm{imp}} = \sum_{i=L,R} U_i/2(\hat{n}_i - n_i)^2 + U_d(\hat{n}_L - n_L)(\hat{n}_R - n_R)$ with $U_d = 0.5\,\mathrm{meV}$ and $\hat{n}_i = \hat{n}_{i\uparrow} + \hat{n}_{i\downarrow}$ being the electron counting operator. Other parameters are identical to parameters used for the NRG calculations presented above. Comparing Fig. 16(a) to Fig. 5(a), the main effect of U_d is to provide an angle on the n_R, n_L parity lines.

In Figs. 15–17 we show GS parity transition lines (black lines) of the S-DQD-S charge stability diagrams for various values of Γ_L and Γ_R, corresponding qualitatively to data in Figs. 6–8. The gate-dependent coupling is seen to account in Fig. 16 for the asymmetric screening around the electron-hole symmetry point occurring when Γ_L is increased, which is necessary to explain the experimental findings in Fig. 7, that is, the observation that the doublet to singlet transition reflected by the vanishing of the two parity transition lines happens faster on the top ($V_{gL} \approx -2.1\mathrm{V}$) than at the bottom ($V_{gL} \approx -2.3\mathrm{V}$).

[1] N. F. Mott, Philos. Mag. A **30**, 403 (1974).
[2] S. Doniach, Physica B+C **91**, 231 (1977).
[3] B. A. Jones and C. M. Varma, Phys. Rev. Lett. **58**, 843 (1987).

[4] A. Georges, G. Kotliar, W. Krauth, and M. J. Rozenberg, Rev. Mod. Phys. **68**, 13 (1996).

[5] A. C. Hewson, *The Kondo Problem to Heavy Fermions*, Vol. 2 (Cambridge University Press, Cambridge, 1997).

[6] P. Coleman, *Heavy Fermions: Electrons at the Edge of Magnetism* (Wiley Online Library, New York, 2007).

[7] H. v. Löhneysen, A. Rosch, M. Vojta, and P. Wölfle, Rev. Mod. Phys. **79**, 1015 (2007).

[8] R. Bulla, T. A. Costi, and T. Pruschke, Rev. Mod. Phys. **80**, 395 (2008).

[9] E. Gull, A. J. Millis, A. I. Lichtenstein, A. N. Rubtsov, M. Troyer, and P. Werner, Rev. Mod. Phys. **83**, 349 (2011).

[10] L. Yu, Acta Phys. Sin. **21**, 75 (1965).

[11] H. Shiba, Prog. Theor. Phys. **40**, 435 (1968).

[12] A. Rusinov, Sov. Phys. JETP **29**, 1101 (1969).

[13] K. Satori, H. Shiba, O. Sakai, and Y. Shimizu, J. Phys. Soc. Jpn. **61**, 3239 (1992).

[14] J. Bauer, A. Oguri, and A. C. Hewson, J. Phys.: Condens. Matter **19**, 486211 (2007).

[15] E. Prada, P. San-Jose, M. W. A. de Moor, A. Geresdi, E. J. H. Lee, J. Klinovaja, D. Loss, J. Nygård, R. Aguado, and L. P. Kouwenhoven, Nat. Rev. Phys. **2**, 575 (2020).

[16] J. A. Van Dam, Y. V. Nazarov, E. P. Bakkers, S. De Franceschi, and L. P. Kouwenhoven, Nature (London) **442**, 667 (2006).

[17] J.-P. Cleuziou, W. Wernsdorfer, V. Bouchiat, T. Ondarçuhu, and M. Monthioux, Nat. Nanotech. **1**, 53 (2006).

[18] K. Grove-Rasmussen, H. I. Jørgensen, and P. E. Lindelof, New J. Phys. **9**, 124 (2007).

[19] H. I. Jørgensen, T. Novotný, K. Grove-Rasmussen, K. Flensberg, and P. E. Lindelof, Nano Lett. **7**, 2441 (2007).

[20] R. Maurand, T. Meng, E. Bonet, S. Florens, L. Marty, and W. Wernsdorfer, Phys. Rev. X **2**, 011009 (2012).

[21] R. Delagrange, D. J. Luitz, R. Weil, A. Kasumov, V. Meden, H. Bouchiat, and R. Deblock, Phys. Rev. B **91**, 241401(R) (2015).

[22] R. Delagrange, R. Weil, A. Kasumov, M. Ferrier, H. Bouchiat, and R. Deblock, Phys. Rev. B **93**, 195437 (2016).

[23] J. C. Estrada Saldaña, A. Vekris, G. Steffensen, R. Žitko, P. Krogstrup, J. Paaske, K. Grove-Rasmussen, and J. Nygård, Phys. Rev. Lett. **121**, 257701 (2018).

[24] J. C. Estrada Saldaña, R. Žitko, J. P. Cleuziou, E. J. H. Lee, V. Zannier, D. Ercolani, L. Sorba, R. Aguado, and S. De Franceschi, Sci. Adv. **5**, eaav1235 (2019).

[25] V. Meden, J. Phys.: Condens. Matter **31**, 163001 (2019).

[26] R. S. Deacon, Y. Tanaka, A. Oiwa, R. Sakano, K. Yoshida, K. Shibata, K. Hirakawa, and S. Tarucha, Phys. Rev. Lett. **104**, 076805 (2010).

[27] B.-K. Kim, Y.-H. Ahn, J.-J. Kim, M.-S. Choi, M.-H. Bae, K. Kang, J. S. Lim, R. López, and N. Kim, Phys. Rev. Lett. **110**, 076803 (2013).

[28] E. J. Lee, X. Jiang, M. Houzet, R. Aguado, C. M. Lieber, and S. De Franceschi, Nat. Nanotech. **9**, 79 (2014).

[29] A. Jellinggaard, K. Grove-Rasmussen, M. H. Madsen, and J. Nygård, Phys. Rev. B **94**, 064520 (2016).

[30] E. J. H. Lee, X. Jiang, R. Žitko, R. Aguado, C. M. Lieber, and S. De Franceschi, Phys. Rev. B **95**, 180502(R) (2017).

[31] J. Gramich, A. Baumgartner, and C. Schönenberger, Phys. Rev. B **96**, 195418 (2017).

[32] K. Grove-Rasmussen, G. Steffensen, A. Jellinggaard, M. Madsen, R. Žitko, J. Paaske, and J. Nygård, Nat. Commun. **9**, 2376 (2018).

[33] Z. Su, A. B. Tacla, M. Hocevar, D. Car, S. R. Plissard, E. P. Bakkers, A. J. Daley, D. Pekker, and S. M. Frolov, Nat. Commun. **8**, 585 (2017).

[34] J. C. Estrada Saldaña, A. Vekris, V. Sosnovtseva, T. Kanne, P. Krogstrup, K. Grove-Rasmussen, and J. Nygård, Commun. Phys. **3**, 1 (2020).

[35] O. Naaman, W. Teizer, and R. C. Dynes, Phys. Rev. Lett. **87**, 097004 (2001).

[36] J. G. Rodrigo, H. Suderow, and S. Vieira, Eur. Phys. J. B **40**, 483 (2004).

[37] M. T. Randeria, B. E. Feldman, I. K. Drozdov, and A. Yazdani, Phys. Rev. B **93**, 161115(R) (2016).

[38] D. Cho, K. M. Bastiaans, D. Chatzopoulos, G. D. Gu, and M. P. Allan, Nature (London) **571**, 541 (2019).

[39] O. Peters, N. Bogdanoff, S. Acero González, L. Melischek, J. R. Simon, G. Reecht, C. B. Winkelmann, F. von Oppen, and K. J. Franke, Nat. Phys. (2020), doi: 10.1038/s41567-020-0972-z.

[40] X. Liu, Y. X. Chong, R. Sharma, and J. C. S. Davis, arXiv:2007.15228 (2020).

[41] P. Krogstrup, N. Ziino, W. Chang, S. Albrecht, M. Madsen, E. Johnson, J. Nygård, C. Marcus, and T. Jespersen, Nat. Mater. **14**, 400 (2015).

[42] H. I. Jørgensen, K. Grove-Rasmussen, K.-Y. Wang, A. Blackburn, K. Flensberg, P. E. Lindelof, and D. Williams, Nat. Phys. **4**, 536 (2008).

[43] G. Kiršanskas, M. Goldstein, K. Flensberg, L. I. Glazman, and J. Paaske, Phys. Rev. B **92**, 235422 (2015).

[44] S. De Franceschi, L. Kouwenhoven, C. Schönenberger, and W. Wernsdorfer, Nat. Nano. **5**, 703 (2010).

[45] J. P. Pekola, V. F. Maisi, S. Kafanov, N. Chekurov, A. Kemppinen, Yu. A. Pashkin, O.-P. Saira, M. Möttönen, and J. S. Tsai, Phys. Rev. Lett. **105**, 026803 (2010).

[46] Y. M. Ivanchenko and L. A. Zil'berman, Sov. Phys. JETP **28**, 1272 (1969).

[47] I. van Weperen, S. R. Plissard, E. P. A. M. Bakkers, S. M. Frolov, and L. P. Kouwenhoven, Nano Lett. **13**, 387 (2013).

[48] A. Steinbach, P. Joyez, A. Cottet, D. Esteve, M. H. Devoret, M. E. Huber, and J. M. Martinis, Phys. Rev. Lett. **87**, 137003 (2001).

[49] K. G. Wilson, Rev. Mod. Phys. **47**, 773 (1975).

[50] M. Ruby, F. Pientka, Y. Peng, F. von Oppen, B. W. Heinrich, and K. J. Franke, Phys. Rev. Lett. **115**, 087001 (2015).

[51] W. G. van der Wiel, S. De Franceschi, J. M. Elzerman, T. Fujisawa, S. Tarucha, and L. P. Kouwenhoven, Rev. Mod. Phys. **75**, 1 (2002).

[52] J.-D. Pillet, P. Joyez, R. Žitko, and M. F. Goffman, Phys. Rev. B **88**, 045101 (2013).

[53] S. Li, N. Kang, P. Caroff, and H. Q. Xu, Phys. Rev. B **95**, 014515 (2017).

[54] J. Pillet, C. Quay, P. Morfin, C. Bena, A. L. Yeyati, and P. Joyez, Nat. Phys. **6**, 965 (2010).

[55] K. Grove-Rasmussen, H. I. Jørgensen, B. M. Andersen, J. Paaske, T. S. Jespersen, J. Nygård, K. Flensberg, and P. E. Lindelof, Phys. Rev. B **79**, 134518 (2009).

[56] A. Eichler, M. Weiss, S. Oberholzer, C. Schönenberger, A. Levy Yeyati, J. Cuevas, and A. Martín-Rodero, Phys. Rev. Lett. **99**, 126602 (2007).
[57] E. J. H. Lee, X. Jiang, R. Aguado, G. Katsaros, C. M. Lieber, and S. De Franceschi, Phys. Rev. Lett. **109**, 186802 (2012).
[58] J. He, D. Pan, G. Yang, M. Liu, J. Ying, Z. Lyu, J. Fan, X. Jing, G. Liu, B. Lu *et al.*, Phys. Rev. B **102**, 075121 (2020).
[59] J. Gramich, A. Baumgartner, and C. Schönenberger, Phys. Rev. Lett. **115**, 216801 (2015).
[60] A. E. Antipov, A. Bargerbos, G. W. Winkler, B. Bauer, E. Rossi, and R. M. Lutchyn, Phys. Rev. X **8**, 031041 (2018).
[61] Z. Su, A. Zarassi, J. F. Hsu, P. San-Jose, E. Prada, R. Aguado, E. J. H. Lee, S. Gazibegovic, R. L. M. OphetVeld, D. Car *et al.*, Phys. Rev. Lett. **121**, 127705 (2018).
[62] M. Deng, S. Vaitiekėnas, E. B. Hansen, J. Danon, M. Leijnse, K. Flensberg, J. Nygård, P. Krogstrup, and C. M. Marcus, Science **354**, 1557 (2016).
[63] H. Nilsson, P. Samuelsson, P. Caroff, and H. Xu, Nano Lett. **12**, 228 (2011).
[64] A. Villas, R. L. Klees, H. Huang, C. R. Ast, G. Rastelli, W. Belzig, and J. C. Cuevas, Phys. Rev. B **101**, 235445 (2020).
[65] M. Ruby, B. W. Heinrich, Y. Peng, F. von Oppen, and K. J. Franke, Phys. Rev. Lett. **120**, 156803 (2018).
[66] H. Huang, C. Padurariu, J. Senkpiel, R. Drost, A. L. Yeyati, J. C. Cuevas, B. Kubala, J. Ankerhold, K. Kern, and C. R. Ast, Nat. Phys. (2020), doi: 10.1038/s41567-020-0971-0.
[67] A. Kumar, M. Gaim, D. Steininger, A. Levy Yeyati, A. Martín-Rodero, A. K. Hüttel, and C. Strunk, Phys. Rev. B **89**, 075428 (2014).
[68] H. Jeong, A. M. Chang, and M. R. Melloch, Science **293**, 2221 (2001).
[69] J. Bork, Y.-h. Zhang, L. Diekhöner, L. Borda, P. Simon, J. Kroha, P. Wahl, and K. Kern, Nat. Phys. **7**, 901 (2011).
[70] S. J. Chorley, M. R. Galpin, F. W. Jayatilaka, C. G. Smith, D. E. Logan, and M. R. Buitelaar, Phys. Rev. Lett. **109**, 156804 (2012).
[71] A. Spinelli, M. Gerrits, R. Toskovic, B. Bryant, M. Ternes, and A. Otte, Nat. Commun. **6**, 10046 (2015).
[72] A. Chang and J. Chen, Rep. Prog. Phys. **72**, 096501 (2009).
[73] A. Georges and Y. Meir, Phys. Rev. Lett. **82**, 3508 (1999).
[74] M. H. Hamidian, S. D. Edkins, S. H. Joo, A. Kostin, H. Eisaki, S. Uchida, M. J. Lawler, E.-A. Kim, A. P. Mackenzie, K. Fujita *et al.*, Nature (London) **532**, 343 (2016).
[75] S.-H. Ji, T. Zhang, Y.-S. Fu, X. Chen, X.-C. Ma, J. Li, W.-H. Duan, J.-F. Jia, and Q.-K. Xue, Phys. Rev. Lett. **100**, 226801 (2008).
[76] A. Kamlapure, L. Cornils, J. Wiebe, and R. Wiesendanger, Nat. Commun. **9**, 3253 (2018).
[77] D. J. Wineland, Rev. Mod. Phys. **85**, 1103 (2013).
[78] D. P. DiVincenzo, Fortschr. Phys. **48**, 771 (2000).
[79] A. Y. Kitaev, Phys.-Usp. **44**, 131 (2001).
[80] J. D. Sau and S. D. Sarma, Nat. Commun. **3**, 964 (2012).
[81] I. C. Fulga, A. Haim, A. R. Akhmerov, and Y. Oreg, New J. Phys. **15**, 045020 (2013).
[82] V. Mourik, K. Zuo, S. M. Frolov, S. R. Plissard, E. P. a. M. Bakkers, and L. P. Kouwenhoven, Science **336**, 1003 (2012).
[83] S. Nadj-Perge, I. K. Drozdov, J. Li, H. Chen, S. Jeon, J. Seo, A. H. MacDonald, B. A. Bernevig, and A. Yazdani, Science **346**, 602 (2014).
[84] M. Ruby, F. Pientka, Y. Peng, F. von Oppen, B. W. Heinrich, and K. J. Franke, Phys. Rev. Lett. **115**, 197204 (2015).
[85] R. Pawlak, M. Kisiel, J. Klinovaja, T. Meier, S. Kawai, T. Glatzel, D. Loss, and E. Meyer, npj Quantum Inf. **2**, 1 (2016).
[86] A. Grivnin, E. Bor, M. Heiblum, Y. Oreg, and H. Shtrikman, Nat. Commun. **10**, 1 (2019).
[87] S. Manna, P. Wei, Y. Xie, K. T. Law, P. A. Lee, and J. S. Moodera, Proc. Natl. Acad. Sci. U. S. A. **117**, 8775 (2020).
[88] https://doi.org/10.17894/ucph.c83b3677-34ff-4d10-8f5a-36785d1ed59e.
[89] D. Vion, M. Götz, P. Joyez, D. Esteve, and M. H. Devoret, Phys. Rev. Lett. **77**, 3435 (1996).
[90] H. Grabert, G.-L. Ingold, and B. Paul, Europhys. Lett. **44**, 360 (1998).
[91] H. Grabert and G.-L. Ingold, Superlattices Microstruct. **25**, 915 (1999).
[92] P. Joyez, Phys. Rev. Lett. **110**, 217003 (2013).

7

NON-EQUILIBRIUM THEORY FOR SUPERCONDUCTING JUNCTIONS

Moving on from zero-bias supercurrent presented in the preceding chapters, we now seek to tackle finite bias measurements of YSR states in S-DQD-S junctions similar to data shown in section 2.4. In this limit, the phase difference ϕ does not localize, as in the Ex-RCSJ model of chapter 3, but winds continually with a constant velocity determined by the applied bias, similar to the resistive branch of supercurrent. To handle this situation we require heavy-duty non-equilibrium theory of which we choose the Keldysh Floquet Green's functions approach, represented in 4×4 Nambu space to include superconductivity. Although the study of these techniques are commonplace (see e.g. Refs [146–148]), we, in this chapter, show how they can be simultaneously implemented to obtain a theory able to include transport to all orders of tunnelling between two voltage-biased superconductors. The results of this chapter, in conjunction with results of chapter 8, is used in chapter 9, and was originally derived in the corresponding supplement.

As a starting point consider the BCS Hamiltonian of a single superconductor,

$$H_0 = \sum_{k\sigma} \epsilon_k c^\dagger_{k\sigma} c_{k\sigma} + \sum_k \left[\Delta c^\dagger_{k\uparrow} c^\dagger_{-k\downarrow} + \Delta^* c_{-k\downarrow} c_{k\uparrow} \right], \tag{7.1}$$

where we assumed that the gap is k independent $\Delta_k = \Delta$ and possibly includes a static phase component $\Delta = |\Delta| e^{i\phi}$. The groundstate energy, in this Hamiltonian, is referenced around the Fermi surface of the given material. If this energy is displaced by a component μ from the Fermi surface, the Hamiltonian is modified to,

$$H_\mu(t) = \sum_{k\sigma} (\epsilon_k - \mu) c^\dagger_{k\sigma} c_{k\sigma} + \sum_k \left[\Delta(t) c^\dagger_{k\uparrow} c^\dagger_{-k\downarrow} + \Delta(t)^* c_{-k\downarrow} c_{k\uparrow} \right], \tag{7.2}$$

where the time dependence of the gap $\Delta(t) = |\Delta(t)| \exp[2i\mu t/\hbar + i\phi]$ stems from the displacement to a new reference μ, for which a cooper-pair have energy 2μ, instead of 0, yielding the trivial time evolution of $\Delta(t)$. Next, we expand the system to include two superconductors, denoted left and right, which we assume to have equal gaps $|\Delta_L| = |\Delta_R| = \Delta$, and are coupled by a single channel tunnel junction. Across this

junction we additionally enforce a voltage bias $eV = \mu_L - \mu_R$, yielding the following system Hamiltonian,

$$H(t) = H_{L\mu_L}(t) + H_{R\mu_R}(t) + H_T \tag{7.3}$$

$$H_{j\mu_j}(t) = \sum_{k\sigma} \left(\epsilon_k - \mu_j\right) c^\dagger_{jk\sigma} c_{jk\sigma} + \sum_k \left[|\Delta| e^{2i\mu_j t/\hbar + i\phi_j} c^\dagger_{jk\uparrow} c^\dagger_{j-k\downarrow} + \text{h. c.}\right] \tag{7.4}$$

$$H_T = t_d \sum_\sigma c^\dagger_{L\sigma} c_{R\sigma} + \text{h. c.} \tag{7.5}$$

where we defined local operators of the junction as $c_{j\sigma} = \sum_k c_{jk\sigma}$ corresponding to real-space coordinate $r = 0$, and with tunnel coupling t_d assumed to be real. Transport in such a junction is characterized by the presence of Multiple Andreev Reflections (MAR) [117] the structure of which was theoretically described for single channels [149, 150], and subsequently measured in atomic-size contacts [151, 152]. To obtain a complete description capturing the effects of MAR we follow the same procedure as Ref. [150] starting from the gauge transformation $U(t) = U_L(t)U_R(t)$ consisting of components,

$$U_j(t) = \exp\left[i\mu_j t N_j/\hbar + i\phi_j/2\right], \tag{7.6}$$

with $N_j = \sum_{\sigma k} c^\dagger_{jk\sigma} c_{jk\sigma}$. This unitary transformations satisfies,

$$U^\dagger(t) c_{jk\sigma} U(t) = e^{i\mu_j t/\hbar} c_{jk\sigma} \tag{7.7}$$

$$U^\dagger(t) c^\dagger_{jk\sigma} U(t) = e^{-i\mu_j t/\hbar} c^\dagger_{jk\sigma} \tag{7.8}$$

which follows from the Baker-Cambell-Hausdorff theorem. We now define a shifted state $\bar{\psi}(t) = U^\dagger(t)\psi(t)$ and seek its corresponding Schrödinger equation,

$$i\hbar\partial_t \psi(t) = H(t)\psi(t) \quad \Rightarrow \quad i\hbar\partial_t \bar{\psi}(t) = \left(U(t)^\dagger H(t) U(t) + \mu_L N_L + \mu_R N_R\right) \bar{\psi}(t). \tag{7.9}$$

In this gauge transformed basis, which corresponds to a shift of the trivial time evolution by μ_j in the interaction picture, we define the effective Hamiltonian as $\bar{H}(t) = U^\dagger(t) H(t) U(t) + \mu_L N_L + \mu_R N_R$,

$$\bar{H}(t) = \bar{H}_{L0} + \bar{H}_{R0} + \bar{H}_T(t) \tag{7.10}$$

$$\bar{H}_j = \sum_{k\sigma} \epsilon_k c^\dagger_{jk\sigma} c_{jk\sigma} + \sum_k \left[|\Delta| c^\dagger_{jk\uparrow} c^\dagger_{j-k\downarrow} + \text{h. c.}\right] \tag{7.11}$$

$$\bar{H}_T(t) = t_d e^{-ieVt/\hbar - i\phi_0/2} \sum_\sigma c^\dagger_{L\sigma} c_{R\sigma} + \text{h. c.} \tag{7.12}$$

with $\phi_0 = \phi_L - \phi_R$ denoting the static phase difference. In this gauge the left and right subsystems have become time-independent, with the tunnel element $\bar{H}_T(t)$ now

capturing the full time-dependence. At this stage, it is clear that time dependence cannot be fully gauged away, but is an inherent feature of the system. This may appear surprising as we have only enforced a time-independent voltage bias across the junction. Looking back at its origin we see that the time dependence stems from the unequal trivial time-evolution of the two BCS mean-fields. This highlights the highly coherent nature of the BCS groundstate, with cooper-pairs collectively oscillating with a frequency set by the Fermi-energy. Consequently, a mismatch of the two Fermi-energies, as in the case of a applied voltage bias, results in two out of sync oscillations, the drift of which is determined by the applied bias eV.

In deriving Green's functions from a superconducting Hamiltonian, one is forced to include anomalous components of the form $\langle c_{\uparrow}^{\dagger} c_{\downarrow}^{\dagger} \rangle$, which are non-zero due to the presence of the BCS mean-field Δ coupling particles and holes. A convenient trick is to use Nambu-Gorkov formalism which keep tab on anomalous terms through matrix structure, allowing one to write equations of motion and solve Dyson equations in a conventional manner. We start by defining a spinor,

$$\Psi_{jk}^{\dagger} = \begin{pmatrix} c_{jk\uparrow}^{\dagger} & c_{j-k\downarrow} & c_{j-k\downarrow}^{\dagger} & -c_{jk\uparrow} \end{pmatrix}. \tag{7.13}$$

Here a 4×4 space is chosen instead of a simpler 2×2 representation, as we later wish to include spin-dependent terms in our Hamiltonians. For this spinor the entrances (1,3) are in particle space and (2,4) in hole space, while (1,2) are in spin-up space and (3,4) in spin-down space. In this basis we can express the Hamiltonian eq. (7.10) as,

$$\bar{H}(t) = \frac{1}{2} \sum_{k} \sum_{j=L,R} \Psi_{jk}^{\dagger} h_{jj,k} \Psi_{jk} + \frac{1}{2} \Psi_{L}^{\dagger} h_{LR}(t) \Psi_{R} + \frac{1}{2} \Psi_{R}^{\dagger} h_{RL}(t) \Psi_{L} \tag{7.14}$$

$$h_{jj,k} = \epsilon_k \tau_z + |\Delta| \tau_x, \tag{7.15}$$

$$h_{LR}(t) = t_d \tau_z e^{-ieVt\tau_z/\hbar - i\phi_0 \tau_z} = h_{RL}^{\dagger}(t) \tag{7.16}$$

resembling the quadratic form of non-interacting electrons. The local spinor is defined as $\psi_j = \sum_k \psi_{jk}$, and τ_i matrices are defined in the particle-hole subspace, while σ_i are in the spin subspace conveniently expressed with assumed tensor products, e.g. $\tau_x = \sigma_0 \otimes \tau_x$ and $\sigma_y \tau_x = \sigma_y \otimes \tau_x$. To illustrate; $\tau_z = \mathrm{diag}\,(1,-1,1,-1)$ and $\sigma_z = \mathrm{diag}\,(1,1,-1,-1)$. In the following we use Green's functions to derive transport equations for Hamiltonians in the general form of eq. (7.14), keeping the same $h_{LR}(t)$ which describes a single tunnelling channel, but for variable time-independent h_{LL} and h_{RR} in preparation for the later inclusion of subgap states. At the end of the derivation we return to the specific example of a superconducting junction with h_{jj} given by eq. (7.15) as an illustrative example.

We define the current operator as the change of electrons on the left lead due to tunnel coupling H_T,

$$I(t) = e\dot{n}_L(t) = \frac{ie}{\hbar}\sum_\sigma \left[H_T, c^\dagger_{L\sigma}(t)c_{L\sigma}(t)\right] \tag{7.17}$$

$$= \frac{ie}{\hbar}\sum_\sigma t_d\left(c^\dagger_{L\sigma}(t)c_{R\sigma}(t) - c^\dagger_{R\sigma}(t)c_{L\sigma}(t)\right) \tag{7.18}$$

with $n_L(t) = \sum_\sigma c^\dagger_{L\sigma}(t)c_{L\sigma}(t)$ denoting local occupation. Performing the ensemble average we find,

$$\langle I(t)\rangle = \frac{ie}{\hbar}\sum_\sigma t_d\left(\langle c^\dagger_{L\sigma}(t)c_{R\sigma}(t)\rangle - \langle c^\dagger_{R\sigma}(t)c_{L\sigma}(t)\rangle\right) \tag{7.19}$$

$$= \frac{ie}{\hbar}\sum_\sigma t_d\left(f(t)\langle c^\dagger_{L\sigma}(t)c_{R\sigma}(t)\rangle_{\bar{H}} - f(t)^*\langle c^\dagger_{R\sigma}(t)c_{L\sigma}(t)\rangle_{\bar{H}}\right),$$

with $f(t) = \exp[-ieVt - i\phi_0]$ and $\langle A\rangle_{\bar{H}}$ indicating that the ensemble average should be taken in regard to the gauge transformed Hamiltonian $H(\bar{t})$. This gauge transformation is simply performed by insertion of identities,

$$\langle c^\dagger_{L\sigma}(t)c_{R\sigma}(t)\rangle = \langle U(t)U^\dagger(t)c^\dagger_{L\sigma}(t)U(t)U^\dagger(t)c_{R\sigma}(t)U(t)U^\dagger(t)\rangle \tag{7.20}$$

$$= f(t)\langle c^\dagger_{L\sigma}(t)c_{R\sigma}(t)\rangle_{\bar{H}}. \tag{7.21}$$

Next, it is convenient to define the 4×4 Nambu lesser Green's function as an outer product of spinors,

$$G^<_{jl,nm}(t,t') = i\langle\Psi^\dagger_{l,m}(t')\Psi_{j,n}(t)\rangle_{\bar{H}} \tag{7.22}$$

here $j,l \in \{L,R\}$ and nm denote entrances in the 4×4 Nambu space. By introduction of a trace eq. (7.19) can be rewritten as,

$$\langle I(t)\rangle = \frac{e}{2\hbar}\,\mathrm{Tr}\left[\tau_z h_{LR}(t)G^<_{RL}(t,t) - \tau_z h_{RL}(t)G^<_{LR}\right] \tag{7.23}$$

$$= \frac{e}{\hbar}\,\mathrm{Tr}\,\mathrm{Re}\left[\tau_z h_{LR}(t)G^<_{RL}(t,t)\right] \tag{7.24}$$

where we in the second line used the property $G^<_{LR,jj}(t,t) = -\left[G^<_{RL,jj}(t,t)\right]^*$. In the following, our goal is to express the cross index dressed lesser Green's function $G^<_{RL}(t,t)$ in terms of uncoupled Green's functions of the left and right subsystem. This can be achieved by use of Keldysh Green's function which for time-dependent non-interacting Hamiltonians, meaning of the form $H(t) = \frac{1}{2}\sum_{ab}\Psi^\dagger_a h_{ab}(t)\Psi_b$, allows us to derive closed equations of motion for dressed Green's functions. Through Langreth rules [146] the dressed lesser component can be expressed in terms of bare retarded,

advanced and lesser Green's functions. Derivation of these relations are shown in Appendix C.

Assuming that the Hamiltonian of the left and right subsystem is non-interacting the cross index Keldysh component is given by $G_{RL}(t,t') = \int_C dt' g_R(t,t') h_{RL}(t') G_{LL}(t',t)$, and by using Langreth rules we find,

$$G^<_{RL}(t,t) = \int_{-\infty}^{\infty} dt' \left(g^<_R(t,t') h_{RL}(t') G^A_{LL}(t',t) + g^R_R(t,t') h_{RL}(t') G^<_{LL}(t',t) \right). \tag{7.25}$$

Defining the left self-energy as,

$$\Sigma^X_{LL}(t,t') = h_{LR}(t) g^X_R(t,t') h_{RL}(t'), \tag{7.26}$$

for $X \in \{R, A, <\}$ we can express the central element in eq. (7.24) as,

$$h_{LR}(t) G^<_{RL}(t,t) = \Sigma^<_{LL} \circ G^A_{LL}(t,t) + \Sigma^R_{LL} \circ G^<_{LL}(t,t), \tag{7.27}$$

utilizing time matrix structure $A \circ B(t,t') = \int_{-\infty}^{\infty} dt'' A(t,t'') B(t'',t')$, with unity $I = \delta(t,t')$. Using Langreth, yet again, we can express the various same index dressed Green's function as,

$$\begin{aligned}
G^R_{LL}(t,t') &= g^R_L(t,t') + g^R_L \circ \Sigma^R_{LL} \circ G^R_{LL}(t,t'), \\
G^A_{LL}(t,t') &= \left[G^R_{LL}(t,t') \right]^\dagger, \\
G^<_{LL}(t,t') &= \left(I + G^R_{LL} \circ \Sigma^R_{LL} \right) \circ g^<_L \circ \left(I + \Sigma^A_{LL} \circ G^A_{LL} \right)(t,t') + G^R_{LL} \circ \Sigma^<_{LL} \circ G^A_{LL}(t,t').
\end{aligned} \tag{7.28}$$

Putting this together the central element can be rewritten as,

$$h_{LR}(t) G^<_{LR}(t,t) = M^R \circ \left(\Sigma^<_{LL} \circ g^A_L + \Sigma^R_{LL} \circ g^<_L \right) \circ M^A(t,t), \tag{7.29}$$

with the matrix M defined as,

$$\begin{aligned}
M^X(t,t') &= I + \Sigma^X_{LL} \circ G^X_{LL}(t,t') \\
&= I + \Sigma^X_{LL} \circ g^X_L \circ M^X(t,t')
\end{aligned} \tag{7.30}$$

for $X \in \{A, R\}$. Inserting this result back into eq. (7.24) we obtain the following closed expression for current,

$$\langle I(t) \rangle = \frac{e}{\hbar} \operatorname{Tr} \operatorname{Re} \left[\tau_z M^R \circ \left(\Sigma^<_{LL} \circ g^A_L + \Sigma^R_{LL} \circ g^<_L \right) \circ M^A(t,t) \right] \tag{7.31}$$

This equation is fully determined by the bare left and right Green's functions, coupling $h_{LR}(t)$, and initial occupation ρ_0 required as a boundary condition to compute time-evolution. In the next section, we investigate a specific choice of boundary condition, which is periodic in eV, yielding solutions that can be neatly expressed in Floquet space.

7.1 FLOQUET SPACE

In the previous section we succeeded in describing the current through simple elements in eq. (7.31), but the complicated time structure involving iterative time convolutions in $M^X(t,t')$ remain. Fortunately, the time dependence is of a particular simple form, namely it is periodic with period $T = 2\pi\hbar/eV$, which allows us to describe it via Floquet theory. The main statement of Floquet theory is that a time-dependent periodic Hamiltonian $H(t) = H(t+T)$ has solutions of the form,

$$i\partial_t |\psi(t)\rangle = H(t)|\psi(t)\rangle \quad \Rightarrow \quad |\psi_a(t)\rangle = e^{-i\epsilon_a t/\hbar}|u_a(t)\rangle\,, \tag{7.32}$$

where $|u_a(t)\rangle = |u_a(t+T)\rangle$ is also periodic. This statement amounts to Bloch's theorem for systems periodic in time, instead of real space. The energy ϵ_a is known as the quasi-energy and substitutes k in Bloch's theorem. If this driven system is additionally coupled to a thermal bath, as is the case of most realistic setups, then in the long time limit, transients due to initial occupation ρ_0 will die-off and the system will end in a time-periodic non-equilibrium steady state (NESS) [148], where energy pumped in by periodic driving eV, balances with energy loss to bath dissipation. This steady state will be composed of Floquet solutions, such that the ensemble average $\langle A(t)\rangle = \langle\psi_S(t_0)|\,A(t)\,|\psi_S(t_0)\rangle$ is taken with regards to a periodic steady state $|\psi_S(t)\rangle = |\psi_S(t+T)\rangle$ here initialized at t_0. Accordingly, as the Green's functions time evolution is solely defined by the time-evolution operator $U(t+T,t'+T) = U(t,t')$ and initial state $|\psi_S(t)\rangle$, which are both periodic, they themself are periodic,

$$G^X(t+T,t'+T) = G^X(t,t') \tag{7.33}$$

with $X \in \{R, A, <\}$. This equation, if taken as a condition, can also be used to define NESS [148]. Although this requirement appears abstract, and theoretically hard to prove for a general case, it, in a classical analogue, amounts to the phenomenon of synchronization, where e.g. a metronome coupled to a periodic drive at time t_0, hones in to the driving frequency through complicated initial transients on a timescale set by dissipation.

Taking NESS as a boundary condition it is convenient to introduce the following Fourier transformations,

$$G^X(t,\omega) = \int_{-\infty}^{\infty} dt' e^{i\omega(t-t')} G^X(t,t') \tag{7.34}$$

$$G^X_n(\omega) = \frac{1}{T}\int_0^T dt e^{ineVt/\hbar} G^X(t,\omega), \tag{7.35}$$

which in essence constitutes a Fourier transform over time-separation $t - t'$ and a discrete Fourier series over the total time $(t + t')/2$ which is periodic in T. The reverse transforms are given by,

$$G^X(t, t') = \frac{1}{2\pi} \int_{\infty}^{\infty} d\omega e^{-i\omega(t-t')} G^X(t, \omega), \tag{7.36}$$

$$G^X(t, \omega) = \sum_{n=-\infty}^{\infty} e^{-ineVt/\hbar} G^X_n(\omega). \tag{7.37}$$

Lastly, one extends the above formalism to include another index m through the definition,

$$G^X_{nm}(\omega) = G^X_{n-m}(\omega + meV) \tag{7.38}$$

which may appear arbitrary, but fulfils the important property that time convolution transforms into matrix multiplication in Floquet space,

$$C(t, t') = A \circ B(t, t') \tag{7.39}$$

$$\Rightarrow \quad C_{nm}(\omega) = \sum_{n'=-\infty}^{\infty} A_{nn'}(\omega) B_{n'm}(\omega) \tag{7.40}$$

which can be readily verified by performing the transformations. With this machinery in place, we now return to transport. If all Green's functions are periodic in T then $\langle I(t) \rangle$, whose time dependence is solely due to Green's functions and couplings $h_{LR}(t)$, is also periodic $\langle I(t + T) \rangle = \langle I(t) \rangle$ and can be expressed via a Fourier decomposition $\langle I_n \rangle = \frac{1}{T} \int_0^T dt e^{ineVt/\hbar} \langle I(t) \rangle$. Transforming eq. (7.31), and exploiting eq. (7.40) multiple times, we find,

$$\langle I_n \rangle = \frac{e}{h} \int_{-\infty}^{\infty} d\omega \, \mathrm{Tr} \, \mathrm{Re} \left[\tau_z \underline{M}^R(\omega) \left(\underline{\Sigma}^<_{LL}(\omega) \underline{g}^A_L(\omega) + \underline{\Sigma}^R_{LL}(\omega) \underline{g}^<_L(\omega) \right) \underline{M}^A(\omega) \right]_{n0} \tag{7.41}$$

where underline denotes matrices in Floquet space with implicit matrix multiplication assumed $[\underline{A}(\omega)\underline{B}(\omega)]_{nm} = \sum_l A_{nl}(\omega) B_{lm}(\omega)$. In experiment, current is measured by averaging over many periods T, and correspondingly we are only interested in the DC component,

$$\langle I_0 \rangle = \frac{e}{h} \int_{-\infty}^{\infty} d\omega \, \mathrm{Tr} \, \mathrm{Re} \left[\tau_z \underline{M}^R(\omega) \left(\underline{\Sigma}^<_{LL}(\omega) \underline{g}^A_L(\omega) + \underline{\Sigma}^R_{LL}(\omega) \underline{g}^<_L(\omega) \right) \underline{M}^A(\omega) \right]_{00} \tag{7.42}$$

Now that we have a closed expression for the DC current, fully specified by $\underline{g}^X_L(\omega)$ and $\underline{\Sigma}^X_{LL}(\omega)$ for $X \in \{R, A, <\}$, let us consider the matrix structure of these components in greater detail. The bare left and right lead Green's function, defined by the uncoupled

Hamiltonian which is time-independent, depends only on time difference $g_j^X(t,t') = g_j^X(t-t')$. Consequently, it has no higher Floquet components,

$$g_{j,n}^X(\omega) = \frac{1}{T}\int_0^T dt e^{ineVt/\hbar} g_j^X(t,\omega) = g_{j,0}^X(\omega)\delta_{n,0}, \tag{7.43}$$

with $j \in \{L,R\}$ and the second index 0 denoting the discrete Floquet index. Rewriting this into the Floquet matrix structure, using eq. (7.38),

$$g_{j,nm}^X(\omega) = g_{j,0}^X(\omega + neV)\delta_{nm}, \tag{7.44}$$

which is recognized as a diagonal matrix in Floquet space, but with each entrance still representing a 4×4 Nambu matrix. The tunnel coupling $h_{LR}(t)$, which can be expressed as $h_{LR}(t,t') = h_{LR}(t')\delta(t-t')$, is an example of the opposite case; it depends on total time $(t+t')/2$, but is diagonal in time difference. It is therefore frequency independent, but not diagonal in Floquet space,

$$h_{LR,n} = \frac{1}{T}\int_0^T dt h_{LR}(t)e^{ineVt/\hbar} = t_d\tau_z\frac{1}{T}\int_0^T dt e^{i(n-\tau_z)eVt/\hbar} = t_d\tau_z\delta_{n,\tau_z}, \tag{7.45}$$

$$h_{LR,nm} = t_d\tau_z\delta_{n,m+\tau_z}, \qquad \text{and} \qquad h_{RL,nm} = t_d\tau_z\delta_{n,m-\tau_z}. \tag{7.46}$$

In these equation we have put the static phase component to zero $\phi_0 = 0$, as any initial phase becomes unimportant in the long time limit. From the structure of $h_{LR,nm}$, we see that the Floquet space has becomes coupled to Nambu space through the delta function $\delta_{n,m+\tau_z}$, which moves the electron subspace one index down in Floquet space (as $\tau_{z,11} = 1$), but moves the hole supspace one index up. Utilizing these relations, we can express the self-energy as a block-diagonal matrix,

$$\begin{aligned}\underline{\Sigma}_{LL,nm}^X(\omega) &= \sum_{n'n''} h_{LR,nn'} g_{R,n'n''}^X(\omega) h_{RL,n''m} \\ &= \begin{pmatrix} \delta_{n,m}t_d^2 g_{R,(11)}^X(\omega+(n-1)eV) & -\delta_{n,m+2}t_d^2 g_{R,(12)}^X(\omega+(n-1)eV) \\ -\delta_{n,m-2}t_d^2 g_{R,(21)}^X(\omega+(n+1)eV) & \delta_{n,m}t_d^2 g_{R,(22)}^X(\omega+(n+1)eV)\end{pmatrix},\end{aligned} \tag{7.47}$$

where the entries refers to particle-hole component, such that $g_{R,(ij)}^X(\omega)$ is a 2×2 matrix in spin-space, with (ij) indicating particle-hole entry in the original 4×4 Nambu space. Returning to eq. (7.42), we find that all off-diagonal Floquet entrances are due to either self-energies $\underline{\Sigma}_{LL}^X(\omega)$, or higher order $\underline{M}(\omega)$ terms. Since all off-diagonal Floquet components in $\underline{M}(\omega)$ also stems from $\underline{\Sigma}_{LL}^x(\omega)$, which only couples even subspaces to even and odd to odd, seen from eq. (7.47), in addition to the initial and final index of the DC current being 0, we find that only even subspaces contribute, and we disregard

the odd subspace entirely. Embedding Nambu into the even-Floquet matrix structure, the self-energy can be visualized as,

$$\underline{\Sigma}^{X}_{LL}(\omega) = t_d^2 \times \tag{7.48}$$

$$\begin{pmatrix}
\ddots & \ddots & & & & & & \\
\ddots & g^{X}_{R,(11)}(\omega_{-3}) & 0 & 0 & 0 & 0 & 0 & \\
 & 0 & g^{X}_{R,(22)}(\omega_{-1}) & -g^{X}_{R,(21)}(\omega_{-1}) & 0 & 0 & 0 & \\
 & 0 & -g^{X}_{R,(12)}(\omega_{-1}) & g^{X}_{R,(11)}(\omega_{-1}) & 0 & 0 & 0 & \\
 & 0 & 0 & 0 & g^{X}_{R,(22)}(\omega_{1}) & -g^{X}_{R,(21)}(\omega_{1}) & 0 & \\
 & 0 & 0 & 0 & -g^{X}_{R,(12)}(\omega_{1}) & g^{X}_{R,(11)}(\omega_{1}) & 0 & \\
 & 0 & 0 & 0 & 0 & 0 & g^{X}_{R,(22)}(\omega_{3}) & \ddots \\
 & & & & & & \ddots & \ddots
\end{pmatrix}$$

with arguments $\omega_n = \omega + neV$. The depicted matrix is centred at Floquet index $nm = 00$, with the neighbouring spaces $nm = 22$ and $nm = -2-2$ in the bottom right and top left. Moreover, the bare left Green's function, which is diagonal in Floquet, can be represented as,

$$\underline{g}^{X}_{L}(\omega) = \tag{7.49}$$

$$\begin{pmatrix}
\ddots & \ddots & & & & & & \\
\ddots & g^{X}_{L,(11)}(\omega_{-2}) & g^{X}_{L,(12)}(\omega_{-2}) & 0 & 0 & 0 & 0 & \\
 & g^{X}_{L,(21)}(\omega_{-2}) & g^{X}_{L,(22)}(\omega_{-2}) & 0 & 0 & 0 & 0 & \\
 & 0 & 0 & g^{X}_{L,(11)}(\omega_{0}) & g^{X}_{L,(12)}(\omega_{0}) & 0 & 0 & \\
 & 0 & 0 & g^{X}_{L,(21)}(\omega_{0}) & g^{X}_{L,(22)}(\omega_{0}) & 0 & 0 & \\
 & 0 & 0 & 0 & 0 & g^{X}_{L,(11)}(\omega_{2}) & g^{X}_{L,(12)}(\omega_{2}) & \\
 & 0 & 0 & 0 & 0 & g^{X}_{L,(21)}(\omega_{2}) & g^{X}_{L,(22)}(\omega_{2}) & \ddots \\
 & & & & & & \ddots & \ddots
\end{pmatrix}$$

By themselves, both of these matrices are block diagonal leaving different Floquet sectors uncoupled, but multiplied together they form a tridiagonal ladder matrix, connecting each 4×4 Nambu block to its neighbour in Floquet space. Returning to the DC current in eq. (7.42), one sees that each $\underline{\Sigma}_{LL}(\omega)\underline{g}_{L}(\omega)$ term pulls one up or down a single step on the Floquet ladder, and since the full equation both starts and ends in index 0, one has to come both up and down the same number of steps. Correspondingly, the upper and lowermost levels of the Floquet space, only influence the DC current if coupling t_d^2 is large compared to the inverse energy scales $g_L(\omega)$ and $g_R(\omega)$. This fact allows us to construct a numerical algorithm in which we truncate

the Floquet matrix space on either side, $n, m \in \{-l, l\}$ with l denoting the number of even levels included, and for a given parameter set choose l large enough to achieve convergence. In this manner, the $\underline{M}^R(\omega)$ matrix can be obtained from iterative matrix multiplication,

$$\underline{M}^R(\omega) = 1 + \underline{\Sigma}^R_{LL}(\omega)\underline{g}^R_L(\omega) + \underline{\Sigma}^R_{LL}(\omega)\underline{g}^R_L(\omega)\underline{\Sigma}^R_{LL}(\omega)\underline{g}^R_L(\omega) + \ldots, \tag{7.50}$$

up to the kept order of t_d^2, but a more direct method is to solve the corresponding Dyson equation in Floquet space,

$$\underline{M}^R(\omega) = \left[I - \underline{\Sigma}^R_{LL}(\omega)\underline{g}^R_L(\omega)\right]^{-1}, \tag{7.51}$$

which is done numerically, as the righthand side is a $4l \times 4l$ matrix. This also has the added benefit of keeping all orders of t_d^2 for the included Floquet levels. In the special case of t_d^2 small enough that $\underline{M}^{R/A} \approx 1$, the full DC current is given by,

$$\langle I_0 \rangle = \frac{e}{h}\int_{-\infty}^{\infty} d\omega \, \mathrm{Tr}\, \mathrm{Re}\left[\tau_z \underline{\Sigma}^R_{LL}(\omega)\underline{g}^<_L(\omega) + \tau_z \underline{\Sigma}^<_{LL}(\omega)\underline{g}^A_L(\omega)\right]_{00} \tag{7.52}$$

and since the inner matrix can only take you one step up or down, the only contribution is the 00 Floquet component of each element. Additionally, as the self-energies anomalous components have been displaced away from the 00 Floquet component, only the diagonal elements in particle-hole space contributes to the trace. Finally, we assume that each side initially is in thermal equilibrium at temperature T, such that the fluctuation-dissipation theorem is upheld $g^<_j(\omega) = iA_j(\omega)n_F(\omega)$ [18, 147]. Here $A_j(\omega) = -2\,\mathrm{Im}\left[g^R_j(\omega)\right]$ is the spectral function and $n_F(\omega)$ the Fermi distribution. This yields,

$$\begin{aligned}\langle I_0 \rangle = \frac{et_d^2}{2h}\int_{\infty}^{\infty} d\omega \, \mathrm{Tr}_\sigma \big[&A_{R,(11)}(\omega - eV)A_{L,(11)}(\omega)\left(n_F(\omega) - n_F(\omega - eV)\right) \\ &- A_{R,(22)}(\omega + eV)A_{L,(22)}(\omega)\left(n_F(\omega) - n_F(\omega + eV)\right)\big],\end{aligned} \tag{7.53}$$

with trace over 2×2 spin-space. This expression is recognized as the standard Fermi's golden rule result for lowest order transport [18]. This amounts to one leads spectral function convoluted by the other over a frequency window determined by the Fermi functions and eV. Understood in this manner, higher orders of $\underline{\Sigma}_{LL}(\omega)\underline{g}_L(\omega)$ appearing in $\underline{M}^X(\omega)$ dress the results of Fermi's golden rule, given by the central matrix element in eq. (7.42). In higher order contributions, where off-diagonal elements in $\underline{M}^X(\omega)$ shift the central matrix up or down by n steps in Floquet space corresponding to,

$$M^R_{0n}\left(\underline{\Sigma}^<_{LL}(\omega)\underline{g}^A_L(\omega) + \underline{\Sigma}^R_{LL}(\omega)\underline{g}^<_L(\omega)\right)_{nn} M^R_{n0}, \tag{7.54}$$

the central element resembles Fermi's golden rule with a shifted frequency window $\omega \to \omega + 2neV$ due to eq. (7.44). Consequently, if the Floquet space is truncated then only frequencies in a finite window D contribute to the DC current in eq. (7.42). In numerics the DC current is then given by,

$$\langle I_0 \rangle = \frac{e}{h} \int_{-D}^{D} d\omega \, \mathrm{Tr} \, \mathrm{Re} \left[\tau_z \underline{M}^R(\omega) \left(\underline{\Sigma}^<_{LL}(\omega) \underline{g}^A_L(\omega) + \underline{\Sigma}^R_{LL}(\omega) \underline{g}^<_L(\omega) \right) \underline{M}^A(\omega) \right]_{00} \tag{7.55}$$

where both D and Floquet space, characterized by l, is truncated. If one increases l then D should be sufficiently increased as well. Next, we discuss our numerical approach to solve this equation. For a given bias eV, the frequency integral in eq. (7.55) is discretized, and for each $d\omega$ step one has to perform a single inversion of the $4l \times 4l$ matrix $\underline{M}^R(\omega)$, with the advanced component given by $\underline{M}^A(\omega) = \left[\underline{M}^R(\omega)\right]^\dagger$, followed by two matrix multiplications with the central element. Convergence is then checked by comparing the result to increased l and D. In this algorithm, the runtime is mainly determined by two factors: (1) The required coarse graining of frequency integrals, which for peaked spectral functions, e.g. the BCS spectra, must be sufficiently fine to accurately capture the peaks. (2) The utilized matrix inversion algorithm, and correspondingly the size of l, which is by far the most costly operation for each $d\omega$ step.

Results presented in this thesis are run either on Cython [153] in a Jupyter landscape, or in C++ with matrix inversion performed by LAPACK algorithms. Even at this level run time was a limitation and further optimization can probably be done *.

This concludes our investigation into the general structure of transport between two superconducting leads, and in the following we return to the specific example of two BCS leads.

7.2 SUPERCONDUCTING JUNCTION

We now return to the Hamiltonian which motivated this whole study, namely eq. (7.14) with BCS superconductors as the left and right leads with equal gaps $\Delta = \Delta_L = \Delta_R$. This model is investigated in Ref. [150] in relation to quantum point contacts (QPC), and calculations presented here are simply to illustrate our ability to correctly capture

* Notice that in the matrix structure of eq. (7.55) only the $0n$ or $n0$ elements of $\underline{M}^X(\omega)$ are required. There exist algorithms able to obtain these elements from block tridiagonal matrices in a faster manner then full matrix inversion, but the author could not find a callable version applicable to C++. Not daring the hubris of trying to write something as efficient as LAPACK algorithms myself, the choice was made to stay with the sub-optimal LAPACK full matrix inversion

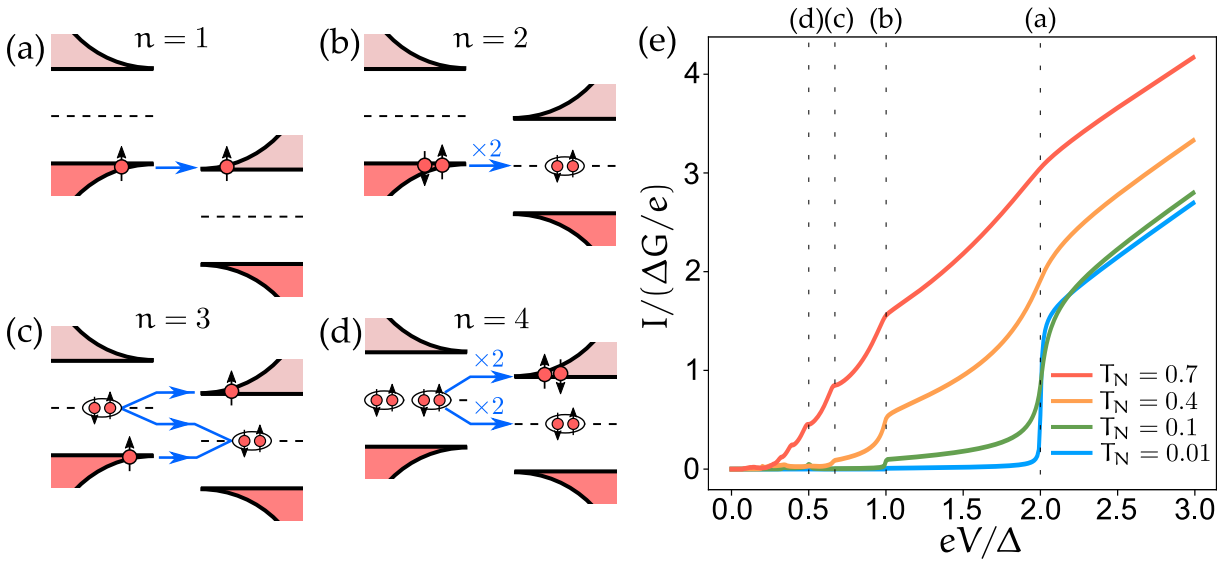

Figure 7.1: (a-d) Sketch of MAR DC current channels at $eV = 2\Delta/n$ for $n = 1, 2, 3, 4$ respectively. Each depiction is in the electron picture with holes depicted as filled electron states. n both represents the $eV = 2\Delta/n$ fraction at which the process contributes, and the number of electrons which coherently cross the junction together in a single event. (e) DC current is calculated using eq. (7.55) with $T = 0$ and $\eta_L = \eta_R = 0.001\Delta$ for four different channel transparencies T_N. Here $G = e^2 T_N/\pi\hbar$ is the normal state conductance of a single channel. For $T_N = 0.01, 0.1, 0.4$ we used $l = 1$ while for $T_N = 0.7$ size $l = 3$ was required. This plot can be compared to fig. 2 of Ref.[149] and Ref.[150].

transport by MAR. The local (momentum summed) bare BCS Green's functions is given by,

$$g_j^R(\omega) = -\pi\nu_j \frac{(\omega + i\eta_j) + \Delta\tau_x}{\sqrt{\Delta^2 - (\omega + i\eta_j)^2}}, \tag{7.56}$$

$$g_j^R(\omega) = \left[g_j^R(\omega)\right]^\dagger, \tag{7.57}$$

with $j \in \{L, R\}L$ which is derived in appendix A.2. We further assume that initially both sides are in thermal equilibrium at temperature T,

$$g_j^<(\omega) = \left(g_j^A(\omega) - g_j^R(\omega)\right) n_F(\omega). \tag{7.58}$$

We note, that as we consider $T \ll \Delta$ we can choose $T = 0$ with no consequences due to the gapped spectrum. These six Green's functions, in addition to t_d and eV fully specify all elements in eq. (7.55), allowing us to numerically calculate DC current, the results of which is shown in fig. 7.1.

The current is normalized to the transparency of a single junction,

$$T_N = \frac{4\pi^2 t_d^2 \nu_L \nu_R}{\left(1 + t_d^2 \pi^2 \nu_L \nu_R\right)^2}, \tag{7.59}$$

which is obtained by solving eq. (7.42) for two metallic leads with constant density of state ν_j. Since normal leads have no anomalous Green's function terms only the $l = 0$ Floquet level contributes to DC current and for a wideband metal the Green's function is simply $g_L^R(\omega) = -i\pi\nu_j$, yielding the conductance,

$$G = \frac{dI}{dV} = \frac{2e}{\hbar} T_N, \tag{7.60}$$

from which the transparency of a single channel T_N is recognized by comparison to the Landauer formula. This transparency dictates the behaviour of the junction; if T_N is small the current resembles the Fermi's golden rule result, and $l = 0$ is sufficient to obtain current. As T_N increases larger l is required to achieve convergence and the $I-V$ curve shows subgap structure with current steps at $eV = 2\Delta/n$ for integer values n. These steps can be associated with processes involving MAR sketched in fig. 7.1 (a-d). From (a) to (d) the number of electrons which coherently crosses the junction at each tunnelling event, increases from one to four. Consequently, if one measures the shot noise (which is a measure of how 'bunched' electrons are) of MAR steps in a QPC, one finds that more charges are carried over at each tunnelling event for lower bias, where higher order MAR processes dominates [154].

Another characteristic of QPC junctions, is that at large bias $eV > \Delta$ the current is larger than what is expected of a metallic junction. This difference is named the *excess current*, which in fig. (7.1) corresponds to the difference between e.g. $T_N = 0.01$ and $T_N = 0.7$ for $eV \gg 2\Delta$, and can be used to find the transparency T_N of a junction. In performing these calculations we chose a finite broadening η_j, required to soften the otherwise divergent BCS peaks. The size of η_j determines the necessary coarse graining in eq. (7.55), which we have chosen sufficiently small to achieve convergence, meaning that smaller η_j does not alter the plot .

7.3 CONCLUSION

In this chapter we have derived an analytical expression for the DC current, given by eq. (7.42), between two arbitrary superconducting leads. This equation is fully defined by the bare single-particle Green's functions of the independent left and right subsystem, and remains valid insofar as the left and right subsystems are

non-interacting, i.e. described by Hamiltonians of quadratic form in Nambu spinors. Additionally, we have shown that this equation can be numerically solved using eq. (7.55) in a algorithmic approach where D and l is increased until convergence is obtained. In the following chapters we will utilize these results to investigate transport in systems containing YSR subgap states.

8

NON-EQUILIBRIUM TRANSPORT WITH YSR SUBGAP STATES

Our goal in investigating non-equilibrium transport between superconductors was to analyse voltage-biased measurements of superconducting junctions containing YSR states. This corresponds to data shown in section 2.4 in which clear signatures of YSR states are present. In this chapter we will detail how one can utilize approximations to obtain non-interacting Green's functions which, with some caveats, realistically describe YSR subgap states. From these non-interacting constituents we can calculate transport using the results of the previous chapter.

The fundamental Hamiltonian for quantum dots hosting YSR bound states is,

$$H = H_D + H_S, \tag{8.1}$$

$$H_S = \sum_{k\sigma} \epsilon_k c^\dagger_{k\sigma} c_{k\sigma} + \sum_k \left[\Delta c^\dagger_{k\uparrow} c^\dagger_{-k\downarrow} + \text{h. c.}\right] + t \sum_\sigma \left[c^\dagger_\sigma d_\sigma + \text{h. c.}\right], \tag{8.2}$$

$$H_D = \sum_\sigma \epsilon_d d^\dagger_\sigma d_\sigma + U d^\dagger_\uparrow d^\dagger_\downarrow d_\downarrow d_\uparrow. \tag{8.3}$$

The common YSR regime, which is also the experimental relevant one, is charging energy much larger than gap $U \gg \Delta$, with tunnel rate $\Gamma = \pi \nu_F t^2$, determining how screened the dot spin-1/2 is. As discussed in section 1.2, various means exist to solve for the YSR bound state.

In calculating transport using eq. (7.55) we require the single particle Green's functions of the dot dressed by the superconductor $g^R(\omega)$ and $g^<(\omega)$, if we wish to include it as e.g. the left subsystem. An immediate obstacle is that H_D is interacting, and as a consequence H cannot be described solely from single particle correlators. In order to continue we therefore need to reduce the Hamiltonian to a non-interacting form, which can be achieved by various approximations. At this stage, let us clarify our goals a bit further; first and foremost we seek a qualitative understanding of transport capturing the essential dynamics at play, as such we are not much concerned about making approximations in which effective parameters are not in one-to-one correspondence with physical parameters - in so far as transport dynamics are qualitatively accounted for in the description.

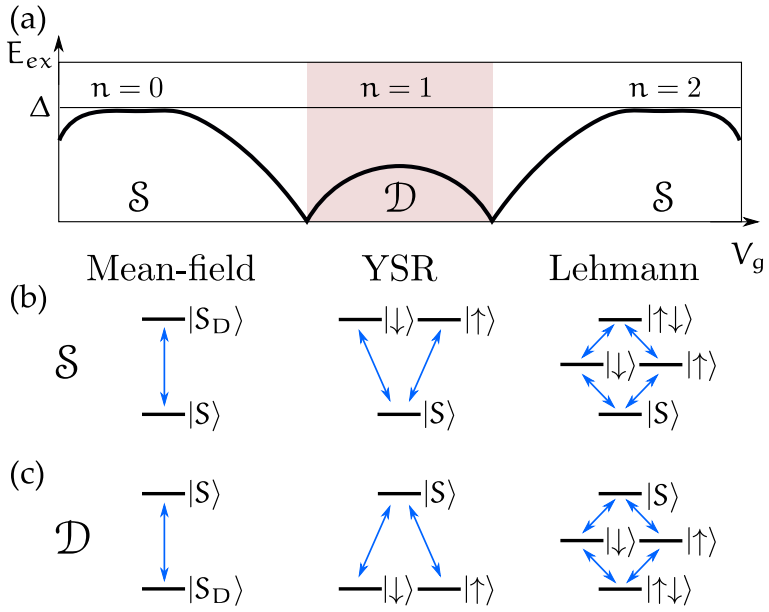

Figure 8.1: (a) Sketch of the YSR state for a QD coupled to a superconductor as a function of gate $V_g \propto -\epsilon_d$. $\mathcal{S}$ and $\mathcal{D}$ denotes groundstate parity. (b) Schematic of the lowest order excitations for a singlet groundstate using three different descriptions: Mean-field, YSR and Lehmann. The bottommost state is the groundstate with arrows indicating excitations by the addition or removal of an electron. (c) Same as in (b) but for a doublet groundstate.

A priori from our knowledge of the YSR state, presented in the introduction, we think of the subgap excitation as being between a two-times degenerate spin-1/2 state and a singlet state. Dependent on gate tuning ϵ_d and coupling rate $\Gamma = \pi\nu_F t^2$ either state can be the groundstate. This is depicted in fig. 8.1 (a), and in (b, c) the YSR label indicate sketches of the excitation map for a YSR state.

The problem is that common approximations, which yield non-interacting Green's functions, either approximate the doublet state into a singlet state (mean-field descriptions [20, 32, 39] and classical-spin descriptions [14–16]), or only yields the many-body spectrum (infinite gap $\Delta \to \infty$ [38], or ZBW approximation [20, 62, 139]). In the second case, the Lehmann representation can be used to obtain a possible Green's function, but if this is used naively it unintentionally extends the Hilbert space with a double excited state. These two approaches yield (approximately) Green' s functions of the characteristic form,

$$g^R_{MF}(\omega) = \frac{1}{\omega + E_0 + i\eta} \begin{pmatrix} v^2 & uv \\ uv & u^2 \end{pmatrix}, \tag{8.4}$$

$$g^R_{Leh}(\omega) = \frac{1}{\omega + E_0 + i\eta} \begin{pmatrix} v^2 & uv \\ uv & u^2 \end{pmatrix} + \frac{1}{\omega - E_0 + i\eta} \begin{pmatrix} u^2 & -uv \\ -uv & v^2 \end{pmatrix}, \tag{8.5}$$

with label MF for mean-field and Leh for Lehmann, and for simplicity written in the basis of 2×2 Nambu spinors $\psi = (d_\uparrow^\dagger, d_\downarrow)$. Here u (v) describes the electron (hole) component of a resonance at $\pm E_0$ with width η. The mean-field Green's function describes a spin-polarized single excitation with the sign of E_0 determining the groundstate, as depicted under the label Mean-Field in fig. 8.1. The Lehmann Green's function in Nambu space is obtained from [18],

$$g_{ij}^R(\omega) = \frac{1}{Z} \sum_{nn'} \frac{\langle n| \psi_i |n'\rangle \langle n'| \psi_j^\dagger |n\rangle}{\omega + i\eta + E_n - E_{n'}} \left(e^{-\beta E_n} + e^{-\beta E_{n'}} \right) \tag{8.6}$$

where $\psi_i^\dagger = \left(d_\uparrow^\dagger, d_\downarrow \right)$ are local Fermionic operators and $|n\rangle$ exact eigenstates with energies E_n of some possibly interacting Hamiltonian H. If one only includes a doublet-to-singlet excitation for a subgap state it reduces to $g_{Leh}^R(\omega)$. Simply inserting $g_{Leh}^R(\omega)$ into the DC current formula - eq. (7.55) - without any modification, which we dub naive usage, is equivalent to extending the Hilbert space with an additional many-body state namely the doubly excited state $|\uparrow\downarrow\rangle$ as depicted under Lehmann in fig. 8.1. This is equivalent to the Hilbert space of an Andreev bound state originating from a resonant level or QPC, where the doubly excited state is part of the spectrum. This is not surprising, as in its essence the Lehmann representation describes all excitations as independent, meaning many-body states composed of multiple excited states can be present, although they are not part of the original Hilbert space. In a non-naive usage, higher order correlators must be included in DC current formula to remedy this issue. Further discussion of this including an example is presented in appendix D. Consequently, in order to obtain a simple description which we can utilize to calculate transport, we either need to artificially extend or reduce the Hilbert space by a single state. We expect both descriptions to miss aspects of transport, and so we have to remain vigilant for spurious results.

In the following, we choose to focus on a spin-polarizing mean-field description which artificially reduces the Hilbert space, as is also common in the literature [23, 46, 155] and appears simpler to analyse.

8.1 SPIN-POLARIZED MEAN-FIELD

The spin-polarising mean-field approximation consist of a lowest order Hartree-Fock expansion in the interaction U, neglecting any further self-consistency calculations. This is performed by approximating,

$$U d_\uparrow^\dagger d_\downarrow^\dagger d_\downarrow d_\uparrow = U n_\uparrow n_\downarrow \approx U\langle n_\uparrow\rangle n_\downarrow + U n_\uparrow \langle n_\downarrow\rangle - U\langle n_\uparrow\rangle\langle n_\downarrow\rangle, \tag{8.7}$$

For a wide parameter range in the normal state one finds $\langle n_\uparrow \rangle = 1/2$ and $\langle n_\downarrow \rangle = -1/2$ [18], which we assume to be valid for the full parameter range of the superconducting case [20, 156]. This approximation may appear crude, but has successfully described many features of YSR transport [39, 67]. In this manner, the approximation consists of replacing $U d_\uparrow^\dagger d_\downarrow^\dagger d_\downarrow d_- \uparrow \approx \frac{U}{2}\left(d_\uparrow^\dagger d_\uparrow - d_\downarrow^\dagger d_\downarrow\right)$ effectively describing interaction as a Zeeman term with magnetic field $B = U/2$, which artificially breaks spin-symmetry. Performing this approximation on eq. (8.1) we obtain the following Hamiltonian in 4×4 Nambu space,

$$H = H_D + H_S, \tag{8.8}$$

$$H_S = \frac{1}{2}\sum_k \Psi_k^\dagger \left[\epsilon_k \tau_z + \Delta \tau_x\right] \Psi_k + \frac{1}{2}\Psi^\dagger t \tau_z \Phi + \frac{1}{2}\Phi^\dagger t \tau_z \Psi, \tag{8.9}$$

$$H_D = \frac{1}{2}\Phi_d^\dagger \left[\epsilon_d \tau_z + \frac{U}{2}\sigma_z\right] \Phi_d. \tag{8.10}$$

with the dot spinor $\Phi_d^\dagger = \left(d_\uparrow^\dagger, d_\downarrow, d_\downarrow^\dagger, -d_\uparrow\right)$. This non-interacting Hamiltonian is equivalent to a resonant level ($U = 0$) under the influence of a magnetic field, with the following retarded Green's function,

$$g^R(\omega) = \left[(g_d(\omega)^R)^{-1} - \Sigma_S^R(\omega) - \Sigma_B^R(\omega)\right]^{-1} \tag{8.11}$$

$$= \left[\omega - \epsilon_d \tau_z - B\sigma_z + \Gamma \frac{\omega - \Delta\tau_x}{E_\Delta} - \Sigma_B^R(\omega)\right]^{-1}, \tag{8.12}$$

with $g_{D/S}^R = \left[\omega + i\eta_{D/S} - H_{D/S}\right]^{-1}$, $\Sigma_S^R(\omega) = t^2 \tau_z g_S^R(\omega) \tau_z$ and $E_\Delta = \sqrt{\Delta^2 - (\omega + i\eta_S)}$ where η_S is a small broadening of the BCS peak necessary for numerical calculations while η_D is infinitesimal and therefore neglected. $\Sigma_B(\omega)$ is a self-energy term stemming from reservoir coupling, currently assumed to be frequency independent and completely imaginary $\Sigma_B(\omega) = -i\eta_B$. This term effectively provides a finite life-time to the subgap resonance. Its origin and influence on subgap state occupation is discussed in the next section. As this Nambu matrix is diagonal in spin-space it is convenient to consider each spin-component individually $\sigma \in \{\uparrow, \downarrow\}$ and define $B_\sigma = \pm B - i\eta_B$ with $+$ $(-)$ for $\sigma = \uparrow$ $(\downarrow)$. Performing the matrix inversion in particle-hole space yields,

$$g_\sigma^R(\omega) = \frac{\omega - B_\sigma + \Gamma\omega/E_\Delta + \epsilon_d \tau_z + \Gamma\Delta/E_\Delta \tau_x}{(\omega - B_\sigma + \Gamma\omega/E_\Delta)^2 - \epsilon_d^2 - \Gamma^2\Delta^2/E_\Delta^2}. \tag{8.13}$$

Subgap state energies are obtained by finding the frequencies $|\omega| < \Delta$ for which the denominator is 0, corresponding to a resonance. In general this yields a fourth order equation in ω which can be solved numerically. However, an analytical expression can

be obtained in the limit of $B, \Gamma \gg \Delta, \epsilon_d$ such that $\omega - B_\sigma \approx -B_\sigma$ [50, 155] where the Green's function simplifies to,

$$g^R_\sigma(\omega) \approx \frac{(\epsilon_d \tau_z - B_\sigma)\, E_\Delta + \Gamma\omega + \Gamma\Delta\tau_x}{\left(B_\sigma^2 - \epsilon_d^2 - \Gamma^2\right) E_\Delta - 2\Gamma B_\sigma \omega}. \tag{8.14}$$

In this case, solving for poles yields,

$$E_0 = \pm\Delta \frac{B_\sigma^2 - \epsilon_d^2 - \Gamma^2}{\sqrt{(\Gamma^2 + (B_\sigma + \epsilon_d)^2)\,(\Gamma^2 + (B_\sigma - \epsilon_d)^2)}}, \tag{8.15}$$

which is strongly reminiscent of the classical spin result [46, 157]. This is easier to see at the electron-hole symmetric point $\epsilon_d = 0$,

$$E_{0\sigma} = \pm\Delta \frac{B_\sigma^2 - \Gamma^2}{B_\sigma^2 + \Gamma^2} = \pm\Delta \frac{1 - J^2}{1 + J^2} \pm \sigma i\eta \tag{8.16}$$

with $J = \Gamma/B$ and effective rate $\eta = 4\Delta \frac{J^2}{(1+J^2)^2} \frac{\eta_B}{B}$ determining the life-time of the resonance, which we obtained by expanding in η_B/B. This J is comparable to the magnetic exchange obtained from a Schrieffer-Wolff transformation of the Anderson model into a Kondo model [22]. Finally, one further simplification can be performed if we are not interested in the gap, but solely on the subgap state. We expand $\omega \approx E_{0\sigma}$ in the denominator of eq. (8.14) and obtain,

$$g^R_\uparrow = \frac{1}{\omega + i\eta + E_0} \begin{pmatrix} v^2 & uv \\ uv & u^2 \end{pmatrix}, \quad g^R_\downarrow = \frac{1}{\omega + i\eta - E_0} \begin{pmatrix} u^2 & -uv \\ -uv & v^2 \end{pmatrix} \tag{8.17}$$

with

$$u^2 = \frac{2\Delta\alpha}{\Gamma} \frac{1 + (\alpha + \beta)^2}{((1 - \alpha^2 + \beta^2)^2 + 4\alpha^2)^{\frac{3}{2}}}, \tag{8.18}$$

$$v^2 = \frac{2\Delta\alpha}{\Gamma} \frac{1 + (\alpha - \beta)^2}{((1 - \alpha^2 + \beta^2)^2 + 4\alpha^2)^{\frac{3}{2}}}, \tag{8.19}$$

where we define $\alpha = B/\Gamma$, $\beta = \epsilon_d/\Gamma$ and $E_0 = \Delta\frac{1-J^2}{1+J^2}$. The full 4×4 matrix is given by,

$$g^R(\omega) = \begin{pmatrix} g^R_\uparrow(\omega) & 0 \\ 0 & g^R_\downarrow(\omega). \end{pmatrix} \tag{8.20}$$

This Nambu structure is identical to that of a classical-spin [21, 46]. In this manner, the spin-polarized mean-field is effectively an extension to the classical spin model, reducing to it for $\epsilon_d \ll U, \Gamma$, but by using eq. (8.13) we can increase ϵ_d to the scale of U, where the conventional classical spin model breaks down. This rewriting was

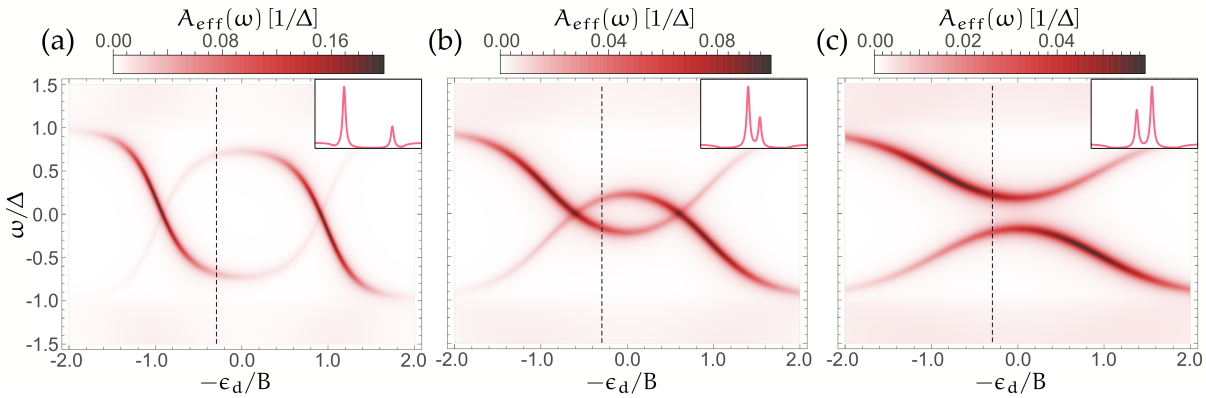

Figure 8.2: Effective spectral function as a function of gate $-\epsilon_d/B$ computed for the Green's function eq. (8.13). Parameters are $B = 500\Delta$, $\eta = 0.1\Delta$, $\eta_s = 10^{-4}\Delta$ and $\Gamma = 200, 400, 600\Delta$ for (a-c) respectively. Insets show line-cuts at $-\epsilon_d/B = -0.15$.

first realized by Ref. [158]. From eq. (8.17) it is clear that this expression treats the subgap state as a singlet-to-singlet excitation for all parameters. The breaking of spin degeneracy, which splits the doublet into two singlet states, is due to the effective magnetic field from the mean-field Hartree-Fock approximation, and so is inherent in the approach. In treatments where higher order corrections to the self-energy are included, this breaking is not remedied [32, 39], and if handled by keeping only spin-conserving contributions to the mean-field a divergence appears at the boundary of the doublet sector, and consequently the approach is only well determined in the singlet sector (see Ref.[33] and reference). In summary, there exist no easy fix to the artificial spin-breaking.

To visualize these Green's functions it is convenient to define an effective spectral function,

$$A_{eff}(\omega) = -2\,\mathrm{Im}\left(g^R_{d11}(\omega)\right) - 2\,\mathrm{Im}\left(g^R_{d22}(-\omega)\right) \tag{8.21}$$

with 11 and 22 referencing entrances in Nambu space. This object corresponds to the spectral function which is probed in the Fermi's golden rule limit of transport, eq. (7.53), by a metallic probe. In fig. 8.2 effective spectral function is depicted as a function of gate which is proportional to $-\epsilon_d$. The spectrum shows the typical eye-like dispersion of an YSR state, which closes as Γ increases, signalling that the screened singlet state is groundstate at the particle-hole symmetrical point.

In plotting fig. 8.2, and in further calculations using spin-polarized mean-field, we obtain the complex self-energy η_B by choosing the effective decay rate at the particle-hole symmetrical point ($\epsilon_d = 0$) using,

$$\eta_B = \frac{B(1+J^2)^2}{4\Delta J^2}\eta. \tag{8.22}$$

This value of η_B is then used for all ϵ_d in numerical calculations of eq. (8.13), although eq. (8.22) is not valid in the whole range. This effectively renders the subgap decay rate, defined as the complex component of the pole in eq. (8.13), gate dependent. This gate dependence is for most parameters we use within a factor two of η. In similar works [67, 155, 158] the decay rate is typically included as a Dynes parameter [159] on the superconducting Green's function $g_s^R(\omega) \to g_s^R(\omega + i\eta)$ in contrast to our approach. The origin and influence of the Σ_B term, which yielded η_B, is explored in the following section.

8.2 RELAXATION, POISONING AND THE LESSER COMPONENT

So far we obtained the retarded Green's function $g^R(\omega)$ which specifies the system's spectrum. In order to calculate transport we additionally require the lesser component $g^<(\omega)$ specifying the occupation of said spectrum. In most contexts one assumes that the system is in thermal equilibrium at temperature T, and accordingly the occupation is determined by a Fermi distribution, yielding the following lesser component [18],

$$g^<(\omega) = \left(g^A(\omega) - g^R(\omega)\right) n_F(\omega), \tag{8.23}$$

with $n_F(\omega) = 1/(1 + e^{\omega/T})$. One of the key interests in superconducting subgap states is the inherent *parity protection* arising due to the presence of a gap Δ, which in theory protects excitations from deexciting through parity switches. For example consider our YSR subgap state consisting of a doublet-to-singlet transition requiring an external electron or hole - i.e. a change of fermion parity - to excite or deexcite. If the subgap state is only coupled to superconducting reservoirs, then the lowest energy an external quasiparticle can have is Δ. Consequently, for reservoir temperatures $T \ll \Delta$ the number of excited quasiparticles is exponentially suppressed $n_F(\Delta) \approx e^{-\Delta/T}$, and the subgap state is expected to have a long lifetime and slow decoherence - a property interesting for quantum information processing. Next, we show how this protection can be expressed using Green's function formalism. From Langreth rules, presented in appendix C, the lesser component is given by,

$$g^< = g_D^< + g_D^R \Sigma^R g^< + g_D^R \Sigma^< g^A + g_D^< \Sigma^A g^A, \tag{8.24}$$

with $\Sigma^X = \Sigma_S^X + \Sigma_B^X$ written with common frequency dependence ω suppressed. Solving for $g^<$ yields,

$$g^< = g^R \left((g_D^R)^{-1} g_D^< (g_D^A)^{-1} + \Sigma^<\right) g^A. \tag{8.25}$$

In this expression $g_D^<(\omega) = \left(g_D^A(\omega) - g_D^R(\omega)\right) f_D(\omega)$ with $f_D(\omega)$ describing the isolated dot's initial distribution, such that $(g_D^R)^{-1} g_D^< (g_D^A)^{-1} = -2i\eta_D f_D(\omega)$ which can be neglected as η_D is infinitesimal. As a consequence, the dressed dot's occupation is purely determined by the self-energies $\Sigma^<$. Furthermore, we assume that the bulk superconductor is at thermal equilibrium $\Sigma_S^<(\omega) = \left(\Sigma_S^A(\omega) - \Sigma_S^R(\omega)\right) n_F(\omega)$ and that $\Sigma_B^<(\omega) = \left(\Sigma_B^A(\omega) - \Sigma_B^R(\omega)\right) f_B(\omega)$ with $f_B(\omega)$ denoting the distribution which the reservoir coupling drives the system towards. In this manner, $f_B(\omega)$ is a distribution of fermions obeying $0 \leqslant f_B(\omega) \leqslant 1$ whose details depend on coupling and the specific choice of reservoir. For frequencies $|\omega| < \Delta$ we find $\Sigma_S^<(\omega) = 0$ as the spectrum is gapped, and consequently,

$$g^< = g^R \Sigma_B^< g^A = \left(g^A(\omega) - g^R(\omega)\right) f_B(\omega), \tag{8.26}$$

where we used the relation $\Sigma^A - \Sigma^R = (g^R)^{-1} - (g^A)^{-1}$. For typical cases we choose $\eta_B \ll \Gamma$ such that $\Sigma^< \approx \Sigma_S^<$ for $|\omega| \geqslant \Delta$. Collecting this we find,

$$g^<(\omega) = \left(g^A(\omega) - g^R(\omega)\right) \begin{cases} f_B(\omega), & \text{for } |\omega| < \Delta, \\ n_F(\omega), & \text{for } |\omega| \geqslant \Delta, \end{cases} \tag{8.27}$$

which amount to our statement of *parity protection*. If one removes coupling to reservoir $\eta_B \to 0$ the subgap state obtains an infinite lifetime, and its occupation is simply given by its initial distribution. If some finite but possibly small coupling exist, then the subgap state obtains a finite lifetime corresponding to the rate at which it approaches the distribution $f_B(\omega)$. To discuss this in further detail we adopt the following nomenclature. The lowest energy subgap state we dub $|0\rangle$ while the excited subgap state is dubbed $|1\rangle$. This means that as a function of gate $|0\rangle$ could be either $|S\rangle$ or $|S_d\rangle$ in the spin-polarizing mean-field description, with labels referencing fig. 8.1. Processes which induce a state transition $|1\rangle \to |0\rangle$ are named relaxation, while the opposing processes $|0\rangle \to |1\rangle$ are named poisoning *. Lastly, we use E_0 as the excitation energy from $|0\rangle$ to $|1\rangle$ which is positive no matter the groundstate. For quantum point contacts, which also contains subgap states (albeit slightly different), measurements of relaxation and poisoning are commonplace and have long been discussed [161, 162], including measurements of similar InAs wires as used in our experiment [163, 164].

* The name "poisoning" has its origin from cooper-pair islands [160], where the change of fermion parity would blockade supercurrent, thereby "poisoning" the supercurrent signal.

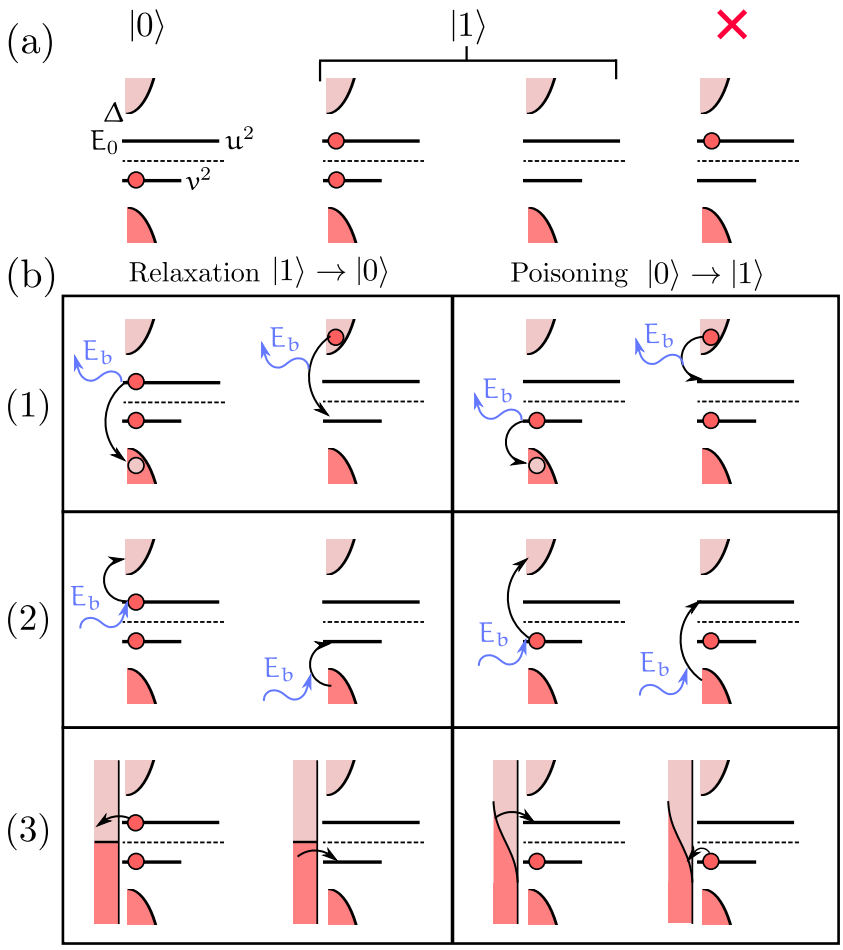

Figure 8.3: (a) Row of figures depicting the ground state $|0\rangle$ and excited state $|1\rangle$ in the electron picture. Spectral weight u^2 and v^2 represents overlap between ground state and excited state through the respective addition or removal of a electron. The second and third sketch both depict $|1\rangle$ as the addition/removal of a cooper-pair connects them. Fourth picture shows an ill-defined state that does not exist as an excitation. (b) Sketches of various relaxation and poisoning processes labelled (1), (2) and (3) from the main text. (1) requires the emission of a boson of energy $E_b = E_{qp} \pm E_0$ for relaxation and poisoning respectively, while (2) requires the absorption of a boson at energy $E_b = E_{qp} \mp E_0$ for relaxation and poisoning. Poisoning utilizing (3) requires that the subgap density of states, if thermally distributed, have $T_B \sim E_0$ while relaxation exist for all temperatures.

Next, we list three possible subgap parity changing mechanisms enabling relaxation and poisoning in a superconducting system:

- (1) There exists a finite population of excited quasiparticles with energy $E_{qp} \geqslant \Delta$, and a density of states of unoccupied bosonic states at energy $E_b = E_{qp} \pm E_0$ coupling quasiparticles to the subgap state. This allows parity switching by absorption of a quasiparticle and emission of a boson.

- (2) There exists a population of excited bosons with energy $E_b \geqslant \Delta \pm E_0$ coupling quasiparticles to subgap states, such that a subgap state can be excited by absorption of a boson and emission of a quasiparticle.
- (3) There exists a finite density of fermionic states at subgap energies tunnel coupled to the subgap state, such that an electron can simply tunnel in or out of the subgap state.

An overview of the three mechanisms, and sketches of corresponding relaxation and poisoning processes, is depicted using the electron picture in fig. 8.3. In the electron picture, hole excitations are depicted as filled electron states, which can lead to some confusion due to double counting. For example, the excitation $|0\rangle \rightarrow |1\rangle$ can be done either by the addition or removal of an electron, each depicted as a line at $\pm E_0$, meaning the state with both lines empty and with both lines filled is the same state, namely $|1\rangle$. Adding or subtracting a cooper-pair connects these two depictions of $|1\rangle$. Lastly, the state with top line filled and bottom empty is ill-defined, as it corresponds to a doubly excited (both by hole and electron) state not part of the Hilbert space.

Using $\eta_{r/p}(\omega)$ as arbitrary positive functions we can rewrite,

$$f_B(\omega) = \frac{\eta_r(\omega)}{\eta_r(\omega)+\eta_p(\omega)}\Theta(-\omega) + \frac{\eta_p(\omega)}{\eta_r(\omega)+\eta_p(\omega)}\Theta(\omega) \tag{8.28}$$

fulfilling the property $0 \leqslant f_B(\omega) \leqslant 1$ and with $\Theta(\omega)$ denoting the heaviside function. By enforcing $\eta_B = \eta_r(\omega)+\eta_p(\omega)$ we identify $\eta_r(\omega)$ as the rate with which a subgap state at energy ω approaches the distribution $\Theta(-\omega)$ where all excited states are unoccupied, and similarly $\eta_p(\omega)$ as the rate for approaching $\Theta(\omega)$, where all excited states are occupied. Consequently, $\eta_r(\omega)$ denotes a relaxation rate driving transitions $|1\rangle \rightarrow |0\rangle$, while $\eta_p(\omega)$ is a poisoning rate driving $|0\rangle \rightarrow |1\rangle$. Next, we discuss the expected balance of relaxation and poisoning stemming from the three processes listed (1), (2) and (3). For process (1) the exact balance depends on details of the boson spectrum and coupling, although it is hard to imagine having relaxation without poisoning for a large region of subgap energies. As an example, consider a frequency independent boson spectrum $A(\omega) \approx$ const. at a low temperature $T_B \ll \Delta$, in addition to a density of non-equilibrium quasiparticles. In this scenario, one would naively expect relaxation and poisoning to be equally likely ($\eta_r \approx \eta_p$), as the rate of boson emission is frequency independent and both processes require a quasiparticle. This yields a highly non-thermal distribution $f_B(\omega) \approx 1/2$ as the subgap state only experiences the non-equilibrium distribution of the quasiparticles, which it thermalizes to. For process (2) an imbalance between relaxation and poisoning would arise if only bosons with energy below a threshold E_T where present. In this case $\eta_r(E_0)$ is large

for $E_0 > \Delta - E_T$ while η_p remains small. To explain finite relaxation at all subgap energies using process (2) one would also expect poisoning to be simultaneously present, since the fine tuned requirement $E_T \approx \Delta$ appears unlikely. Observations of non-thermal distributions and frequency dependent relaxation and poisoning rates have been done in quantum point contacts [165], and explained using balances of process (1) and (2) in Ref.[166, 167], where both phonons and photons where present as bosonic reservoirs. Process (3), which could arise from the unintentional coupling to a nearby metallic lead or a finite subgap density of state in the superconductor (known as a soft gap), would typically yield relaxation for all subgap energies. Poisoning processes are only available if $E_0 < T_B$ assuming the lead is thermally occupied. In this scenario $f_B(\omega) = n_F(\omega)$ and rate η_B is given by the tunnel rate to the subgap density of state.

For YSR states, these rates have been measured in STM setups [46, 51] and some theoretical estimates exist for bulk systems [168], but to the authors knowledge no detailed account exist for YSR states in quantum dots. In experiment we do not a priori know which mechanism is present, and one of our goals is to identify it. In the next section we will calculate transport in systems containing YSR states, and illustrate how relaxation and poisoning influences results.

8.3 TRANSPORT WITH YSR SUBGAP STATES

In this section we investigate transport in S-QD-N and S-QD-S setups, where the YSR state is formed on the S-QD part, with the dot additionally coupled to a probe which can be either metallic (N) or superconducting (S). Many results in this section are shown elsewhere, but we include them to highlight the importance of relaxation and poisoning in transport, and to illustrate how various limits can be obtained using the Floquet Keldysh methodology. The quantum dot is assumed to be in equilibrium with its attached superconductor (S), such that the application of a bias creates a voltage drops between dot and probe. Lastly, we use the spin-polarized approximation to describe the S-QD part which we define as the left (L) subsystem, while the probe is defined as the right (R). In this manner H_L is given by eq. (8.8) and the full system is,

$$H = H_L + H_R(t) + H_T, \tag{8.29}$$

$$H_R(t) = \frac{1}{2}\Psi^\dagger_{Lk}\left[(\epsilon_k - eV)\tau_z + \Delta_R(t)\tau_x\right]\Psi_{Lk}, \tag{8.30}$$

$$H_T = \frac{1}{2}\Psi^\dagger_L t_d \tau_z \Phi_d + \text{h. c.} \tag{8.31}$$

here $\Psi_L = \sum_k \Psi_{Lk}$ in the conventional Nambu basis, and time dependence resides solely on the superconducting phase $\Delta_R(t) = \Delta e^{2ieVt\tau_z/\hbar}$. As this Hamiltonian is completely non-interacting we can follow the procedure of chapter 7 ending up with eq. (7.42), where we here repeat some relevant definitions for good measure,

$$\begin{aligned}
\langle I_0 \rangle &= \frac{e}{h}\int_{-\infty}^{\infty} d\omega \,\mathrm{Tr}\,\mathrm{Re}\left[\tau_z \underline{M}^R(\omega)\left(\underline{\Sigma}^<_{LL}(\omega)\underline{g}^A_L(\omega) + \underline{\Sigma}^R_{LL}(\omega)\underline{g}^<_L(\omega)\right)\underline{M}^A(\omega)\right]_{00}, \\
\underline{M}^X(\omega) &= 1 + \underline{\Sigma}^X_{LL}(\omega)\underline{g}^X_L(\omega)\underline{M}^X(\omega), \qquad (8.32)\\
\underline{\Sigma}^X_{LL,nm}(\omega) &= \begin{pmatrix} \delta_{n,m}t_d^2 g^X_{R,(11)}(\omega+(n-1)eV) & -\delta_{n,m+2}t_d^2 g^X_{R,(12)}(\omega+(n-1)eV) \\ -\delta_{n,m-2}t_d^2 g^X_{R,(21)}(\omega+(n+1)eV) & \delta_{n,m}t_d^2 g^X_{R,(22)}(\omega+(n+1)eV)\end{pmatrix},
\end{aligned}$$

with $g^R_L(\omega)$ given by eq. (8.13) and $g^<_L(\omega)$ by eq. (8.27).

8.3.1 *Metallic probe*

We start by investigating a metallic probe $\Delta_R = 0$, which yields the following Green's function in the wideband limit,

$$g^R_R(\omega) = -i\nu_R \quad \text{and} \quad g^<_R(\omega) = 2i\nu_R n_F(\omega), \qquad (8.33)$$

with ν_R denoting the assumed constant density of state. This Green's function has no off-diagonal components in Nambu space, meaning that $\underline{\Sigma}^X_{LL}(\omega)$ is diagonal in Nambu-Floquet space. Consequently, no tridiagonal ladder is formed when the self-energy is multiplied with $\underline{g}^X_L(\omega)$ and the various Floquet sectors remain unconnected. This simplifies the DC current greatly,

$$\langle I_0 \rangle = \frac{e}{h}\int_{-\infty}^{\infty} d\omega \,\mathrm{Tr}\,\mathrm{Re}\left[\tau_z M^R(\omega)\left(\Sigma^<_{LL}(\omega)g^A_L(\omega) + \Sigma^R_{LL}(\omega)g^<_L(\omega)\right)M^A(\omega)\right], \qquad (8.34)$$

with all Nambu matrices in the 00 Floquet component. Next, as $g^R_R(\omega)$ and $g^A_R(\omega) = \left[g^R_R(\omega)\right]^\dagger$ are both frequency independent, then $\Sigma^{R/A}_{LL}(\omega) = \mp i\Gamma_R$, with $\Gamma_R = \pi\nu_R t_d^2$, are also frequency and bias independent. Consequently, all bias dependence resides on $\Sigma^<_{LL}(\omega) = 2i\Gamma_R n_F(\omega - eV\tau_z)$, and for $T = 0$ the differential conductance takes a particularly simple form,

$$\frac{d\langle I_0\rangle}{dV} = -\frac{2e^2}{h}\int_{-\infty}^{\infty} d\omega \,\mathrm{Tr}\,\mathrm{Re}\left[\tau_z M^R(\omega) i\Gamma_R \tau_z \delta(\omega - eV\tau_z) g^A_L(\omega) M^A(\omega)\right], \qquad (8.35)$$

In this expression $g^<_L(\omega)$ vanished, as it is bias independent, indicating that subgap state occupation $f_B(\omega)$, discussed in the previous section, plays no influence on conductance. The relaxation and poisoning rate characterized by η is quite important

though. This can be seen from $g^R_L(\omega)$ expanded around E_0, yielding the approximate form eq. (8.17), where we further assume that bias is at resonance $eV = E_0$. In this limit, $g^R_L(\pm eV)$ denominators are either $1/(2E_0 + i\eta) \approx 0$ or $-i/\eta$. Considering the second term we find $\Sigma^R_{LL}(\pm E_0)g^R_L(\pm E_0) \propto \Gamma_R/\eta$, which $M^R(\omega)$ is a series expansion of. In chapter 7 we showed that for $M^R(\omega) \approx 1$ transport reduces to Fermi's golden rule. In this manner, the size of Γ_R/η determines the transport regime, which for $\Gamma_R/\eta \ll 1$ is given by Fermi's golden rule. In the opposing regime $\Gamma_R/\eta \gg 1$ higher order terms of $M^R(\omega)$ gain importance and transport is dominated by resonant processes. Intuitively, this can be understood as a competition between rates, with Γ_R characterizing the rate of electron transfer and η the rate at which subgap states return to equilibrium. Fermi's golden rule assumes that each lead reaches equilibrium between each transport process, in accordance with $\Gamma_R/\eta \ll 1$, while in the opposing regime many transport processes occur between equilibration, and the subgap state's occupation is therefore non-equilibrium.

Using the Green's function eq. (8.17) the conductance formula eq. (8.35) can be simplified into [169],

$$\frac{d\langle I_0\rangle}{dV} = \frac{2e^2}{h}\left[\frac{2\Gamma_e\Gamma_h + \Gamma_e\eta}{(eV - E_0)^2 + \Gamma^2} + \frac{2\Gamma_e\Gamma_h + \Gamma_h\eta}{(eV + E_0)^2 + \Gamma^2}\right], \tag{8.36}$$

with $\Gamma_e = u^2\Gamma_R$ and $\Gamma_h = v^2\Gamma_R$ denoting the transfer rate into subgap state electron and hole component respectively, and $\Gamma = \Gamma_e + \Gamma_h + \eta$ is the total decay rate of the fully dressed subgap excitation. Deriving this expression from eq. (8.35) is a bit tricky since eq. (8.17) cannot be inverted. Some useful relations for this purpose are,

$$\begin{aligned}
&g^A_L(\omega)M^A(\omega) = G^A_{LL}(\omega)\\
&M^R(\omega) = I + \Sigma^R_{LL}(\omega)G^R_{LL}(\omega)\\
&G^R_{LL\uparrow}(\omega) = \frac{1}{\omega + i\Gamma + E_0}\begin{pmatrix} v^2 & uv \\ uv & u^2\end{pmatrix}, \quad G^R_{LL\downarrow}(\omega) = \frac{1}{\omega + i\Gamma - E_0}\begin{pmatrix} u^2 & -uv \\ -uv & v^2\end{pmatrix}
\end{aligned} \tag{8.37}$$

with $G^R_{LL\sigma}(\omega)$ denoting the solution to the Dyson series of the two decoupled spin-sectors $G^R_{LL\sigma} = g^R_{L\sigma} + g^R_{L\sigma}\Sigma^R_{LL\sigma}G^R_{LL\sigma}$. Eq. (8.36) shows that in the limit of $\eta \gg \Gamma_e, \Gamma_h$ conductance at $eV = E_0$ ($eV = -E_0$) is proportional to corresponding electron (hole) spectral height u^2 (v^2), in concord with Fermi's golden rule. Conductance is therefore a direct measure of the spectral function in this limit. In the opposing limit $\eta \ll \Gamma_e, \Gamma_h$ both peaks are proportional to $\Gamma_e\Gamma_h$ and are therefore bias symmetrical, and reach the conductance quantum $2e^2/h$ at $\Gamma_e = \Gamma_h$, indicating a highly resonant process. Although this transport cycle involves Andreev reflections, it occurs incoherently, meaning that each intermediate step is on shell and not virtual, and consequently

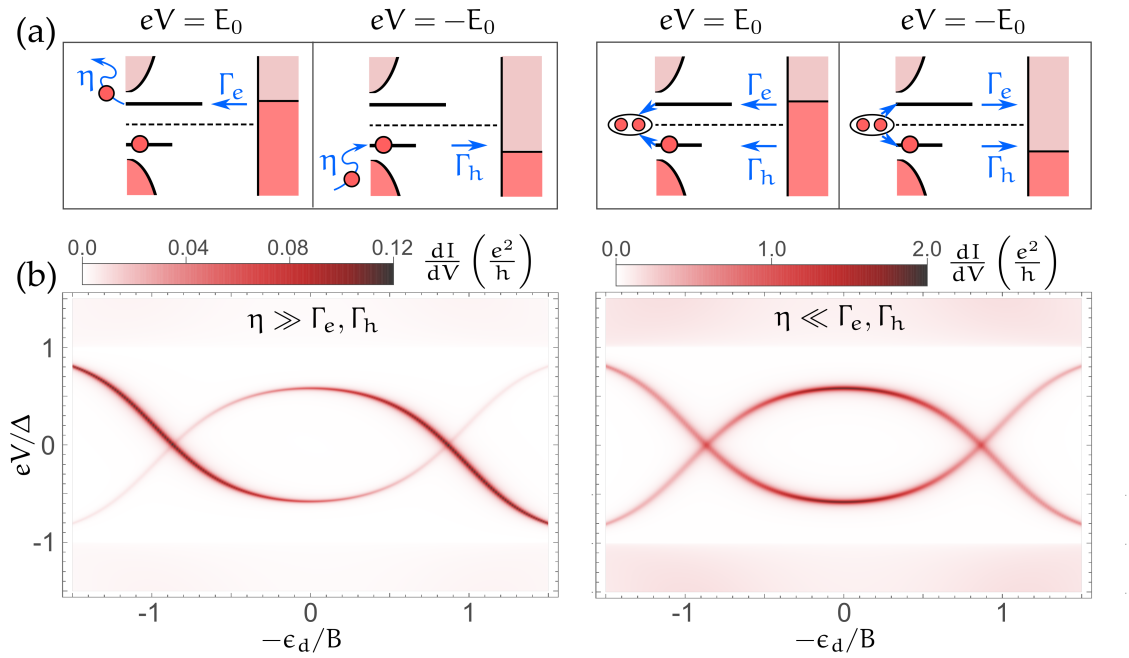

Figure 8.4: (a) Schematics of normal lead to subgap state transport processes, inspired by Ref. [169]. The two left processes dominate for $\eta \gg \Gamma_e, \Gamma_h$ and the right processes dominate for $\eta \ll \Gamma_e, \Gamma_h$. (b) Differential conductance as a function of gate and bias calculated from eq. (8.35) with parameters: $B = 20$, $\Gamma_L = 10$, $\Delta_R = 0$, $T = 0$ and $\Gamma_R = 0.01$, $\eta = 0.01$ for the left plot, and $\Gamma_R = 0.5$, $\eta = 0.001$ for the right. All in units of Δ_L.

shot-noise would still measure single electron transfers. This is supported in chapter 9, where we describe a similar process using master equations. The limit $\eta \gg \Gamma_e, \Gamma_h$ was also investigated for a quantum dot YSR state in Ref.[23] using a Kondo model for a classical and a lowest order quantum spin. In fig. 8.4 schematics of the two processes alongside plots of conductance are shown.

Although a number of experiments probing YSR states in S-QD-N setups have been performed [54, 57–59, 62, 63], there have been no observation of the $\Gamma_e\Gamma_h$ limit with symmetrical peaks and conductance at $2e^2/h$, with the possible exception of Refs. [60, 61] where due to resolution it is hard to determine the symmetry.

8.3.2 *Superconducting probe*

Next, we move to the case of a superconducting right lead for which $g_R^R(\omega)$ is both frequency dependent and contains anomalous terms, meaning that DC current calculations using eq. (8.32) evades simplification. As a consequence, results presented in the remaining subsections are obtained numerically, as simple analytical limits, similar to

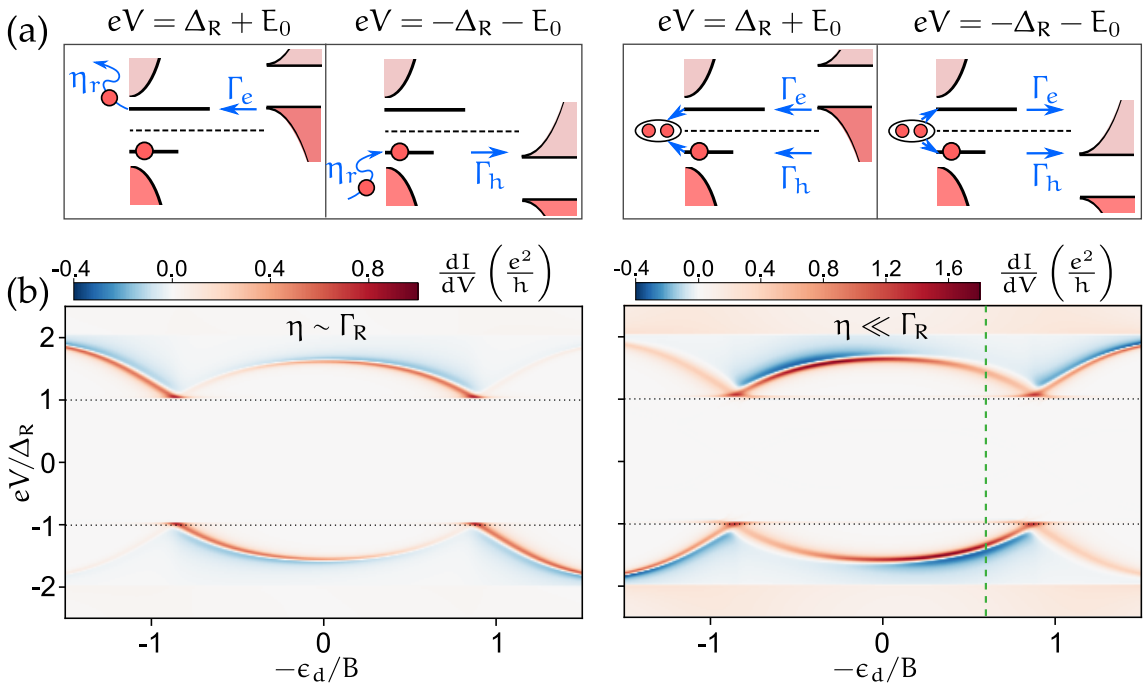

Figure 8.5: (a) Schematics of superconductor to subgap state transport processes, inspired by Ref. [46]. The two left processes dominate for $\eta \gg \Gamma_e, \Gamma_h$ and the right processes dominate for $\eta \ll \Gamma_e, \Gamma_h$. (b) Differential conductance as a function of gate and bias calculated from eq. (8.32) for $l = 0$ with parameters: $B = 20$, $\Gamma_L = 10$, $\Delta_R = 1$, $T = 0$ and $\Gamma_R = 0.04$, $\eta = 0.02$ for the left plot, and $\Gamma_R = 0.4$, $\eta = 0.002$ for the right. All in units of Δ_L. Green line indicate position of cut shown in fig 8.6.

eq. (8.36), are hard to obtain. First, we investigate the scenario where only relaxation is present, amounting to $\eta_B = \eta_R$ and $f_B(\omega) = \Theta(-\omega)$. Furthermore, we initially keep only the zeroth Floquet band ($l = 0$), which is the limit investigated in Ref. [46] where some analytical relations are tractable. Results of this calculation is shown in fig. 8.5.

The main conductance features are located at $eV = \pm\Delta_R \pm E_0$ corresponding to the resonance between a BCS peak and opposing subgap state. Transport cycles at this resonance resembles the normal lead cycles, shown in fig. 8.4, with the caveat that the density of state is frequency dependent $\nu_R(\omega) = -\operatorname{Im}\left[g_R^R(\omega)\right]$, which is carried over to the rates $\Gamma_e(\omega) = \pi u^2 \nu_R(\omega) t_d^2$ and $\Gamma_h(\omega) = \pi v^2 \nu_R(\omega) t_d^2$. For large η, single electron processes dominate and transport amounts to Fermi's golden rule. In this limit, the negative differential conductance (NDC) is due to the decrease of $\nu_R(\omega)$ as eV becomes larger than $E_0 + \Delta_R$, resulting in a decrease of current as the subgap state is no longer in resonance with the BCS peak. In the opposing limit, bias asymmetry appears reversed compared to the Fermi's golden rule limit. This is due to the frequency dependency of $\nu_R(\omega)$; as an example consider the resonance $eV = \Delta_R + E_0$ using transport cycles of

$\Gamma_e\Gamma_h$, for which it is the rate $\Gamma_h(-\Delta - 2E_0)$ which intuitively limits transport as the rate $\Gamma_e(-\Delta)$ is greatly enhanced by the BCS peak. This results in transport cycles limited by v^2, although it is a u^2 peak that is in contact with the BCS peak, thereby reversing the bias asymmetry.

The switching of conductance peak asymmetry has been observed as a function of Γ_R in STM where it was used to extract subgap state relaxation rate, but to the authors knowledge it has not been demonstrated in S-QD-S junctions. The Fermi's golden rule limit has been identified in experiments with weak probe coupling [67, 69, 71, 72], with transport given by a simple convolution. Lastly, a word of caution; if one probes a subgap state with a superconducting lead then in order to validate a BCS deconvolution, as done in e.g. Ref. [67], one must a priori know that $\eta > \Gamma_R$ as the deconvolution assumes Fermi's golden rule transport. Due to gap parity protection this demand is not automatically satisfied for a 'weakly' coupled probe.

8.3.3 *YSR MAR*

We now consider the effects of higher Floquet bands, thereby including high order MAR processes in transport. The validity of only keeping the zeroth Floquet band, as in the previous subsection, hinges on small coupling compared to charging $\Gamma_R \ll B$, and/or large relaxation $\eta \gg \Gamma_R$, disfavouring highly coherent processes such as MAR. This leads to the formations of conductance peaks at integer values of lower order peaks, similar to MAR channels shown in section 7.2. For simplicity we focus on the asymmetric limit $\Gamma_R \ll \Gamma_L$, where the YSR state forms on only one superconductor, while the other lead acts like a probe. In previous work [170] using a Kondo model expanded to second order in J, it was found that in the symmetrical limit ($\Gamma_R \sim \Gamma_L$) spectroscopy mimics a S-S junction with no impurity present, while the asymmetrical limit corresponds to YSR state spectroscopy. Lastly, in a recent article *Villas et al.* [155] did a thorough investigation of the same limit presented here, using an almost identical model. Although, there investigation was aimed at STM setups there results also applies to quantum dot YSR states modelled by a spin-polarizing mean-field. In general our calculations are in complete agreement with there results.†.

In fig. 8.6 we show effects of including more Floquet bands ($l = 2$), and for simplicity we assume $\Delta = \Delta_L = \Delta_R$. We find that MAR processes only becomes prominent for large coupling $\Gamma_R \sim \Delta$ with our parameters, corresponding to the limit $\Gamma_R \gg \eta$ with

† For context, the full Floquet Keldysh model employed here, was derived with the intend of exploring MAR in YSR states, but as the recent paper [155] covers the subject in detail we present only a few key results.

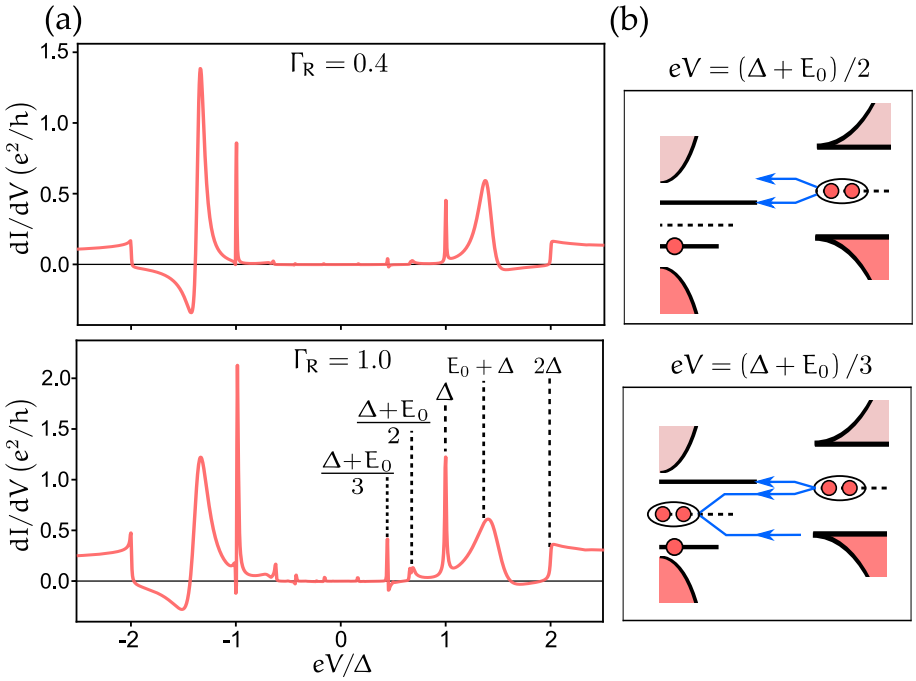

Figure 8.6: (a) Conductance as a function of bias at $-\epsilon_d = 12$ - shown as a green line in fig. 8.5 - with $l = 2$. Parameters are similar to fig. 8.5 except $\Gamma_R = 1\Delta$ in the lower plot. (b) Schematics of the MAR processes at $eV = (\Delta + E_0)/n$ for $n = 2, 3$, inspired by Ref. [155].

reversed conductance peak asymmetry. We observe integer features at both $eV = 2\Delta/n$ and $eV = (\Delta + E_0)/n$, which some surprising caveats due to the weakened gap of the YSR hosting superconductor. Firstly, $eV = 2\Delta/n$ steps are less prominent then for similar coupling without YSR states, additionally the $eV = (E_0 + \Delta)/3$ feature is more prominent than the $eV = (E_0 + \Delta)/2$ feature even though it is a higher order process. As depicted in fig. 8.6 (b) this is related to the $n = 2$ process using the weakened peak for transport, while the $n = 3$ process uses the opposing sharp BCS peak. In contrast to Ref. [155], where a soft-gap from a finite dynes parameter is included, we see no feature at $eV = E_0$. One could imagine processes at $eV = E_0$ with a full cooper-pair tunnelling into the subgap state, but in our model this is prohibited as the subgap excitation is spin-polarized - an artefact of our mean-field. In the physical system such MAR processes could be present a singlet groundstate $|S\rangle$ where excitations to both $|\uparrow\rangle$ and $|\downarrow\rangle$ are possible. We believe though that it will be limited by Δ/η, as the excited $|\sigma\rangle$ state (from the first electron) needs to relax before the other constituent electron of the cooper-pair can enter, leaving a virtual quasiparticle at $E_{qp} \geqslant \Delta$ until relaxation occurs. Oddly, the tiny inner most peaks in fig. 8.6 (a) fit with $E_0/2$, show NDC, and disappears for $l = 0$ indicating that it originates from MAR. The transport cycle behind these peaks is not presently understood. An important result is that the

peak at $eV = E_0 + \Delta$ is unmodified by higher Floquet bands, such that the theory of Ref. [46] remain valid even when other MAR signatures are present.

From the perspective of S-QD-S experiments, these novel MAR lines at $eV = (E_0 + \Delta)/n$ could be identified by there slope as a function of gate, appearing as replicas of the $eV = E_0 + \Delta$ feature shown in fig. 8.5 at lower bias with half or third of the slope. MAR like features have been observed in multiple S-QD-S experiments [64, 66, 68, 74, 116], with features of integer slope of $eV = E_0 + \Delta$ visible in Ref. [70]. YSR MAR processes have also been identified in STM [46, 48, 49].

8.3.4 *Poisoning and subgap metallic density*

In the previous subsections we assumed that the superconductor contained no subgap density of state, and that the YSR state experienced only relaxation. Next, we investigate the effects of finite poisoning by either assuming a finite temperature of the subgap distribution $f_B(\omega) = n_F(\omega)$, or by assuming the presence of a finite η_p with $f_B(\omega)$ given by eq. (8.28). This leads to low order transport processes occuring at subgap bias, since transport cycles are possible when the hole (electron) YSR state is aligned with the hole (electron) BCS peak at $eV = \Delta - E_0$ ($eV = -\Delta + E_0$). Schematics of these processes, and results of calculations in the $\eta \ll \Gamma_R$ limit with $l = 0$ is shown in fig. 8.7.

The conductance features visible at bias $|eV| < \Delta_R$ in fig. 8.7, stemming from the poisoning driven processes, we name *poisoning lines*. These lines have opposite slopes of the $eV = \pm\Delta \pm E_0$ features, like mirror images around $\pm\Delta$. In the case of finite temperature, they are only visible close to groundstate transitions, since $E_0 \sim T$ before excited states are populated. For a frequency independent poisoning rate, as shown in the right plot, the poisoning line exists for all subgap state energies.

Another effect creating low order transport at subgap bias, is if the superconducting probe contains a finite subgap density of state - known as a soft-gap. This can be modelled by a dynes parameter [159], but we model it as the addition of a metallic density of state to the probe, similar as in Ref. [73],

$$\Sigma^R_{LL}(\omega) = -\Gamma_R \frac{\omega - \Delta\tau_x}{\sqrt{\Delta^2 - (\omega + i\eta_s)^2}} - i\Gamma_N \tag{8.38}$$

with coupling Γ_N. In this case, both the superconducting and metallic conductance lines are visible simultaneously, as shown in fig. 8.8, where we plot differential conductance both in the large and small η regime. In the small η regime, we see a subgap inner lobe crossing zero, similar to transport with a normal lead. In this limit, results of the superconducting and metallic probe are basically overlain, with broader peaks at

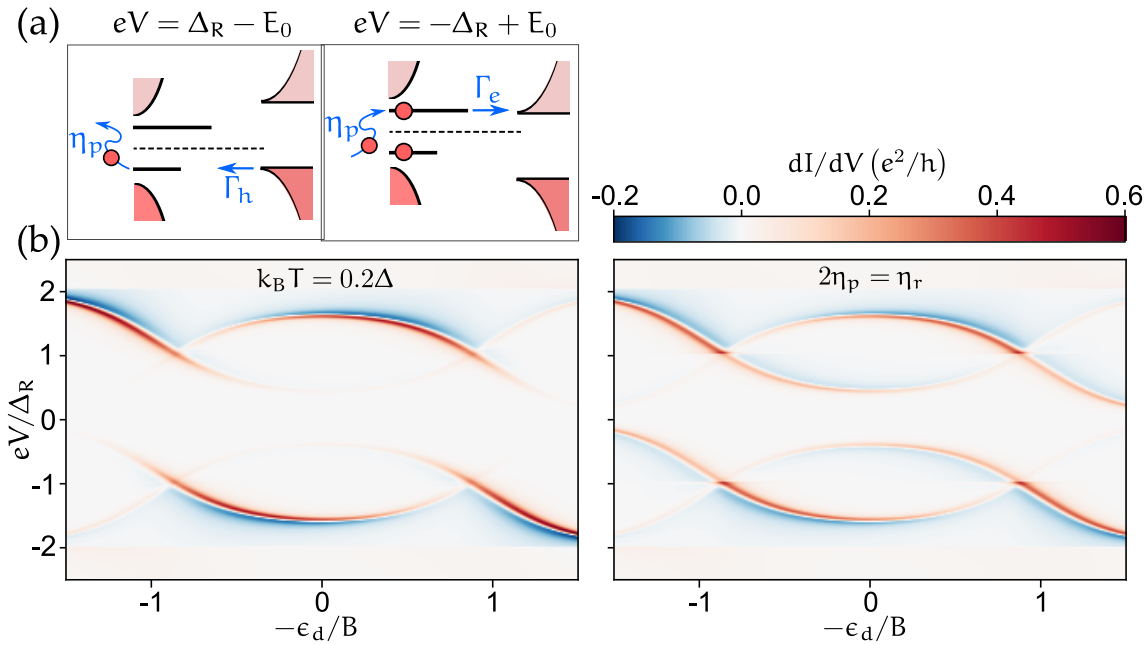

Figure 8.7: (a) Schematics of transport processes starting from an excited subgap state $|1\rangle$, driven by the poisoning rate η_p. (b) Conductance as a function of gate and bias using the same parameters as for the left plot in fig. 8.5, apart from finite $T = 0.2\Delta$ in the left plot, and $\eta_p = \eta/3$, $\eta_r = 2\eta/3$ in the right. Plotted on the same conductance scale.

$eV = \pm E + \pm\Delta_R$ due to induced lifetime from the metallic probe. In fig. (8.8) (b) we show induced poisoning lines stemming from normal lead transport. For bias $|eV| > E_0$ current runs from the subgap state into the normal density of state. This induces a non-equilibrium population of the excited YSR state, and due to this poisoning cycles sketched in fig. 8.7 becomes possible, leading to the appearance of poisoning lines. These lines vanish at $eV = \pm E_0$ supporting this interpretation.

In experiment, this feature is recognizable by the inner lobe showing identical slope to the $eV = \pm\Delta \pm E_0$ feature. Another characteristic is that it crosses zero-bias at $E_0 = 0$, in contrast to MAR lines at $eV = \pm(\Delta + E_0)/n$ which cannot cross zero. This inner lobe, coined an Andreev mirage [73], is a common feature and has been observed in a number of S-QD-S experiments [65, 66]. Measuring this mirage while increasing temperature has additionally shown the appearance of poisoning lines Refs. [71, 72], in concord with the model under the assumption that subgap density of states is thermally occupied, such that it poisons the subgap state at higher temperatures. In STM experiments, which are typically performed at temperatures $T \sim 1$ k, thermal poisoning has been observed [46, 51], and for tuneable systems appear enhanced at the crossing of $E_0 = 0$ [45, 47, 49]. This is also visible in the STM experiment we analyse in chapter 12. In S-QD-S systems, thermal poisoning has only been observed in the

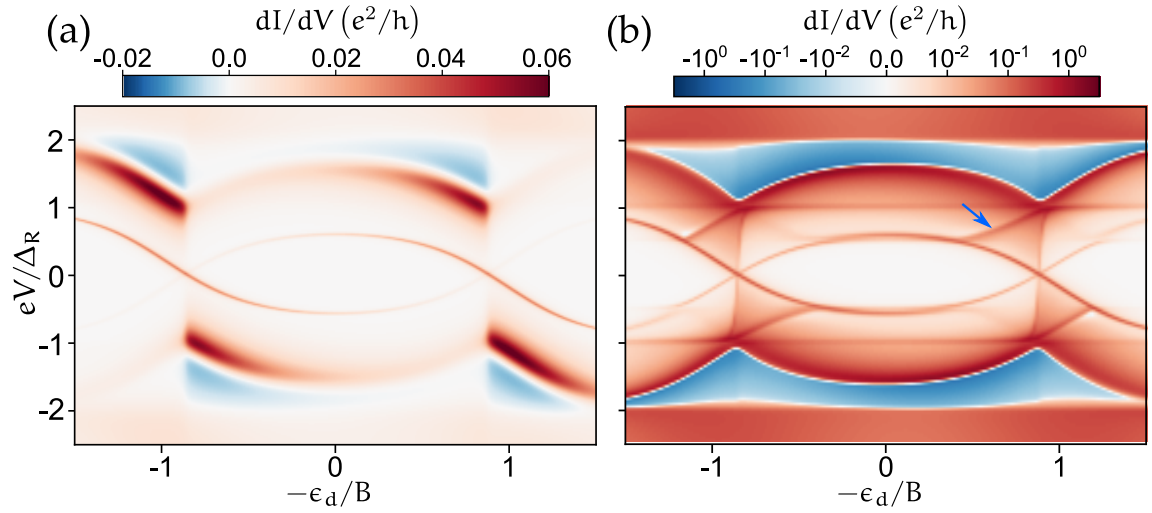

Figure 8.8: Calculation of conductance as function of bias and gate for $l = 0$. Parameters: $B = 20$, $\Gamma_L = 10$, $\Delta_R = 1$, $T = 0$ and $\Gamma_R = 0.02$, $\eta = 0.01$, $\Gamma_N = 0.004$ for (a), and $\Gamma_R = 0.4$, $\eta = 0.002$, $\Gamma_N = 0.012$ for (b). All in units of Δ_L. (b) Is shown in logarithmic scale, and the blue arrow indicates an induced poisoning line.

aforementioned heightened temperature measurements also featuring mirages. To the author's knowledge, no YSR experiment exists showing poisoning lines stemming from constant poisoning rate as seen in fig. 8.7.

8.3.5 *Artificial singlet-to-doublet reduction*

As stated, the spin-polarizing mean-field approximation, applied in this section, artificially renders the doublet state into a singlet state. The effects of this on transport has been discussed in the review [39], where the main point is that due to the availability of both spin species in the probe (superconducting or not), the effect of spin-polarization is minor. We expect though some discrepancy to arise due to multiplicity which we discuss next. The singlet to doublet reduction decreases the number of available transport channels for a singlet groundstate $|S\rangle$. In this case either a spin-up or down electron (or hole) can be added to drive transitions to $|\sigma\rangle$, while for the doublet grounstate $|\sigma\rangle$ only a spin-σ electron (or hole) can be removed to drive transitions to $|S\rangle$. In this manner, the $|S\rangle$ groundstate has double the amount

of channels to excite if coupled to an unpolarized lead. Consequently, for a metallic probe in the limit $\eta \gg \Gamma_e, \Gamma_h$ we naively expect eq. (8.36) to change into,

$$\frac{d\langle I_0\rangle}{dV} = \begin{cases} \frac{2e^2}{h}\left[\frac{2\Gamma_e\eta}{(eV-E_0)^2+\eta^2} + \frac{2\Gamma_h\eta}{(eV+E_0)^2+\eta^2}\right], & \text{for } |g\rangle = |S\rangle \\ \frac{2e^2}{h}\left[\frac{\Gamma_e\eta}{(eV-E_0)^2+\eta^2} + \frac{\Gamma_h\eta}{(eV+E_0)^2+\eta^2}\right], & \text{for } |g\rangle = |\sigma\rangle \end{cases} \tag{8.39}$$

where $|g\rangle$ denotes the groundstate, which amounts to a factor of two change in peak conductance on transitioning from a singlet to a doublet groundstate at $E_0 = 0$. We expect similar changes of factor twos in conductance to occur for superconducting probes and higher order Andreev processes as well, but apart from such prefactors we speculate that our calculations capture most physical transport processes. In experiment, there are indications of a reduction in conductance at singlet-to-doublet transitions [67, 75], although it is not consistently seen in all measurements of the literature.

8.4 CONCLUSION

In this chapter we have discussed how to pick a suitable Green's function to calculate transport via the Floquet Keldysh methodology. In picking the lesser component a discussion of relaxation and poisoning rates, and where they could stem from, was necessary. Lastly, we showed resulting maps of differential conductance for various limits and parameters as a function of gate, using the spin-polarizing mean-field approximation to obtain Green's functions. Our hope is that these maps covers most realistic S-QD-N and S-QD-S experiments, and provides us with a language to associate measurements to underlying transport processes.

Something too note, is that most experiments in S-QD-S systems shows sign of finite relaxation, which drives current processes even for low coupling, but little sign of poisoning (no visible poisoning lines) exists in the literature. In addition, subgap mirages are visible in several experiments, and when poisoning lines are observed it is induced by increasing temperature. Relating these facts to our discussion of possible origins for relaxation and poisoning in section 8.2, we speculate that the existence of a finite subgap metallic density of states is the most likely candidate for relaxation and poisoning in experiments. Whether this subgap density is due to a soft-gap or stray coupling to a nearby metallic reservoir remains an open question, and can vary from setup to setup. In the case of excess high energy bosons or quasiparticles it requires some fine tuning to explain the presence of relaxation without poisoning across a large range of E_0, which in experiments, is tuned by gate.

In the next chapter, we use the spin-polarized mean-field approximation and Floquet Keldysh Green's functions to analyse data of direct transport between two opposing subgap states. In the supplement of this paper presented in chapter 10, we additionally derive Lindblad master equations yielding identical results to the Floquet Keldysh approach. In this framework we can include the full singlet-to-doublet Hilbert space to account for the artificial reduction, introduced by the mean-field. As an outlook to this chapter, it could be interesting to utilize the Lindblad approach to try and capture the various transport regimes, shown in section 8.3, and use it to explore doublet-to-singlet dynamics.

9

PROJECT 3

Next, we present the submitted version of project 3, currently published on arXiv [3]. In this project, we investigate transport between two opposing subgap states, specifically on shell Z from chapter 2, where both interdot tunnel coupling t_d and interdot charging U_d are small compared to U_L, U_R. In this limit the full S-DQD-S setup can be decomposed into two independent S-QD subsystems, coupled by a weak (compared to U_L, U_R) tunnel probe. Since both the left and right S-QD system forms a YSR state at energy E_L and E_R respectively, a transport resonance occurs at bias $eV = \pm(E_L + E_R)$ where the two subgap states are aligned, which is realized in experiment. This paper is largely inspired by Ref. [51] where a similar signal is measured in a STM setup, and additional MAR relaxation processes, whose accessibility depends on E_L and E_R, are identified. Our experiment has the advantage of being fully tuneable, such that MAR mediated relaxation processes can be turned on-and-off by tuning of E_L and E_R. A similar feature have been measured in a previous S-DQD-S experiment [101], but they model it in the $\Delta \to \infty$ limit [38], and conductance features are quite broad due to a large soft-gap density of state. Additionally, they do not observe the MAR mediated relaxation channels. In our experiment, no poisoning lines are observed and only week relaxation, compared to tunnel rates, is present. Since transport through opposing subgap states is only feasible using relaxation processes, these measurements constitute a direct probe of subgap state dynamics.

In modelling, we use the spin-polarized mean-field model, given by Hamiltonian eq. (8.8), to describe the left and right lead, and couple them via a tunnelling term H_T. In doing so, we choose the mean-field magnetic terms to point in orthogonal directions, in order to avoid artificial spin-blockade at certain groundstate configurations. To support these calculations we present Lindblad master equations, inspired by Ref. [51], and find perfect agreement with the Floquet Keldysh approach in regard to the $eV = \pm(E_L + E_R)$ feature. This method allows us to derive closed analytical formulas for conductance, and to extend the Hilbert space to treat the odd state as a realistic two-fold degenerate doublet state. These calculations, and further details, can be found in the supplemental material presented in chapter 10.

Direct Transport between Superconducting Subgap States in a Double Quantum Dot

G. O. Steffensen[1], J. C. Estrada Saldaña[1], A. Vekris[1,2], P. Krogstrup[1,3], K. Grove-Rasmussen[1], J. Nygård[1], A. L. Yeyati[4], and J. Paaske[1]

[1] *Center for Quantum Devices, Niels Bohr Institute, University of Copenhagen, 2100 Copenhagen, Denmark*

[2] *Sino-Danish College (SDC), University of Chinese Academy of Sciences*

[3] *Microsoft Quantum Materials Lab Copenhagen, Niels Bohr Institute, University of Copenhagen, 2100 Copenhagen, Denmark and*

[4] *Departamento de Física Teórica de la Materia Condensada, Condensed Matter Physics Center (IFIMAC), and Instituto Nicolás Cabrera, Universidad Autónoma de Madrid, 28049 Madrid, Spain*

We demonstrate direct transport between two opposing sets of Yu-Shiba-Rusinov (YSR) subgap states realized in a double quantum dot. This sub-gap transport relies on intrinsic quasiparticle relaxation, but the tunability of the device allows us to explore also an additional relaxation mechanism based on charge transferring Andreev reflections. The transition between these two relaxation regimes is identified in the experiment as a marked gate-induced stepwise change in conductance. We present a transport calculation, including YSR bound states and multiple Andreev reflections alongside with quasiparticle relaxation, due to a weak tunnel coupling to a nearby normal metal, and obtain excellent agreement with the data.

Superconductors are characterized by the existence of a Cooper-pair condensate with quasiparticle excitations, appearing above the superconducting gap, Δ. The interplay between superconductivity and various types of impurities [1–4], junctions [5, 6] and barriers [7, 8] can lead to the formation of localized quasiparticle states with energies smaller than the superconducting gap. Such subgap bound states are receiving increasing attention, as the parity protection offered by the gap makes them amenable to quantum coherent manipulation [9–12]. This attribute makes subgap states excellent candidates for qubits in quantum information processing.

Nevertheless, many experiments have shown the existence of quasiparticle relaxation and poisoning, which break parity and decohere the subgap states [6, 11, 13]. The physics behind relaxation and poisoning processes differs from system to system as it depends on fabrication details and on the electromagnetic environment. It is therefore a priori difficult to estimate its origin and magnitude [14–16]. The transport properties of subgap states depend strongly on the relaxation and poisoning rates and can therefore be used to probe the subgap states population dynamics [17, 18]. In a recent paper [19], direct transport between two sets of YSR states induced by magnetic impurities was observed in a scanning tunnelling microscopy setup, yielding a clear measure of subgap dynamics independent of temperature and environmental broadening.

In this Letter, we investigate the subgap dynamics in a setup based on Coulomb blockaded quantum dots coupled to superconductors, which provides *continuous* tunability of the subgap state energies. This tunability gives us unprecedented access to the full phase diagram of relaxation processes within a single device.

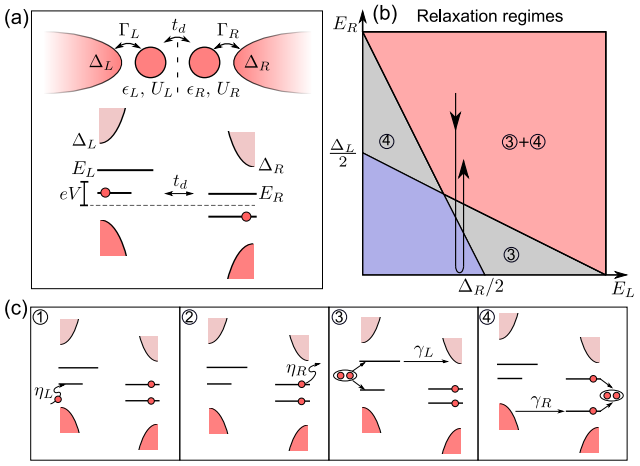

FIG. 1. (a) Schematic of the S-DQD-S system and energy level diagram for direct bound state to bound state transport at $eV = E_L + E_R$. System shown in the $|0,0\rangle$ state. (b) Bound state energy map delineating regions with different relaxation processes, indicated by numbers and illustrated in (c). Processes 1 and 2 are available in all sectors of the diagram. The indicated path corresponds to the change in relaxation regimes seen in Fig.2(c) as the plunger gate voltage of the right dot is swept. (c) Four different relaxation mechanisms available at different subgap state energies. Processes 1 and 3 (2 and 4) relate to the left (right) quantum dot and are all depicted starting from the doubly excited state $|1,1\rangle \to |0,1\rangle$ ($|0,1\rangle$). Processes 1 and 2 refer to intrinsic quasiparticle relaxation, while 3 and 4 employ Andreev reflection via the continuum of the opposite side and transfers a net charge.

To explain the transport signatures, we utilize Floquet Keldysh Green functions [20, 21] to calculate the current across different relaxation regimes, and we demonstrate that these results can be understood in terms of master equations as in Ref. 19, which we extend here to all

relaxation regimes.

The interaction between a superconductor and the spin localized on a quantum dot leads to the formation of a YSR state [22–24]. The quantum dot is characterized by a charging energy, U, a level position, ϵ, and a tunnel coupling to a superconductor characterized by a tunnelling rate Γ. By tuning a gate voltage to change ϵ, one can manipulate both the excitation energy and the ground state of the superconductor-dot system. We use an InAs nanowire based double quantum dot (DQD) coupled to two superconductors [25–27] to obtain two independent subgap states at energies E_L and E_R, shown schematically in Fig. 1(a).

In the limit of low tunnel coupling between the dots, t_d, compared to the dot-superconductor tunnelling rates, Γ_L and Γ_R, each dot will be in equilibrium with its respective superconductor, and a bias voltage, V, applied across the superconductors will cause a voltage drop across the two dots. At the resonances, $eV = \pm(E_L + E_R)$, the electron component of one subgap state is aligned with the hole component of the other, and direct electron transfer can take place. This will excite both subgap systems, i.e. $|0,0\rangle \leftrightarrow |1,1\rangle$, where 0(1) denote the ground(excited) state in the corresponding left, or right subgap system. The potential for such resonant transitions to carry a current relies entirely on the availability of relaxation channels to reset the subgap systems back to $|0,0\rangle$ after each inter-dot tunnelling process.

A diagram showing the different relaxation regimes and a schematic of available relaxation processes are presented in Figs. 1 (b) and (c). The intrinsic relaxation processes 1 and 2, with rates $\eta_{L/R}$, in Fig.1 (c) are active at all energies, while processes 3 and 4, with rates $\gamma_{L/R}$, only become available for subgap states with $E_{R/L} + 2E_{L/R} > \Delta_{R/L}$, where an Andreev reflection, followed by a single quasiparticle transfer to the opposing continuum may serve to reset the subgap excitations. Since these additional relaxation channels themselves transfer charge, a full transport cycle using both processes 3 and 4 constitutes a transfer of three electrons in total. Notice that, unlike multiple Andreev reflection (MAR) processes between two superconductors [28], this 3-electron transfer occurs incoherently. In total, one should therefore expect a higher relaxational current through electron/hole-aligned subgap states when the $eV = E_L + E_R$ resonance occurs above the threshold bias, i.e. for $|eV| > \min(|\Delta_L - E_R|, |\Delta_R - E_L|)$ corresponding to the grey and red regions of Fig. 1(b).

Measurements are carried out in a device investigated earlier at different gate settings in Refs. 25 and 29, based on a 110 nm-diameter InAs nanowire with 7 nm superconducting aluminum grown in-situ epitaxially on three facets of the wire. The wire is deposited on top of an array of gates insulated by 20 nm of hafnium oxide, which is used to define the double dot architecture, and contacted by Ti/Au leads on each side. Aluminum is etched away before contact deposition to form a 350 nm long junction. The device is equipped with a global Si/SiOx substrate backgate. A scanning tunneling micrograph of the device is shown in Fig. 2(a). Gates 1, 3 and 5 control the tunnel couplings, Γ_L, t_d and Γ_R, and are set to constant voltages. Plunger gates 2 and 4 control the filling of the corresponding left and right dots.

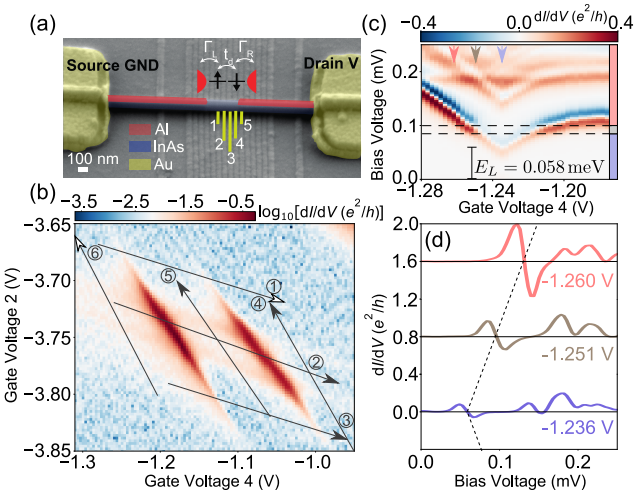

FIG. 2. (a) False colored scanning tunneling micrograph of the device. A schematic of the dots is shown at the junction. (b) Zero-bias conductance charge diagram in logarithmic scale. Arrows indicate linecuts plotted in (c) and in Fig. 3. Gates 1, 3, 5 are set to -9.05 V, -8.7 V, and 0.74 V, respectively, and the backgate is set to 11.15 V. (c) Conductance as a function of bias, and gate voltages following half the range of linecut 1 in (a) parametrized by gate 4. A vertical colorbar on the right indicates relaxation regimes for $E_L = 0.058$ meV (read off as indicated) with colors indicating the corresponding regime in Fig. 1(b). Arrows in the top mark cuts shown in (d) and dashed horizontal lines indicate changes in relaxation regimes. (d) Conductance vs. bias voltage along three vertical cuts in (c) placing the $eV = E_L + E_R$ resonance in different relaxation regimes, as indicated by color. Each cut is vertically displaced by $0.8e^2/h$. The dotted line traces the movement of the resonance.

This device and its connecting circuitry has been characterized in Refs. 25 and 29, where it was tuned up to measure (critical) supercurrent for different regimes of YSR screening. In this work, the device is adjusted differently to explore the relaxational bound-state-to-bound-state currents illustrated in Fig. 1. To this end, we scan zero-bias conductance using standard lock-in measurements and locate a shell with no apparent anti-cross between charge sectors, indicative of weak inter-dot tunnel coupling, t_d, and charging energy, U_d. A logarithmic map of the conductance is shown in Fig. 2 (b). Pairs of vertical and horizontal stripes in the map are due to a combination of supercurrent and subgap resonances crossing zero energy [29, 30]. From independent measurements [30], we find U_L, $U_R \approx 2$ meV and Δ_L, $\Delta_R \approx 0.14$ meV con-

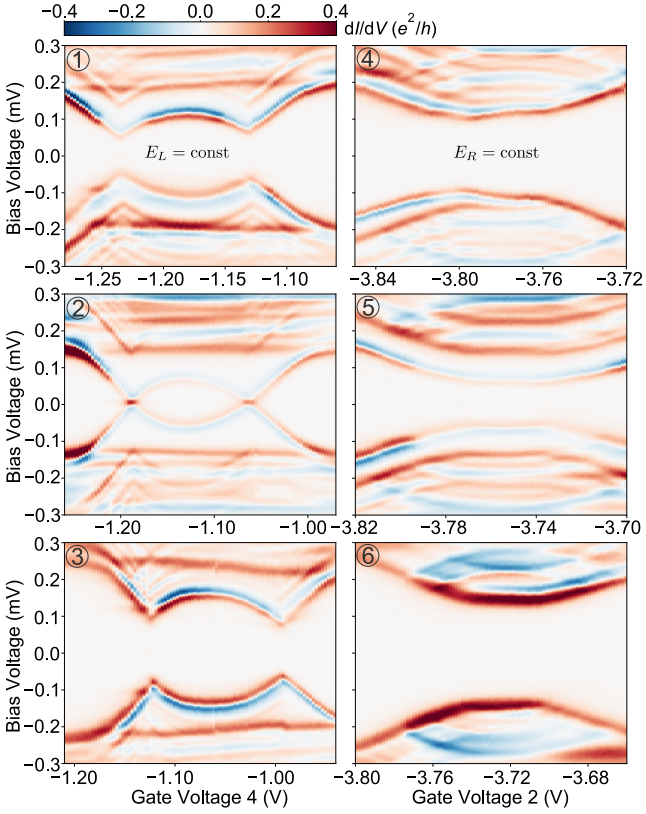

FIG. 3. Experimental data showing conductance as a function of gate, and bias voltage for the six line cuts shown in Fig. 2(b). Cuts 1-3 (4-6) are parametrized by gate 4 (2), but gate 2 (4) is also tuned for each cut to fullow the lines indicated in Fig. 2(b). Cuts 1-3 are horizontal cuts tuning the right dot, while cuts 4-6 are vertical cuts tuning the left dot. All plots are made with the same color scale.

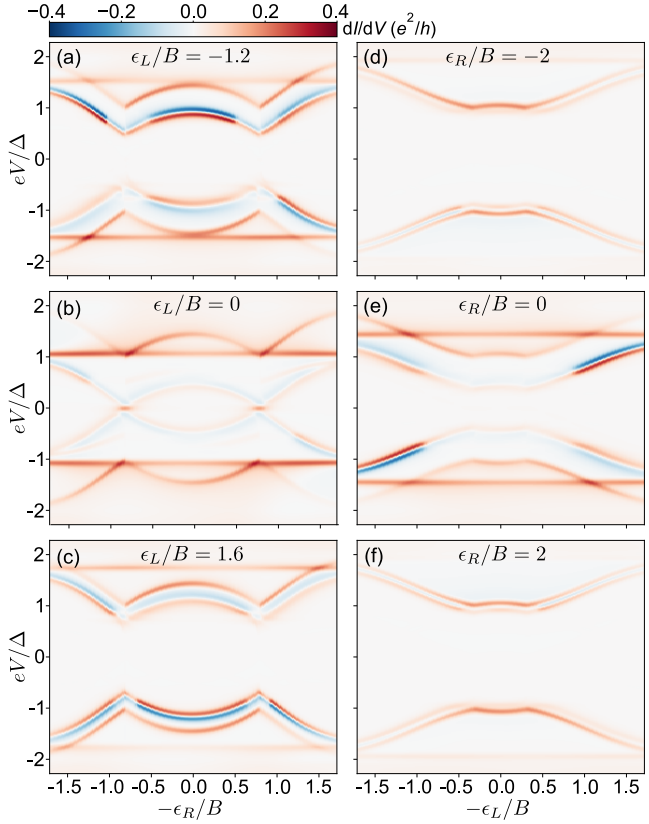

FIG. 4. Conductance as a function of normalized gate, and bias voltage for six linecuts, calculated using Keldysh Floquet Green functions [30]. $\epsilon_{L/R}$ are chosen so as to match the cut in the corresponding panel in Fig. 3. All plots are made with the parameters listed in [31], using the same color scale as in Fig. 3.

sistent with a YSR interpretation of subgap states.

In Fig. 2(c), we show half of the gate extension of the central line cut of differential conductance versus bias and gate voltages labeled 2 in Fig. 2(b). To interpret this cut, we assume that the energy of the left subgap state, E_L, remains constant as the right dot is gated, and identify the lowest lying feature as the $eV = E_L + E_R$ resonance, supported by the negative differential conductance (NDC) immediately following the conductance peak. As gate 4 is tuned, a sudden change of slope occurs at -1.236 V, which indicates that $E_R = 0$, signalling a change of ground state of the right dot-superconductor system, and allows us to infer that $E_L = 0.058$ meV$< \Delta_R/2$.

Strikingly, as the $eV = E_L + E_R$ feature in Fig. 2(c) moves with gate 4, stepwise changes in conductance are observed before and after the phase transition. The position of these thresholds fits with changes in the available relaxation processes, estimated from the bound-state energies, shown as horizontal lines in Fig. 2(c) and as the path in Fig. 1(b). This path shows that as gate increases the resonance moves from red→blue→red with grey regions only observed as transitional steps. In Fig. 2(d), three linecuts show the decrease in conductance of the lowest lying peak-dip features by approximately a factor of 4 between the top, and bottom curves. This pronounced contrast in conductance marks a gate tunable transition between three different relaxation regimes.

These types of changes in conductance at special thresholds are widespread in our data and their positions match expectations from Fig. 1(b). In Fig. 3 we plot the 6 linecuts indicated in Fig. 2(b), where the lowest lying feature corresponds to $eV = E_L + E_R$. From the slope of this feature we infer that the right dot is intermediately coupled to the superconductor showing a characteristic eye shape, while the left dot is more strongly coupled and close to the phase transition at the particle-hole symmetric point [32].

Additional conductance features at higher bias in Fig. 2(c) are identified as a peak at $eV = E_R + \Delta_L$ dispersing like the $eV = E_L + E_R$ feature, and a peak at $eV = E_L + \Delta_R$, which is independent of gate 4,

supporting that E_L remains constant as E_R is tuned by gate 4. In all cuts shown in Fig. 3, replicas of the $eV = E_{L/R} + \Delta_{R/L}$ features are seen above the first such feature. In cuts 1-3, these appear as repetitions of the $E_{L/R} + \Delta_{R/L}$ features, while in cuts 4-6 features with the opposite slope of the subgap state also appear. Similar features have been observed in other devices [33, 34] and we ascribe them to multiple sub-bands in the proximitized InAs nanowire [29]. In this scenario, a conductance peak would appear for each sub-band coherence peak as the bias voltage is increased [30].

We model the DQD as two Anderson models with superconducting leads and an additional interdot tunnel coupling. For simplicity, we employ a spin-polarized mean field approximation [21, 35], which is known to capture the characteristic gate-dependence of the YSR state [24, 36]. This artificially spin-polarized description omits inter-dot exchange, which is anyway negligible since $t_d \ll U_{L/R}$. To circumvent artificial spin-blockade, the spin-polarizing mean fields are chosen to point in orthogonal directions on each dot: $\boldsymbol{B}_L = \hat{\boldsymbol{z}} U_L/2$ and $\boldsymbol{B}_R = \hat{\boldsymbol{x}} U_R/2$ [35]. With these caveats, we regard the model as a qualitative description of the experimental situation.

To calculate the nonlinear $I-V$ characteristics, we employ Keldysh Floquet Green functions incorporating both MAR, and relaxation processes. The current is $P(E)$-broadened by a Gaussian of width $\sigma = 0.04\Delta \approx 6\,\mu$eV before calculating the conductance [30]. Results of the calculations are shown in Fig. 4. Parameters are kept fixed except for ϵ_L and ϵ_R, which are chosen so as to match the linecuts shown in Fig. 3. Tunnelling rates, $\Gamma_{L/R}$, are chosen such that the slope with gate voltage of each YSR state matches the experiment. Intrinsic relaxation rates are assumed symmetric, $\eta_L = \eta_R$, and together with t_d they are tuned to match the overall conductance scale and the size of conductance steps between different relaxation regimes. In the calculations shown in Fig. 4, we observe the previously described $eV = E_L + E_R$ and $eV = \Delta_{L/R} + E_{R/L}$ features alongside the stepwise changes in conductance at transitions between different relaxation regimes.

Some analytical insight on the relaxational current carried at $eV = E_L + E_R$ can be obtained by solving a phenomenological master equation of the Lindblad form [37] As detailed in the supplement, this leads to a Lorentzian current peak,

$$I = \frac{e}{h} \frac{2\pi\gamma_e^2 \left[\Lambda_L \left(1 + \frac{\gamma_R}{\Lambda_R}\right) + \Lambda_R \left(1 + \frac{\gamma_L}{\Lambda_L}\right)\right]}{\gamma_e^2 \frac{(\Lambda_L+\Lambda_R)^2}{\Lambda_L \Lambda_R} + \frac{(\Lambda_L+\Lambda_R)^2}{4} + (eV - E_L - E_R)^2}, \quad (1)$$

where $\gamma_e^2 = v_L^2 u_R^2 t_d^2$ is the rate of electron transfer between the left hole component with amplitude v_L, and the right electron component with amplitude u_R. The total relaxation rate for each side is $\Lambda_{L/R} = \eta_{L/R} + \gamma_{L/R}$ with $\eta_{L/R}$ being the intrinsic relaxation rate, and $\gamma_{L/R}$ the rate of relaxation occurring via Andreev reflections as sketched in Fig. 1(c). Using Fermi's golden rule, we infer the rates to be $\gamma_L = \pi u_L^2 t_d^2 d_R(2E_L + E_R)$ and $\gamma_R = \pi v_R^2 t_d^2 d_L(-2E_R - E_L)$ with u_L (v_R) being the corresponding electron (hole) component amplitudes and $d_{L/R}(E)$ the density of states at energy E. For the corresponding $eV = -E_L - E_R$ peak let $E_{L/R} \to -E_{L/R}$, substitute u and v, and the above formulas apply. As shown in the Supplemental Material, these formulas perfectly match the results obtained from Keldysh Floquet Green functions for $eV = \pm(E_L + E_R)$. In the limit $\eta_{L/R} \gg \gamma_{L/R}, \gamma_e$, Eq. (1) reduces to Fermi's golden rule, and the bias asymmetry reflects directly the ratio between electron and hole amplitudes, $u_R^2 v_L^2 / v_R^2 u_L^2$. For $\eta_L = \eta_R$ and $\gamma_L = \gamma_R = 0$, which is the regime relevant in the blue region of Fig. 1(b), Eq. (1) reproduces the results of Ref. [19]. In the regime relevant for the present experiment, $t_d \gg \eta_{L/R}$ and hence $\gamma_e, \gamma_{L/R} \gg \eta_{L/R}$ when outside of the blue region in Fig. 1(b), the bias asymmetry appears reversed compared to the Fermi's golden rule limit [30]. Comparing Figs. 3 and 4 (a, e), this asymmetry is seen to be reproduced by the transport calculation. A similar reversed asymmetry has been observed also by STM spectroscopy of YSR states probed by a superconducting continuum at $eV = E_{L/R} + \Delta_{R/L}$ [18].

Extending the master equation to include the doublet nature of the odd-parity subgap states, we find that the relaxational current generally depends on the ground state (odd-parity doublet or even-parity singlet), and that a finite spin relaxation rate, Γ_s, must be included in order to avoid spin-blockade. Such spin relaxation has been measured in a similar device [12]. Consistency with the experimental data requires that $\gamma_e \gg \Gamma_s \gg \eta_{L,R}$ [30].

Without independent estimates of t_d, Γ_s and the continuum density of states $d_{L/R}(E)$, we cannot confidently extract intrinsic relaxation rates $\eta_{L,R}$. Nevertheless, a number of qualitative conclusions can be drawn: 1) We observe only very weak subgap mirages [33, 38] indicative of a hard gap [30]; 2) Intrinsic relaxation must be present and be largely independent of the bound-state energy; 3) No quasiparticle poisoning, spontaneously exciting the ground state, is observed, since this would lead to lines at $eV = E_L - E_R$ [19] and $eV = \Delta_{L/R} - E_{R/L}$ [38] with opposite gate-voltage curvature. The last two observations indicate that the intrinsic relaxation is neither due to quasiparticle poisoning in the leads nor to high-energy phonon/photon modes [14]. More likely, the nearby normal metallic Ti/Au leads act as quasiparticle traps with a weak tunnel coupling to the quantum dots. This is consistent with our modelling of subgap-state relaxation as arising from a weak tunnel coupling to a large-bandwidth metallic lead, which also explains the weak low-voltage mirages observed in the experiment [30].

In conclusion, we have presented measurements of direct transport between two subgap states in a DQD setup. The electrical tunability of this setup allowed us

to explore the transition between two different relaxation regimes, identified as stepwise changes in conductance along the $eV = E_L + E_R$ subgap resonance. We developed a model for the gateable subgap states, including intrinsic relaxation via weak tunnel coupling to a nearby normal metal, and a transport calculation combining MAR and relaxation was found to explain the observed signatures and provided excellent agreement with the experimental data. The presented bound-state-to-bound-state measurements hinge on the availability of intrinsic relaxation processes, yielding key insights into the underlying population dynamics of gateable subgap states relevant for future designs of superconducting qubits.

The authors thank Juan Carlos Cuevas and Christian Ast for fruitful discussion. The project received funding from the European Union's Horizon 2020 research and innovation program under the Marie Sklodowska-Curie grant agreement No. 832645. We additionally acknowledge financial support from the Carlsberg Foundation, the Independent Research Fund Denmark, QuantERA 'SuperTop' (NN 127900), the Danish National Research Foundation, Villum Foundation project No. 25310, and the Sino-Danish Center. P. K. acknowledges support from Microsoft and the ERC starting Grant No. 716655 under the Horizon 2020 program. J.N., K.G-R and A.L.Y. acknowledge European Union's Horizon 2020 research and innovation programme for financial support grant No. 828948 (AndQC). A.L.Y. acknowledges support by Spanish MICINN through grants FIS2017-84860-R and through the "María de Maeztu" Programme for Units of Excellence in R&D (Grant No. MDM-2014-0377).

[1] A. V. Balatsky, I. Vekhter, and J.-X. Zhu, Rev. Mod. Phys. **78**, 373 (2006).
[2] A. Yazdani, B. A. Jones, C. P. Lutz, M. F. Crommie, and D. M. Eigler, Science **275**, 1767 (1997).
[3] K. J. Franke, G. Schulze, and J. I. Pascual, Science **332**, 940 (2011).
[4] D. Chatzopoulos, D. Cho, K. M. Bastiaans, G. O. Steffensen, D. Bouwmeester, A. Akbari, G. Gu, J. Paaske, B. M. Andersen, and M. P. Allan, Nat. Commun. **12**, 1 (2021).
[5] C. W. J. Beenakker and H. van Houten, Phys. Rev. Lett. **66**, 3056 (1991).
[6] L. Tosi, C. Metzger, M. F. Goffman, C. Urbina, H. Pothier, S. Park, A. L. Yeyati, J. Nygård, and P. Krogstrup, Phys. Rev. X **9**, 011010 (2019).
[7] E. Prada, P. San-Jose, M. W. A. de Moor, A. Geresdi, E. J. H. Lee, J. Klinovaja, D. Loss, J. Nygård, R. Aguado, and L. P. Kouwenhoven, Nat. Rev. Phys. **2**, 575 (2020).
[8] F. Nichele, A. C. C. Drachmann, A. M. Whiticar, E. C. T. O'Farrell, H. J. Suominen, A. Fornieri, T. Wang, G. C. Gardner, C. Thomas, A. T. Hatke, P. Krogstrup, M. J. Manfra, K. Flensberg, and C. M. Marcus, Phys. Rev. Lett. **119**, 136803 (2017).
[9] C. Janvier, L. Tosi, L. Bretheau, Ç. Ö. Girit, M. Stern, P. Bertet, P. Joyez, D. Vion, D. Esteve, M. F. Goffman, H. Pothier, and C. Urbina, Science **349**, 1199 (2015).
[10] T. W. Larsen, K. D. Petersson, F. Kuemmeth, T. S. Jespersen, P. Krogstrup, J. Nygård, and C. M. Marcus, Phys. Rev. Lett. **115**, 127001 (2015).
[11] M. Hays, G. de Lange, K. Serniak, D. J. van Woerkom, D. Bouman, P. Krogstrup, J. Nygård, A. Geresdi, and M. H. Devoret, Phys. Rev. Lett. **121**, 047001 (2018).
[12] M. Hays, V. Fatemi, D. Bouman, J. Cerrillo, S. Diamond, K. Serniak, T. Connolly, P. Krogstrup, J. Nygård, A. L. Yeyati, A. Geresdi, and M. H. Devoret, arXiv (2021), 2101.06701.
[13] M. Zgirski, L. Bretheau, Q. Le Masne, H. Pothier, D. Esteve, and C. Urbina, Phys. Rev. Lett. **106**, 257003 (2011).
[14] D. G. Olivares, A. L. Yeyati, L. Bretheau, Ç. Ö. Girit, H. Pothier, and C. Urbina, Phys. Rev. B **89**, 104504 (2014).
[15] C. Wang, Y. Y. Gao, I. M. Pop, U. Vool, C. Axline, T. Brecht, R. W. Heeres, L. Frunzio, M. H. Devoret, G. Catelani, L. I. Glazman, and R. J. Schoelkopf, Nat. Commun. **5**, 1 (2014).
[16] M. Marín-Suárez, J. T. Peltonen, and J. P. Pekola, Nano Lett. **20**, 5065 (2020).
[17] I. Martin and D. Mozyrsky, Phys. Rev. B **90**, 100508 (2014).
[18] M. Ruby, F. Pientka, Y. Peng, F. von Oppen, B. W. Heinrich, and K. J. Franke, Phys. Rev. Lett. **115**, 087001 (2015).
[19] H. Huang, C. Padurariu, J. Senkpiel, R. Drost, A. L. Yeyati, J. C. Cuevas, B. Kubala, J. Ankerhold, K. Kern, and C. R. Ast, Nat. Phys. **16**, 1227 (2020).
[20] J. C. Cuevas, A. Martín-Rodero, and A. L. Yeyati, Phys. Rev. B **54**, 7366 (1996).
[21] A. Villas, R. L. Klees, H. Huang, C. R. Ast, G. Rastelli, W. Belzig, and J. C. Cuevas, Phys. Rev. B **101**, 235445 (2020).
[22] A. Jellinggaard, K. Grove-Rasmussen, M. H. Madsen, and J. Nygård, Phys. Rev. B **94**, 064520 (2016).
[23] E. J. H. Lee, X. Jiang, M. Houzet, R. Aguado, C. M. Lieber, and S. De Franceschi, Nat. Nanotechnol. **9**, 79 (2014).
[24] J.-D. Pillet, C. H. L. Quay, P. Morfin, C. Bena, A. L. Yeyati, and P. Joyez, Nat. Phys. **6**, 965 (2010).
[25] J. C. Estrada Saldaña, A. Vekris, G. Steffensen, R. Žitko, P. Krogstrup, J. Paaske, K. Grove-Rasmussen, and J. Nygård, Physical Review Letters (2018).
[26] Z. Su, A. B. Tacla, M. Hocevar, D. Car, S. R. Plissard, E. P. A. M. Bakkers, A. J. Daley, D. Pekker, and S. M. Frolov, Nat. Commun. **8**, 1 (2017).
[27] D. Bouman, R. J. J. van Gulik, G. Steffensen, D. Pataki, P. Boross, P. Krogstrup, J. Nygård, J. Paaske, A. Pályi, and A. Geresdi, Phys. Rev. B **102**, 220505 (2020).
[28] D. Averin and A. Bardas, Phys. Rev. Lett. **75**, 1831 (1995).
[29] J. C. Estrada Saldaña, A. Vekris, R. Žitko, G. Steffensen, P. Krogstrup, J. Paaske, K. Grove-Rasmussen, and J. Nygård, Phys. Rev. B **102**, 195143 (2020).
[30] See Supplemental Material at [URL] for supporting data, and details of the theory and modelling, which includes Refs. [17–21, 25, 29, 31, 33, 35–41].
[31] Parameters used in plots: $\Delta_L = \Delta_R = \Delta = 0.14$meV,

$B_L = B_R = 7$, $\Gamma_L = 6.65$, $\Gamma_R = 4.2$, $t_d = 0.73$, $\eta_L = \eta_R = 3.75 \times 10^{-4}$, $T = 10^{-3}$ and $\sigma = 0.04$ all in units of Δ. The BCS density of states of the superconducting leads are broadened by $\eta_s = 10^{-6}\Delta$ for numerical reasons.

[32] J. Bauer, A. Oguri, and A. C. Hewson, J. Phys.: Condens. Matter **19**, 486211 (2007).

[33] Z. Su, A. Zarassi, J.-F. Hsu, P. San-Jose, E. Prada, R. Aguado, E. J. H. Lee, S. Gazibegovic, R. L. M. Op het Veld, D. Car, S. R. Plissard, M. Hocevar, M. Pendharkar, J. S. Lee, J. A. Logan, C. J. Palmstrøm, E. P. A. M. Bakkers, and S. M. Frolov, Phys. Rev. Lett. **121**, 127705 (2018).

[34] A. M. Whiticar, A. Fornieri, A. Banerjee, A. C. C. Drachmann, S. Gronin, G. C. Gardner, T. Lindemann, M. J. Manfra, and C. M. Marcus, arXiv (2021), 2101.09706.

[35] A. Villas, R. L. Klees, G. Morrás, H. Huang, C. R. Ast, G. Rastelli, W. Belzig, and J. C. Cuevas, Phys. Rev. B **103**, 155407 (2021).

[36] M. Žonda, V. Pokorný, V. Janiš, and T. Novotný, Sci. Rep. **5**, 1 (2015).

[37] H.-P. Breuer and F. Petruccione, in *The Theory of Open Quantum Systems* (Oxford University Press, Oxford, England, UK, 2007).

[38] A. Kumar, M. Gaim, D. Steininger, A. L. Yeyati, A. Martín-Rodero, A. K. Hüttel, and C. Strunk, Phys. Rev. B **89**, 075428 (2014).

[39] J.-d. Pillet, *Tunneling spectroscopy of the Andreev bound states in a carbon nanotube*, Ph.D. thesis, l'Université Pierre et Marie Curie (2011).

[40] A. I. Rusinov, JETP Lett. **9**, 85 (1969), [Zh. Eksp. Teor. Fiz. **9**, 146 (1968)].

[41] D. Manzano, AIP Adv. **10**, 025106 (2020).

10

ARTICLE 3 - SUPPLEMENT

In this chapter we present the supplement of project 3, slightly edited to fit the structure of the thesis. Unedited version can be found at Ref.[3]. References to main article and Fig. 1-4 relate to the attached article in chapter 9.

10.1 EXPERIMENTAL DETAILS

10.1.1 *Parameter extraction*

We obtain the charging energies, U_L and U_R, from Coulomb-diamond spectroscopy. The data, shown in Fig. 10.1, were taken in the same shell as those shown in the main article, but for a slightly different gate configuration, which corresponds to the zero-bias differential conductance colormap shown in Fig. 10.1 (a), through which gates 2 and 4 were swept to obtain the Coulomb diamond plots for both quantum dots in the superconducting state. This change in gate configuration was done to reduce the coupling of the left quantum dot to the left lead, and thereby obtain sharper Coulomb diamonds. The charging energies are given by the distance in bias voltage between the edge of the superconducting gap and the apex of the central diamond in Figs. 10.1 (b, c) and they correspond to $U_L \approx U_R \approx 2$ meV.

The superconducting gap is extracted using the same gate setting as in the main text, focusing on the nearly gate independent lowermost conductance peak right outside the $eV = E_L + E_R$ feature in Fig. 10.1 (d). These lines are due to transport between subgap state and opposing gap at $eV = E_{L/R} + \Delta_{R/L}$. At the gate voltage where $eV = E_L + E_R = 0$, we infer that $E_L = E_R = 0$ and read off the values $\Delta_L \approx \Delta_R \approx 0.14$ meV directly from these peak positions (for positive and negative V, respectively).

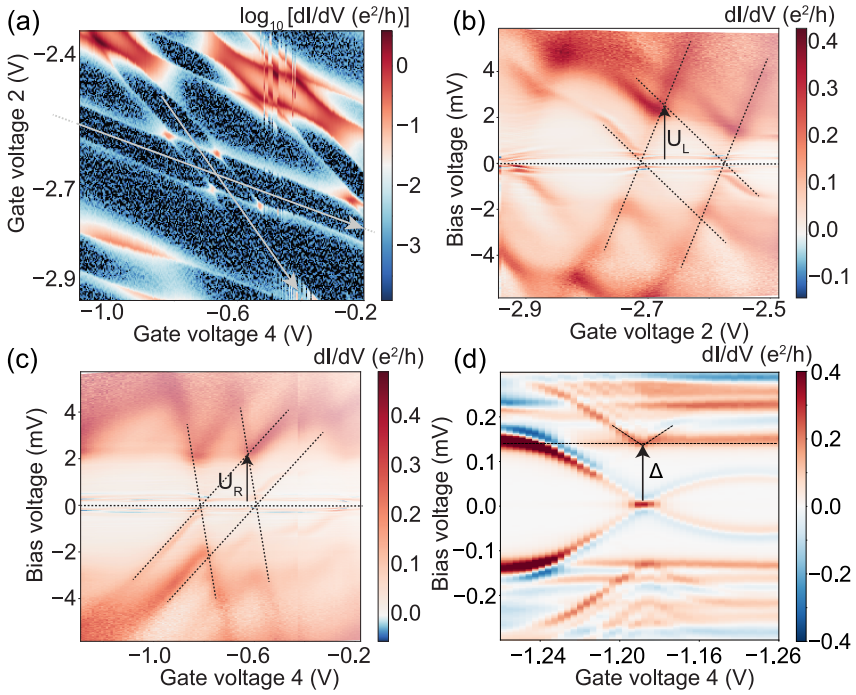

Figure 10.1: (a) Colormap of zero-bias differential conductance in logarithmic scale versus gates 2 and 4, with gates 1, 3, 5 set at -9.2 V, -9 V, and -0.36 V, respectively, and the backgate set at 10.4 V. Arrows show gate sweep trajectories in (b) and (c). (b, c) Colormaps of differential conductance versus bias voltage and gate voltage representing Coulomb-diamond spectroscopy of each quantum dot, with the other quantum dot conducting in series in cotunnelling. Dashed lines are drawn on top of the diamonds as a guide to the eye, with the same slope as higher bias features. (d) Colormap of differential conductance versus bias and gate voltage following half the range of linecut 2 in Fig. 3 in the main text. Dotted lines indicate $eV = \Delta_{L/R} + E_{R/L}$ features.

10.1.2 *Zero-bias conductance*

In Fig. 2 (b) of the main text, we showed zero-bias conductance in a logarithmic scale versus gate voltages 2 and 4. In that diagram, the horizontal features are noted to be sixty times fainter than the vertical features. The faint features cannot be distinguished in the data in Fig. 3 of the main text, as their conductance is too small for the color scale shown there. In Fig. 10.2, we show differential conductance colormaps which correspond to low-bias versions of Fig. 3 of the main text, with adjusted color scales to highlight the faint features. A zero-bias peak traverses all colormaps, which we attribute to a dissipative supercurrent discussed is chapter 3 and 4. This zero-bias feature is visible in all subplots except (b) where the scale is set by the $eV = E_L + E_R$ which continues to zero bias. The dissipative supercurrent peak is only one component

of the zero-bias conductance in Fig. 2 (b) of the main text. A second component comes from the crossing of low-bias mirages of the subgap states (similar to those discussed in subsection 8.3.4), which are too faint to be seen in Fig. 3 of the main text but clearly visible in Figs. 10.2 (a-f). We associate these low-bias mirages with transport between the subgap state and a small residual metallic density of states in the superconducting Al leads, which is consistent with our modelling, as demonstrated below in subsection 10.2.3.

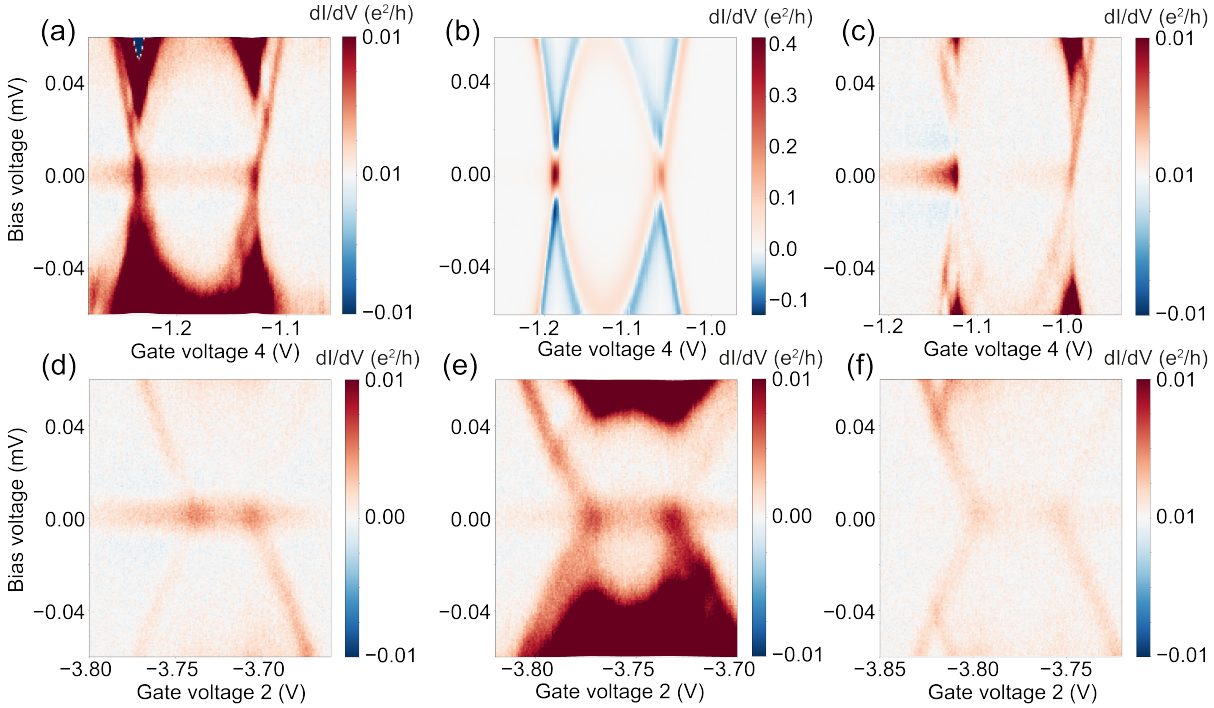

Figure 10.2: (a-f) Colormaps of differential conductance versus bias voltage taken through the same gate trajectories as in Fig. 3 of the main text, but with a much reduced bias voltage range.

10.2 FLOQUET GREEN'S FUNCTIONS

In this section we detail the Floquet Green's function calculation underlying results shown in Fig. 4 in the main text. The Green's functions need to include tunnelling to all orders, since the relaxation rate of the subgap states is a small parameter compared to tunneling [46, 169]. Additionally, to capture the Andreev mediated relaxation channels utilizing the opposing gap, our model is required to include multiple Andreev reflections, which is achieved via a Floquet representation [150].

We start with the S-DQD-S Hamiltonian where we from the smallness of t_d compared to $\Gamma_{L/R}$ assume that each dot is in bias equilibrium with its neighbouring superconductor yielding,

$$H(t) = H_L(t) + H_R(t) + H_T, \tag{10.1}$$

$$H_j(t) = H_{jS}(t) + H_{jd}, \qquad j \in \{L, R\} \tag{10.2}$$

$$H_{jS}(t) = \sum_{k\sigma} (\epsilon_k - \mu_j) c^\dagger_{jk\sigma} c_{jk\sigma} + \sum_k \left(\Delta_j(t) c^\dagger_{jk\uparrow} c^\dagger_{jk\downarrow} + \text{h. c.} \right), \tag{10.3}$$

$$H_{jd} = \sum_\sigma (\epsilon_j - \mu_j) d^\dagger_{j\sigma} d_{j\sigma} + U_j d^\dagger_{j\uparrow} d^\dagger_{j\downarrow} d_{j\downarrow} d_{j\uparrow} + t_j \sum_\sigma \left(d^\dagger_{j\sigma} c_{j\sigma} + \text{h. c.} \right), \tag{10.4}$$

$$H_T = t_d \sum_\sigma d^\dagger_{L\sigma} d_{R\sigma} + \text{h. c.}, \tag{10.5}$$

This Hamiltonian describes a left and right QD-S system in equilibrium at $\mu_{L/R}$, coupled by a tunnel element t_d much smaller than $U_{L/R}$, such that exchange interaction can be neglected, but not necessarily small on the order of relaxation rates $\eta_{L/R}$ important for transport. The difference in equilibrium is enforced by the voltage bias $eV = \mu_L - \mu_R$. The time dependence of $H_{Sj}(t)$ resides solely on the phase $\Delta_j(t) = \Delta e^{2i\mu_j t/\hbar}$, enforcing the Josephson relation as discussed in chapter 7. Next, we follow the recipe of chapter 7 starting with the gauge transformation $U(t) = U_L(t) U_R(t)$ with,

$$U_j(t) = \exp\left[i\mu_j t/\hbar \sum_\sigma \left(d^\dagger_{j\sigma} d_{j\sigma} + \sum_k c^\dagger_{jk\sigma} c_{jk\sigma} \right) \right], \tag{10.6}$$

which forms a new effective Hamiltonian with $\mu_{L/R}$ and the time dependence of Δ gauged onto a time-dependent tunnel coupling $\bar{H}_T(t)$. In this form we can calculate transport to all orders using,

$$\begin{aligned}
\langle I_0 \rangle &= \frac{e}{h}\int_{-\infty}^{\infty} d\omega \, \mathrm{Tr}\,\mathrm{Re}\left[\tau_z \underline{M}^R(\omega)\left(\underline{\Sigma}^<_{LL}(\omega)\underline{g}^A_L(\omega) + \underline{\Sigma}^R_{LL}(\omega)\underline{g}^<_L(\omega)\right)\underline{M}^A(\omega)\right]_{00}, \\
\underline{M}^X(\omega) &= 1 + \underline{\Sigma}^X_{LL}(\omega)\underline{g}^X_L(\omega)\underline{M}^X(\omega), \\
\underline{\Sigma}^X_{LL,nm}(\omega) &= \begin{pmatrix} \delta_{n,m}t_d^2 g^X_{R,(11)}(\omega+(n-1)eV) & -\delta_{n,m+2}t_d^2 g^X_{R,(12)}(\omega+(n-1)eV) \\ -\delta_{n,m-2}t_d^2 g^X_{R,(21)}(\omega+(n+1)eV) & \delta_{n,m}t_d^2 g^X_{R,(22)}(\omega+(n+1)eV) \end{pmatrix},
\end{aligned} \tag{10.7}$$

if we can describe the left/right side by a single particle Green's function from a non-interacting Hamiltonian. As discussed in chapter 8 this requires an approximation to handle the interaction $U_{L/R}$. The main focus of the present calculation is to capture the peak-to-peak transport processes between two opposing supgab states, and the influence of various relaxation processes depicted in Fig. 1. Next, we present a minimal model which captures these processes before we move on to the full calculations used in the main text.

10.2.1 *Minimal Model*

The additional Andreev mediated relaxation processes $\gamma_{L/R}$ stems from the interaction between subgap state and quasiparticles with energy $E_{qp} \geqslant \Delta$, and competes with intrinsic relaxation $\eta_{L/R}$. As a minimal left and right Green's function we therefore propose,

$$\begin{aligned}
g^R_L(\omega) &= \frac{1}{\omega + i\eta_L/2 - E_L}\begin{pmatrix} 1 & 1 \\ 1 & 1 \end{pmatrix} + i\nu_L\theta(|\omega|-\Delta_L), \\
g^R_R(\omega) &= \frac{1}{\omega + i\eta_R/2 + E_R}\begin{pmatrix} 1 & 1 \\ 1 & 1 \end{pmatrix} + i\nu_L\theta(|\omega|-\Delta_R), \\
g^<_{L/R}(\omega) &= \left(g^A_{L/R}(\omega) - g^R_{L/R}(\omega)\right) n_F(\omega),
\end{aligned} \tag{10.8}$$

which consists of two subgap states at energy $E_{L/R}$ with relaxation $\eta_{L/R}$ and a for simplicity assumed constant gap described by $\nu_{L/R}$. The factor of two in $\eta_{L/R}$ is chosen to better compare with master equations, such that $\eta_{L/R}$ corresponds to the relaxation rate of an excitation in the Lindblad approach. The subgap state, modelled in 2×2 Nambu with spinor $\Phi_{L/R} = \left(d_{L/R\uparrow}, d^\dagger_{L/R\downarrow}\right)$, is of a classical spin form with equal electron and hole component $u_{L/R} = \nu_{L/R} = 1$. This can also be obtained as a limit of the spin-polarized mean-field approximation as shown in section 8.1. The choice of

different signs of E_L and E_R in the denominator is due to the spin-polarized nature of the subgap state. As we want a current to run for $eV = E_L + E_R$, where the left electron component is aligned with right hole component, we need to make sure both are the same spin species, guaranteed by the sign. If $\mathrm{sgn}(E_L) = \mathrm{sgn}(E_R)$ transport will be spin-blockaded as of the spin-polarized nature.

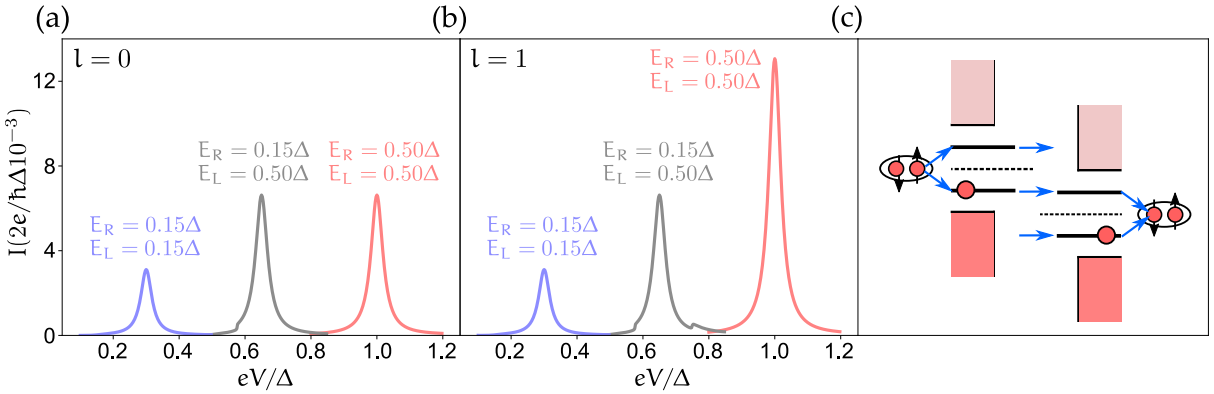

Figure 10.3: (a, b) Plot of current peaks around $eV = E_L + E_R$ using eq. (10.7) and Green's functions eq. (10.8) for various E_L and E_R. Colors match the diagram shown in Fig. 2 (b) in the main text indicating the presence of Andreev mediated relaxation processes. l is the number of included Floquet subbands and calculations are done with $t_d = 0.01\Delta$, $\eta_L = \eta_R = 0.002\Delta$, $\nu_L = \nu_R = 5\Delta$, and temperature $T = 0$. Convergence is obtained already at $l = 1$. (c) Schematic of the transport process requiring both γ_L and γ_R which is not captured by $l = 0$.

In fig. 10.3 we show current peaks at $eV = E_L + E_R$ for various energies, corresponding to the three different regimes shown in Fig. 1 (b) of the main text. Calculations are done with $t_d \gg \eta_L, \eta_R$ such that higher order transport processes dominate, and we are not in the Fermi's golden rule limit. Here we find higher current peaks at positions where Andreev mediated relaxation processes are available, and we find that additional Floquet supbands, $l = 1$, are required to capture this effect. This is markedly different than results of section 8.3.3 where additional subbands where only necessary for MAR processes appearing at integer values of other processes, e.g. $eV = 2\Delta/n$ or $eV = (E_L + \Delta_R)/n$. In contrast, here we see amplification of a peak already appearing at $l = 0$, indicating that to capture peak-to-peak transport at $eV = E_L + E_R$ higher order Floquet is required. Setting ν_L and ν_R to zero makes all peaks have the same height in fig. 10.3, highlighting the influence of Andreev processes.

10.2.2 *Spin-Polarized Mean-field model*

To describe the interaction between superconductor and quantum dot, we utilize a non-self-consistent spin-polarized mean field approximation in which the charging energy, U, is replaced by an effective magnetic field $B = U/2$ as presented in section 8.1. Whereas this approximation omits dynamical spin-flips of the dot spin (and hence Kondo-correlations) altogether, it is known to correctly capture many aspects of YSR states [33]. Importantly, this approximation incorrectly describes the odd-parity groundstate of the dot-superconductor system as a singlet state. As we discuss using master equations in section 10.3.2, this does affect the relaxational transport cycles, albeit in a manner which only leads to quantitative differences in the relaxation rates that one might attempt to infer from a transport experiment. Furthermore, since the mean-field approximation causes the odd-parity singlet state to be spin-polarized, some groundstate configurations would show artificial spin blockade. To circumvent this, we choose the magnetic mean-fields on each dot to be orthogonal, such that transport occurs via projections between orthogonal spin-spaces allowing transport in all groundstate configurations [158].

In this model we approximate the dot Hamiltonian in eq. (10.1) to,

$$\bar{H}_{jd} = \frac{1}{2}\Phi_j^\dagger \left(\epsilon_j \tau_z + B_j \sigma_j\right) \Phi_j \tag{10.9}$$

with $j \in \{L, R\}$, Pauli matrices $\sigma_L = \sigma_z$, $\sigma_R = \sigma_x$ and using the 4×4 spinor $\Phi_j = \left(d_{j\uparrow}, d_{j\downarrow}, d_{j\downarrow}^\dagger, -d_{j\uparrow}^\dagger\right)$, and bar indicates that μ_j is gauge transformed away. The left and right dot Green's function are then tractable, and includes a superconducting self-energy term $\Sigma_{jS}(\omega)$ and a relaxation term $\bar{\eta}_j$,

$$g_j^R(\omega) = \left[\omega + i\bar{\eta} - \epsilon_j \tau_z - B_j \sigma_j - \Sigma_{jS}^R(\omega)\right]^{-1} \tag{10.10}$$

$$\Sigma_{jS}^R(\omega) = -\Gamma_j \frac{\omega - \Delta_j \tau_x}{\sqrt{\Delta^2 - (\omega + i\eta_s)^2}} \tag{10.11}$$

where η_S is included purely for numerical purposes. Following the derivations of section 8.1 this Green's function yield a spectrum with a single subgap state and an effective relaxation rate,

$$\eta_j = 8\bar{\eta}_j B_j \Delta_j \Gamma_j^2 / (B_j^2 + \Gamma_j^2)^2 \tag{10.12}$$

valid around $\epsilon_j = 0$, again with a factor of two difference to better with master equations. As we in experiment only observe features we associate with relaxation processes, we simply choose the lesser component to be given by the fluctuation-dissipation theorem,

$$g_j^<(\omega) = \left(g_j^A(\omega) - g_j^R(\omega)\right) n_F(\omega) \tag{10.13}$$

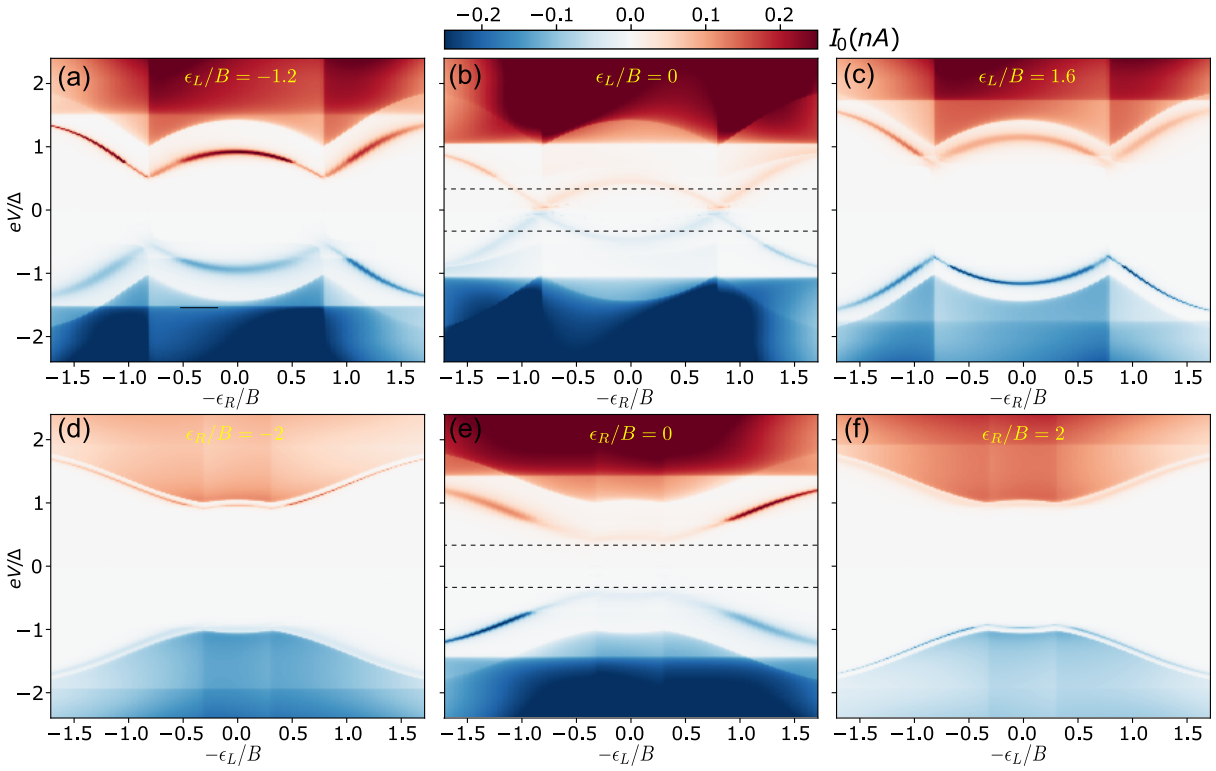

Figure 10.4: (a-f) Calculation of current as a function of bias and dot tuning ϵ_i with $l = 1$. Dot tuning is chosen to match linecuts in Fig. 3 in the main article. Dotted lines in (b) and (e) indicate the bias range shown in figs. 10.5. Parameters used in plots: $\Delta_L = \Delta_R = \Delta = 0.14$ meV, $B_L = B_R = 7$, $\Gamma_L = 6.65$, $\Gamma_R = 4.2$, $t_d = 0.73$, $\eta_L = \eta_R = 3.75 \times 10^{-4}$, $T = 10^{-3}$ all in units of Δ. The BCS density of states of the superconducting leads are broadened by $\eta_s = 10^{-6}\Delta$ for numerical reasons.

with $T = 10^{-3}\Delta$ effectively corresponding to $T = 0$ for our purposes. These Green's function are then used as left and right lead to calculate current through the Floquet Keldysh equations, eq. (10.7).

In fig. 10.4 we show current calculated in this manner with $l = 1$ which is enough to ensure convergence of the salient features observed in Fig. 10.4. In the low-bias region of these plots however, additional fine structure which requires more sidebands exist. These will be in investigated further in the next subsection 10.2.3.

In comparison to the experimental data, these calculations show large changes in width of the $eV = E_L + E_R$ peaks for different dot tunings, and the sharp features in current will therefore dominate the non-linear conductance, dI_0/dV. These differences are in realistic descriptions smeared out by an additional $P(E)$ broadening, reflecting the inevitable fluctuations in bias voltage, which are present in realistic circuits. This we implement as a convolution of current, $I(V) = \int_{-\infty}^{\infty} dE I_0(E) P(E - V)$, with a gaussian

distribution, $P(E) = e^{-E^2/2\sigma^2}/\sqrt{2\pi}\sigma$, with a spread $\sigma = 0.04\Delta \approx 6\,\mu eV$, chosen to make the width of conductance peaks similar to observed peak width in experiment. The plots presented in Fig. 4 in the main text are obtained from such $P(E)$-broadening of the plots shown in Figs. 10.4 along the bias axis, followed by numerical differentiation to obtain the conductance.

10.2.3 *Low bias features*

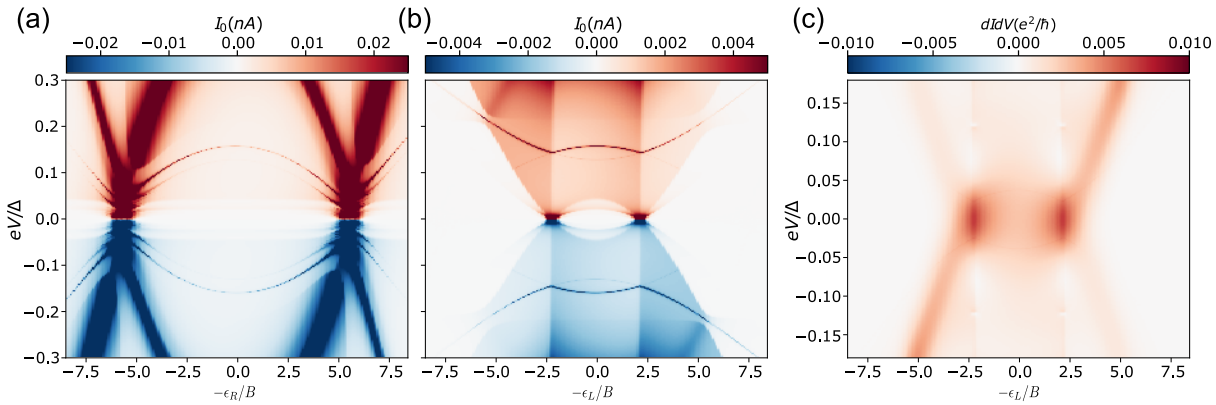

Figure 10.5: Calculations of low bias current with (a) $\epsilon_L = 0$ and (b) $\epsilon_R = 0$ corresponds to (b) and (e) in Fig. 10.5. (c) Conductance obtained by convolving and differentiating current in (b). All plots are with the same parameters as in fig. 10.4. and using 4 sidebands.

In this subsection we investigate the effects of multiple Andreev reflections for small bias, for which it is necessary to include more Floquet bands to assure convergence. In Figs. 10.5 (a) and (b) we show low-bias current calculations using $l = 2$. This is enough to observe a number of sharp lines of current at integer fractions of the previously described features, i.e. $eV = (E_{L/R} + \Delta_{R/L})/n$ (cf. also Ref. [155]) and $eV = (E_L + E_R)/n$ [158]). As the areas under these current peaks are much smaller than for the $n = 1$ peaks at higher bias, the subsequent $P(E)$ broadening used above renders these low-bias features unobservable in the experiment. In Fig. 10.5 (b) we also identify current plateaus starting at $eV = E_{L/R}$, which we identify as the weak metallic density of states (DOS), which we use to model the intrinsic relaxation, probing the subgap state [71, 155]. In Fig. 10.5 (c) we show the nonlinear conductance obtained by $P(E)$-broadening and subsequent differentiation of the current in Fig. 10.5 (b). This is seen to smear out the sharp MAR signal and leaves a marked set of conductance peaks of height comparable to those observed in the experimental data shown in Figs. 10.2. The fact that the weak metallic DOS, which we have included as a model

for the intrinsic relaxation needed to describe the $eV = E_L + E_R$ peaks in experiment, also yields a consistent description of the weak replicas crossing zero in experiment suggests that the metallic DOS is a real feature of the experiment rather than a just a simple means of modelling relaxation.

10.2.4 *Multigap model*

In the experiment, multiple higher-lying replicas of the $eV = E_{L/R} + \Delta_{R/L}$ feature are observed. In this subsection we illustrate how such replicas can arise from including multiple subbands in the proximitized InAs wires comprising the leads. Modelling the DOS of each of the two superconducting leads ($i = L, R$) by a sum of BCS peaks for each subband (indexed here by $j = 1, 2, 3, 4, 5$) with each their gap, $\Delta_{ij} \in \{1.0, 1.1, 1.2, 1.3, 1.4\}\Delta$ with $\Delta = 0.14$ meV, the left and right tunnelling self-energies are readily found as,

$$\Sigma^R_{ii}(\omega) = -\Gamma_i \sum_j \frac{\omega + \Delta_{ij}\tau_x}{\sqrt{\Delta_{ij}^2 - (\omega + i\eta_s)^2}}. \tag{10.14}$$

This self-energy is then used to compute the left, and right Green's functions as to obtain the current using the Keldysh Floquet formula eq. (10.7).

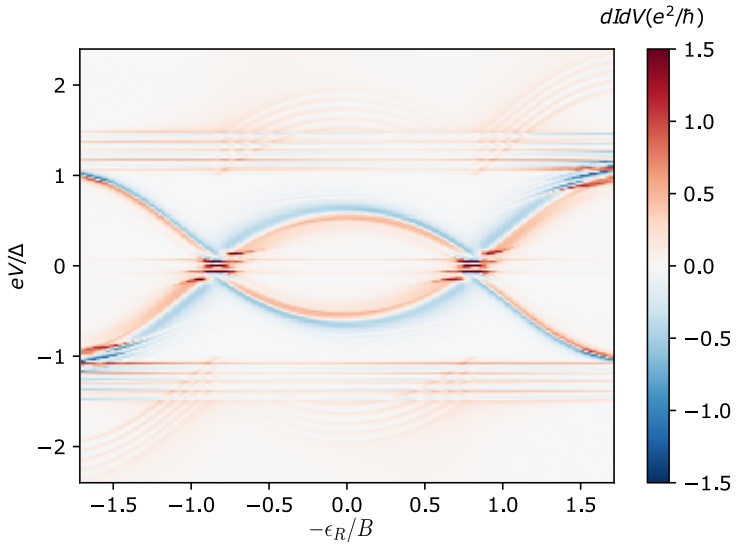

Figure 10.6: Calculation of conductance using Eq. (10.14) as a function of energy tuning with $\epsilon_L = 0$. Calculations are truncated at two Floquet sub-bands so results close to zero $eV < 0.2\Delta$ could contain additional contributions. With similar parameters as in fig. 10.3 but with $\Gamma_L = 1.3$ and $\Gamma_R = 0.8$ in units of Δ.

Results of this calculations are shown in Fig. 10.6, which corresponds linecut 2 in Fig. 3 in the main text. One observes replicas of the $eV = E_{L/R} + \Delta_{R/L}$ feature appearing as individual subband BCS peaks probe the opposing subgap state. At the same time, only one subgap state is formed on either side, yielding only a single $eV = E_L + E_R$ feature. We note that earlier calculations using the zero-bandwidth approximation have shown similar results [73]. Interestingly, as the bound state acquires quasiparticle spectral weight from 5 different subbands, their individual BCS peaks remain relatively sharp, unlike for a single subband for which the YSR state depletes its BCS peak altogether. These residual BCS peaks in a multi-subband system therefore lead to enhanced MAR processes and the $eV = E_{L/R} + \Delta_{R/L}$ features exhibit negative differential conductance. All these features of course depend on the tunnelling rates of the individual subbands, all of which were here assumed to be equal for simplicity.

10.3 MASTER EQUATIONS FOR SUBGAP STATE TRANSPORT

To obtain a more complete understanding of the relaxational transport between two subgap states at resonance, we support the Green's function analysis above by a separate calculation of the current using master equations of the Lindblad form for the boundstate density matrix (cf. e.g. Refs. [171, 172], and references therein). This approach follows the procedure used in ref. [51] to describe subgap transport with intrinsic relaxation, but here expanded to also include relaxation by Andreev reflections.

With the simplifying assumption that both groundstate and excited state of each subgap system are non-degenerate (singlets) the full Hilbert space of the system is spanned by $|0,0\rangle$, $|0,1\rangle$, $|1,0\rangle$ and $|1,1\rangle$ where left and right number refers to the state of left and right subgap state respectively, which can be either in its groundstate, 0, or in its excited state, 1. In terms of the bias-voltage detuning, $e\delta V = eV - E_L - E_R$, the coherent dynamics of the subgap system is captured by the 2×2 Hamiltonian of the even-parity subspace $\{|0,0\rangle, |1,1\rangle\}$,

$$H_{2\times 2} = \begin{pmatrix} -e\delta V/2 & \gamma_e \\ \gamma_e & e\delta V/2 \end{pmatrix} \tag{10.15}$$

with tunnelling amplitudes for transitions $|0,0\rangle \leftrightarrow |1,1\rangle$ denoted by γ_e. This amplitude is given by $\gamma_e = v_L u_R t_d$, if the left hole peak is aligned with the right electron peak ($\delta V = 0$) as in Fig. 10.7 (c), and by $\gamma_e = u_L v_R t_d$ in the opposite case for negative bias ($eV = -E_L - E_R$). By themselves, these coherent transitions do not carry any net

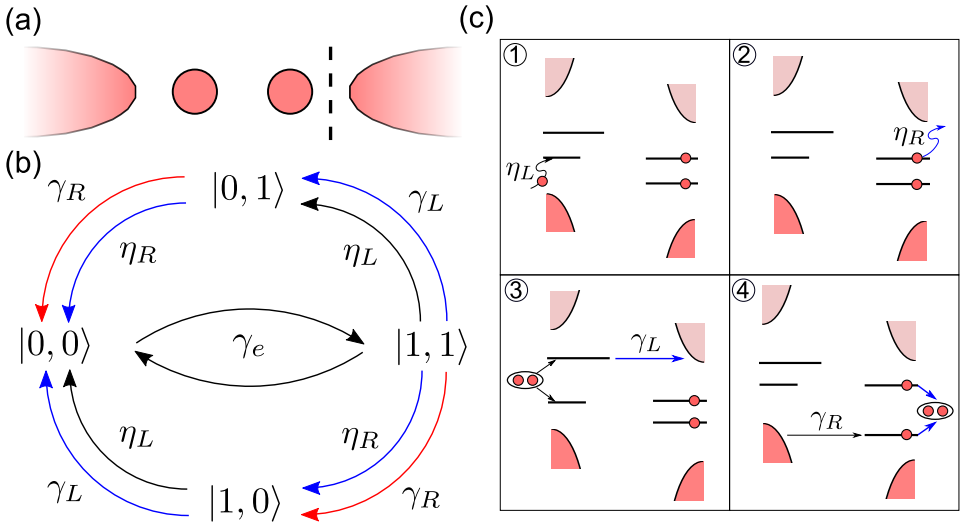

Figure 10.7: (a) System schematic. Dashed line indicates where current is counted. (b) Diagram of transport dynamics. Black lines transfer no electrons, while blue lines transfer one electron and red lines transfer two electrons. (c) Schematic drawing of relaxation processes where blue lines indicate when an electron pass the barrier in (a).

current, and for this we need to include incoherent relaxation processes. We include four independent relaxation rates, η_i and γ_i for $i \in \{L, R\}$ shown in Figs. 10.7 (c), where η_i describes intrinsic relaxation processes occurring in each lead independently, while γ_i describe relaxation through Andreev reflection employing the density of states in the opposing lead .

We choose to calculate the current as the rate of electrons leaving the right subgap state and entering the right lead. With this definition, η_R and γ_L both transfer one electron while γ_R transfers two electrons as shown in fig. 10.7 (c). The current can then be written as,

$$I = 2\pi\frac{e}{h}\left[(2\gamma_R + \gamma_L + \eta_R)P_{11} + (2\gamma_R + \eta_R)P_{10} + \gamma_L P_{01}\right], \tag{10.16}$$

where $P_i = \rho_{ii}$ is the occupation probability of state $|i\rangle$, found as the diagonal elements, ρ_{ii}, of the 4×4 density matrix operating in the full Hilbert space spanned by states $\{|0,0\rangle, |0,1\rangle, |1,0\rangle, |1,1\rangle\}$. In order to determine the density matrix, the total relaxation rates on either side, $\Lambda_i = \eta_i + \gamma_i$, are included via jump operators

$$L_1 = \sqrt{\Lambda_L}\,|0,1\rangle\langle 1,1|, \quad L_2 = \sqrt{\Lambda_R}\,|1,0\rangle\langle 1,1|, \tag{10.17}$$

$$L_3 = \sqrt{\Lambda_L}\,|0,0\rangle\langle 1,0|, \quad L_4 = \sqrt{\Lambda_R}\,|0,0\rangle\langle 0,1|, \tag{10.18}$$

whereby the density matrix is found by solving the Lindblad master equation:

$$\hbar\frac{d\rho}{dt} = i\left[H_{2\times2}, \rho\right] + \sum_i \left(L_i \rho L_i^\dagger - \frac{1}{2}\{L_i^\dagger L_i, \rho\}\right), \tag{10.19}$$

where $\{\cdot,\cdot\}$ denotes an anti-commutator. Rewriting this equation, and keeping only off-diagonal terms for $|1,1\rangle$ and $|0,0\rangle$ where tunnel coupling builds coherence, we obtain,

$$\begin{aligned}\hbar\frac{d\rho}{dt} = i\left[H_{2x2}, \rho\right] &- (\Lambda_R + \Lambda_L)P_{11}\,|1,1\rangle\langle 1,1| + (\Lambda_R P_{10} + \Lambda_L P_{01})\,|0,0\rangle\langle 0,0| \\ &+ (\Lambda_L P_{11} - \Lambda_R P_{01})\,|0,1\rangle\langle 0,1| + (\Lambda_R P_{11} - \Lambda_L P_{10})\,|1,0\rangle\langle 1,0| \\ &- \frac{(\Lambda_R + \Lambda_L)}{2}\left(\rho_{11,00}\,|1,1\rangle\langle 0,0| + \rho_{00,11}\,|0,0\rangle\langle 1,1|\right),\end{aligned} \tag{10.20}$$

which we solve for the steady state occupation numbers by enforcing $\frac{d\rho}{dt} = 0$ and $\sum_i P_i = 1$. This yields $P_{01} = \frac{\Lambda_L}{\Lambda_R}P_{11}$, $P_{10} = \frac{\Lambda_R}{\Lambda_L}P_{11}$ and

$$P_{11} = \frac{\gamma_e^2}{\gamma_e^2\frac{(\Lambda_L+\Lambda_R)^2}{\Lambda_L\Lambda_R} + \frac{(\Lambda_L+\Lambda_R)^2}{4} + e^2\delta V^2}. \tag{10.21}$$

From this, we obtain the expression for the current presented in the main text describing a Lorentzian peaked around $eV = E_L + E_R$:

$$I = 2\pi\frac{e}{h}\frac{\gamma_e^2\left[\Lambda_L\left(1+\frac{\gamma_R}{\Lambda_R}\right) + \Lambda_R\left(1+\frac{\gamma_L}{\Lambda_L}\right)\right]}{\gamma_e^2\frac{(\Lambda_L+\Lambda_R)^2}{\Lambda_L\Lambda_R} + \frac{(\Lambda_L+\Lambda_R)^2}{4} + e^2\delta V^2}. \tag{10.22}$$

If we extract the bound state energies, E_i, and the effective relaxation rates, η_i, from the denominator in eq. (10.11), in addition to the coherence factors u_i and v_i, we can calculate the Andreev mediated relaxation rate by Fermi's golden rule:

$$\gamma_L = \pi u_L^2 t_d^2 d_R(2E_L + E_R) \quad \text{and} \quad \gamma_R = \pi v_R^2 t_d^2 d_L(-2E_R - E_L), \tag{10.23}$$

for positive biases where the left hole peak is aligned with the right electron peak. For the opposite case, left electron sector aligned with right hole sector, let $u_i \to v_i$, $v_i \to u_i$ and $E_i \to -E_i$. In fig. 10.8 we compare results obtained from the master equation and the Keldysh Floquet Green's functions, respectively. Apart from the continuum, which is not included in the former, this demonstrates an excellent match between the two different methods when it comes to describing the relaxational current peaks at $eV = \pm(E_L + E_R)$.

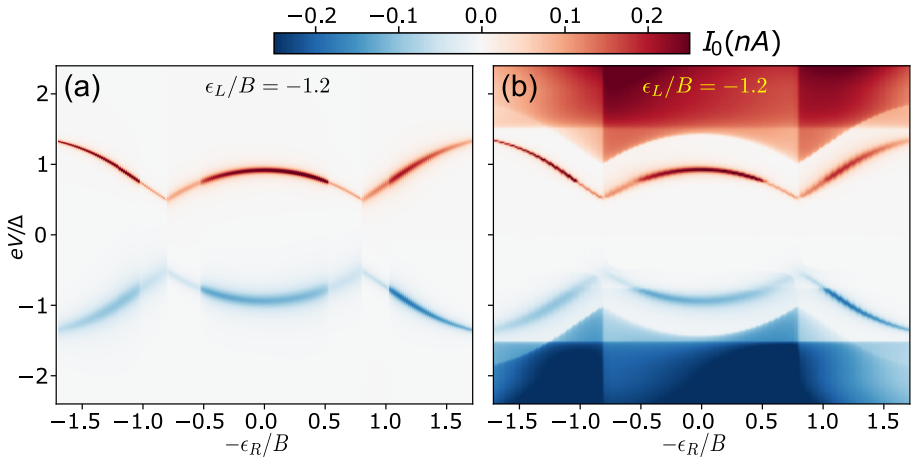

Figure 10.8: Calculation of current using master equations. (a) is calculated using eq. (10.22) and (b) shows plot fig. 10.4 (a). Parameters used for the master equation are similar as in fig. 10.4.

10.3.1 *Conductance asymmetry*

Both data and theory show a notable bias asymmetry in conductance near $eV = \pm(E_L + E_R)$. In the limit, $\eta_i \gg t_d$, where current can be calculated using Fermi's golden rule, we expect this asymmetry to reflect directly the frequency asymmetry of the underlying spectral function, which is present for $u_i \neq v_i$ away from the particle-hole symmetric point. As the width of conductance features is provided by $P(E)$-broadening, the interesting quantity to compare is the integral of eq. (10.22), since this area under the current peak determines the conductance. In the limit of $\eta_i \gg \gamma_i, \gamma_e$ we find this area to be

$$A_I = 4\pi^2 \frac{e}{h} \gamma_e^2. \tag{10.24}$$

Since γ_e^2 is proportional to the spectral weight of the aligned peaks ($\gamma_e^2 \propto v_L^2 u_R^2$ for left hole aligned with right electron sector) the asymmetry of this area matches that of the underlying spectral functions, and the bias asymmetry is set by the ratio $v_L^2 u_R^2 / u_L^2 v_L^2$. In the opposite limit where $t_d \gg \eta_i$, we instead obtain

$$A_I = 4\pi^2 \frac{e}{h} \frac{\gamma_e^2}{\sqrt{\frac{\gamma_e^2}{\gamma_L \gamma_R} + \frac{1}{4}}} \tag{10.25}$$

for which it is the factor $v_L^2 u_R^2 / u_L^2 v_L^2$ in competition with $\pi^2 t_d^2 d_L(2E_L + E_R) d_R(-2E_R - E_L)$, which determines the bias asymmetry This complicated relation strongly depends on the energy levels ϵ_i (set by the gate voltages in the experiment) which determine the coherence factors u_i, v_i, and for the parameters extracted for the present experiment

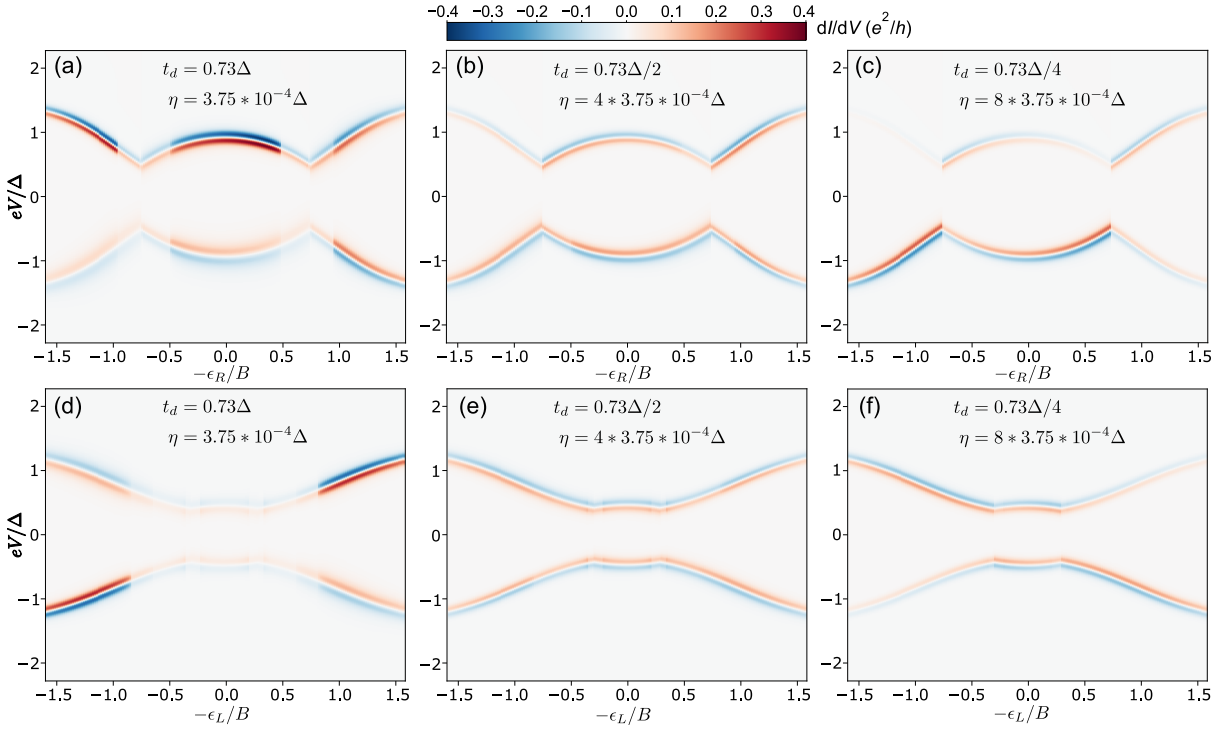

Figure 10.9: Calculation of conductance using eq. (10.22) with a P(E) convolution for three different values of η_i. (a-c) are with $\epsilon_L/B = -8.4$ and (d-f) are with $\epsilon_R/B = 0$. Other parameters used similar as in fig. 10.4. Plots (c) and (f) correspond to the Fermi's golden rule limit.

the marked conductance asymmetry is opposite to that of the Fermi's golden rule limit, as seen in Fig. 10.9, indicating a relatively weak intrinsic relaxation rate, $\eta_i \ll t_d$. This reversal of asymmetry is similar to the one demonstrated for S-QD-S systems in subsection 8.3.2, and measured in STM [46]

10.3.2 *Singlet-to-doublet Master Equations*

So far, we have simplified the transport calculations by using spin-polarized mean-field theory, which has lead to non-degenerate subgap states. There is, however, no reason to believe that spin rotational invariance should be broken in this system and each of the (left/right) subgap excitations are therefore expected to be comprised of a singlet and a doublet state. The total number of states for the two subgap state system is then 9, instead of 4, with states $|S,S\rangle$, $|S,\sigma\rangle$, $|\sigma,S\rangle$ and $|\sigma,\sigma'\rangle$ with $\sigma \in \{\uparrow,\downarrow\}$ and left/right position denoting left/right subgap state. In this final section, we extend the master equations to deal with the full spin-degenerate problem. This allows us to assess the

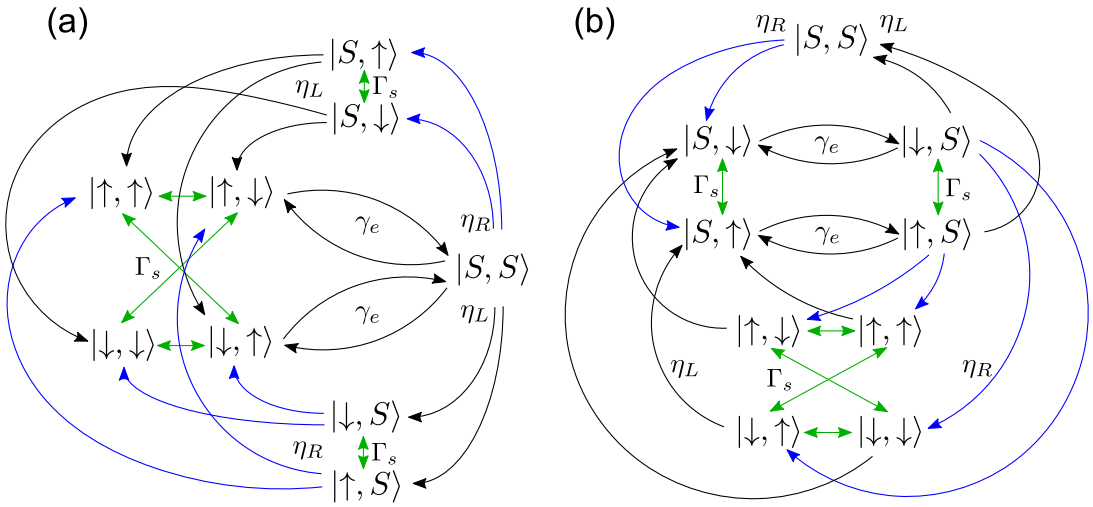

Figure 10.10: Schematic of transport dynamics. (a) is for the $|\sigma,\sigma'\rangle$ groundstate while (b) is for the $|S,\sigma\rangle$ groundstate. Black lines indicate processes that transfer no electrons while blue lines indicate processes that transfer a single electron. Green lines indicate spin-flip processes that does not change fermion parity. Lines with γ_e we treat as coherent processes the rest are modelled as jump operators. To obtain the corresponding diagram for the $|S,S\rangle$ and $|\sigma,S\rangle$ groundstate flip direction of all η_i lines in (a) and (b) correspondingly.

potential shortcomings of the spin-polarized mean field approximation in the transport calculations presented above and in the main text.

Our approach follows the template from the singlet-to-singlet master equation. For simplicity, we assume that relaxation by Andreev reflection can be ignored, i.e. $\gamma_i \approx 0$, corresponding to the blue regime in Fig. 1 (b). We assume that relaxation occurs independently on either side, such that a doublet $|\sigma\rangle$ relaxes to singlet state $|S\rangle$, while a singlet relaxes either to $|\uparrow\rangle$ or $|\downarrow\rangle$. Both processes are assumed to take place with rates η_i. As such, singlet states experience a higher total relaxation rate than doublet states. In fig. 10.10 (a) we show a heuristic diagram of the governing dynamics when both subgap states are in a doublet groundstate, $|\sigma,\sigma'\rangle$, with bias $eV = E_L + E_R + e\delta V$ such that coherent tunneling can drive transitions $|\uparrow,\downarrow\rangle$, $|\downarrow,\uparrow\rangle \leftrightarrow |S,S\rangle$. The coherent part is described by the Hamiltonian,

$$H_{DD-SS} = \begin{pmatrix} e\delta V/2 & \gamma_e & -\gamma_e \\ \gamma_e & -e\delta V/2 & 0 \\ -\gamma_e & 0 & -e\delta V/2 \end{pmatrix} \tag{10.26}$$

where the first entrance is the $|S,S\rangle$ state and second and third are $|\uparrow,\downarrow\rangle$ and $|\downarrow,\uparrow\rangle$, respectively. In this relaxation scheme, the system may end up in triplet state, $|\sigma,\sigma\rangle$, which will block the current. A similar spin blockade were observed in Ref. [101],

although there calculations are in a very different formalism. To lift this Pauli spin blockade, we include a spin-flip rate, Γ_s, which flips the spin of the subgap state without changing fermion parity. These are included as Markovian jump operators, just as for the quasiparticle relaxation, and are represented by green arrows in fig. 10.10.

The Lindblad master equation now takes the following form:

$$\hbar\frac{d\rho}{dt} = i\left[H_{DD-SS},\rho\right] + \sum_i \left[L_i\rho L_i^\dagger - \frac{1}{2}\{L_i^\dagger L_i,\rho\}\right], \tag{10.27}$$

where ρ is a 9×9 density matrix. For each arrow in fig. 10.10 (indexed by i in the summation in eq. (10.27)) pointing from state l to a state k, we include a jump operator $L = \sqrt{X}\,|k\rangle\langle l|$ with rate X. Since only the 3×3 block of eq. (10.26) builds coherence, we can set all other non-diagonal components to zero. Solving the diagonal part of the master equation for the non-coherent part allows one to simplify the remaining master equation to a 3×3 matrix equation, $\hbar\dot{\rho} = i\left[H_{DD-SS},\rho\right] + M$, with M given by

$$M_{DD} = \begin{pmatrix} -2\eta_T\rho_{11} & -(\eta_T+\Gamma_s)\rho_{12} & -(\eta_T+\Gamma_s)\rho_{13} \\ -(\eta_T+\Gamma_s)\rho_{21} & \eta_T\rho_{11} & -2\Gamma_s\rho_{23} \\ -(\eta_T+\Gamma_s)\rho_{31} & -2\Gamma_s\rho_{32} & \eta\rho_{11} \end{pmatrix}, \tag{10.28}$$

for doublet-doublet groundstate, and

$$M_{SS} = \begin{pmatrix} 2c\eta_T\rho_{22} & -(\eta_T/2+\Gamma_s)\rho_{12} & -(\eta_T/2+\Gamma_s)\rho_{13} \\ -(\eta_T/2+\Gamma_s)\rho_{21} & -c\eta_T\rho_{22} & -(\eta_T+2\Gamma_s)\rho_{23} \\ -(\eta_T+\Gamma_s)\rho_{31} & -(\eta_T+2\Gamma_s)\rho_{32} & -c\eta_T\rho_{22} \end{pmatrix}, \tag{10.29}$$

for singlet-singlet groundstate. Here $\eta_T = \eta_L+\eta_R$ and $c = (\eta_T+2\Gamma_s)/(\eta_T+4\Gamma_s)$, and the state indices on ρ have been defined as $SS = 1$, $\uparrow\downarrow = 2$ and $\downarrow\uparrow = 3$. Spin rotational invariance dictates that $\rho_{22} = \rho_{33}$. Solving for the normalized ($\mathrm{Tr}[\rho] = 1$) steady state ($\dot{\rho} = 0$) density matrix, and counting transported electrons from the η_R process, similar to eq. (10.16), we obtain the following currents for the different groundstate configurations

$$I_{DD} = 2\pi\frac{e}{h}\frac{\gamma_e^2(\eta_T+2\Gamma_s)}{e^2\delta V^2 + (\eta_T+2\Gamma_s)^2 + \frac{1}{2}\gamma_e^2\frac{\eta_T+2\Gamma_s}{\eta_T}\left[3+\frac{\eta_T^2}{\eta_L\eta_R}+\frac{5}{2}\frac{\eta_T}{\Gamma_s}\right]}, \tag{10.30}$$

$$I_{SS} = 2\pi\frac{e}{h}\frac{2\gamma_e^2(\eta_T+\Gamma_s)}{e^2\delta V^2 + \frac{(\eta_T+\Gamma_s)^2}{4} + \gamma_e^2\frac{\eta_T+\Gamma_s}{\eta_T}\left[2+2\frac{\eta_L^2+\eta_R^2}{\eta_L\eta_R}+\frac{\eta_T}{\eta_T+\Gamma_s}\right]}. \tag{10.31}$$

Both formulas are Lorentzians and for $\Gamma_s \to 0$ we find $I_{DD} \to 0$ while I_{SS} remains finite, reflecting the triplet blockade occurring if no spin-relaxation is present. In the

case of a singlet-doublet groundstate configuration, $|S,\sigma\rangle$, the $eV = E_L + E_R$ resonance drives transitions $|S,\sigma\rangle \leftrightarrow |\sigma,S\rangle$ as seen in fig. 10.10 (b). We setup up a master equation in a similar manner as before but now the system is composed of two symmetrical 2×2 blocks,

$$H_{SD-DS} = \begin{pmatrix} e\delta V/2 & \gamma_e \\ \gamma_e & -e\delta V/2 \end{pmatrix} \text{ and } M_{SD} = \begin{pmatrix} -\hat{\eta}\rho_{11} & -(\Gamma_s + \hat{\eta}/2)\rho_{12} \\ -(\Gamma_s + \hat{\eta}/2)\rho_{21} & \hat{\eta}\rho_{11} \end{pmatrix}, \tag{10.32}$$

in the basis $\{|S,\uparrow\rangle, |\uparrow,S\rangle\}$ and with $\hat{\eta} = \eta_R + 2\eta_L$. Similarly, the corresponding equation for a doublet singlet configuration, $|\sigma,S\rangle$, is obtained with $\hat{\eta} = 2\eta_R + \eta_L$. Utilizing again the spin-rotational invariance, we solve for the steady state density matrix and obtain the following current:

$$I_{SD} = 2\pi\frac{e}{h}\frac{\gamma_e^2(\bar{\eta}+\Gamma_s)}{e^2\delta V^2 + \frac{(\bar{\eta}+2\Gamma_s)^2}{4} + \gamma_e^2\frac{\bar{\eta}+2\Gamma_s}{2\bar{\eta}}\frac{\bar{\eta}^2}{\eta_L+\eta_R}}, \tag{10.33}$$

which again takes a Lorentzian form.

Next, we compare these results with experimental findings. A low-bias region, corresponding to the relaxational regime without Andreev mediated relaxation considered in this subsection, is clearly visible in linecuts 1, 2 and 5 presented in Fig. 3 of the main text. Following the $eV = E_L + E_R$ features through the gate voltage at which they change slope and the subgap system changes groundstate, we do not observe any notable change in conductance. This observation enforces restrictions on parameters if current is indeed described by eqs. (10.30), (10.31), and (10.33). The fact that we observe a finite conductance in the doublet-doublet sector means that Γ_s cannot be zero. Overall, the experimental data are consistent with the assumption that $\gamma_e \gg \Gamma_s \gg \eta_L = \eta_L = \eta$, which ensures the lifting of Pauli spin blockade. As discussed in the previous subsection, the conductance is best described in terms of the area under the current peak, since this is independent of the $P(E)$ broadening. In the said limit of rates, one finds,

$$A_{SS} = 2\pi\frac{e}{h}\frac{2}{\sqrt{3}}\gamma_e\sqrt{\eta\Gamma_s}, \tag{10.34}$$

$$A_{DS} = 2\pi\frac{e}{h}\sqrt{\frac{2}{3}}\gamma_e\sqrt{\eta\Gamma_s}, \tag{10.35}$$

$$A_{DD} = 2\pi\frac{e}{h}\sqrt{\frac{2}{7}}\gamma_e\sqrt{\eta\Gamma_s}, \tag{10.36}$$

with $A_{ij} = \int_{-\infty}^{\infty} d\delta V I_{ij}(\delta V)$. The fact that these three areas are equal up to a factor of approximately $\sqrt{2}$, and remain so in a wide parameter range without requiring fine

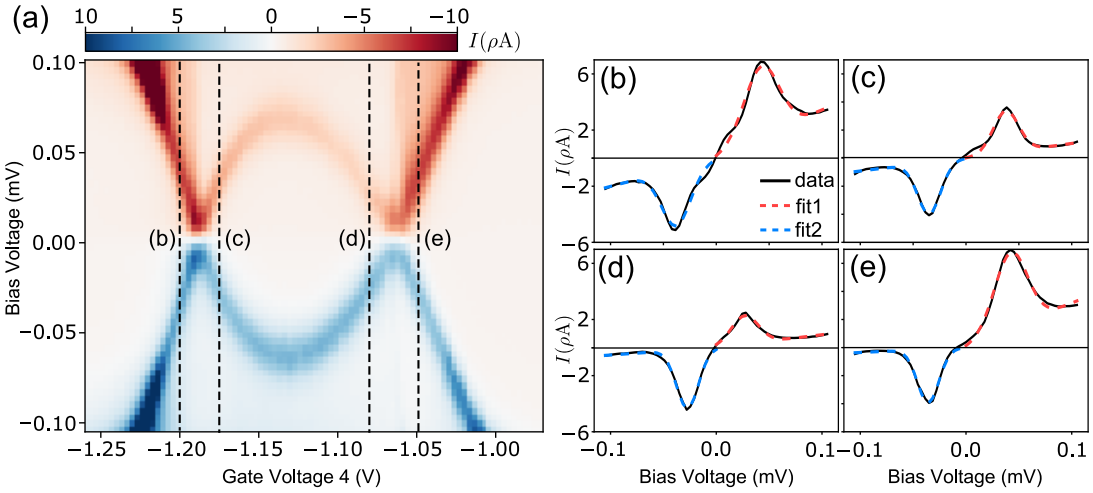

Figure 10.11: (a) Experimentally acquired current as a function of bias and gate following linecut 2 in Fig. 3 of the main text. Dashed lines indicate cuts shown in (b-e). (b-e) Current as a function of bias for cuts on either side of the two phase transitions. The positive and negative peak are fitted by a Gaussian function plus a linear function accounting for tails.

tuning of rates is consistent with the experimental observation that the peak to peak conductance is largely constant across the phase transitions (changes in groundstate).

To test this finding in greater detail, we consider again linecut 2 from Fig. 3 in the main text, for which $eV = E_L + E_R$ crosses zero two times within the regime where there is no Andreev mediated relaxation (cf. fig. 10.11 (a)). In Fig. 10.11 (b-e) we show the results of fitting a Gaussian plus a linear function to the current peaks. From these fits, we extract the area under the positive and negative current peaks, excluding any contribution from the linear part, before and after the phase transition at the two crossings. Going from (b) to (c), or from (e) to (d), corresponds to a phase transition from a DS, to a DD groundstate, as can be inferred from the charge diagram in Fig. 2 (b) of the main text. Comparing the area of the negative (positive) bias peaks in the DS sector with the area of the positive (negative) bias peak in the DD sector, we find that

$$\frac{A_{b+}}{A_{c-}} \approx 2.3, \quad \frac{A_{b-}}{A_{c+}} \approx 1.9, \quad \frac{A_{e+}}{A_{d-}} \approx 2.2, \quad \frac{A_{e-}}{A_{d+}} \approx 1.3, \tag{10.37}$$

where A_{b+} denotes the area of the fitted Gaussian positive-bias peak at gate voltage indicated by the dashed line at (b), not including the contribution from the linear part of the fit, which is required in order to fit the tails. In the small distance between (b) and (c), and (e) and (d), respectively, it is reasonable to assume that coherence factors, u_i and v_i, are approximately constant, such that γ_e remains constant. The ratio between

expressions (10.35) and (10.36) should therefore be constant, i.e. $\frac{A_{DS}}{A_{DD}} = \sqrt{\frac{7}{3}} \approx 1.5$, slightly smaller then what we find by fitting.

In conclusion, we find that reinstalling spin-rotational invariance by including an odd-parity doublet groundstate results in Lorenztian current peaks at the $eV = E_L + E_R$ resonance, just as for the singlet-singlet modeling building on the spin-polarized mean field approximation. Including the doublet state, however, it becomes apparent that the observation of relaxational peak-to-peak current in the doublet-doublet phase relies on a large spin-flip rate, $\Gamma_s \gg \eta$. At the same time, the observation of a stepwise change in conductance at the boundary between two different relaxation regimes requires strong interdot tunnelling, $\gamma_e \gg \Gamma_s$. Altogether, the hierarchy $\gamma_e \gg \Gamma_s \gg \eta_i$ with $\eta_L \approx \eta_R$, as employed in the main text, provides a consistent description of the experimental data. This includes the observation that the current peaks at $eV = E_L + E_R$ only change by a minor factor of approximately $\sqrt{2}$ when undergoing groundstate transitions.

11

PROJECT 4

In this project we investigate a very similar device, consisting of an InAs nanowire with epitaxial aluminium removed in a central region, where a double quantum dot is gated. The nanowire is placed in a SQUID geometry, allowing for measurements of the full CPR. In contrast to our previous device, where we extracted critical current I_c by fitting of zero-bias peaks, we in this device measure the S-DQD-S junctions switching current I_{DQD}. If no noise is present we expect $I_{DQD} \approx I_c$ [117], but for the low I_{DQD} measured in this junction $I_{DQD} \ll I_c$ is more likely due to noise-activated switching, although I_{DQD} and I_c are still positively correlated. The major advantage of this setup is the ability to identify the 0 and π phase through the CPR, which can be compared to groundstate inferred from the charge diagram. Here we find complete agreement between data and predictions from 4^{th} order perturbation theory and ZBW models, presented in chapter 4. These capabilities are used to investigate the supercurrent analogue of triplet blockade, characterized by a reduction of I_{DQD} in the (1,1) charge sector, when a magnetic field changes the groundstate from an exchange singlet to a triplet state.

The theory for this paper was made in collaboration with Dávid Pataki and András Pályi. Although, we are in the weekly coupled regime where 4^{th} order perturbation is valid, we use ZBW in the main paper due to its simplicity. Apart from collaborating on modelling, my main contribution to this project was the sign arguments presented in subsection 4.2.1 and in appendix B. These simple rules guarantees the sign of I_c, thereby I_{DQD}, from the parity of the groundstate. This shows that the triplet groundstate is firmly 0 phase, although one could think of it as a minimal ferromagnet known to host π phase [173]. The decrease of supercurrent in the triplet phase, amounting to the blockade, is not complete, and stems primarily from the reduction of available cooper-pair paths for the triplet groundstate. Curiously, the blockade is complete both in the limit of $\Delta \to \infty$ and $U \to \infty$, which is shown in the papers supplement [4]. In this project, we also included finite spin-orbit coupling, as is necessary for InAs wires in finite magnetic field. The primary effect of this was the formation of an anti-cross between the exchange singlet and the triplet state in the (1, 1) charge sector.

Rapid Communications

Triplet-blockaded Josephson supercurrent in double quantum dots

Daniël Bouman,[1] Ruben J. J. van Gulik,[1] Gorm Steffensen,[2] Dávid Pataki,[3] Péter Boross,[4] Peter Krogstrup,[2] Jesper Nygård,[2] Jens Paaske,[2] András Pályi,[3] and Attila Geresdi[1,5,*]

[1]*QuTech and Kavli Institute of Nanoscience, Delft University of Technology, NL-2600 GA Delft, The Netherlands*
[2]*Center for Quantum Devices, Niels Bohr Institute, University of Copenhagen, DK-2100 Copenhagen, Denmark*
[3]*Department of Theoretical Physics and MTA-BME Exotic Quantum Phases Research Group, Budapest University of Technology and Economics, H-1111 Budapest, Hungary*
[4]*Institute for Solid State Physics and Optics, Wigner Research Centre for Physics, P.O. Box 49, H-1525 Budapest, Hungary*
[5]*Quantum Device Physics Laboratory, Department of Microtechnology and Nanoscience, Chalmers University of Technology, SE-41296 Gothenburg, Sweden*

(Received 12 August 2020; accepted 2 December 2020; published 21 December 2020)

Serial double quantum dots created in semiconductor nanostructures provide a versatile platform for investigating two-electron spin quantum states, which can be tuned by electrostatic gating and an external magnetic field. In this Rapid Communication, we directly measure the supercurrent reversal between adjacent charge states of an InAs nanowire double quantum dot with superconducting leads, in good agreement with theoretical models. In the even charge parity sector, we observe a supercurrent blockade with increasing magnetic field, corresponding to the spin singlet to triplet transition. Our results demonstrate a direct spin to supercurrent conversion, the superconducting equivalent of the Pauli spin blockade. This effect can be exploited in hybrid quantum architectures coupling the quantum states of spin systems and superconducting circuits.

DOI: 10.1103/PhysRevB.102.220505

Semiconductor quantum dots, where the orbital and spin states of single localized electrons can be controlled [1], are one of the leading platforms for quantum information processing [2]. Specifically, double quantum dots (DQDs) connected in a series [3] became the preferred physical implementation of spin [4], and spin-orbit quantum bits [5] in low-dimensional semiconductor nanodevices, such as heterostructures hosting a two-dimensional electron gas or semiconductor nanowires. In these devices, the readout of the spin quantum state relies on spin-dependent single electron tunneling processes, which then enable charge readout via direct electronic transport [1], charge sensing techniques [6], or dipole coupling to a microwave resonator [7,8].

In a superconducting nanodevice, the dissipationless supercurrent I_S at zero voltage bias is driven by the quantum mechanical phase difference φ up to a maximum amplitude, I_C, the critical current [9]. In the lowest order of tunneling, the supercurrent-phase relationship (CPR) [10] is sinusoidal, $I_S(\varphi) = I_C \sin(\varphi)$, which describes the coherent transfer of single Cooper pairs through the weak link. When the weak link is a nonmagnetic tunnel barrier, a zero phase difference is energetically favorable in the absence of supercurrent, which is described by a positive critical current, $I_C > 0$. In contrast, a negative coupling yields a supercurrent reversal, $I_C < 0$, often denoted a π junction due the π phase shift in the CPR. This negative coupling has been observed in ferromagnetic weak links [11,12], out-of-equilibrium electron systems [13], and semiconductor quantum dot junctions [14,15].

The dependence of the critical current on the spin state and charge state of a DQD has also been addressed theoretically [16–22], and the recent progress in materials science of superconductor-semiconductor hybrid nanostructures [23] enabled measurements of the amplitude of the critical current as well [24,25], in correlation with the charge states of the DQD.

In this Rapid Communication, we report on direct measurements of the CPR through a DQD weak link formed by an electrostatically gated InAs nanowire. By employing a phase-sensitive measurement scheme, where the DQD is embedded in a superconducting quantum interference device (SQUID), we characterize the full CPR of the DQD, enabling a signful measurement of I_C. The direct observation of the supercurrent reversal in the total charge number boundaries allowed us to identify the even and odd occupied states. Finally, the magnetic field dependence of the supercurrent amplitude in the even occupied state reveals the presence of a supercurrent blockade in the spin-triplet ground state, in agreement with numerical calculations.

We built our device (Fig. 1) from an approximately 7-μm-long InAs nanowire grown by molecular beam epitaxy, and *in situ* partially covered by a 6-nm-thick epitaxial aluminum shell with a typical superconducting gap of $\Delta \approx 200$ μeV [23,26]. We formed two segments with the aluminum layer

*Corresponding author: geresdi@chalmers.se

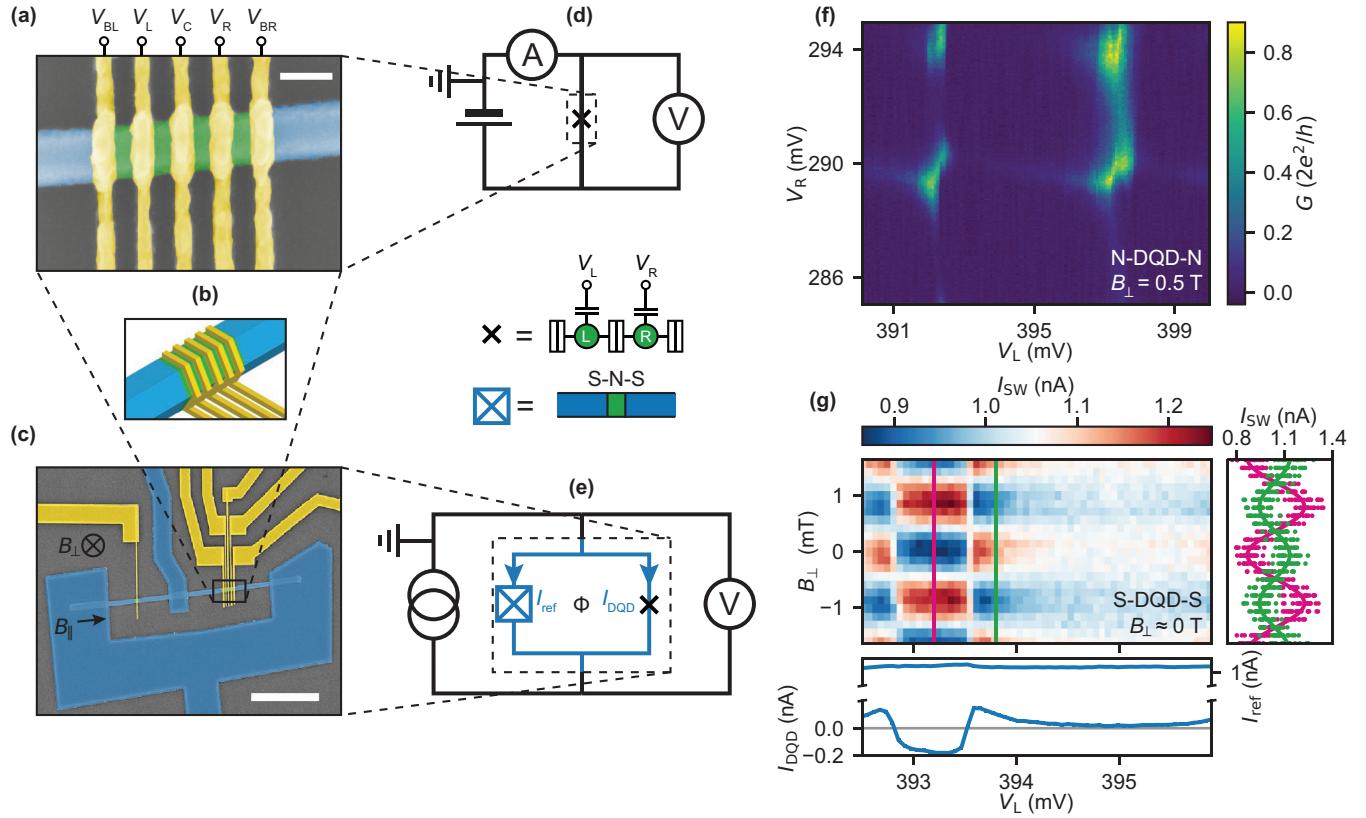

FIG. 1. Device layout and characterization. (a) Color-enhanced electron micrograph of the nanowire DQD junction with five wrap-around gates (yellow) which provide the confining potential. The V_{BL}, V_C, and V_{BR} gate voltages define the barriers, while V_L and V_R control the number of electrons on the dots. The aluminum shell (blue) is selectively etched away in the weak link section (green denotes bare InAs). The scale bar denotes 100 nm. (b) Perspective drawing of the DQD junction highlighting the conformal gates. (c) Color-enhanced electron micrograph of the DC SQUID made of sputtered NbTiN film (in blue) with the reference junction in the left arm and the DQD junction in the right arm. The scale bar denotes 2 μm. (d) The circuit diagram for the normal-state characterization with the reference arm depleted. (e) The measurement scheme of the switching current measurements in the SQUID geometry. (f) Charge stability diagram of the DQD in the normal state at a large magnetic field $B_\perp = 0.5$ T. (g) Switching current color map through three charge states of the DQD and the flux Φ induced by a small $B_\perp$. Each pixel is an average of 18 measurements. The side panel shows all switching current data taken along the magenta and green line, respectively. The solid lines denote the sinusoidal fit yielding the signful oscillation amplitude I_{DQD} and offset I_{ref} (see text). The standard deviation of the phase is $6 \times 10^{-3}\pi$ and $1.2 \times 10^{-2}\pi$ for the magenta and green lines, respectively. The bottom panel displays the fitted I_{ref} and I_{DQD}. The DQD was tuned along the total energy axis [see the solid black line in Fig. 2(a)] and we display the corresponding V_L range on the horizontal axis.

selectively removed where the DQD and the reference arm would be defined. Next, we created the SQUID loop from a sputtered NbTiN superconducting film, and covered the device with a 10-nm-thick AlO_x dielectric by conformal atomic layer deposition. Finally, 40-nm-wide and 50-nm-thick Ti/Au gates [in yellow in Fig. 1(a)] were evaporated under three angles to ensure a conformal coverage around the wire [schematically shown in Fig. 1(b)]. Five gates defined the DQD (on the right) and a single gate controlled the reference arm [on the left in Fig. 1(c)]. Details on the device fabrication are shown in the Supplemental Material [27]. All of our measurements were performed in a dilution refrigerator with a base temperature of approximately 30 mK.

We first characterize the DQD with the leads driven to the normal state by a large magnetic field, $B_\perp = 0.5$ T. We measure the differential conductance dI/dV of the DQD with the reference arm fully depleted [Fig. 1(d)]. We control the coupling to the leads with the gate voltages V_{BL} and V_{BR}, and the interdot coupling is tuned by V_C [Fig. 1(a)]. A characteristic honeycomb diagram is plotted in Fig. 1(f), where the charge occupancy of the dots (n_L, n_R) is set by the voltages applied on the two plunger gates, V_L and V_R.

We perform the CPR measurements with the leads being superconducting and with the reference arm of the SQUID opened with its electrostatic gate so that it exhibits a higher critical current than the DQD arm. Due to this asymmetry, the phase drop over the DQD junction is determined by the magnetic flux Φ through the SQUID loop area [Fig. 1(e)] [14,28], which is proportional to the applied magnetic field $B_\perp$. We measure the switching current I_{SW} of the SQUID by ramping a current bias in a sawtooth wave form and recording the bias current value when the junction switches to the resistive state marked by a threshold voltage drop of the order of 10 μV. We show a typical data set in Fig. 1(g), where each pixel in the main panel is an average of 18 measurements. The right side panel shows the raw data points at two plunger gate settings denoted by the magenta and green lines in the main panel, as well as the fitted sinusoidal curves in the following functional

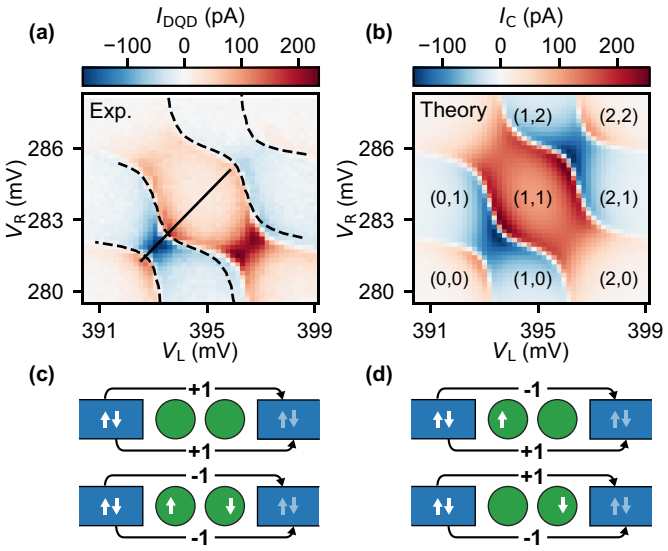

FIG. 2. The supercurrent charge-stability diagram at zero magnetic field. (a) Color map of the measured I_{DQD} as a function of the plunger gate voltages V_L and V_R revealing a supercurrent sign reversal between the adjacent total charge sectors. The dashed lines denote the numerically calculated charge boundaries (see the text). Measurements along the solid line are shown in Figs. 1(g) and 3(a). (b) The ZBW calculation of the critical current I_C of the DQD using the same parameters. The charge occupation of the dots is indicated in parentheses. Visual representations of a Cooper pair transfer when the DQD has an (c) even and (d) odd charge occupation. The ± 1 values indicate the spin permutation parity for each spin species, which yields a supercurrent reversal for an odd charge occupation of the DQD (see the text).

form,

$$I_{SW} = I_{ref} + I_{DQD} \sin \varphi, \tag{1}$$

where $\varphi = 2\pi(B_\perp - B_o)/B_p$, with $B_p \approx 1.7$ mT being the magnetic field periodicity corresponding to a flux change equal to the superconducting flux quantum $\Phi_0 = h/2e$ and B_o being the offset perpendicular magnetic field. The switching current values I_{ref} and I_{DQD} represent the reference arm and the DQD junction contributions, respectively. We show these fitted values as a function of the gate voltage V_L in the lower subpanel of Fig. 1(g), which displays the sign change of I_{DQD} at the charge state boundaries. We note that the change in the environmental impedance [29] causes a slight modulation of I_{ref} as well, despite the lack of any capacitive coupling between the two weak links. However, in our measurements $I_{ref} > 5|I_{DQD}|$ is always fulfilled, enabling a reliable observation of the supercurrent reversal in the DQD.

In Fig. 2(a), we plot I_{DQD} as a function of the plunger gate voltages V_L and V_R, resulting in the zero magnetic field charge-stability diagram of the DQD mapped by the supercurrent. Remarkably, our phase-sensitive measurement directly shows that the supercurrent reversal is associated with the change in the total charge number, and it is absent in the case of internal charge transfers with $(n_L, n_R) \rightarrow (n_L \pm 1, n_R \mp 1)$. However, $|I_{DQD}|$ exhibits maxima near all charge boundaries, consistently with earlier experiments [25].

We understand these data using a two-orbital Anderson model, where each dot with an on-site charging energy U_i hosts a single spinful level at ε_i with the dot index $i = L, R$. In the experiment, this corresponds to a quantum dot orbital level spacing which is larger than the charging energy [14]. We consider an interdot charging energy term $U_C n_L n_R$ and an effective interdot tunneling amplitude t_C. The tunnel coupling energies to the superconducting leads are denoted by $\Gamma_{L,R}$.

We consider the leading term of the supercurrent in the weak-coupling limit where $t_C, \Gamma_L, \Gamma_R \ll \Delta \ll U_i$ [18,30], and evaluate the current operator $I(\varphi) = i\frac{e}{\hbar}[H, n_R]$, where H is the Hamiltonian of the system at a phase difference of φ between the superconducting leads (see the Supplemental Material [27]). We numerically evaluate $\langle I(\varphi)\rangle = I_C \sin\varphi$ to find the signful I_C. We perform a global fit of the calculated sign reversal contours [see the dashed lines in Fig. 2(a)] against the experimental data set and recover $U_L = 596.6$ μeV, $U_R = 465.9$ μeV, $U_C = 41.5$ μeV, and $t_C = 85$ μeV. We match the critical current amplitude scale with the experimental data by setting $\Gamma_L = \Gamma_R = 33.2$ μeV. The width of the even-odd transitions establishes an upper bound on the electron temperature of the DQD, $T < 80$ mK. We use these parameters to display $I_C(V_L, V_R)$ in Fig. 2(b) and find a good correspondence with the experimental data using a zero bandwidth (ZBW) approximation [25,31] (see the Supplemental Material [27]).

The observed supercurrent reversal [14,32] is linked to the number of permutations of fermion operators required to transfer a spin-singlet Cooper pair through the DQD (see the Supplemental Material [27]). In the weak-coupling limit, this amounts to counting the number of same-spin dot electrons, which each electron in the Cooper pair crosses. Each such crossing contributes with a factor of -1 to I_C, which we illustrate for a DQD with even [Fig. 2(c)] and odd charge occupations [Fig. 2(d)]. Consequently, the sign of I_C is determined by the ground-state charge parity of the DQD.

Next, we focus on the magnetic field dependence of I_{DQD} [Fig. 3(a)] along the total energy axis [solid line in Fig. 2(a)] spanning both even and odd charge states. At $B_\parallel = 0$, a finite t_C results in a singlet-triplet splitting Δ_{ST} in the even occupied (1,1) charge state [1]. We model the DQD with an effective identical g-factor on both dots, which results in a spin-polarized triplet ground state above a threshold magnetic field, $B_{ST} = \Delta_{ST}/(g^*\mu_B)$. To account for spin-orbit coupling, we refine our interdot tunneling Hamiltonian to include both spin-conserving and spin-flip tunneling amplitudes t_0 and t_x, resulting in an effective $t_C = \sqrt{t_0^2 + t_x^2}$ (see the Supplemental Material [27]).

With a global fit to the experimental data [Figs. 3(a) and 3(b)], we extract $t_0 = 80$ μeV, $t_x = 30$ μeV, and $g^* = 15.9$. This g-factor is in agreement with earlier experimental values measured on InAs quantum dots [5,33–35] and ballistic channels with superconducting leads [26,36]. We estimate the spin-orbit length $l_{SO} = l_{dot} t_0/(\sqrt{2}t_x) \approx 75$ nm [37], using the gate pitch as an estimate of the dot length, $l_{dot} = 40$ nm. This coupling length yields an energy scale $E_{SO} = \hbar^2/(2m^* l_{SO}^2) = 290$ μeV with an effective electron mass of $m^* = 0.023 m_e$, which is similar to earlier experimental results on semiconductor nanowires in the presence of strong electrostatic confinement [38,39].

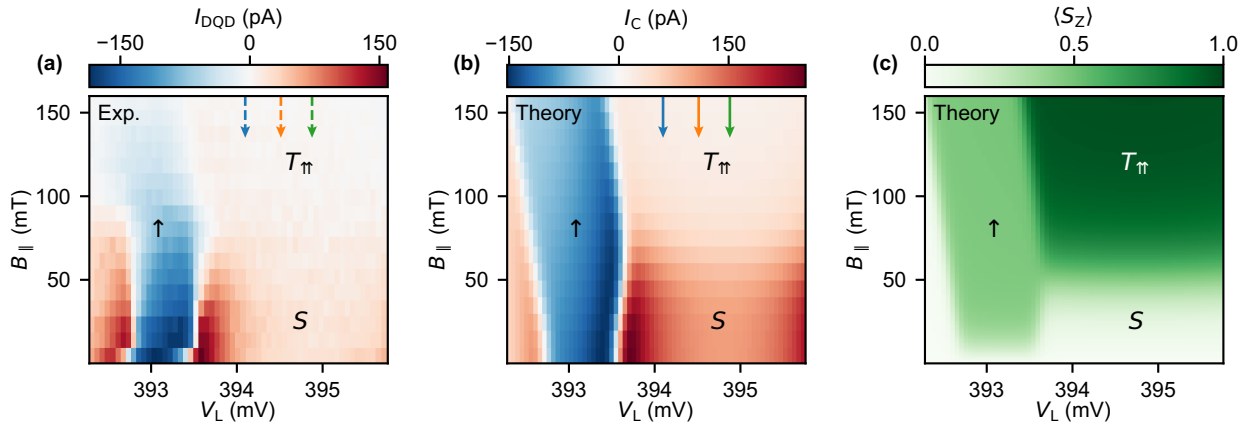

FIG. 3. The superconducting DQD in finite magnetic fields. (a) The measured signful supercurrent oscillation amplitude I_{DQD} as a function of the total energy [see the solid line in Fig. 2(a)] and magnetic field. Note the slight charge shift between the zero magnetic field line and the rest of the data. (b) The corresponding ZBW calculation of the signful critical current (see the text). (c) The calculated spin expectation value in the ground state showing the singlet to triplet transition in the even occupied state as a function of the magnetic field. In (b) and (c), we use the parameters extracted in Fig. 2(b).

In Fig. 3(c), we plot the calculated expectation value $\langle S_Z \rangle$ of the total spin z component of the DQD, which visualizes the transition between the spin-singlet state $\langle S_Z \rangle = 0$ and the spin-polarized triplet state, where $\langle S_Z \rangle = 1$, as a function of the magnetic field. This transition point at B_{ST} is accompanied by a drop of the critical current in the (1,1) sector, however, this sudden decrease is absent in the odd sector [see the blue regions in Fig. 3(b)]. We note that the gradual global decrease in I_{DQD} is consistent with the orbital effect of the magnetic field applied along the nanowire [40].

We analyze these data in Fig. 4, where we first find the charge state boundary at each value of $B_\parallel$ at $I_{DQD} = 0$ [blue dots and error bars in Fig. 4(a)] and overlay the calculated boundary [black solid line, corresponding to Fig. 3(b)]. We quantify $B_{ST} \approx 80$ mT, which agrees consistently with the characteristic cutoff magnetic field of I_{DQD} at several plunger gate values [dots in Fig. 4(b), colors corresponding to the arrows in Fig. 3(a)]. However, we observe a deviation between the calculated and measured charge boundary near B_{ST}, which may stem from the microscopic details of the spin-orbit coupling that our model does not account for. We find an excellent agreement with the calculated critical current $I_C(B)$ [solid lines in Fig. 4(b)] with a common scaling factor of 0.29, which may be the result of the reduced switching current inside the charge state due to thermal activation compared to the corresponding critical current [29].

The suppression of the Josephson supercurrent through a DQD in the spin-triplet sector can be understood considering the virtual states involved in the Cooper pair transfer. Starting from the (1, 1) $T_{\uparrow\uparrow}$ state close to the charge boundary with the single occupation sector, we always encounter a virtual state with a double occupation on one of the dots [magenta circle in Fig. 4(c)]. In the $U \gg \Delta$ limit corresponding to our experiments, this configuration is energetically unfavorable and suppresses Cooper pair tunneling. In contrast, a spin-singlet starting condition can avoid this configuration [Fig. 4(d)]. We finally note that the opposite limit, where $U \ll \Delta$, also leads to a triplet supercurrent blockade [20] (see the Supplemental Material [27]), which persists with a finite residual supercurrent in the spin-triplet state when $U \sim \Delta$.

In conclusion, we directly measured the supercurrent reversal associated with the even-odd charge occupation in an InAs DQD, where the large level spacing allows us to use a single orbital for each dot in our quantitative modeling. In the (1,1) charge sector, we showed that the singlet to triplet transition is accompanied by a supercurrent blockade. This enables a direct spin to supercurrent conversion [36,41] in

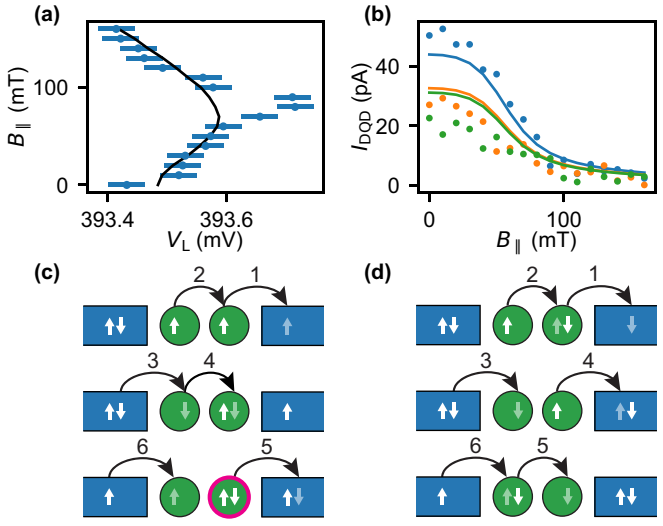

FIG. 4. Triplet-blockaded supercurrent. (a) The measured (blue dots and error bars) and calculated (black solid line) even-odd charge boundary extracted from Figs. 3(a) and 3(b). (b) Dots: The measured I_{DQD} at three plunger gate settings in the even (1,1) sector [see the corresponding arrows in Fig. 3(a)]. Scaled theoretical values are shown as solid lines (see the text). Representative sixth-order tunneling processes are shown (c) in the $T_{\uparrow\uparrow}$ and (d) in the singlet regime. The white arrows denote an initial occupied electron state including the spin. The gray arrows visualize the final state for each numbered process.

hybrid semiconductor nanodevices [30] used for quantum information processing.

Raw data sets and computer code are available at the Zenodo repository [42].

The authors thank J. Danon for helpful discussions, A. Proutski and D. Laroche for their technical input, as well as J. Mensingh, M. Sarsby, O. Benningshof, and R. N. Schouten for technical assistance. This work was supported by the QuantERA project SuperTop, by the NANOCOHYBRI COST Action No. CA16218, by the Netherlands Organization for Scientific Research (NWO), by the Danish National Research Foundation, by the National Research Development and Innovation Office of Hungary within the Quantum Technology National Excellence Program (Project No. 2017-1.2.1-NKP-2017-00001), under OTKA Grants No. 124723 and No. 132146, and the BME Nanotechnology and Materials Science TKP2020 IE grant (BME IE-NAT TKP2020), and by the European Union's Horizon 2020 research and innovation programme under Grants No. 716655 (ERC Stg HEMs-DAM), No. 804988 (ERC Stg SiMS), and No. 828948 (FET Open AndQC).

[1] R. Hanson, L. P. Kouwenhoven, J. R. Petta, S. Tarucha, and L. M. K. Vandersypen, Spins in few-electron quantum dots, Rev. Mod. Phys. **79**, 1217 (2007).

[2] D. Loss and D. P. DiVincenzo, Quantum computation with quantum dots, Phys. Rev. A **57**, 120 (1998).

[3] W. G. Van der Wiel, S. De Franceschi, J. M. Elzerman, T. Fujisawa, S. Tarucha, and L. P. Kouwenhoven, Electron transport through double quantum dots, Rev. Mod. Phys. **75**, 1 (2002).

[4] K. C. Nowack, F. H. L. Koppens, Y. V. Nazarov, and L. M. K. Vandersypen, Coherent control of a single electron spin with electric fields, Science **318**, 1430 (2007).

[5] S. Nadj-Perge, S. M. Frolov, E. P. A. M. Bakkers, and L. P. Kouwenhoven, Spin-orbit qubit in a semiconductor nanowire, Nature (London) **468**, 1084 (2010).

[6] M. Field, C. G. Smith, M. Pepper, D. A. Ritchie, J. E. F. Frost, G. A. C. Jones, and D. G. Hasko, Measurements of Coulomb Blockade with a Noninvasive Voltage Probe, Phys. Rev. Lett. **70**, 1311 (1993).

[7] T. Frey, P. J. Leek, M. Beck, A. Blais, T. Ihn, K. Ensslin, and A. Wallraff, Dipole Coupling of a Double Quantum Dot to a Microwave Resonator, Phys. Rev. Lett. **108**, 046807 (2012).

[8] K. D. Petersson, L. W. McFaul, M. D. Schroer, M. Jung, J. M. Taylor, A. A. Houck, and J. R. Petta, Circuit quantum electrodynamics with a spin qubit, Nature (London) **490**, 380 (2012).

[9] B. D. Josephson, Possible new effects in superconductive tunnelling, Phys. Lett. **1**, 251 (1962).

[10] A. A. Golubov, M. Y. Kupriyanov, and E. Il'ichev, The current-phase relation in Josephson junctions, Rev. Mod. Phys. **76**, 411 (2004).

[11] V. V. Ryazanov, V. A. Oboznov, A. Y. Rusanov, A. V. Veretennikov, A. A. Golubov, and J. Aarts, Coupling of Two Superconductors through a Ferromagnet: Evidence for a π Junction, Phys. Rev. Lett. **86**, 2427 (2001).

[12] T. Kontos, M. Aprili, J. Lesueur, F. Genêt, B. Stephanidis, and R. Boursier, Josephson Junction through a Thin Ferromagnetic Layer: Negative Coupling, Phys. Rev. Lett. **89**, 137007 (2002).

[13] J. J. A. Baselmans, A. F. Morpurgo, B. J. van Wees, and T. M. Klapwijk, Reversing the direction of the supercurrent in a controllable Josephson junction, Nature (London) **397**, 43 (1999).

[14] J. A. van Dam, Y. V. Nazarov, E. P. A. M. Bakkers, S. De Franceschi, and L. P. Kouwenhoven, Supercurrent reversal in quantum dots, Nature (London) **442**, 667 (2006).

[15] R. Delagrange, R. Weil, A. Kasumov, M. Ferrier, H. Bouchiat, and R. Deblock, 0-π quantum transition in a carbon nanotube Josephson junction: Universal phase dependence and orbital degeneracy, Phys. Rev. B **93**, 195437 (2016).

[16] M.-S. Choi, C. Bruder, and D. Loss, Spin-dependent Josephson current through double quantum dots and measurement of entangled electron states, Phys. Rev. B **62**, 13569 (2000).

[17] Y. Zhu, Q.-F. Sun, and T.-H. Lin, Probing spin states of coupled quantum dots by a dc Josephson current, Phys. Rev. B **66**, 085306 (2002).

[18] A. Martín-Rodero and A. L. Yeyati, Josephson and Andreev transport through quantum dots, Adv. Phys. **60**, 899 (2011).

[19] C. Karrasch, S. Andergassen, and V. Meden, Supercurrent through a multilevel quantum dot close to singlet-triplet degeneracy, Phys. Rev. B **84**, 134512 (2011).

[20] S. Droste, S. Andergassen, and J. Splettstoesser, Josephson current through interacting double quantum dots with spin–orbit coupling, J. Phys.: Condens. Matter **24**, 415301 (2012).

[21] A. Brunetti, A. Zazunov, A. Kundu, and R. Egger, Anomalous Josephson current, incipient time-reversal symmetry breaking, and Majorana bound states in interacting multilevel dots, Phys. Rev. B **88**, 144515 (2013).

[22] V. Pokorný, M. Žonda, G. Loukeris, and T. Novotný, Second order perturbation theory for a superconducting double quantum dot, JPS Conf. Proc. **30**, 011002 (2020).

[23] P. Krogstrup, N. Ziino, W. Chang, S. Albrecht, M. Madsen, E. Johnson, J. Nygård, C. Marcus, and T. Jespersen, Epitaxy of semiconductor–superconductor nanowires, Nat. Mater. **14**, 400 (2015).

[24] D. Szombati, S. Nadj-Perge, D. Car, S. Plissard, E. Bakkers, and L. Kouwenhoven, Josephson ϕ_0-junction in nanowire quantum dots, Nat. Phys. **12**, 568 (2016).

[25] J. C. Estrada Saldaña, A. Vekris, G. Steffensen, R. Žitko, P. Krogstrup, J. Paaske, K. Grove-Rasmussen, and J. Nygård, Supercurrent in a Double Quantum Dot, Phys. Rev. Lett. **121**, 257701 (2018).

[26] D. J. van Woerkom, A. Proutski, B. Van Heck, D. Bouman, J. I. Väyrynen, L. I. Glazman, P. Krogstrup, J. Nygård, L. P. Kouwenhoven, and A. Geresdi, Microwave spectroscopy of spinful Andreev bound states in ballistic semiconductor Josephson junctions, Nat. Phys. **13**, 876 (2017).

[27] See Supplemental Material at http://link.aps.org/supplemental/10.1103/PhysRevB.102.220505 for the details of sample fabrication, device paramaters, and numerical modeling.

[28] M. L. Della Rocca, M. Chauvin, B. Huard, H. Pothier, D. Esteve, and C. Urbina, Measurement of the Current-Phase

Relation of Superconducting Atomic Contacts, Phys. Rev. Lett. **99**, 127005 (2007).

[29] Y. Ivanchenko and L. Zil'Berman, The Josephson effect in small tunnel contacts, Zh. Eksp. Teor. Fiz. **55**, 2395 (1968) [Sov. Phys. JETP **28**, 1272 (1969)].

[30] S. De Franceschi, L. Kouwenhoven, C. Schonenberger, and W. Wernsdorfer, Hybrid superconductor-quantum dot devices, Nat. Nanotechnol. **5**, 703 (2010).

[31] E. Vecino, A. Martín-Rodero, and A. Levy Yeyati, Josephson current through a correlated quantum level: Andreev states and π junction behavior, Phys. Rev. B **68**, 035105 (2003).

[32] B. I. Spivak and S. A. Kivelson, Negative local superfluid densities: The difference between dirty superconductors and dirty Bose liquids, Phys. Rev. B **43**, 3740(R) (1991).

[33] C. Fasth, A. Fuhrer, L. Samuelson, V. N. Golovach, and D. Loss, Direct Measurement of the Spin-Orbit Interaction in a Two-Electron InAs Nanowire Quantum Dot, Phys. Rev. Lett. **98**, 266801 (2007).

[34] S. Csonka, L. Hofstetter, F. Freitag, S. Oberholzer, C. Schonenberger, T. S. Jespersen, M. Aagesen, and J. Nygård, Giant fluctuations and gate control of the *g*-factor in InAs nanowire quantum dots, Nano Lett. **8**, 3932 (2008).

[35] M. D. Schroer, K. D. Petersson, M. Jung, and J. R. Petta, Field Tuning the *g* Factor in InAs Nanowire Double Quantum Dots, Phys. Rev. Lett. **107**, 176811 (2011).

[36] L. Tosi, C. Metzger, M. F. Goffman, C. Urbina, H. Pothier, S. Park, A. L. Yeyati, J. Nygård, and P. Krogstrup, Spin-Orbit Splitting of Andreev States Revealed by Microwave Spectroscopy, Phys. Rev. X **9**, 011010 (2019).

[37] J. Danon, Spin-flip phonon-mediated charge relaxation in double quantum dots, Phys. Rev. B **88**, 075306 (2013).

[38] S. Nadj-Perge, V. S. Pribiag, J. W. G. van den Berg, K. Zuo, S. R. Plissard, E. P. A. M. Bakkers, S. M. Frolov, and L. P. Kouwenhoven, Spectroscopy of Spin-Orbit Quantum Bits in Indium Antimonide Nanowires, Phys. Rev. Lett. **108**, 166801 (2012).

[39] Z. Scherübl, G. Fülöp, M. H. Madsen, J. Nygård, and S. Csonka, Electrical tuning of Rashba spin-orbit interaction in multigated InAs nanowires, Phys. Rev. B **94**, 035444 (2016).

[40] K. Zuo, V. Mourik, D. B. Szombati, B. Nijholt, D. J. van Woerkom, A. Geresdi, J. Chen, V. P. Ostroukh, A. R. Akhmerov, S. R. Plissard, D. Car, E. P. A. M. Bakkers, D. I. Pikulin, L. P. Kouwenhoven, and S. M. Frolov, Supercurrent Interference in Few-Mode Nanowire Josephson Junctions, Phys. Rev. Lett. **119**, 187704 (2017).

[41] M. Hays, V. Fatemi, K. Serniak, D. Bouman, S. Diamond, G. de Lange, P. Krogstrup, J. Nygård, A. Geresdi, and M. H. Devoret, Continuous monitoring of a trapped superconducting spin, Nat. Phys. **16**, 1103 (2020).

[42] D. Bouman, R. J. J. van Gulik, G. Steffensen, D. Pataki, P. Boross, P. Krogstrup, J. Nygård, J. Paaske, A. Pályi, and A. Geresdi, Triplet-blockaded Josephson supercurrent in double quantum dots (2020), http://doi.org/10.5281/zenodo.3978236.

12

PROJECT 5

In this last project of the thesis, we investigate STM measurements of sub-surface impurities found on the unconventional superconductor $FeTe_{0.55}Se_{0.45}$, theorized to host Majorana zero-modes [174]. Measurements are done with a superconducting tip, and a single subgap state is observed around each impurity. The energy of these state are found to disperse as a function of both tip height Δd and impurity tip displacement Δr. By tuning these distances a zero-energy crossing of the subgap state is observed. These measurements are explained via a superconducting Anderson model, by assuming that the needle effectively gate the sub-surface impurity through electrostatic differences of the tip and substrate work functions. In this manner, the impurity is tuned by a penetrating electric field, similarly to gating in a quantum dot, explaining groundstate transitions as a function of tip distance. Other tip dependent energy dispersions in STM have been explained via a force exerted on the adatom by the tip, thereby lifting it and changing exchange coupling J [44, 49]. This effect we exclude as the impurity is sub-surface.

My contributions to this project was primarily ZBW modelling, in collaboration with Damianos Chatzopoulos, and transport calculations. The experimental measurements were explained using a S-QD-S Anderson model, solved in the ZBW limit, with transport calculated for low coupling Γ_t compared to relaxation, $\Gamma_r \gg \Gamma_t$. Conductance is in this limit given by a convolution of tip and sample spectral functions, amounting to Fermi's golden rule. The subgap spectrum is obtained via a Lehmann representation of the ZBW model. Here the spurious double excited state, discussed in chapter 8, does not play a role in transport, as relaxation occurs fast compared to electron transfer such that no two-particle excitation is involved in transport cycles. We also observe clear conductance features at $eV = \pm(\Delta_t - E_{ig})$ in the vicinity of subgap state zero-crossings $E_{ig} \approx 0$, originating from thermally excited poisoning. This project shows that impurities can be gated by a STM needle on substrates which only weakly screens electric fields, and highlight that measurements of zero-bias conductance on topological superconductors can originate from trivial subgap states, similarly to debates regarding zero-bias measurements done on topological nanowires.

nature COMMUNICATIONS

ARTICLE

https://doi.org/10.1038/s41467-020-20529-x OPEN

Spatially dispersing Yu-Shiba-Rusinov states in the unconventional superconductor $FeTe_{0.55}Se_{0.45}$

Damianos Chatzopoulos[1,8], Doohee Cho[1,2,8], Koen M. Bastiaans[1,8], Gorm O. Steffensen[3], Damian Bouwmeester[1,4], Alireza Akbari[5,6], Genda Gu[7], Jens Paaske[3], Brian M. Andersen[3] & Milan P. Allan[1✉]

By using scanning tunneling microscopy (STM) we find and characterize dispersive, energy-symmetric in-gap states in the iron-based superconductor $FeTe_{0.55}Se_{0.45}$, a material that exhibits signatures of topological superconductivity, and Majorana bound states at vortex cores or at impurity locations. We use a superconducting STM tip for enhanced energy resolution, which enables us to show that impurity states can be tuned through the Fermi level with varying tip-sample distance. We find that the impurity state is of the Yu-Shiba-Rusinov (YSR) type, and argue that the energy shift is caused by the low superfluid density in $FeTe_{0.55}Se_{0.45}$, which allows the electric field of the tip to slightly penetrate the sample. We model the newly introduced tip-gating scenario within the single-impurity Anderson model and find good agreement to the experimental data.

[1] Leiden Institute of Physics, Leiden University, Niels Bohrweg 2, Leiden, CA 2333, The Netherlands. [2] Department of Physics, Yonsei University, Seoul 03722, Republic of Korea. [3] Center for Quantum Devices, Niels Bohr Institute, University of Copenhagen, Universitetsparken 5, Copenhagen Ø 2100, Denmark. [4] Kavli Institute of Nanoscience, Delft University of Technology, Lorentzweg 1, Delft, CJ 2628, Netherlands. [5] Max Planck Institute for the Chemical Physics of Solids, Dresden D-01187, Germany. [6] Max Planck POSTECH Center for Complex Phase Materials, and Department of Physics, POSTECH, Pohang, Gyeongbuk 790-784, Korea. [7] Condensed Matter Physics and Materials Science Department, Brookhaven National Laboratory, Upton, NY 11973, USA. [8] These authors contributed equally: Damianos Chatzopoulos, Doohee Cho, Koen M. Bastiaans. ✉email: allan@physics.leidenuniv.nl

The putative $s_{\pm}$ superconductor $FeTe_{0.55}Se_{0.45}$ is peculiar because it has a low Fermi energy and an unusually low and inhomogeneous superfluid density[1–7]. It has been predicted to host a topological superfluid and Majorana zero-mode states[8–10]. These predictions have been supported by recent experiments: photoemission has discovered Dirac-like dispersion of a surface state[11] while tunneling experiments have concentrated on in-gap states in vortex cores, which have been interpreted as Majorana bound states[12,13] since the low Fermi energy allows to distinguish them from conventional low-energy Caroli-Matricon-de Gennes states[14].

In-gap states have a long history of shining light into the properties of different host materials, and have allowed to bring insight into gap symmetry and structure, symmetry breaking, or the absence of scattering in topological defects, to name a few[15–24]. Impurity bound states have also been investigated in chains or arrays of magnetic impurities on superconducting surfaces where they can lead to Majorana edge-states[25–28]. In the case of $FeTe_{0.55}Se_{0.45}$, zero-bias in-gap resonances have become a primary way to identify Majorana bound states at magnetic impurity sites or in vortex cores. At impurity sites, robust zero-bias peaks have been reported at interstitial iron locations which suggest the presence of Majorana physics[29]. In addition, very recently STM experiments reported signatures of reversibility between magnetic impurity bound states and Majorana zero modes by varying the tip-sample distance on magnetic adatoms[30]. Interestingly, there have also been signatures of spatially varying in-gap impurity states[31,32] which are not yet understood.

Here we report the detection of in-gap states at sub-surface impurities, which are spatially dispersing, i.e., they change energy when moving away from the impurity site by a distance of Δy. The energy can also be tuned by changing the tip-sample distance (Δd). We argue that the most likely explanation of our observations involves a magnetic impurity state of the YSR type affected by the electric field of the tip. We show good agreement between our experimental findings and the single impurity Anderson model.

Results

Detection of a particle-hole symmetric in-gap state in $FeTe_{0.55}Se_{0.45}$. We use $FeTe_{0.55}Se_{0.45}$ samples with a critical temperature of $T_C = 14.5$ K. They are cleaved at ~30 K in ultra-high vacuum, and immediately inserted into a modified Unisoku STM at a base temperature of 2.2 K, for preventing surface reconstruction and contamination. To increase the energy resolution, we perform all tunneling experiments using a superconducting tip, made by indenting mechanically ground Pt-Ir tips into a clean Pb(111) surface. With the superconducting tip and to leading order in the tunnel coupling, the current-voltage ($I-V$) characteristic curves are proportional to the convolution of the density of states of Bogoliubov quasiparticles in the tip and the sample

$$I(\mathbf{r},V) \sim \int D_t(\omega+eV)D_s(\mathbf{r},\omega)[f(\omega,T)-f(\omega+eV,T)]d\omega, \quad (1)$$

where $D_{s(t)}$ is the density of states of the quasiparticles in the sample (tip), $f(\omega, T)$ is the Fermi-Dirac distribution at temperature T and e is the electron charge. In such a superconducting tunnel junction the coherence peaks in the conductance spectra, $dI/dV(\mathbf{r}, V)$, appear at energies: $\pm(\Delta_t + \Delta_s)$, where $\Delta_{s(t)}$ is the quasiparticle excitation gap of the sample (tip). In addition, the energy resolution is far better than the conventional thermal broadening of $\sim 3.5k_BT$ (k_B is the Boltzmann constant) since it is enhanced by the sharpness of the coherence peaks of D_t[33–35]. To obtain the intrinsic local density of states (LDOS) of the sample, $D_s(\mathbf{r}, \omega)$, we numerically deconvolute our measured $dI/dV(\mathbf{r}, V)$ spectra while retaining the enhanced energy resolution (for more details see Supplementary Note 1). For this, we use our knowledge of the density of states of the tip with a gap of $\Delta_t = 1.3$ meV from test experiments on the Pb(111) surface using the same tip.

Figure 1a shows a topography of the cleaved surface of $FeTe_{0.55}Se_{0.45}$ obtained with a Pb coated tip (see inset). Brighter (darker) regions correspond to Te (Se) terminated areas of the

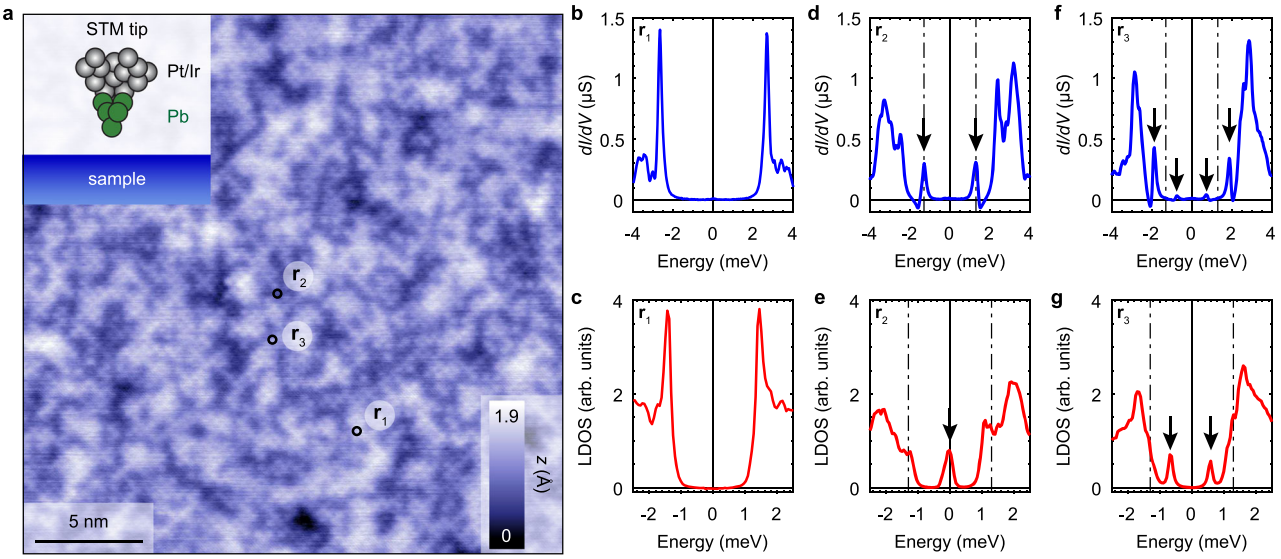

Fig. 1 Scanning Tunneling Microscopy on $FeTe_{0.55}Se_{0.45}$ with a superconducting tip. a Atomically resolved topographic image (z-height map, 25 × 25 nm^2) of $FeTe_{0.55}Se_{0.45}$ cleaved surface acquired with a Pb coated Pt/Ir tip (see inset) at 2.2 K in ultra-high vacuum. Setup condition: $V_{set} = -8$ mV, $I_{set} = -100$ pA. **b**, **d**, **f** Spatially averaged differential conductance spectra in the areas ($\mathbf{r}_1$, $\mathbf{r}_2$, $\mathbf{r}_3$) marked by the black circles in **a**. $\mathbf{r}_1$: no in-gap states. $\mathbf{r}_2$: two in-gap resonances at ± 1.3 meV. $\mathbf{r}_3$: two sets of peaks symmetric in energy around the Fermi level. **c**, **e**, **g** Deconvolution of the spectra shown in **b**, **d**, **f**, respectively, provide information about the intrinsic LDOS of the sample in the indicated areas. In $\mathbf{r}_2$ a zero-bias impurity state is recovered and in $\mathbf{r}_3$ two in-gap states are observed. Setup conditions: **b** $V_{set} = 6$ mV, $I_{set} = 1.2$ nA, **d, f** $V_{set} = 5$ mV, $I_{set} = 2$ nA. Lock-in modulation is $V_{mod} = 30$ μV peak-to-peak for all measured spectra.

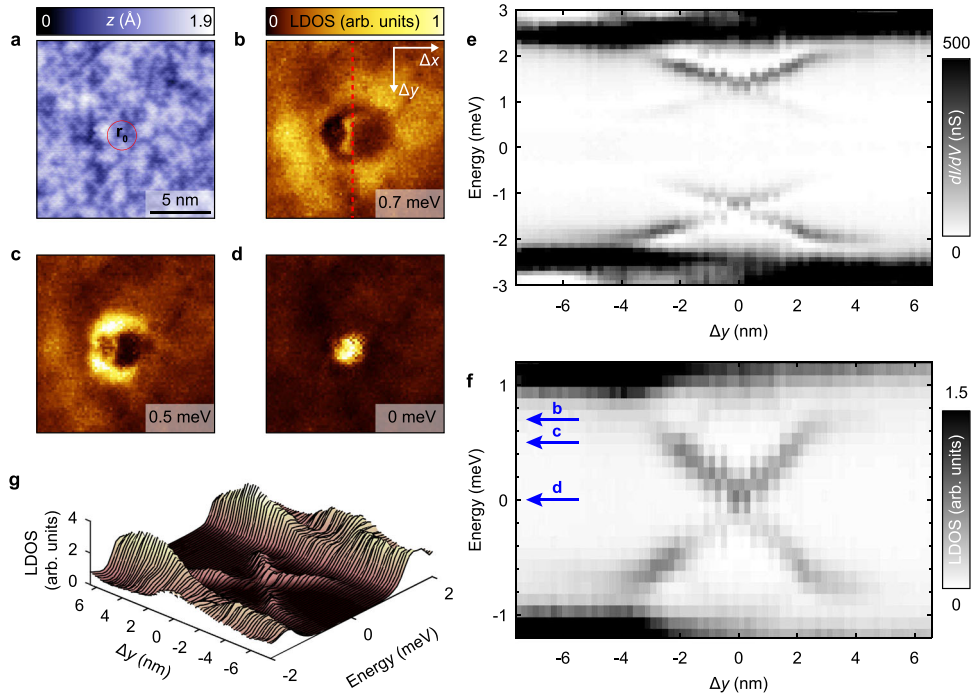

Fig. 2 X-shaped spatial dispersion of impurity resonances in $FeTe_{0.55}Se_{0.45}$. **a** Topographic image at the impurity location ($\mathbf{r}_0$ indicates the impurity center). No clear signature of the impurity is observed. Setup conditions: $V_{set} = -8$ mV, $I_{set} = -100$ pA. **b**–**d** Spatially resolved LDOS maps at different energies obtained by deconvolution of a dI/dV ($\mathbf{r}$, V) map in the same field-of-view as in **a**. The energy of each LDOS map is indicated at the bottom right corner. **e** Measured differential conductance intensity plot of a vertical linecut passing through the impurity center $\mathbf{r}_0$ ($\Delta y = 0$ nm). The linecut was taken along the red dashed line in **b**. A crossing of the in-gap resonances at the impurity center is observed. Setup conditions: $V_{set} = -8$ mV, $I_{set} = -1.6$ nA. Lock-in modulation is $V_{mod} = 100$ μV peak-to-peak, **f** Deconvolution of the measured spectra in **e** shows an X-shaped dispersion of the sub-gap states crossing the Fermi level at the impurity center. The blue arrows indicate the energy of the maps in **b**–**d**. **g** Series of LDOS spectra depicting the X-shaped spatial dispersion shown in **f**.

cleaved surface which has a tetragonal crystal structure. Our samples exhibit no excess Fe atoms or clusters on the cleaved surface. Spatially resolved scanning tunneling spectroscopy shows that most locations have a flat gap, as shown in Fig. 1b, c. However, when we acquire spectra at specific points indicated by black circles ($\mathbf{r}_2$ and $\mathbf{r}_3$) in Fig. 1a, we find sharp in-gap states. Figure 1d–e and f–g shows such states, both in the raw data as well as in the deconvoluted results. The measured in-gap state is symmetric in energy, i.e., it is visible at $\pm E_{ig}$ (Fig. 1g), or at the Fermi level, $E_{ig} = 0$ (Fig. 1e). In the raw data (before numerical deconvolution) the states are located at energies $\pm(\Delta_t \pm E_{ig})$ (see arrows in Fig. 1d and f) due to the use of the superconducting tip.

Spatial dispersion of the in-gap state. In order to characterize the impurity in more detail we acquire a spatially resolved dI/dV ($\mathbf{r}$, V) map in the area shown in Fig. 2a. Three energy layers of the deconvoluted map depicting the LDOS variations are shown in Fig. 2b–d. The impurity exhibits a clear ring-shaped feature which eventually becomes a disk with smaller radius at the Fermi level. A spatial line cut profile along the red dashed line shown in Fig. 2b reveals two symmetric resonances around zero energy that extend over ~10 nm in space (Fig. 2e). Importantly, the energies of the in-gap states vary spatially as shown in the spatial cuts (Fig. 2e–g) obtained from the same conductance map. The dispersion of the in-gap states shows an X-shaped profile where the crossing point is indicated with $\mathbf{r}_0$ (Fig. 2a). In more detail, the state is at zero energy at $\mathbf{r}_0$, and then moves away from the Fermi level, before fading out slightly below the gap edge. We will show later that the character of this dispersion is dependent on the tip-sample distance, and that there can also be zero or two crossing points. By inspecting the topography at $\mathbf{r}_0$ we find no signature of irregularities, which points towards a sub-surface impurity defect as the cause of the observed in-gap peaks in the spectra. We note that these impurities are sparse; we found a total of 5 in a 45×45 nm^2 field-of-view. These all show the same characteristic dispersions, but the X point is estimated at different tip heights. For details, see Supplementary Note 7. Similar observations have been reported previously on $FeTe_{0.55}Se_{0.45}$, but without a clear energy cross at the Fermi level[31,32].

YSR impurity states. Our observations are reminiscent of YSR states caused by magnetic impurities in conventional superconductors[35–39]. When a single magnetic impurity is coupled to a superconductor with energy gap Δ via an exchange coupling J then the ground state of the many-body system depends on the interplay between superconductivity and the Kondo effect (described by the Kondo temperature T_K). For $\Delta \gtrsim k_B T_K$ the superconducting ground state prevails (unscreened impurity) whereas for $\Delta < k_B T_K$ the Kondo ground state dominates (screened impurity). In each case, quasiparticle excitations above the ground state give rise to resonances symmetrically around the Fermi level inside the superconducting gap. In an STM experiment, this results in peaks in the conductance spectrum at the energy of the two YSR excitations which is determined by the product $\nu_F JS$, where S is the impurity spin and ν_F the normal state density of states in the superconducting host ($FeTe_{0.55}Se_{0.45}$ in our case).

It is important to note that the $s_\pm$ symmetry of the order parameter in $FeTe_{0.55}Se_{0.45}$ can lead to a very similar phenomenology between magnetic and potential scatterers. While in conventional s-wave superconductors, magnetic impurities are required to create in-gap (YSR) states, in $s_\pm$ superconductors, sub-gap resonances can also occur for non-magnetic scattering

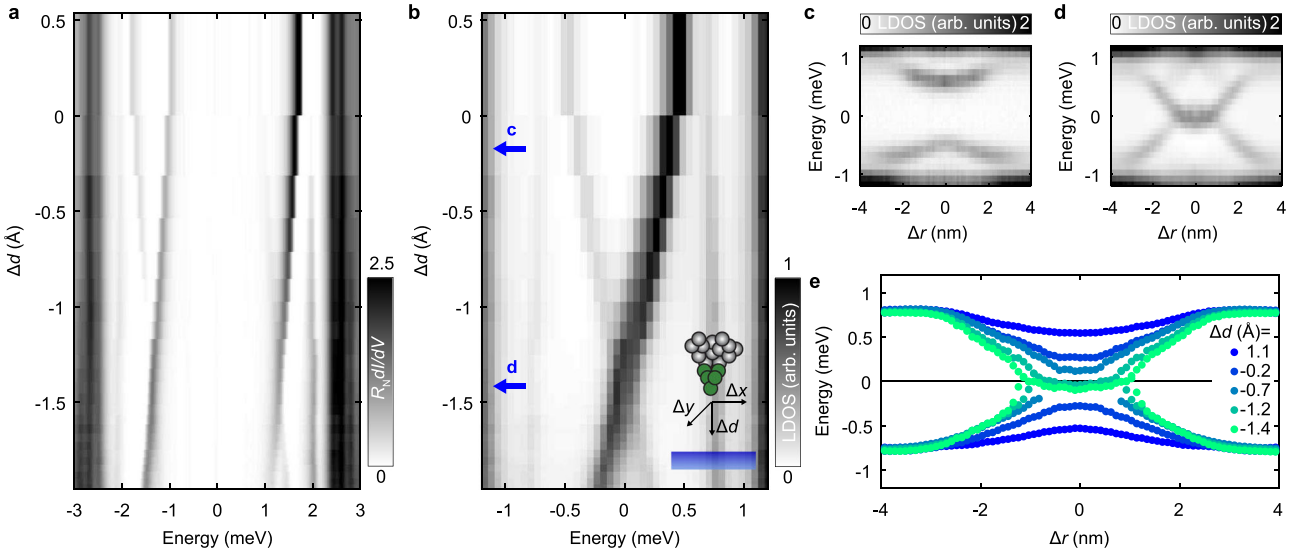

Fig. 3 Energy dispersion of the sub-gap resonances as a function of the tip-sample distance. a Conductance intensity plot for varying tip-sample distance (Δd) normalized by the normal state resistance R_N. The in-gap states disperse and cross at the Fermi level. **b** Same as in **a** for the deconvoluted LDOS data. Inset: schematic representation of the tip movement when we vary the tip-sample distance (Δd) and when the tip scans laterally (Δy and Δx) at a constant height. **c**, **d** Azimuthally-averaged radial profiles at different tip-sample distances indicated by blue arrows in **b**. Δr, indicates the radial offset $\sqrt{\Delta x^2 + \Delta y^2}$ from the impurity center ($\Delta r = 0$). **e** Energy of the impurity bound state for varying tip-sample distance, extracted by fitting a lorentzian curve in 5 intensity plots (see Supplementary Note 3) similar to **c**, **d**.

centers. This can be shown using different theoretical techniques, including T-matrix method[40,41], Bogoliubov-de Gennes equations[42,43] and Green's functions[44–46] applied to multiband systems with $s_\pm$ symmetry. The similarity of magnetic and potential scatterers makes a distinction between these cases more challenging (but possible, with an external magnetic field[30]). In either case, theory predicts energy-symmetric in-gap states with particle-hole asymmetric intensities.

The X-shaped phenomenology of the in-gap states shown above shares also similarities with bound-states that have been observed in Pb/Co/Si(111) stacks[47], where they have been interpreted as topological[47,48]. However, as we will show here, in our experiments the single point of zero bias is just one particular case of a manifold of dispersions that depend on the tip-sample distance.

Tuning the energy of the in-gap state with the tip. Figure 3a shows an intensity plot of a series of spectra above $\mathbf{r}_0$, the location showing the zero-bias impurity state, with changing tip-sample distance (see inset for a schematic). We normalized each spectrum by the normal state resistance $R_N = V_{set}/I_{set}$. In order to reduce the distance, we control the tip in constant current feedback and increase the set-point for the current while keeping the voltage bias constant. In addition, we measure the tip-sample distance relative to the set-point: $V_{set} = 5$ mV, $I_{set} = 0.4$ nA. Strikingly, we observe a shift in the energy of the in-gap state with varying the tip-sample distance Δd. When the tip is brought closer to the sample surface, the sub-gap resonances shift towards the Fermi energy (Fig. 3b) where they cross and split again. We also point out that there is a strong particle-hole asymmetry in the intensity of the in-gap resonances. It can be clearly seen in Fig. 3b that the relative intensity between the positive (p) and negative (n) resonances ($I_p - I_n$) changes sign after the cross at the Fermi level. Further, we note that the energy shift for varying Δd is stronger than the spatial dispersion. This can likely be explained by the tip shape, which can be approximated as a sphere of roughly 20 nm. As the tunneling current falls off exponentially with distance, one always tunnels to the point closest to the surface. However, the field is algebraic in the distance, and thus a change horizontally has less of an effect than a change vertically, as shown in Supplementary Note 5.

To obtain a more complete picture of the tuning of the in-gap states as we vary Δd, we measured five $dI/dV(\mathbf{r}, V)$ maps (each at different tip-sample distance) and analyzed azimuthally-averaged radial profiles through the impurity center (Fig. 3c–d shows two of these profiles. See Supplementary Note 3 for the other 3). We extract the energy of the resonances by Lorentzian fits (Fig. 3e), to observe that they cross the Fermi level at the impurity center when being close to the sample. This is the first time that such a crossing has been observed in an unconventional superconductor.

Microscopic origin. The important question that arises is: what tunes the impurity resonances that we observe? In previous experiments with magnetic ad-atoms or ad-molecules on conventional superconductors[49,50], it has been shown that the force of the tip changes the coupling between moment and substrate, and that the coupling J and the YSR energy could be tuned in this way. In this case, when the energy crosses the Fermi level at the critical coupling J_C, a first-order quantum phase transition between the singlet (screened) and the doublet (unscreened) ground state is expected[49,51]. Very recently, a similar force-based scenario has been reported in different systems involving magnetic ad-atoms on top of superconductors[15], including Fe(Te,Se)[30]. As discussed in Supplementary Note 2, a similar scenario can in principle explain the sub-gap dispersion discovered here. However, as the impurity is not loosely bound on top of the surface in the present case, a movement between a sub-surface impurity and the superconductor due to the tip force as the cause for the tuning, seems unlikely. Therefore, we pursue alternative mechanisms. Motivated by the phenomenology of semiconductors[52] or Mott insulators[53], where the tip can act as a local gate electrode (mediated by the poor screening), we propose a similar gating scenario for YSR states in the present case: the electric field of the tip can tune the energy of the impurity state and thus lead to a dispersing YSR state.

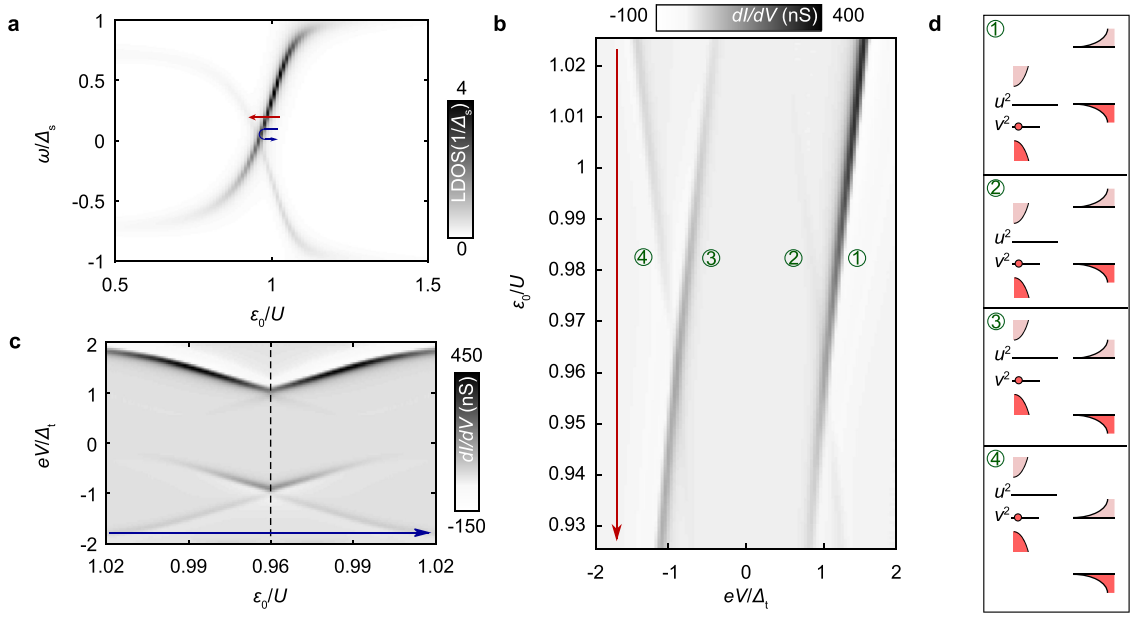

Fig. 4 Anderson impurity model for Yu-Shiba-Rusinov bound states. a Local density of states as a function of level energy ϵ_0. The impurity spectral function was calculated within the zero-bandwidth approximation using the Lehmann spectral representation for the retarded Green's function (see Supplementary Note 2). Red and blue lines indicate the two different ϵ_0 sweeps plotted in **b** and **c**, respectively. **b**, **c** Relaxation dominated tunneling conductance calculated to leading order in the tip-impurity tunneling rate Γ_t. Labels in **b** refer to processes in **d**. The dashed line in **c** shows the turning point of the blue line in **a**. **d** Guide to the eye for different conductance contributions in **b** and **c**. Processes 2–3 require a finite population of the excited state, in this case supplied by temperature. For all panels we use $U = 20$, $\Gamma_s = 3$, $\Gamma_t = 0.04$, $\gamma = \Gamma_r = 0.035$ and $k_BT = 0.2$, all in units of Δ_s.

First, we note that there can be a significant difference between the work functions of the tip and the sample. Typical work functions are in the range of a few electronvolts, and differences between chemically different materials of the order of an electronvolt are common (see Supplementary Note 5). Hence, it is possible to have a voltage drop between them that is larger than the applied bias. Secondly, the low carrier density in $FeTe_{0.55}Se_{0.45}$ leads to a non-zero screening length giving rise to penetration of the electric field of the tip inside the sample. An estimation of the penetration depth in the sample can be made in the Thomas-Fermi approximation (cf. e.g.[54]). In this framework, the screening length is given by $\lambda_{TF} = (\pi a_0/4k_F)^{1/2}$, where a_0 is the Bohr radius and k_F the Fermi wave-vector. Using reported parameters[11,12], this yields $\lambda_{TF} = 0.5$ nm, which is comparable to the inter-layer distance[55]. This implies that in principle, an impurity residing between the topmost layers can be affected by the electric field of the tip. In Supplementary Note 6 we further test this possibility by performing an estimate of the potential shift in the impurity, when the tip-sample distance is varied using a simple model for screening (image charges method) to estimate that the shift is comparable to the charging energy of the impurity. We note that this estimate is approximative, as some key parameters are unknown for $FeTe_{0.55}Se_{0.45}$.

Based on these considerations, we conclude that it is possible that the tip acts as a local gate electrode that influences the energy levels of the impurity, which in turn influences the energy of the in-gap states, as we will demonstrate in the modelling carried out below. By adjusting the tip-sample distance the field penetration is modulated leading to an energy shift of the in-gap resonances. The spatial dependence can be explained similarly: when moving the tip over the impurity location, we change the local electric field, which is at a maximum when the tip is right above the impurity. We emphasize that, similar to experiments on semiconductors and Mott insulators, we expect that the details of the gating process depend on the tip shape Supplementary Note 5.

Gate-tunable single impurity Anderson model. We model the sub-gap state as a YSR state arising from the magnetic moment of a sub-surface impurity level, whose energy is effectively gated by the tip-induced electric field. It should be noted that the sub-gap states arising in an $s_{\pm}$-wave superconductor from a simple non-magnetic impurity can produce a dispersive cross in the in-gap energies as a function of the impurity potential. However, this is only true for a particular range of potentials, and will not generally trace out a single dispersive cross as a function of the impurity strength[42,44]. Therefore, we are led to conclude that the impurity at hand involves a finite magnetic moment. Local impurity-induced magnetic moments may indeed be particularly prominent in correlated systems like FeSe where even non-magnetic disorder, in conjunction with electron interactions, can generate local moments[56]. Because of the magnetic nature of the impurity site, the results of our calculations are qualitatively independent on whether we treat the system as an s or $s_{\pm}$-wave superconductor. For simplicity, we perform our calculations assuming standard s-wave pairing.

The superconducting single impurity Anderson model[57] involves an impurity level ϵ_0 with charging energy U coupled via a tunneling rate Γ_s to a superconducting bath with energy gap Δ_s[58–60]. We represent the sample by a simple s-wave Bardeen–Cooper–Schrieffer (BCS) superconductor, and use the zero-bandwidth approximation, including only a single spin-degenerate pair of quasiparticles at energy Δ_s[59,61]. We further assume that the gating from the tip changes the impurity level ϵ_0 linearly with distance. We then obtain the YSR states by calculating the local impurity spectral function, $D_I(\omega, \epsilon_0)$, as a function of ϵ_0 (and thus of gating) using the Lehmann representation (see Supplementary Note 2 for details). The result is plotted in Fig. 4a, where the observed crossing of the sub-gap states indicates a change between singlet, and a doublet ground state[62]. From the spectral function we can determine the current using leading-order perturbation theory in the tunnel coupling

connecting the impurity to the tip, t_t:

$$I(V) = \frac{e|t_t|^2}{\hbar}\int D_t(\omega + eV, \Delta_t, \gamma_t) D_I(\omega, \epsilon_0)[f(\omega, T) - f(\omega + eV, T)]d\omega, \quad (2)$$

here $D_t(\omega, \Delta_t, \gamma_t)$ is the spectral function of the superconducting tip with a finite quasiparticle broadening incorporated as a Dynes parameter[63], γ_t and $\hbar$ the reduced Planck's constant. A phenomenological relaxation rate, Γ_r, is incorporated into the Lehmann representation, (see Supplementary Note 2), to construct $D_I(\omega, \epsilon_0)$. This parameter accounts for quasiparticle relaxation of the YSR resonances at $\omega = \pm E_{ig}$. The validity of the expansion in $\Gamma_t = \pi\nu_F|t_t|^2$, which captures only single electron transport and omits Andreev reflections, rests on the assumption that the sub-gap state thermalizes with rate Γ_r between each tunneling event. In the opposite limit, $\Gamma_t \gg \Gamma_r$, transport takes place via resonant Andreev reflections, and the sub-gap conductance peaks at $eV = \pm(\Delta_t + E_{ig})$ display a bias asymmetry that is reversed compared to the bias asymmetry of the single electron transport regime[39]. In principle, these two regimes can be differentiated by varying Γ_t, since the conductance peaks increase linearly with Γ_t in the single electron regime, and sublinearly in the resonant Andreev regime[39,64]. The experimental data shown in Fig. 3 display a marked asymmetry, consistent with our assumption of relaxation dominated transport where conductance asymmetry will follow the asymmetry of the underlying spectral function.

Next, we investigate the situations where the tip moves over the impurity along the surface, or towards the impurity as a function of tip-sample distance Δd. These situations are marked with blue and red arrows in Fig. 4a, respectively. In Fig. 4b, c we then plot sub-gap conductance as a function of level position, ϵ_0, corresponding to the red/blue traces, assuming a linear dependence of ϵ_0 with tip-sample distance. The agreement between our model and the data is good, both in terms of the energy dispersion and the asymmetry. Also, in both experiment and theory, additional conductance peaks at $eV = \pm(\Delta_t - E_{ig})$ are visible close to the singlet-doublet phase transition. We interpret these lines as the additional single electron processes shown in Fig. 4d, which arise from thermal population of the excited state close to the phase transition where $E_{ig} \lesssim k_B T$. The conductance peaks at $\Delta_t \pm E_{ig}$ meet at the point where the YSR states cross zero energy, signaling the change between singlet, and doublet ground states, and the asymmetry in intensity between the conductance peaks at $eV = \pm(\Delta_t + E_{ig})$ switches around.

The good agreement between this simple model (Fig. 4b, c) and the data presented in Fig. 2e and a, supports our interpretation that the tip exerts an effective gating of the impurity. We discuss alternative scenarios further in Supplementary Note 2, but the fact that our impurity is below the surface and the excellent agreement between the model and the data lead us to conclude that the gating scenario is most likely in the present case.

In summary, we have reported on the properties of energy symmetric in-gap states in $FeTe_{0.55}Se_{0.45}$ that can be tuned through the Fermi level. These states extend over a large (~10 nm) area around the center locations. Our data point towards a sub-surface magnetic impurity embedded in a low-density superfluid with large screening length that leads to YSR-like in-gap states. We propose a novel tip-gating mechanism for the dispersion and perform calculations within the single impurity Anderson model that show excellent agreement with the data. Such a mechanism could also play a role in previous experiments on elemental superconductors or heterostructures. How such states are related to the topological superconductivity in $FeTe_{0.55}Se_{0.45}$ remains an open question. Our work further shows that one needs to be careful when interpreting zero-bias peaks in putative topological states, and junction resistance dependent experiments are a necessary—ideally combinded with other techniques such as noise spectroscopy[65–67] (see also Supplementary Note 4), spin-polarized STM[68], or photon-assisted tunneling[69] will allow for better understanding. Independent of this, tunable impurity states like the one we report here could offer a platform to study quantum phase transitions, impurity scattering, and the screening behavior of superfluids.

Methods

Sample preparation. The $FeTe_{0.55}Se_{0.45}$ single crystal samples were grown using the Bridgman method and show a critical temperature of $T_C = 14.5$ K. We cleave them at ultra-high vacuum ($P_{base} \sim 1 \times 10^{-10}$ mbar) and low temperature (~30 K) and immediately insert them to our pre-cooled STM (USM-1500, Unisoku Co., Ltd). The STM tips used in this work are mechanically sharpened Pt-Ir wires. They are Pb-coated by indenting them on a Pb(111) surface which was first cleaned by repetitive cycles of Ar sputtering ($P_{base} \sim 5 \times 10^{-5}$ mbar) followed by thermal annealing.

Measurement. Standard lock-in technique is employed for the tunnelling conductance measurements at 887 Hz. All measurements were performed at 2.2 K.

Data availability

The data of this work are available from the corresponding author upon request.

Code availability

The code used in this work is available from the corresponding author upon request.

Received: 29 June 2020; Accepted: 7 December 2020;
Published online: 12 January 2021

References

1. Bendele, M., Weyeneth, S., Puzniak, R., Maisuradze, A. & Pomjakushina, E. et al. Anisotropic superconducting properties of single-crystalline $FeSe_{0.5}Te_{0.5}$. *Phys. Rev. B* **81**, 224520 (2010).
2. Homes, C. C., Dai, Y. M., Wen, J. S., Xu, Z. J. & Gu, G. D. $FeTe_{0.55}Se_{0.45}$: a multiband superconductor in the clean and dirty limit. *Phys. Rev. B* **91**, 144503 (2015).
3. Cho, D., Bastiaans, K. M., Chatzopoulos, D., Gu, G. D. & Allan, M. P. A strongly inhomogeneous superfluid in an iron-based superconductor. *Nature* **571**, 541 (2019).
4. Lubashevsky, Y., Lahoud, E., Chashka, K., Podolsky, D. & Kanigel, A. Shallow pockets and very strong coupling superconductivity in $FeSe_xTe_{1-x}$. *Nat. Phys.* **8**, 309 (2012).
5. Rinott, S., Chashka, K. B., Ribak, A., Rienks, E. D. L., Taleb-Ibrahimi, A. et al. Tuning across the BCS-BEC crossover in the multiband superconductor $Fe_{1+y}Se_xTe_{1-x}$: an angle-resolved photoemission study. *Sci. Adv.* 3, 10.1126/sciadv.1602372 (2017).
6. Miao, H., Brito, W. H., Yin, Z. P., Zhong, R. D. & Gu, G. D. et al. Universal $2\Delta_{max}/k_B T_c$ scaling decoupled from the electronic coherence in iron-based superconductors. *Phys. Rev. B* **98**, 020502 (2018).
7. Kreisel, A., Hirschfeld, P. J. & Andersen, B. M. On the remarkable superconductivity of FeSe and its close cousins. *Symmetry* **12**, 1 (2020).
8. Wu, X., Qin, S., Liang, Y., Fan, H. & Hu, J. Topological characters in $Fe(Te_{1-x}Se_x)$ thin films. *Phys. Rev. B* **93**, 115129 (2016).
9. Wang, Z., Zhang, P., Xu, G., Zeng, L. K. & Miao, H. et al. Topological nature of the $FeSe_{0.5}Te_{0.5}$ superconductor. *Phys. Rev. B* **92**, 115119 (2015).
10. Xu, G., Lian, B., Tang, P., Qi, X.-L. & Zhang, S.-C. Topological superconductivity on the surface of Fe-based superconductors. *Phys. Rev. Lett.* **117**, 047001 (2016).
11. Zhang, P., Yaji, K., Hashimoto, T., Ota, Y. & Kondo, T. et al. Observation of topological superconductivity on the surface of an iron-based superconductor. *Science* **360**, 182 (2018).
12. Wang, D., Kong, L., Fan, P., Chen, H. & Zhu, S. et al. Evidence for Majorana bound states in an iron-based superconductor. *Science* **362**, 333 (2018).
13. Zhu, S., Kong, L., Cao, L., Chen, H. & Papaj, M. et al. Nearly quantized conductance plateau of vortex zero mode in an iron-based superconductor. *Science* **367**, 189 (2020).
14. Chen, M., Chen, X., Yang, H., Du, Z. & Zhu, X. et al. Discrete energy levels of Caroli-de Gennes-Matricon states in quantum limit in $FeTe_{0.55}Se_{0.45}$. *Nat. Commun.* **9**, 970 (2018).

15. Huang, H., Drost, R., Senkpiel, J., Padurariu, C. & Kubala, B. et al. Quantum phase transitions and the role of impurity-substrate hybridization in Yu-Shiba-Rusinov states. *Commun. Phys.* **3**, 199 (2020).
16. Ménard, G. C., Guissart, S., Brun, C., Pons, S. & Stolyarov, V. S. et al. Coherent long-range magnetic bound states in a superconductor. *Nat. Phys.* **11**, 1013 (2015).
17. Heinrich, B. W., Pascual, J. I. & Franke, K. J. Single magnetic adsorbates on s-wave superconductors. *Prog. Surf. Sci.* **93**, 1 (2018).
18. Hudson, E. W., Lang, K. M., Madhavan, V., Pan, S. H. & Eisaki, H. et al. Interplay of magnetism and high-T_c superconductivity at individual Ni impurity atoms in $Bi_2Sr_2CaCu_2O_{8+\delta}$. *Nature* **411**, 920 (2001).
19. Zhou, B. B., Misra, S., da Silva Neto, E. H., Aynajian, P. & Baumbach, R. E. et al. Visualizing nodal heavy fermion superconductivity in $CeCoIn_5$. *Nat. Phys.* **9**, 474 (2013).
20. Hoffman, J. E., McElroy, K., Lee, D. H., Lang, K. M. & Eisaki, H. et al. Imaging quasiparticle interference in $Bi_2Sr_2CaCu_2O_{8+\delta}$. *Science* **297**, 1148 (2002).
21. Allan, M. P., Massee, F., Morr, D. K., Dyke, J. V. & Rost, A. W. et al. Imaging Cooper pairing of heavy fermions in $CeCoIn_5$. *Nat. Phys.* **9**, 468 (2013).
22. Allan, M. P., Chuang, T.-M., Massee, F., Xie, Y. & Ni, N. et al. Anisotropic impurity states, quasiparticle scattering and nematic transport in underdoped $Ca(Fe_{1-x}Co_x)_2As_2$. *Nat. Phys.* **9**, 220 (2013).
23. Rosenthal, E. P., Andrade, E. F., Arguello, C. J., Fernandes, R. M. & Xing, L. Y. et al. Visualization of electron nematicity and unidirectional antiferroic fluctuations at high temperatures in NaFeAs. *Nat. Phys.* **10**, 225 (2014).
24. Beidenkopf, H., Roushan, P., Seo, J., Gorman, L. & Drozdov, I. et al. Spatial fluctuations of helical Dirac fermions on the surface of topological insulators. *Nat. Phys.* **7**, 939 (2011).
25. Sticlet, D. & Morari, C. Topological superconductivity from magnetic impurities on monolayer $NbSe_2$. *Phys. Rev. B* **100**, 075420 (2019).
26. Palacio-Morales, A., Mascot, E., Cocklin, S., Kim, H., Rachel, S. et al. Atomic-scale interface engineering of Majorana edge modes in a 2D magnet-superconductor hybrid system. *Sci. Adv.* **5**, eaav6600 (2019).
27. Pöyhönen, K., Sahlberg, I., Weststrom, A. & Ojanen, T. Amorphous topological superconductivity in a Shiba glass. *Nat. Commun.* **9**, 2103 (2018).
28. Nadj-Perge, S., Drozdov, I. K., Li, J., Chen, H. & Jeon, S. et al. Observation of Majorana fermions in ferromagnetic atomic chains on a superconductor. *Science* **346**, 602 (2014).
29. Yin, J.-X., Wu, Z., Wang, J.-H., Ye, Z.-Y. & Gong, J. et al. Observation of a robust zero-energy bound state in iron-based superconductor Fe(Te,Se). *Nat. Phys.* **11**, 543 (2015).
30. Fan, P., Yang, F., Qian, G., Chen, H., Zhang, Y.-Y. et al. Reversible transition between Yu-Shiba-Rusinov state and Majorana zero mode by magnetic adatom manipulation in an iron-based superconductor, https://arxiv.org/abs/arXiv:2001.07376.
31. Machida, T., Sun, Y., Pyon, S., Takeda, S. & Kohsaka, Y. et al. Zero-energy vortex bound state in the superconducting topological surface state of Fe(Se, Te). *Nat. Mater.* **18**, 811 (2019).
32. Wang, Z., Rodriguez, J. O., Jiao, L., Howard, S. & Graham, M. et al. Evidence for dispersing 1D Majorana channels in an iron-based superconductor. *Science* **367**, 104 (2020).
33. Pan, S. H., Hudson, E. W. & Davis, J. C. Vacuum tunneling of superconducting quasiparticles from atomically sharp scanning tunneling microscope tips. *Appl. Phys. Lett.* **73**, 2992 (1998).
34. Rodrigo, J. G., Suderow, H. & Vieira, S. On the use of STM superconducting tips at very low temperatures. *Eur. Phys. J. B* **40**, 483 (2004).
35. Franke, K. J., Schulze, G. & Pascual, J. I. Competition of superconducting phenomena and kondo screening at the nanoscale. *Science* **332**, 940 (2011).
36. Yu, L. Bound state in superconductors with paramagnetic impurities. *Acta Phys. Sin.* **21**, 75 (1965).
37. Shiba, H. Classical spins in superconductors. *Prog. Theor. Phys.* **40**, 435 (1968).
38. Rusinov, A. Superconcductivity near a paramagnetic impurity. *J. Exp. Theor. Phys.* **9**, 85 (1969).
39. Ruby, M., Pientka, F., Peng, Y., von Oppen, F. & Heinrich, B. W. et al. Tunneling processes into localized subgap states in superconductors. *Phys. Rev. Lett.* **115**, 087001 (2015).
40. Bang, Y., Choi, H.-Y. & Won, H. Impurity effects on the ± *s*-wave state of the iron-based superconductors. *Phys. Rev. B* **79**, 054529 (2009).
41. Kreisel, A., Nelson, R., Berlijn, T., Ku, W. & Aluru, R. et al. Towards a quantitative description of tunneling conductance of superconductors: Application to LiFeAs. *Phys. Rev. B* **94**, 224518 (2016).
42. Kariyado, T. & Ogata, M. Single-impurity problem in iron-pnictide superconductors. *J. Phys. Soc. Jpn.* **79**, 16 (2010).
43. Tsai, W.-F., Zhang, Y.-Y., Fang, C. & Hu, J. Impurity-induced bound states in iron-based superconductors with *s*-wave $\cos k_x \cdot \cos k_y$ pairing symmetry. *Phys. Rev. B* **80**, 064513 (2009).
44. Gastiasoro, M. N., Hirschfeld, P. J. & Andersen, B. M. Impurity states and cooperative magnetic order in Fe-based superconductors. *Phys. Rev. B* **88**, 220509 (2013).
45. Ng, T. K. & Avishai, Y. In-gap bound states induced by nonmagnetic impurities in two-band $s_\pm$ superconductors. *Phys. Rev. B* **80**, 104504 (2009).
46. Beaird, R., Vekhter, I. & Zhu, J.-X. Impurity states in multiband *s*-wave superconductors: analysis of iron pnictides. *Phys. Rev. B* **86**, 140507 (2012).
47. Ménard, G. C., Guissart, S., Brun, C., Leriche, R. T. & Trif, M. et al. Two-dimensional topological superconductivity in Pb/Co/Si(111). *Nat. Commun.* **8**, 2040 (2017).
48. Garnier, M., Mesaros, A. & Simon, P. Topological superconductivity with deformable magnetic skyrmions. *Commun. Phys.* **2**, 126 (2019).
49. Farinacci, L., Ahmadi, G., Reecht, G., Ruby, M. & Bogdanoff, N. et al. Tuning the coupling of an individual magnetic impurity to a superconductor: quantum phase transition and transport. *Phys. Rev. Lett.* **121**, 196803 (2018).
50. Malavolti, L., Briganti, M., Hänze, M., Serrano, G. & Cimatti, I. et al. Tunable spin-superconductor coupling of Spin 1/2 vanadyl phthalocyanine molecules. *Nano Lett.* **18**, 7955 (2018).
51. Balatsky, A. V., Vekhter, I. & Zhu, J.-X. Impurity-induced states in conventional and unconventional superconductors. *Rev. Mod. Phys.* **78**, 373 (2006).
52. Wijnheijmer, A. P., Garleff, J. K., Teichmann, K., Wenderoth, M. & Loth, S. et al. Single Si dopants in GaAs studied by scanning tunneling microscopy and spectroscopy. *Phys. Rev. B* **84**, 125310 (2011).
53. Battisti, I., Fedoseev, V., Bastiaans, K. M., de la Torre, A. & Perry, R. S. et al. Poor electronic screening in lightly doped Mott insulators observed with scanning tunneling microscopy. *Phys. Rev. B* **95**, 235141 (2017).
54. Koyama, T. Comment on "Charge expulsion and electric field in superconductors". *Phys. Rev. B* **70**, 226503 (2004).
55. Sales, B. C., Sefat, A. S., McGuire, M. A., Jin, R. Y. & Mandrus, D. et al. Bulk superconductivity at 14 K in single crystals of $Fe_{1+y}Te_xSe_{1-x}$. *Phys. Rev. B* **79**, 094521 (2009).
56. Song, S. Y., Martiny, J. H. J., Kreisel, A., Andersen, B. M. & Seo, J. Visualization of local magnetic moments emerging from impurities in Hund's metal states of FeSe. *Phys. Rev. Lett.* **124**, 117001 (2020).
57. Anderson, P. W. Theory of localized magnetic states in metals. *J. Appl. Phys.* **37**, 1194 (1966).
58. Jellinggaard, A., Grove-Rasmussen, K., Madsen, M. H. & Nygård, J. Tuning yu-shiba-rusinov states in a quantum dot. *Phys. Rev. B* **94**, 064520 (2016).
59. Kiršanskas, G., Goldstein, M., Flensberg, K., Glazman, L. I. & Paaske, J. Yu-Shiba-Rusinov states in phase-biased superconductor–quantum dot–superconductor junctions. *Phys. Rev. B* **92**, 235422 (2015).
60. Žitko, R. Numerical subgap spectroscopy of double quantum dots coupled to superconductors. *Phys. Rev. B* **91**, 165116 (2015).
61. Grove-Rasmussen, K., Steffensen, G., Jellinggaard, A., Madsen, M. H. & Žitko, R. et al. Yu-Shiba-Rusinov screening of spins in double quantum dots. *Nat. Commun.* **9**, 2376 (2018).
62. Bauer, J., Oguri, A. & Hewson, A. C. Spectral properties of locally correlated electrons in a Bardeen–Cooper–Schrieffer superconductor. *J. Phys. Condens. Matter* **19**, 486211 (2007).
63. Dynes, R. C., Narayanamurti, V. & Garno, J. P. Direct measurement of quasiparticle-lifetime broadening in a strong-coupled superconductor. *Phys. Rev. Lett.* **41**, 1509 (1978).
64. Huang, H., Padurariu, C., Senkpiel, J., Drost, R., Yeyati, A. L. et al. Tunneling dynamics between superconducting bound states at the atomic limit. *Nat. Phys.* **16**, 1227-1231. https://doi.org/10.1038/s41567-020-0971-0. (2020).
65. Jonckheere, T., Rech, J., Zazunov, A., Egger, R. & Yeyati, A. L. et al. Giant shot noise from majorana zero modes in topological trijunctions. *Phys. Rev. Lett.* **122**, 97003 (2019).
66. Golub, A. & Horovitz, B. Shot noise in a Majorana fermion chain. *Phys. Rev. B* **83**, 153415 (2011).
67. Bastiaans, K. M., Cho, D., Chatzopoulos, D., Leeuwenhoek, M. & Koks, C. et al. Imaging doubled shot noise in a Josephson scanning tunneling microscope. *Phys. Rev. B* **100**, 104506 (2019).
68. Wiesendanger, R. Spin mapping at the nanoscale and atomic scale. *Rev. Mod. Phys.* **81**, 1495 (2009).
69. Tang, H.-Z., Zhang, Y.-T. & Liu, J.-J. Photon-assisted tunneling through a topological superconductor with Majorana bound states. *AIP Adv.* **5**, 127129 (2015).

Acknowledgements

We acknowledge J. de Bruijckere, J.F. Ge, M.H. Fischer, P.J. Hirschfeld, D.K. Morr, P. Simon, J. Zaanen, and H.S.J. van der Zant for fruitful discussions. This work was supported by the European Research Council (ERC StG SpinMelt) and by the Netherlands Organization for Scientific Research (NWO/OCW), as part of the Frontiers of Nanoscience programme, as well as through a Vidi grant (680-47-536). G.G. is supported by the Office of Basic Energy Sciences, Materials Sciences and Engineering Division, US Department of Energy (DOE) under contract number de-sc0012704. B.M.A. acknowledges support from the Independent Research Fund Denmark grant number DFF-8021-

00047B. The Center for Quantum Devices is funded by the Danish National Research Foundation. D. Cho was supported by the National Research Foundation of Korea (NRF) grant funded by the Korea government (MSIT) (No. 2020R1C1C1007895 and 2017R1A5A1014862) and the Yonsei University Research Fund of 2019-22-0209. A.A. acknowledges the support of the Max Planck-POSTECH-Hsinchu Center for Complex Phase Materials, and financial support from the National Research Foundation (NRF) funded by the Ministry of Science of Korea (Grant No. 2016K1A4A01922028).

Author contributions

D. Chatzopoulos, D. Cho, and K.M.B. performed the experiments and data analysis. D. Chatzopoulos, G.O.S., D.B., A.A., J.P., and B.M.A. performed the simulations. G.G. grew and characterized the samples. All authors contributed to the interpretation of the data and writing of the manuscript. M.P.A. supervised the project.

Competing interests

The authors declare no competing interests.

Additional information

Supplementary information is available for this paper at https://doi.org/10.1038/s41467-020-20529-x.

Correspondence and requests for materials should be addressed to M.P.A.

Peer review information *Nature Communications* thanks the anonymous reviewer(s) for their contribution to the peer review of this work. Peer reviewer reports are available.

Reprints and permission information is available at http://www.nature.com/reprints

Publisher's note Springer Nature remains neutral with regard to jurisdictional claims in published maps and institutional affiliations.

13

CONCLUSION AND OUTLOOK

This thesis has explored transport in S-DQD-S junctions formed on InAs nanowires hosting YSR subgap states. We have shown in chapter 3 that measurements of zero-bias supercurrent in the overdamped, voltage biased, and noise-dominated regime allows for characterization of charge diagrams and extraction of critical current I_c. This technique yielded a consistent measure of I_c for all dot occupations, although fitting could only be done up to a global scaling λ due to limited knowledge of circuit parameters. In future experiments one could think of intentionally designing circuits with this measurement in mind as the noise-dominated signal has some advantages compared to the overdamped current biased signal, previously used to extract I_c in S-QD-S junctions [115, 116]. First of all, it allows for measurements of very small I_c as the zero-bias conductance feature's width is independent of I_c and therefore not limited by bias resolution. In current biased setups on the other hand, measurements are limited by current resolution compared to switching current I_s, which for small I_c is significantly reduced by noise. Secondly, the noise-dominated signal follows a simple Lorentzian form, always scaling with I_c^2, which allows easy fitting compared to the complicated Bessel functions of the low noise regime. To eliminate the scaling degree of freedom λ plaguing our measurements, one requires an individual measurement of either I_c, noise temperature T, or resistance R in conjunction with a fitted zero-bias peak. Here one could design the resistance R between capacitor C and junction, and characterize it beforehand, or one could look for a high I_c compared to noise for which the noise-dominated limit fails. In measurement this would be signalled by a change in width of the zero-bias peak, with flanking NDC peaks moving further out in source-drain bias. The peak to width ratio at this point would yield an independent measure of noise temperature T.

Using 4^{th} order perturbation theory in chapter 4 we calculated I_c for both single dots and double dots, and illustrated how the various regimes of U compared to Δ can be understood in terms of cooper-pair cotunneling paths. Additionally, this approach can be used to calculate I_c in arbitrary diagonalizable systems, such as N sites in a chain or multi-orbital dots, with all contributions characterized by one of

three Q_j integrals. Lastly, we have shown that the sign of a given contribution to I_c can be inferred by the number of same spin electrons each constituent electron of the cooper-pair crosses during tunnelling. It is the author's hope that these rules can be used to gain some intuition by others calculating supercurrent in complicated geometries where interactions cannot be neglected.

In chapter 7 we derived expressions for the DC current using Keldysh-Floquet Green's functions, which are valid for non-interacting Hamiltonians and includes MAR to all orders. This was utilized in chapter 8 to analyse transport in S-QD-N and S-QD-S junctions hosting YSR states, which we describe via the spin-polarized mean-field approximation. Results of this chapter highlights the importance of relaxation and poisoning rates on transport measurements, and identifies tunnel coupling compared to relaxation, t_d/η, as a key scale for determining the importance of higher order transport through subgap states. In chapter 9 these techniques were utilized to characterize and fit measurements of transport between opposing subgap states, where Andreev mediated relaxation channels can be turned on and off through tuning of gates. The surprising (to the author) realization that Lindblad master equations are in complete agreement with Keldysh-Floquet Green's functions, in conjunction with the fact that the doublet degeneracy can be included in the Lindblad master equations, makes this an intriguing approach to investigate in further work.

This concludes our work on transport in devices hosting quantum dots. New challenges are bound to appear as hybrid semiconductor-superconductor devices of ever growing complexity are being fabricated. In this regard it is crucial that both theoretical tools and accompanying intuition is developed *on par* with experiment. This work constitutes my contribution to this mission.

APPENDIX

A

NAMBU GREEN'S FUNCTIONS

In this appendix we detail how Nambu Green's functions of superconducting systems are obtained, with specific focus on the localized BCS Green's function utilized throughout this thesis.

A.1 NAMBU DETAILS

First we have to consider some pesky details of the 4×4 Nambu space, which are required if we are to obtain Green's functions through equations of motion. The spinor we use throughout this thesis is,

$$\Psi_{jk}^{\dagger} = \begin{pmatrix} c_{jk\uparrow}^{\dagger} & c_{j-k\downarrow} & c_{j-k\downarrow}^{\dagger} & -c_{jk\uparrow} \end{pmatrix}, \tag{A.1}$$

containing lead index j and a momentum k, and from its definition it obeys the following commutation relations,

$$\{\Psi_{jk,a}^{\dagger}, \Psi_{j'k',b}\} = \delta_{k,k'}\delta_{j,j'}\delta_{ab}, \qquad \{\Psi_{jk,a}^{\dagger}, \Psi_{j'k',b}^{\dagger}\} = \delta_{-k,k'}\delta_{j,j'}(\sigma_y\tau_y)_{ab}, \tag{A.2}$$

with a and b specifying entrances in Nambu space. Here the first relation is quite standard and compares to the normal fermionic relation $\{c, c^{\dagger}\} = 1$, while the second is not as we are used to $\{c^{\dagger}, c^{\dagger}\} = 0$ no matter the index. Additionally, the matrix in the second term has the special property $\Psi_k^{\dagger} = \sigma_y\tau_y\Psi_k$. Next, we investigate the effects of this second relation on equation of motion structures for non-interacting Hamiltonians of the form,

$$H(t) = \frac{1}{2}\sum_{kk'}\sum_{ij}\Psi_{ik}^{\dagger}h_{ijkk'}(t)\Psi_{jk'}. \tag{A.3}$$

Starting from the retarded Green's function defined as,

$$G_{ijkk',ab}^{R}(t,t') = -i\Theta(t-t')\langle\{\Psi_{ik,a}, \Psi^{d}agger_{jk',b}\}\rangle, \tag{A.4}$$

we take the time derivative and obtain,

$$i\partial_t G_{ijkk',ab}(t,t') = \delta(t-t')\langle\{\Psi_{ik,a}(t), \Psi_{jk',b}^{\dagger}(t')\}\rangle + i\theta(t-t')\langle\{[H(t), \Psi_{ik,a}](t), \Psi_{jk',b}^{\dagger}(t')\}\rangle. \tag{A.5}$$

Here the first term gives the usual identity in all index, $\delta(t-t')\delta_{k,k'}\delta_{ij}\delta_{ab}$, but the commutator in the second term needs to be considered in greater detail. For clarity we suppress time arguments and find,

$$\begin{aligned}
&[H, \Psi_{ik.b}] \\
&= \frac{1}{2}\sum_{j_1 j_2}\sum_{k_1,k_2,a_1 a_2}\left(\Psi^\dagger_{j_1 k_1 a_1} h_{j_1 j_2 k_1 k_2, a_1 a_2}\Psi_{j_2 k_2, a_2}\Psi_{ik,b} - \Psi_{ik,b}\Psi^\dagger_{j_1 k_1 a_1} h_{j_1 j_2 k_1 k_2, a_1 a_2}\Psi_{j_2 k_2, a_2}\right) \\
&= \frac{1}{2}\sum_{j_1 k_1 a_1}\left(\Psi^\dagger_{j_1 k_1, a_1}\sum_{a_2} h_{j_1 i k_1 - k, a_1 a_2}(\sigma_y\tau_y)_{a_2 b} - h_{ij_1 k k_1, b a_1}\Psi_{j_1 k_1, a_1}\right) \qquad \text{(A.6)} \\
&= -\sum_{j_1 k_1 a_1} h_{ij_1 k k_1, b a_1}\Psi_{j_1 k_1, a_1}
\end{aligned}$$

To go from the second line to the third line we used two properties of the Hamiltonian,

$$h_{-kk'} = h_{kk'}, \qquad \sum_{a_2} h_{j_1 i k_1 k, a_1 a_2}\,(\sigma_y\tau_y)_{a_2 b} = \sum_{a_2}(\sigma_y\tau_y)_{a_1 a_2}\, h_{ij_1 k k_1, b a_2}. \qquad \text{(A.7)}$$

As all k-dependent Hamiltonians we consider in this thesis are momentum symmetric the first property is always upheld. The second property corresponds to $\sigma_y\tau_y h = h^T\sigma_y\tau_y$ with the transpose operating on all index. Utilizing $h^T = h^*$, which is true for hermitian matrices, the second property can be rewritten as,

$$(\sigma_y\tau_y K)h = h(\sigma_y\tau_y K) \qquad \text{(A.8)}$$

where K is an operator performing complex conjugation. Recognizing $T = i\sigma_y K$ as the time-reversal operator and defining $C = -i\tau_y$, we find that this requirement is equivalent to $\{h, CT\} = 0$ [96]. All Hamiltonian in this thesis will satisfy this demand and so we assume eq. (A.6) to be valid. Utilizing these results eq. (A.5) reduces to,

$$i\partial_t G^R_{ijkk'}(t,t') = \delta(t-t')\delta_{ij}\delta(kk') + \sum_{j_1 k_1} h_{ij_1 k k_1} G^R_{j_1 j k_1 k'}, \qquad \text{(A.9)}$$

with assumed Nambu matrix multiplication between elements. This equation resembles the normal equation of motion structure for non-Nambu Green's functions, and allow us to derive Dyson series as usual. Assuming that the Hamiltonian is time-invariant and only depends on one k allows us to simplify the Green's function, $G^R_{kk'}(t,t') = G^R_k(t-t')\delta_{kk'}$, for which the equation of motion can be solved via a Fourier transformation in time-difference,

$$G^R_k(\omega) = [\omega + i\eta - h_k]^{-1}, \qquad \text{(A.10)}$$

with the inverse taken in regard to 4×4 Nambu structure and η added to achieve convergence.

A.2 BARE SUPERCONDUCTING GREEN'S FUNCTION

Throughout this thesis we repeatedly use the bare Green's function of a local BCS superconductor, and although the derivations is common we include it here for consistency. The Hamiltonian of a three dimensional BCS superconductor is in Nambu space given by,

$$H = \frac{1}{2}\sum_k \Psi_k^\dagger \left[\epsilon_k \tau_z + \mathrm{Re}(\Delta)\tau_x + \mathrm{Im}(\Delta)\tau_y \Delta\right] \Psi_k \tag{A.11}$$

and from equations of motion eq. (A.10) we find,

$$g_k^R(\omega) = \left[\omega + i\eta - \epsilon_k \tau_z - \Delta_R \tau_x - \Delta_I \tau_y\right]^{-1} \tag{A.12}$$

$$= \frac{\omega + i\eta + \epsilon_k \tau_z + \Delta_R \tau_x + \Delta_I \tau_y}{(\omega + i\eta)^2 - \epsilon_k^2 - |\Delta|^2} \tag{A.13}$$

with the common Fourier convergence factor $i\eta$ which should be taken to zero at the end of calculations, and defining $\mathrm{Re}(\Delta) = \Delta_R$, $\mathrm{Im}(\Delta) = \Delta_I$. Next, we integrate over all k to obtain the local Green's function at $r = 0$ which we dub $g^R(\omega)$, and introduce an assumed constant density of state $\nu_F(\epsilon_k)$ fulfilling $\int d^3k g_k^R(\omega) = \nu_F \int d\epsilon_k g_k^R(\omega)$. With this we obtain,

$$g^R(\omega) = -\nu_F \int_{-\infty}^{\infty} d\epsilon_k \frac{\omega + i\eta + \epsilon_k \tau_z + \Delta_R \tau_x + \Delta_I \tau_y}{\left(\epsilon_k - \sqrt{(\omega + i\eta)^2 + |\Delta|^2}\right)\left(\epsilon_k + \sqrt{(\omega + i\eta)^2 + |\Delta|^2}\right)}. \tag{A.14}$$

In this expression the anti-symmetric term proportional to ϵ_k integrates to zero. Next, we choose a branch cut in the complex plane and perform the contour integral to obtain,

$$g^R(\omega) = -\pi\nu_F \frac{\omega + i\eta + \Delta_R \tau_x + \Delta_I \tau_y}{\sqrt{|\Delta|^2 - (\omega + i\eta)^2}} \tag{A.15}$$

which is the local BCS Green's function. We also wish to obtain the local Green's function as a function of imaginary time at finite temperature. The corresponding Matsubara Green's function is given by,

$$g(i\omega_n) = \nu_F \int_{-\infty}^{\infty} d\epsilon_k \frac{i\omega_n + \Delta_R \tau_x + \Delta_I \tau_y}{(i\omega_n - E_\Delta)(i\omega_n + E_\Delta)} \tag{A.16}$$

with $E_\Delta = \sqrt{\epsilon_k^2 + |\Delta|^2}$. To obtain the imaginary time Green's function we need to perform,

$$g(\tau) = \frac{1}{\beta}\sum_n e^{-i\omega_n \tau} g(i\omega_n) \tag{A.17}$$

which is easily done since $g(i\omega_n)$ has two simple poles. Doing the contour integral as in Ref. [18] we find,

$$g(\tau) = -\sum_j \mathrm{Res}_{z=z_j}\left[g(z)\right] n_F(-z_j)e^{-z_j\tau} \tag{A.18}$$

where j is a sum over all simple poles. Consequently,

$$g(\tau) = \nu_F \frac{1}{2}\int_{-\infty}^{\infty} d\epsilon_k \left[\frac{E_\Delta + \Delta_R\tau_x + \Delta_I\tau_y}{E_\Delta} n_F(-E_\Delta)e^{-E_\Delta\tau} + \frac{E_\Delta - \Delta_R\tau_x - \Delta_I\tau_y}{E_\Delta} n_F(E_\Delta)e^{E_\Delta\tau}\right], \tag{A.19}$$

this last expression can be simplified by substituting $x = E_\Delta = \sqrt{\epsilon_k^2 + |\Delta|^2}$ in the integral yielding,

$$\begin{aligned} g(\tau) = \nu_F \int_\Delta^\infty \frac{dx}{\sqrt{x^2 - |\Delta|^2}} \Big[& x\left(n_F(-x)e^{-x\tau} + n_F(x)e^{x\tau}\right) \\ & + \left(\Delta_R\tau_x + \Delta_I\tau_y\right)\left(n_F(-x)e^{-x\tau} - n_F(x)e^{x\tau}\right)\Big]. \end{aligned} \tag{A.20}$$

which constitutes our results for the imaginary time BCS superconductor. Lastly, we in section 4.4 also require the ZBW Green's function. We start with,

$$g_{ZBW}(i\omega_n) = \frac{1}{\omega_n - \Delta_R\tau_x - \Delta_I\tau_y} = \frac{i\omega_n + \Delta_R\tau_x + \Delta_I\tau_y}{(i\omega_n - \Delta)(i\omega_n + \Delta)} \tag{A.21}$$

and going through the same calculations we find,

$$g_{ZBW}(\tau) = \frac{1}{2|\Delta|}\left[|\Delta|\left(n_F(-x)e^{-x\tau} + n_F(x)e^{x\tau}\right) + \left(\Delta_R\tau_x + \Delta_I\tau_y\right)\left(n_F(-x)e^{-x\tau} - n_F(x)e^{x\tau}\right)\right] \tag{A.22}$$

which by comparison to the BCS Greens function motivates the definition $\nu_{ZBW} = \frac{1}{2\Delta}$.

B

SIGN OF CRITICAL CURRENT

In this section, we demonstrate that the sign of the critical current I_c to lowest order in dot-lead couplings is given by the groundstate parity for a large range of parameters for a S-DQD-S junction. This section is copied from the supplement of project 4 [4] with minor alterations to fit into the structure of the thesis. Compared to the Hamiltonian investigated in chapter 4 we additionally add a spin-orbit and Zeeman term yielding the full Hamiltonian,

$$H = H_0 + H_d + H_{SO} + H_{BCS} + H_T \tag{B.1}$$

$$H_0 = \sum_{\sigma,i=L,R} (\epsilon_i + \sigma g_i B) n_{i\sigma} + \sum_{i=L,R} U_i n_{i\uparrow} n_{i\downarrow} + U_C (n_{L\uparrow} + n_{L\downarrow})(n_{R\uparrow} + n_{R\downarrow}) \tag{B.2}$$

$$H_D = t_d \sum_{\sigma} (d^\dagger_{L\sigma} d_{R\sigma} + d^\dagger_{R\sigma} d_{L\sigma}) \tag{B.3}$$

$$H_{SO} = \sum_{j=x,y,z} \sum_{\sigma,\sigma'} \left(i t_j \tau^j_{\sigma\sigma'} d^\dagger_{L\sigma} d_{R\sigma'} - i t_j \tau^j_{\sigma\sigma'} d^\dagger_{R\sigma} d_{L\sigma'} \right) \tag{B.4}$$

$$H_{BCS} = \sum_{k,\sigma,i=L,R} \xi_i c^\dagger_{ik\sigma} c_{ik\sigma} + \sum_{k,i=L,R} \left(\Delta_i c^\dagger_{ik\uparrow} c^\dagger_{i-k\downarrow} + \Delta_i^* c_{i-k\downarrow} c_{ik\uparrow} \right) \tag{B.5}$$

$$H_T = \sum_{k,\sigma,i=L,R} t_i \left(c^\dagger_{ik\sigma} d_{i\sigma} + d^\dagger_{i\sigma} c_{ik\sigma} \right) \tag{B.6}$$

Here, $n_{i\sigma}$ denotes the electron occupation operator for dot $i \in \{L, R\}$ with spin $\sigma \in \{\uparrow, \downarrow\}$. t_x, t_y and t_z are interdot spin-orbit tunneling amplitudes, and τ^j is the vector of Pauli matrices [175]. Next, we calculate the sign of I_c to lowest order in dot-lead couplings, and demonstrate that it is determined from the double dot groundstate through the simple rules stated in subsection 4.2.1. We start from eq. (4.27) valid for a general Hamiltonian between a left and right lead,

$$I_c = \sum_{ijkl} I_{ijkl} = \frac{4e}{\hbar} |\Delta|^2 \Gamma_R \Gamma_L \sum_{ijkl} \frac{1}{\beta} \int_0^\beta d\tau_i \int_0^{\tau_i} d\tau_j \int_0^{\tau_j} d\tau_k \int_0^{\tau_k} d\tau_l \tag{B.7}$$
$$\times f^*(\tau_1 - \tau_2) f(\tau_3 - \tau_4) \mathcal{B}_{ijkl}(\tau_1, \tau_2, \tau_3, \tau_4)$$

With the object $\mathcal{B}_{ijkl}$ containing all DQD operators,

$$\mathcal{B}_{ijkl}(\tau_1, \tau_2, \tau_3, \tau_4) = \epsilon_{ijkl} \left\langle d_i(\tau_i) d_j(\tau_j) d_k(\tau_k) d_l(\tau_l) \right\rangle_0, \tag{B.8}$$

with the definitions $d_1(\tau_1) = d^\dagger_{L\uparrow}(\tau_1)$, $d_2(\tau_2) = d^\dagger_{L\downarrow}(\tau_2)$, $d_3(\tau_3) = d_{R\downarrow}(\tau_3)$ and $d_4(\tau_4) = d_{R\uparrow}(\tau_4)$. At zero temperature, the dot system is in a definite groundstate, $|g\rangle$, of the full dot Hamiltonian with,

$$\mathcal{B}_{ijkl}(\tau_1,\tau_2,\tau_3,\tau_4) = \epsilon_{ijkl}\,\langle g|\, d_i U(\tau_i,\tau_j) d_j U(\tau_j,\tau_k) d_k U(\tau_k,\tau_l) d_l\,|g\rangle\,, \tag{B.9}$$

where we have separated the trivial time evolution of the isolated dots due to H_0 from the evolution generated by $H_D + H_{SO}$, which couples the dots. The time evolution operator above is defined in the interaction picture,

$$U(\tau_i,\tau_j) = e^{-(H_0-E_g)\tau_i}\, T_\tau\, e^{-\int_{\tau_j}^{\tau_i} d\tau' \bar{H}_D(\tau')} e^{(H_0-E_g)\tau_j} \tag{B.10}$$

with $\bar{H}_D(\tau) = e^{H_0\tau}(H_D + H_{SO})e^{-H_0\tau}$, where T_τ is the τ-ordering operator. In eq. (B.7) we expand the time evolution operators appearing in eq. (B.9) to N'th order in $\bar{H}_D$. From now on we will discuss generic contributions to this expansion, which we label $I^{(a,b,c)}_{ijkl}$ with $I_c = \sum_{ijkl=1}^{4}\sum_{abc=0}^{\infty} I^{(a,b,c)}_{ijkl}$. The integers a, b and c specify the order of expansion (counting from left) of each time evolution operator in eq. ((B.9)). A single N'th order ($a+b+c=N$) contribution can, in terms of the amplitudes

$$\langle g|\, \mathcal{C}^{(a,b,c)}_{ijkl}\,|g\rangle = \epsilon_{ijkl}(-1)^N \langle g|\, d_i (H_D+H_{SO})^a d_j (H_D+H_{SO})^b d_k (H_D+H_{SO})^c d_l\,|g\rangle \tag{B.11}$$

be expressed as,

$$\begin{aligned}
&I^{(a,b,c)}_{ijkl} \\
&= \frac{4e}{\hbar}|\Delta|^2\Gamma_R\Gamma_L \int_0^\beta d\tau_i \prod_{\mu=0}^{N+2}\left(\int_0^{\tau'_\mu} d\tau'_{\mu+1} e^{-(E_\mu-E_g)(\tau'_\mu-\tau'_{\mu+1})}\right) f^*(\tau_1-\tau_2) f(\tau_3-\tau_4)\,\langle g|\, \mathcal{C}^{(a,b,c)}_{ijkl}\,|g\rangle \\
&= \frac{4e}{\hbar}\Gamma_L\Gamma_R|\Delta|^2 \int_\Delta^\infty \frac{d\omega}{\sqrt{\omega^2-\Delta^2}} \int_\Delta^\infty \frac{d\omega'}{\sqrt{\omega'^2-\Delta^2}} \prod_{m=1}^{n}\left(\frac{1}{E_m - E_g + \omega + \omega'}\right) \\
&\quad\times \prod_{m'=1}^{n'}\left(\frac{1}{E_{m'}-E_g+\omega}\right) \prod_{m''=1}^{n''}\left(\frac{1}{E_{m''}-E_g+\omega'}\right) \prod_{m'''=1}^{n'''}\left(\frac{1}{E_{m'''}-E_g}\right) \langle g|\, \mathcal{C}^{(a,b,c)}_{ijkl}\,|g\rangle\,,
\end{aligned} \tag{B.12}$$

with the definition $\tau_i = \tau'_0$, $\tau_j = \tau'_{a+1}$, $\tau_k = \tau'_{a+b+2}$ and $\tau_l = \tau'_{N+3}$. In the second line $n + n' + n'' + n''' = N + 3$ are positive integers whose values are specified by both the expansion in a, b and c and the ordering ijkl, while E_n are energies of the uncoupled charge basis H_0.

Next comes the critical statement: since all fractions in eq. (B.12) are positive, the sign is determined solely by $\mathcal{C}^{(a,b,c)}_{ijkl}$. For this to be true, the groundstate energy of $H_0 + H_D + H_{SO}$, E_g, must satisfy that $E_g \leqslant E_n$ where E_n are eigenenergies of H_0. For a hermitian matrix, A, with diagonal entries a_{nn} and minimal (maximal) eigenvalues

$\lambda_{\min}$ ($\lambda_{\max}$), the min-max theorem [176] states that $\lambda_{\min} \leqslant a_{nn} \leqslant \lambda_{\max}$. In the charge basis, $H_D + H_{SO}$ only contains off-diagonal elements, and with $A = H_0 + H_D + H_{SO}$, we may therefore conclude that $E_g = \lambda_{\min} < a_{nn} = E_n$, as needed. Note that this perturbation series breaks down if $E_{m'''} = E_g$ in the denominator $1/(E_{m'''} - E_g)$. Such a denominator occurs only if $E_{m'''}$ relates to a state with ± 2 electrons compared to the groundstate. In such instances one would have to go to higher order in t_L, t_R.

By removing the integrals $\int_\Delta^\infty \frac{d\omega}{\sqrt{\omega^2-\Delta^2}}$, setting $\omega, \omega' = \Delta$ in the denominators and using $\Gamma_i = \pi t_{i,ZBW}^2/2\Delta$, one would obtain the corresponding I_c expansion for a ZBW description of the superconductors. As such, the previous and following arguments about the sign of I_c also holds for a ZBW description.

B.0.1 *Sign of all contributions to critical current*

We now turn our attention to the time independent part $\mathcal{C}_{ijkl}^{(a,b,c)}$, which specifies the total sign, and we wish to show that no matter the value of a, b, c or i, j, k, l, the sign of a contribution to I_c is determined by the groundstate. In this subsection we neglect spin-orbit coupling, H_{SO}, the effect of which we discuss in a following subsection.

It is convenient to work in a spin-sorted basis of the many-body state $\langle 2,2| = \langle 0| d_{L\uparrow} d_{R\uparrow} d_{L\downarrow} d_{R\downarrow}$. With this choice, one can make use of the fact that H_D conserves spin and therefore commutes with operators of opposite spin to sort $\mathcal{C}_{ijkl}^{(a,b,c)}$ as

$$\langle g| \mathcal{C}_{ijkl}^{(a,b,c)} |g\rangle = \sum_{n,m} \alpha_n \alpha_m^* \left\langle n_\uparrow \right| \mathcal{C}_{\uparrow,i'j'}^{(a_\uparrow b_\uparrow c_\uparrow)} \left| m_\uparrow \right\rangle \left\langle n_\downarrow \right| \mathcal{C}_{\downarrow,i''j''}^{(a_\downarrow b_\downarrow c_\downarrow)} \left| m_\downarrow \right\rangle, \tag{B.13}$$

where we have expressed the ground state as a tensor product state between the two spin sectors, $|g\rangle = \sum_n \alpha_n \left|n_\uparrow\right\rangle \otimes \left|n_\downarrow\right\rangle$, with α_n being prefactors from the diagonalization of $H_0 + H_D$. The indexes of $\mathcal{C}_{\sigma,i'j'}^{(a_\sigma,b_\sigma,c_\sigma)}$ are specified by the $ijkl$ index as follows: $i', j' \in \{1,4\}$ for spin-up and $i'', j'' \in \{2,3\}$ for spin-down, while ordering is the same as in $ijkl$ for each subset independently, e.g $\mathcal{C}_{3124}^{(a,b,x)}$ corresponds to $\mathcal{C}_{\uparrow,14}^{(a_\uparrow,b_\uparrow,c_\uparrow)}$ and $\mathcal{C}_{\downarrow,32}^{(a_\downarrow,b_\downarrow,c_\downarrow)}$. Finally, the powers a_σ, b_σ and c_σ denote the number of H_D operators containing spin-σ, such that $\sum_\sigma a_\sigma + b_\sigma + c_\sigma = a + b + c = N$, where we do not permute any operators of same spin in the sorting. This yields the following object, which determines the sign of each spin independently:

$$\langle n_\sigma| \mathcal{C}_{\sigma,ij}^{(a_\sigma b_\sigma c_\sigma)} |m_\sigma\rangle = \epsilon_{ij} (-1)^{a_\sigma + b_\sigma + c_\sigma} \langle n_\sigma| (H_{D\sigma})^{a_\sigma} d_i (H_{D\sigma})^{b_\sigma} d_j (H_{D\sigma})^{c_\sigma} |m_\sigma\rangle, \tag{B.14}$$

with the Levi-Civita symbols, ϵ_{ij}, defined with $\epsilon_{14} = 1$ and $\epsilon_{23} = 1$. Additionally we defined $H_{D\sigma} = t_d d_{L\sigma}^\dagger d_{R\sigma} + h.c.$

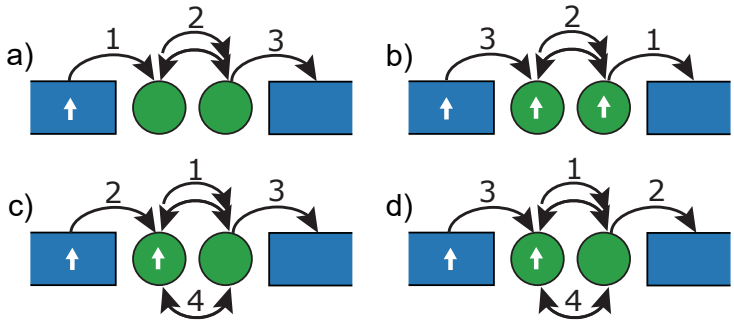

Figure B.1: The paths transferring one electron across the DQD for various ground states. The numbers represent the order of operations applied to $\langle n_\uparrow|$ to reach $|n_\uparrow\rangle$. Lines with arrows in both directions indicate an integer number of back-and-forth jumps each yielding t_0^2. a) $|n_\uparrow\rangle = |0,0\rangle$, b) $|n_\uparrow\rangle = |1,1\rangle$ c), one ordering of $|n_\uparrow\rangle = |1,0\rangle$, d) another ordering of $|n_\uparrow\rangle = |1,0\rangle$.

We will now consider a few specific spin contributions. We start with the state where both dots are void of spin-up electrons such that $|n_\uparrow\rangle = |m_\uparrow\rangle = |0,0\rangle$ where left and right number in the kets refer to the number of spin-up electrons on the left and right dots respectively. Such a contribution yields

$$\begin{aligned}\langle 0,0|\, \mathcal{C}_{\uparrow,ij}^{(a_\uparrow b_\uparrow c_\uparrow)} |0,0\rangle &= \epsilon_{ij}(-1)^{a_\uparrow+b_\uparrow+c_\uparrow} \langle 0,0|\, (H_{D\uparrow})^{a_\uparrow} d_i (H_{D\uparrow})^{b_\uparrow} d_j (H_{D\uparrow})^{c_\uparrow} |0,0\rangle \\ &= \delta_{i4}\delta_{j1}\delta_{a_\uparrow 0}\delta_{c_\uparrow 0}\epsilon_{41}(-1)^1 t_d^{b_\uparrow} \langle 0,0|\, d_{R\uparrow} d_{R\uparrow}^\dagger d_{L\uparrow} d_{L\uparrow}^\dagger |0,0\rangle \geqslant 0,\end{aligned} \tag{B.15}$$

where the disappearance of $H_{D\uparrow}^{b_\uparrow}$ stems from the fact that the only non-zero contribution arises when $b_\uparrow$ is odd and $H_{D\uparrow}^{b_\uparrow}$ contains a single $t_d d_{L\uparrow}^\dagger d_{R\uparrow}$ multiplied by $(b_\uparrow - 1)/2$ back-and-forth operators of the type $t_d^2 d_{L\uparrow}^\dagger d_{R\uparrow} d_{R\uparrow}^\dagger d_{L\uparrow}$. A visual representation of such processes is shown in fig.B.1 a). If the two dots are void of spin-up electrons, the spin-up part will therefore yield a positive sign to eq. (B.13) to all orders of H_D.

Due to the electron-hole symmetry, a very similar derivation follows for the doubly occupied spin-up state

$$\begin{aligned}\langle 1,1|\, \mathcal{C}_{\uparrow,ij}^{(a_\uparrow b_\uparrow c_\uparrow)} |1,1\rangle &= \epsilon_{ij}(-1)^{a_\uparrow+b_\uparrow+c_\uparrow} \langle 1,1|\, (H_{D\uparrow})^{a_\uparrow} d_i (H_{D\uparrow})^{b_\uparrow} d_j (H_{D\uparrow})^{c_\uparrow} |1,1\rangle \\ &= \delta_{i1}\delta_{j4}\delta_{a_\uparrow 0}\delta_{b_\uparrow 0}\epsilon_{14}(-1)^1 t_d^{b_\uparrow} \langle 1,1|\, d_{L\uparrow}^\dagger d_{R\uparrow}^\dagger d_{L\uparrow} d_{R\uparrow} |1,1\rangle \geqslant 0,\end{aligned} \tag{B.16}$$

where a visual representation is shown in fig. B.1 b).

The odd groundstate configurations are a little more complicated, as there is more than one way of organizing operators. Consider contributions with $|n_\uparrow\rangle = |m_\uparrow\rangle = |1,0\rangle$ meaning one spin-up electron on the left dot,

$$\begin{aligned}\langle 1,0|\, \mathcal{C}^{(a_\uparrow b_\uparrow c_\uparrow)}_{\uparrow,ij} \,|1,0\rangle &= \epsilon_{ij}(-1)^{a_\uparrow+b_\uparrow+c_\uparrow} \langle 1,0|\, (H_{D\uparrow})^{a_\uparrow} d_i (H_{D\uparrow})^{b_\uparrow} d_j (H_{D\uparrow})^{c_\uparrow} \,|1,0\rangle \\ &= \delta_{b_\uparrow 0} t_d^{a_\uparrow+c_\uparrow}(-1)^1 \Big(\delta_{i1}\delta_{j4}\epsilon_{14} \langle 1,0|\, d^\dagger_{L\uparrow} d_{R\uparrow} d^\dagger_{R\uparrow} d_{L\uparrow} \,|1,0\rangle \\ &\qquad + \delta_{i4}\delta_{j1}\epsilon_{41} \langle 1,0|\, d_{R\uparrow} d^\dagger_{L\uparrow} d^\dagger_{R\uparrow} d_{L\uparrow} \,|1,0\rangle\Big) \\ &\leqslant 0,\end{aligned} \tag{B.17}$$

which shows that all such non-zero contributions are negative. By symmetry, exchanging spin-up with spin-down yields precisely the same signs. Similar calculations can be done for the other configurations and here we list the results:

$$\langle 0,1|\, \mathcal{C}^{(a_\sigma b_\sigma c_\sigma)}_{\sigma,ij} \,|0,1\rangle \leqslant 0, \tag{B.18a}$$

$$\langle 1,0|\, \mathcal{C}^{(a_\sigma b_\sigma c_\sigma)}_{\sigma,ij} \,|0,1\rangle \geqslant 0, \tag{B.18b}$$

$$\langle 0,1|\, \mathcal{C}^{(a_\sigma b_\sigma c_\sigma)}_{\sigma,ij} \,|1,0\rangle \geqslant 0. \tag{B.18c}$$

With these results it is straightforward to compute the sign of the critical current for a given groundstate using eq. (B.13). Here we will show some results to illustrate the methodology:

$$\langle 0,0|\, \mathcal{C}^{(a,b,c)}_{ijkl} \,|0,0\rangle = \langle 0,0|\, \mathcal{C}^{(a_\uparrow b_\uparrow c_\uparrow)}_{\uparrow,ij} \,|0,0\rangle \langle 0,0|\, \mathcal{C}^{(a_\downarrow b_\downarrow c_\downarrow)}_{\downarrow,ij} \,|0,0\rangle \geqslant 0 \tag{B.19a}$$

$$\langle 2,2|\, \mathcal{C}^{(a,b,c)}_{ijkl} \,|2,2\rangle = \langle 1,1|\, \mathcal{C}^{(a_\uparrow b_\uparrow c_\uparrow)}_{\uparrow,ij} \,|1,1\rangle \langle 1,1|\, \mathcal{C}^{(a_\downarrow b_\downarrow c_\downarrow)}_{\downarrow,ij} \,|1,1\rangle \geqslant 0 \tag{B.19b}$$

$$\langle \uparrow,0|\, \mathcal{C}^{(a,b,c)}_{ijkl} \,|\uparrow,0\rangle = \langle 1,0|\, \mathcal{C}^{(a_\uparrow b_\uparrow c_\uparrow)}_{\uparrow,ij} \,|1,0\rangle \langle 0,0|\, \mathcal{C}^{(a_\downarrow b_\downarrow c_\downarrow)}_{\downarrow,ij} \,|0,0\rangle \leqslant 0 \tag{B.19c}$$

$$\langle 2,\uparrow|\, \mathcal{C}^{(a,b,c)}_{ijkl} \,|2,\uparrow\rangle = \langle 1,1|\, \mathcal{C}^{(a_\uparrow b_\uparrow c_\uparrow)}_{\uparrow,ij} \,|1,1\rangle \langle 1,0|\, \mathcal{C}^{(a_\downarrow b_\downarrow c_\downarrow)}_{\downarrow,ij} \,|1,0\rangle \leqslant 0 \tag{B.19d}$$

What we have shown is that, independent of ordering and order of H_D, all contributions to I_c in eq. (B.12) have the same sign, proving that the signs shown above must also be the sign of I_c for the respective groundstates. This method can also be used to compute the sign of I_c for ground states that are not eigenstates of H_0, but eigenstates of $H_0 + H_D$. Consider for example the groundstate with a single electron delocalized across the dots, $|\uparrow\rangle = a\,|\uparrow,0\rangle - b\,|0,\uparrow\rangle$, where a and b have the same sign. Then it follows that

$$\begin{aligned}\langle \uparrow|\, \mathcal{C}^{(a,b,c)}_{ijkl} \,|\uparrow\rangle = \langle 0,0|\, \mathcal{C}^{(a_\downarrow b_\downarrow c_\downarrow)}_{\downarrow,ij} \,|0,0\rangle \Big(&a^2 \langle 1,0|\, \mathcal{C}^{(a_\uparrow b_\uparrow c_\uparrow)}_{\uparrow,ij} \,|1,0\rangle + b^2 \langle 0,1|\, \mathcal{C}^{(a_\uparrow b_\uparrow c_\uparrow)}_{\uparrow,ij} \,|0,1\rangle \\ &- ab \langle 1,0|\, \mathcal{C}^{(a_\uparrow b_\uparrow c_\uparrow)}_{\uparrow,ij} \,|0,1\rangle - ab \langle 0,1|\, \mathcal{C}^{(a_\uparrow b_\uparrow c_\uparrow)}_{\uparrow,ij} \,|1,0\rangle\Big) \\ \leqslant 0,\end{aligned} \tag{B.20}$$

which proves that the sign of I_c in the delocalized single electron doublet sector is negative to all orders in t_d. Using the same methodology on other groundstates, we find:

$$\langle\uparrow\downarrow| \mathcal{C}^{(a,b,c)}_{ijkl} |\uparrow\downarrow\rangle \geqslant 0, \tag{B.21a}$$

$$\langle\sigma| \mathcal{C}^{(a,b,c)}_{ijkl} |\sigma\rangle \leqslant 0, \tag{B.21b}$$

$$\langle\uparrow\downarrow\,\sigma| \mathcal{C}^{(a,b,c)}_{ijkl} |\uparrow\downarrow\,\sigma\rangle \leqslant 0, \tag{B.21c}$$

$$\langle\uparrow\uparrow| \mathcal{C}^{(a,b,c)}_{ijkl} |\uparrow\uparrow\rangle \geqslant 0, \tag{B.21d}$$

for eigenstates of $H_0 + H_D$ with electrons delocalized across the dots:

$$|\uparrow\downarrow\rangle = a\,|\uparrow,\downarrow\rangle + b\,|\downarrow,\uparrow\rangle - c\,|2,0\rangle - d\,|0,2\rangle\,, \tag{B.22a}$$

$$|\uparrow\downarrow\,\sigma\rangle = f\,|2,\sigma\rangle - g\,|\sigma,2\rangle\,, \tag{B.22b}$$

defined with positive prefactors, a, b, c, d, f, g, on all components.

Crucially for this experiment, we have shown that both a triplet groundstate, $|\uparrow\uparrow\rangle$, and a singlet groundstate, $|\uparrow\downarrow\rangle$, will guarantee a positive I_c. This concludes the proof that for the serial double dot, neglecting spin-orbit coupling, the sign of I_c to lowest order in dot-lead couplings is completely determined by the charge groundstate.

Even though these derivations are quite technical, the results can be summarized as a rather simple rule: For each spin in a cooper-pair in the left lead, count the number of same-spin dot electrons it crosses to get from left to right lead. For each such same-spin crossing attribute a minus sign. The sign of I_c will then be equal to the product of all such crossing signs. This rule can be inferred from eqs. (B.13) and (B.18), noticing that for a delocalized groundstate all contributions yield the same sign as resulting from one of its localized constituents. For a serial double dot this rule clearly implies that the sign of I_c is determined by the total charge parity of the dots: the sign is negative for odd parity and positive for even parity, regardless of spin configurations.

B.0.2 *Discussion of spin-orbit coupling*

So far we have established that the sign of the critical current for a double dot without spin-orbit coupling can be inferred solely from the groundstate. In this subsection, we discuss the possible implications of a finite spin-orbit coupling on the two quantum dots, implemented as a spin-dependent interdot tunneling amplitude. We begin by

considering only the spin-conserving tunnel coupling, t_z, and write the total interdot tunneling Hamiltonian as

$$\begin{aligned} H_D + H_{SO} &= \sum_\sigma \left((t_d + i\sigma t_z) d^\dagger_{L\sigma} d_{R\sigma} + h.c \right) \\ &= t_{eff} \sum_\sigma \left(e^{i\sigma\theta} d^\dagger_{L\sigma} d_{R\sigma} + h.c \right), \end{aligned} \tag{B.23}$$

where t_{eff} is the modulus and θ the complex phase of $t_d + it_z$. On this system we can perform a gauge transformation $e^{i\sigma\theta} d^\dagger_{L\sigma} = \tilde{d}^\dagger_{L\sigma}$ which removes θ from the interdot coupling and moves it onto the left dot-lead tunneling amplitude,

$$H_{TL} = t_L \sum_{k\sigma} \left(e^{i\sigma\theta} c^\dagger_{Lk\sigma} \tilde{d}_{L\sigma} + h.c \right). \tag{B.24}$$

Since the expansion in t_L, t_R in eq. (B.7) contains two electrons of opposite spin jumping from the superconductor lead to the dot, this phase cancels out in I_c, and the only effect of t_z is simply to renormalize the interdot coupling $t_{eff} = \sqrt{t_d^2 + t_z^2}$, leaving the sign of I_c unchanged.

Including either t_x or t_y, interdot tunnelling is no longer spin conserving, and therefore disrupts the spin-sorted arguments used above to show that all contributions to I_c have the same sign. This is most easily illustrated with an example. Consider a specific term arising from the combination $H_{SO} H_D H_{SO}$ with a finite t_y,

$$H_{SO} H_d H_{SO} = -t_y^2 t_d d^\dagger_{L\uparrow} d_{R\downarrow} d^\dagger_{R\downarrow} d_{L\downarrow} d^\dagger_{L\downarrow} d_{R\uparrow} + \dots \tag{B.25}$$

When acting on $|0,\uparrow\rangle$, this operator is equivalent to $-t_y^2 H_D$. Such combinations of operators will arise in eq. (B.11), where, for example, a contribution with $a = 1$ would contain H_D while a contribution with $a = 3$ would contain $H_{SO} H_D H_{SO}$. As these two terms have different signs, we observe that not all contributions to I_c have the same sign removing the guaranteed protection.

Without any external magnetic field, one may choose the spin quantization axis to be aligned with the spin-orbit field, such that only t_z is non-zero. As such the sign of I_c is still completely determined by the groundstate of the DQD. With a finite external magnetic field, however, t_x and t_y components are unavoidable unless the field is carefully aligned with the spin-orbit field. In this case, I_c will sample amplitudes of different signs and the overall sign of I_c cannot be guaranteed analytically, since the magnitudes of the individual terms now also matter. Instead, we have done this numerically to confirm the observed signs of I_c in the plots presented in the main text of chapter 11. To lowest order in H_D and H_{SO}, it can be shown analytically, that the sign of I_D remains determined by the groundstate, and that it is only higher order terms including both H_D and H_{SO}, such as eq.(B.25), which yield contributions of different signs. To leading order, the sign of I_c thus remains determined by the groundstate.

C

KELDYSH GREEN'S FUNCTIONS

In this appendix we cover the basic Keldysh Green's function relations required to derive transport equations in chapter 7. In regular equilibrium physics one expects that if a time-independent quantum system is initialized with some density matrix ρ_0 describing the state at $t = 0$ and coupled to a thermal bath of temperature T, then in the long time limit $\rho_0 \to \rho_\beta$ with $\rho_\beta = e^{-H/k_B T}/Z(\beta)$ i.e. the system will reach thermal equilibrium and the ground state will be described by a Gibbs distribution. The description of such systems is the subject of equilibrium Green's function theory, notable the Matsubara description [18]

If the Hamiltonian is time-dependent the system does not necessarily equilibrate, since time-evolution can possibly excite the system and drive it away from equilibrium. In one wish to describe such systems using Green's functions a different contour than Matsubara is required. This can be achieved by use of the *Schwinger-Keldysh contour* [177–179] which extends the regular equilibrium contour with a backwards path. The derivations presented in this section are based on Ref. [146–148], and are by no means an exhaustive walk-through of this large subject, as we focus primarily on the necessities for transport calculations. The first step is to motivate and define this new contour.

For a general Hamiltonian, which can be time dependent, the time evolution of the density matrix is given by,

$$\rho(t) = U(t, -\infty)\rho_0 U(-\infty, t), \tag{C.1}$$

with $\rho_0 = \rho(-\infty)$, and the time evolution is the solution to the time dependent Schrödinger equation $\partial_t |\psi(t)\rangle = H(t) |\psi(t)\rangle$ given by,

$$U(t, t') = \begin{cases} T_t e^{-i\int_t^{t'} dt'' H(t'')/\hbar} & t > t' \\ \bar{T}_t e^{i\int_{t'}^{t} dt'' H(t'')/\hbar} & t < t' \end{cases} \tag{C.2}$$

such that $|\psi(t)\rangle = U(t, t') |\psi(t')\rangle$ and fulfilling $U(t', t) = U(t, t')^\dagger$. T_t ($\bar{T}_t$) denotes time (anti-time) ordering which sorts operators in time, with lowest to the left (right) and

highest to the right (left). For fermions this operation comes with a sign for each exchange,

$$T_t\left(A(t)B(t')\right) = \Theta(t-t')A(t)B(t') - \Theta(t'-t)B(t')A(t) \tag{C.3}$$

with $A(t)$ and $B(t)$ denoting fermionic operators. If we now consider the expectation value of some operator O,

$$\langle O(t)\rangle = \frac{1}{Z}\operatorname{Tr}\left[O\rho(t)\right] = \frac{1}{Z}\operatorname{Tr}\left[OU(t,-\infty)\rho_0 U(-\infty,t)\right], \tag{C.4}$$

where we assumed that the system at time $t = \infty$ was initialized in some known state ρ_0. In this equation, we use the cyclicity of the trace and insert a unity to obtain,

$$\langle O(t)\rangle = \frac{1}{Z}\operatorname{Tr}\left[U(-\infty,\infty)U(\infty,t)OU(t,-\infty)\rho(-\infty)\right] \tag{C.5}$$

which sketches a time integral running from $t_i = -\infty$ to $t_m = \infty$ and then back again to $t_f = -\infty$ applying the operator O at time t on this path. This path we define as the Keldysh contour depicted in Fig. C.1. In this manner we rewrite,

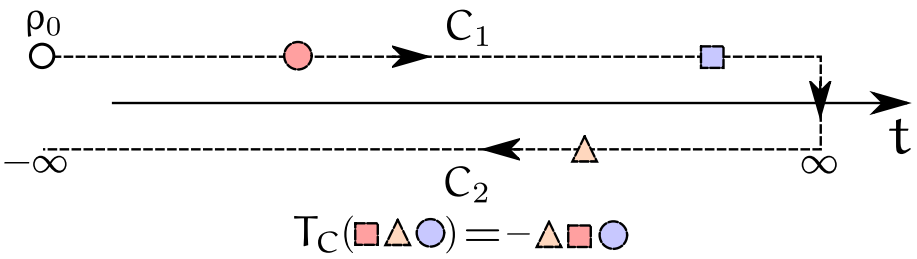

Figure C.1: Sketch of the Keldysh contour following t: $-\infty \to \infty \to -\infty$ with three operators applied along the way. T_C showcases the contour ordering, sorting operators by the position on the contour.

$$\langle O(t)\rangle = \frac{1}{Z}\operatorname{Tr}\left[T_C e^{-i\int_C dt' H(t')/\hbar} O(t)\rho_0\right]. \tag{C.6}$$

where T_C is defined as the time-ordering along the Keldysh contour sketched in fig. C.1. The top branch following $-\infty \to \infty$ is labelled C_1 while the bottom branch going back is C_2. Next, we define the single-particle Green's functions in Nambu space on the Keldysh contour as,

$$G_{ab}(t,t') = -i\langle T_C \Psi_a(t)\Psi_b^\dagger(t')\rangle \tag{C.7}$$

$$= -i\Theta_C(t,t')\langle \Psi_a(t)\Psi_b^\dagger(t')\rangle + i\Theta_C(t',t)\langle \Psi_a^\dagger(t')\Psi_a(t)\rangle \tag{C.8}$$

where a and b are index specifying the fermion type e.g left/right lead. $\Theta_C(t,t')$ is the step function on the Keldsyh contour, such that if t is farther along the contour

than t' we define $\Theta_C(t,t') = 1$ and 0 otherwise. At this juncture we limit ourselves to non-interacting Hamiltonians which can be cast in the form $H(t) = \frac{1}{2}\sum_{ab}\Psi_a^\dagger h_{ab}(t)\Psi_b$. To start, we consider only the diagonal part $H_0(t) = \sum_a c_a^\dagger h_{aa}(t) c_a$ whose Green's functions we label $g_a(t,t')$, defined with a single index as the Hamiltonian is diagonal. The corresponding equation of motion is obtained by taking the time derivative of eq. (C.8),

$$\begin{aligned} i\partial_t g_a(t,t') &= \delta_C(t,t')\langle[\Psi_a(t),\Psi_a^\dagger(t')]\rangle + i\langle T_C\left[H_0(t),\Psi_a\right](t)\Psi_a^\dagger(t')\rangle \\ &= \delta_C(t,t') + h_{aa}(t)g_a(t,t'). \end{aligned} \tag{C.9}$$

To obtain this result we used $\{\Psi_a,\Psi_a^\dagger\} = I$, which is the identity in Nambu space, and,

$$[H(t),\Psi](t) = h_{aa}(t)\Psi(t) \tag{C.10}$$

which we show in appendix A. In these equations Nambu matrix multiplication is assumed between each element. Lastly, we defined the delta function on the Keldysh contour,

$$\delta_c(t,t') = \begin{cases} \delta(t-t') & t,t' \in C_1 \\ \delta(t-t') & t,t' \in C_2 \\ 0 & t \in C_i, t' \in C_j, i \neq j \end{cases} \tag{C.11}$$

which satisfy $\int_C dt\delta(t,t')f(t') = f(t)$ for $t' \in C$. Rearranging eq. (C.9) we obtain,

$$\left[i\partial_t - h_a(t)\right] g_a(t,t') = \delta_C(t,t'), \tag{C.12}$$

which defines $g_a(t,t')$ also known as the bare Green's function. Regarding the two time variables t,t' in eq. (C.9) as matrix indices we recognize $\delta_C(t,t')$ on the right hand side as the identity. In this view the inverse matrix is given by,

$$g^{-1}(t,t') = \left[i\partial_t - h_{aa}(t)\right], \tag{C.13}$$

which satisfies the following identity,

$$1 = \int_C dt'' g^{-1}(t,t'')g(t'',t'), \tag{C.14}$$

with contour integrals $\int_C dt$ as inner products. Returning to the full Hamiltonian, including off diagonal terms, we find the following equation of motion,

$$i\partial_t G_{aa}(t,t') = \delta_C(t,t') + h_{aa}G_{aa}(t,t') + \sum_{b\neq a} h_{ab}(t)G_{ba}(t,t'), \tag{C.15}$$

which can be rewritten as,

$$[i\partial_t - h_{aa}]\, G_{aa}(t,t') = \delta_C(t,t') + \sum_{b\neq a} h_{ab}(t) G_{ba}(t,t'). \tag{C.16}$$

Recognizing the inverse bare Green's function on the left hand side we multiply with $g(t'',t)$ in a matrix manner and find,

$$G_{aa}(t,t') = g_a(t,t') + \sum_{b\neq a} \int_C g_a(t,t'') h_{ab}(t'') G_{ab}(t'',t') \tag{C.17}$$

$$= g_a(t,t') + \sum_{b\neq a} g_a \circ h_{ab} \circ G_{ba}(t,t'), \tag{C.18}$$

where we define $f \circ g(t,t') = \int_C dt'' f(t,t'') g(t'',t')$ and $h_{ab}(t,t') = h_{ab}(t)\delta_C(t,t')$. For the cross index Green function $G_{ab}(t,t')$ with $a \neq b$ the anti-commutator $\{\Psi_b(t), \Psi_a(t)\} = 0$ but otherwise derivations are similar yielding,

$$G_{ab}(t,t') = \sum_{c\neq a} g_a \circ h_{ac} \circ G_{cb}(t,t') \quad \text{for} \quad a \neq b. \tag{C.19}$$

The two equations eq. (C.18, C.19), allows us to derive Dyson equations for the Keldysh Green's function, enabling us to include couplings h_{ab} to all orders. Next, we will show some general properties of such equations. For simplicity assume that state a couples to a number of states b through h_{ab}, but b does not couple to anything else $h_{bc} = 0$ for $c \neq a$. In this case insertion of eq. (C.19) into eq. (C.18) yields,

$$G_{aa}(t,t') = g_a(t,t') + g_a \circ \Sigma_{aa} \circ G_{aa}(t,t') \tag{C.20}$$

$$\Sigma_{aa}(t,t') = \sum_b h_{ab}(t) g_b(t,t') h_{ba}(t') \tag{C.21}$$

where the last term is known as the self-energy $\Sigma_{aa}(t,t')$. Because of the iterative structure this equation can be solved as a Dyson equation,

$$G_{aa}(t,t') = \left[(g_a)^{-1} - \Sigma_{aa}\right]^{-1}(t,t') \tag{C.22}$$

where the inverse is in regard to both Nambu and time structure.

At this point, we have developed the necessary equations of motion for our needs and in the following we seek to relate Keldysh Green's functions to the types of Green's functions appearing in calculations, namely retarded, advanced, and lesser. Common definitions include,

$$\begin{aligned}
G^R_{ab}(t,t') &= -i\Theta(t-t')\langle\{\Psi_a(t), \Psi_b^\dagger(t')\}\rangle, & G^A(t,t') &= i\Theta(t'-t)\langle\{\Psi_a(t), \Psi_b^\dagger(t')\}\rangle, \\
G^<_{ab}(t,t') &= i\langle\Psi_b^\dagger(t')\Psi_a(t)\rangle, & G^>_{ab}(t,t') &= -i\langle\Psi_a(t)\Psi_b^\dagger(t')\rangle, \\
G^T_{ab}(t,t') &= -i\langle T_t \Psi_a(t)\Psi_b^\dagger(t')\rangle, & G^{\bar{T}}_{ab}(t,t') &= -i\langle \bar{T}_t \Psi_a(t)\Psi_b^\dagger(t')\rangle.
\end{aligned} \tag{C.23}$$

With the subscripts $(R, A, <, >, T, \bar{T})$ denoting retarded, advanced, lesser, greater, time-ordered and anti-time ordered respectively. The Keldysh time-ordering allow us to connect these various elements, by specifying the time branches, $t \in \{C_1, C_2\}$, on the regular Keldysh Green's function,

$$G(t,t') = \begin{cases} G^T(t.t') & \text{for} \quad t \in C_1, t' \in C_1 \\ G^<(t.t') & \text{for} \quad t \in C_1, t' \in C_2 \\ G^>(t.t') & \text{for} \quad t \in C_2, t' \in C_1 \\ G^{\bar{T}}(t.t') & \text{for} \quad t \in C_2, t' \in C_2, \end{cases} \tag{C.24}$$

These relation are due to the fact that T_C always sorts along the Keldsyh contour, so for example $t \in C_1, t' \in C_2$ will by Keldysh ordering place t to the left of t' which is per definition the lesser Green's function. Other important relations that follow from definitions are,

$$G^R(t,t') = G^T(t,t') - G^<(t,t') = G^>(t,t') - G^{\bar{T}}(t,t'), \tag{C.25}$$

$$G^A(t,t') = G^T(t,t') - G^>(t,t') = G^<(t,t') - G^{\bar{T}}(t,t'). \tag{C.26}$$

If we now regard the inner product between two functions $A(t,t')$ and $B(t,t')$ on the Keldysh contour,

$$C(t,t') = A \circ B(t,t') = \int_C dt'' A(t,t'')B(t'',t') \tag{C.27}$$

$$= \int_{C_1} dt'' A(t,t'')B(t'',t') + \int_{C_2} dt'' A(t,t'')B(t'',t') \tag{C.28}$$

we can by specifying time-ordering in $C(t,t')$ in combination with $\int_C dt'' A(t) = \int_{C_1} dt'' A(t) + \int_{C_2} dt'' B(t)$ find the following relations,

$$C^<(t,t') = \int_{C_1} dt'' A^T(t,t'')B^<(t,t') + \int_{C_2} A^<(t,t'')B^{\bar{T}}(t'',t') \tag{C.29}$$

$$C^T(t,t') = \int_{C_1} dt'' A^T(t,t'')B^T(t,t') + \int_{C_2} A^<(t,t'')B^>(t'',t') \tag{C.30}$$

Lastly, we utilize $\int_{C_1} dt = \int_{-\infty}^{\infty} dt$ and $\int_{C_2} dt = \int_{\infty}^{-\infty} dt$ in conjunction with the above relations to obtain,

$$C^<(t,t') = \int_{-\infty}^{\infty} dt'' \left[A^R(t,t'')B^<(t'',t) + A^<(t,t'')B^A(t'',t') \right]$$

$$= A^R \circ B^<(t,t') + A^< \circ B^A(t,t'), \tag{C.31}$$

$$C^R(t,t') = \int_{-\infty}^{\infty} dt'' \left[A^R(t,t'')B^R(t'',t') \right] = A^R \circ B^R(t,t'), \tag{C.32}$$

$$C^A(t,t') = \int_{-\infty}^{\infty} dt'' \left[A^A(t,t'')B^A(t'',t') \right] = A^A \circ B^A(t,t'). \tag{C.33}$$

Here we defined the inner time-product for non-Keldysh components as $A \circ B(t,t') = \int_{-\infty}^{\infty} dt'' A(t,t'')B(t'',t')$. These equations are collectively known as Langreth rules, and allow us to specify all Green's function components from Keldysh equations of motion. Next, we apply these rules to obtain the equations used in chapter 7. First, the cross index lesser component in eq. (7.25) is obtained by application of Langreth rules on eq. (C.19),

$$G^<_{RL}(t,t') = \int_{-\infty}^{\infty} dt'' \left[g^<_R(t,t'')h_{RL}(t'')G^A_{LL}(t'',t') + g^R_R(t,t'')h_{RL}(t'')G^<_{LL}(t'',t') \right]. \tag{C.34}$$

Next, we need the same index retarded and lesser Green's function used in eq. (7.28). Using Langreth rules on eq. (C.18) we find,

$$G^R_{LL}(t,t') = g^R_L(t,t') + g^R_L \circ \Sigma^R_{LL} \circ G^R_{LL}(t,t') \tag{C.35}$$
$$G^<_{LL}(t,t') = g^<_L(t,t') + g^<_L \circ \Sigma^A_{LL} \circ G^A_{LL}(t,t') + g^R_L \circ \Sigma^<_{LL} \circ G^A_{LL}(t,t') + g^R_L \circ \Sigma^R_{LL} \circ G^<_{LL}(t,t').$$

In the last equation we need to solve for $G^<_{LL}(t,t')$, which is done by subtracting the last term on either side and recognizing,

$$I - g^R_L \circ \Sigma^R_{LL}(t,t') = \left[I + G^R_{LL} \circ \Sigma^R_{LL} \right]^{-1}(t,t') \tag{C.36}$$

which is a rewriting of the Dyson series $G^R_{LL}(t,t') = \left[(g^R_L)^{-1} - \Sigma^R_{LL} \right]^{-1}$. Multiplying with this matrix finally yields,

$$G^<_{LL}(t,t') = \left(I + G^R_{LL} \circ \Sigma^R_{LL} \right) \circ g^<_L \circ \left(I + G^A_{LL} \circ \Sigma^A_{LL} \right)(t,t') + G^R_{LL} \circ \Sigma^<_{LL} \circ G^A_{LL}(t,t') \tag{C.37}$$

which is the final equation we need in order to derive transport.

D

NAIVE LEHMANN USAGE

In this appendix we elaborate on the issues of naive usage of Lehmann Green's functions. The Lehmann representation of a Nambu Green's function, which for simplicity we define in 2×2 Nambu, is given by,

$$G^R_{ij}(\omega) = \frac{1}{Z} \sum_{nn'} \frac{\langle n| \psi_i |n'\rangle \langle n'| \psi^\dagger_j |n\rangle}{\omega + i\eta + E_n - E_{n'}} \left(e^{-\beta E_n} + e^{-\beta E_{n'}} \right) \tag{D.1}$$

where $\psi^\dagger_i = \left(d^\dagger_\uparrow, d_\downarrow \right)$ are local Fermionic operators and $|n\rangle$ exact eigenstates, with energies E_n, of some possibly interacting Hamiltonian H. This expression is a convenient way of obtaining the single particle Green's function for systems that can be diagonalized, such as ZBW Hamiltonians, but includes interactions. The question is then, can we use this Green's function to calculate current through eq. (7.42) if the Hamiltonian includes interactions? In deriving eq. (7.42) we explicitly assumed that the bare Hamiltonians was non-interacting. If we included interactions, the DC current would also depend on higher order correlators of fermionic operators which cannot be reduced to single particle correlators as Wick's theorem is not applicable. In light of this, the answer is no. Inputting the Lehmann Green's function of an interacting Hamiltonian in eq. (7.42) does not yield the correct DC current. The follow up question is then, what do you obtain if you do it anyway? This we dub naive usage of Lehmann Green's function and to illustrate the consequences we follow an example.

Consider the S-QD Hamiltonian but with $U = 0$ known as the resonant level,

$$H = H_D + H_S, \tag{D.2}$$

$$H_S = \sum_{k\sigma} \epsilon_k c^\dagger_{k\sigma} c_{k\sigma} + \sum_k \left[\Delta c^\dagger_{k\uparrow} c^\dagger_{-k\downarrow} + \text{h. c.} \right] + t \sum_\sigma \left[c^\dagger_\sigma d_\sigma + \text{h. c.} \right], \tag{D.3}$$

$$H_D = \sum_\sigma \epsilon_d d^\dagger_\sigma d_\sigma. \tag{D.4}$$

In this limit, the dot is characterized by a simple Green's function in Nambu space, $g_d^R(\omega) = [\omega + i\eta - \epsilon_d\tau_z]^{-1}$, such that the dot Green's function dressed by the superconductor is,

$$g^R(\omega) = \left[\omega + i\eta - \epsilon_d\tau_z - t^2\tau_z g_s^R(\omega)\tau_z\right]^{-1} \tag{D.5}$$

where $g_s^R(\omega)$ is the local superconducting Green's function. If we choose now to consider only low frequencies compared to the gap $\omega \ll \Delta$ then we can approximate $g_s(\omega) = -\pi\nu_F\tau_x$, and we find,

$$g^R(\omega) = \frac{\omega + i\eta + \epsilon_d\tau_z + \Gamma\tau_x}{(\omega + i\eta + E_b)(\omega + i\eta - E_b)} \tag{D.6}$$

$$= \frac{1}{\omega + i\eta - E_b}\begin{pmatrix} v_0^2 & u_0v_0 \\ u_0v_0 & u_0^2 \end{pmatrix} + \frac{1}{\omega + i\eta + E_b}\begin{pmatrix} u_0^2 & -u_0v_0 \\ -u_0v_0 & v_0^2 \end{pmatrix} \tag{D.7}$$

with $\Gamma = \pi\nu_F t^2$, $E_b = \sqrt{\epsilon_d^2 + \Gamma^2}$, $u_0 = \sqrt{\frac{1}{2}}\sqrt{1 - \frac{\epsilon_d}{E_b}}$ and $v_0 = \sqrt{\frac{1}{2}}\sqrt{1 + \frac{\epsilon_d}{E_b}}$. To go from line two to three we used $\frac{1}{ab} = \frac{1}{b+a}\left(\frac{1}{a} + \frac{1}{b}\right) = \frac{1}{b-a}\left(\frac{1}{a} - \frac{1}{b}\right)$. From this form we recognize two simple poles corresponding to excitations at energy $\omega = \pm E_b$.

Now let us consider a slightly different model, where we add the interaction $H_U = Ud_\uparrow^\dagger d_\downarrow^\dagger d_\downarrow d_\uparrow$ to the Hamiltonian. Still considering the limit of large Δ compared to all other scales we solve first for $H_0 + H_S$, and obtain the Green's function eq. (D.5) which we rewrite as $g_0(\omega) = [\omega + i\eta - H_{eff}]$. From this, we recognize an effective Hamiltonian for the dot system with the superconductor integrated out,

$$\bar{H} = H_{eff} + H_U = \epsilon_d \sum_\sigma d_\sigma^\dagger d_\sigma + \Gamma d_\uparrow^\dagger d_\downarrow^\dagger + \Gamma d_\downarrow d_\uparrow + Ud_\uparrow^\dagger d_\downarrow^\dagger d_\downarrow d_\uparrow, \tag{D.8}$$

$$= \xi_d \sum_\sigma d_\sigma^\dagger d_\sigma + \Gamma d_\uparrow^\dagger d_\downarrow^\dagger + \Gamma d_\downarrow d_\uparrow + \frac{U}{2}\left(\sum_\sigma d_\sigma^\dagger d_\sigma - 1\right)^2 \tag{D.9}$$

which corresponds to the large Δ limit investigated in Ref. [38] using $\xi_d = \epsilon_d + U/2$. If we span this Hamiltonian in number states we find that the odd states $|\sigma\rangle$ are eigenstates with energy $E_\sigma = \xi_d$, while $|0\rangle$ couples to $|2\rangle$ through the anomalous term. This even subspace we diagonalize and find,

$$|+\rangle = u|0\rangle + v|2\rangle, \quad E_+ = \xi_d + \frac{U}{2} + \sqrt{\xi_d^2 + \Gamma^2} \tag{D.10}$$

$$|-\rangle = -v|0\rangle + u|2\rangle, \quad E_- = \xi_d + \frac{U}{2} - \sqrt{\xi_d^2 + \Gamma^2} \tag{D.11}$$

with $u = \sqrt{\frac{1}{2}}\sqrt{1 - \frac{\xi_d}{\sqrt{\xi_d^2+\Gamma^2}}}$ and $v = \sqrt{\frac{1}{2}}\sqrt{1 - \frac{\xi_d}{\sqrt{\xi_d^2+\Gamma^2}}}$. Consequently, if we set $U = 0$ the groundstate is always $|-\rangle$, and the first excitation is to the two $|\sigma\rangle$ states with

excitation energies $E_\sigma - E_- = E_b$, connecting us to the resonant level model with Green's function eq. (D.6). Next, we choose U finite and set $\sqrt{\xi_d^2 + \Gamma^2} = U/2 + \delta$, with δ being a small positive number compared to U. The system is now effectively described by the three levels $|-\rangle$ and the two $|\sigma\rangle$, as $|+\rangle$ is far away in energy. Using the Lehmann representation for $T = 0$ we obtain the following single particle Green's function,

$$g_{ij}^R = \sum_n \frac{\langle g|\psi_i|n\rangle\langle n|\psi_j^\dagger|g\rangle}{\omega + i\eta + E_g - E_n} + \sum_n \frac{\langle g|\psi_i|n\rangle\langle n|\psi_j^\dagger|g\rangle}{\omega + i\eta - E_g + E_n}, \tag{D.12}$$

where $|g\rangle$ is the ground state. For our choice of parameters $|g\rangle = |-\rangle$ and we find,

$$g_U^R(\omega) = \frac{1}{\omega + i\eta - \delta}\begin{pmatrix} v^2 & uv \\ uv & u^2 \end{pmatrix} + \frac{1}{\omega + i\eta + \delta}\begin{pmatrix} u^2 & -uv \\ -uv_0 & v^2 \end{pmatrix} \tag{D.13}$$

here the subscript U remind us that this is a Green's function for finite and large charging $U \gg \delta$. Notice the striking similarity between this Green's function and eq. (D.6). Next, if we in eq. (D.6) choose $\epsilon_d = 0$ and for finite U choose $\xi_d = 0$ we find $u = v = u_0 = v_0 = \frac{1}{2}$ and the two Green's functions are completely identical, apart from the denominator δ compared to E_b. Finally, since eq. (D.6) was exact and derived from the Hamiltonian $H_D + H_S$ we can ascribe eq. (D.13) as an exact solution of,

$$\hat{H} = \delta\hat{d}_\uparrow^\dagger\hat{d}_\downarrow^\dagger + \delta\hat{d}_\downarrow\hat{d}_\uparrow \tag{D.14}$$

$$\neq \bar{H}(\xi_d = 0) = \left(\frac{U}{2} - \delta\right)\left(d_\uparrow^\dagger d_\downarrow^\dagger + d_\downarrow d^\uparrow\right) + \frac{U}{2}\left(\sum_\sigma d_\sigma^\dagger d_\sigma - 1\right)^2 \tag{D.15}$$

here we highlight that the new effective Hamiltonian of the Green's function is not equal the original one. This fact becomes more obvious when we the consider excitations. $\hat{H}$ has four eigenstates with energies $\hat{E}_i \in \{-\delta, 0, 0, \delta\}$ while $\bar{H}(\xi_d = 0)$ also has four eigenstates, but with $\bar{E}_i \in \{-\delta, 0, 0, U + \delta\}$. Consequently, the lowest excitation $E_{ex} = \delta$ is the same, but the next excitation is very different. So what have we learned? We see that the Lehmann representation is not a one-to-one map as multiple Hamiltonians can have the same single particle Green's function. In order to pair eq. (D.13) with its correct Hamiltonian, we would require higher order correlators than single particle, which would differ between $\hat{H}$ and $\bar{H}(\xi_d = 0)$. Crucially, $\hat{H}$ is specifically the non-interacting(!) Hamiltonian yielding the same single particle Green's function as $\bar{H}(\xi_d = 0)$. From this we recognize that to naively use a Lehmann's Green's function in DC current calculations, eq. (7.42), corresponds to assuming that the Hamiltonian is effectively its non-interacting counter-part, similar to $\hat{H}$ for $\bar{H}(\xi_d = 0)$. Additionally, the Lehmann Green's function that describes the excitation from a singlet

to a doublet state with energy δ, corresponds to a resonant level Hamiltonian in which the doubly excited state (which we label $|\uparrow\downarrow\rangle$), with energy 2δ above the groundstate, is also an allowed many-body state. This correspondence is not restricted to $\xi_d = 0$ or the infinite gap model, as from eq. (D.12) any model including only a singlet to doublet excitation will yield a Green's function of the form eq. (D.13) with a mirror in eq. (D.6), and consequently a corresponding non-interacting resonant level Hamiltonian. Lastly, in case the doublet state is the groundstate (consider δ slightly negative) and for a infinitesimal temperature, such that the $|g\rangle$ is a thermal mixture of $|\uparrow\rangle$ and $|\downarrow\rangle$, we find $\bar{G}^R_D(\omega) = \frac{1}{2}\bar{G}^R_U(\omega)$ by use of eq. (D.1). This still resembles the resonant level but with half coupling. This concludes our studies into the Lehmann Green's function, which if naively used i.e. neglecting higher order correlators, corresponds to assuming that the dot Hamiltonian is a resonant level Hamiltonian.

BIBLIOGRAPHY

[1]J. C. E. Saldaña, A. Vekris, G. Steffensen, R. Žitko, P. Krogstrup, J. Paaske, K. Grove-Rasmussen, and J. Nygård, "Supercurrent in a Double Quantum Dot", Phys. Rev. Lett. **121**, 257701 (2018).

[2]J. C. Estrada Saldaña, A. Vekris, R. Žitko, G. Steffensen, P. Krogstrup, J. Paaske, K. Grove-Rasmussen, and J. Nygård, "Two-impurity Yu-Shiba-Rusinov states in coupled quantum dots", Phys. Rev. B **102**, 195143 (2020).

[3]G. O. Steffensen, J. C. E. Saldaña, A. Vekris, P. Krogstrup, K. Grove-Rasmussen, J. Nygård, A. L. Yeyati, and J. Paaske, "Direct Transport between Superconducting Subgap States in a Double Quantum Dot", arXiv (2021).

[4]D. Bouman, R. J. J. van Gulik, G. Steffensen, D. Pataki, P. Boross, P. Krogstrup, J. Nygård, J. Paaske, A. Pályi, and A. Geresdi, "Triplet-blockaded Josephson supercurrent in double quantum dots", Phys. Rev. B **102**, 220505 (2020).

[5]D. Chatzopoulos, D. Cho, K. M. Bastiaans, G. O. Steffensen, D. Bouwmeester, A. Akbari, G. Gu, J. Paaske, B. M. Andersen, and M. P. Allan, "Spatially dispersing Yu-Shiba-Rusinov states in the unconventional superconductor FeTe0.55Se0.45", Nat. Commun. **12**, 1–8 (2021).

[6]R. C. Ashoori, "Electrons in artificial atoms - Nature", Nature **379**, 413–419 (1996).

[7]J. Kondo, "Resistance Minimum in Dilute Magnetic Alloys", Prog. Theor. Phys. **32**, 37–49 (1964).

[8]A. C. Hewson, *The Kondo Problem to Heavy Fermions*, Cambridge Studies in Magnetism (Cambridge University Press, 1993).

[9]D. Goldhaber-Gordon, H. Shtrikman, D. Mahalu, D. Abusch-Magder, U. Meirav, and M. A. Kastner, "Kondo effect in a single-electron transistor - Nature", Nature **391**, 156–159 (1998).

[10]R. M. Potok, I. G. Rau, H. Shtrikman, Y. Oreg, and D. Goldhaber-Gordon, "Observation of the two-channel Kondo effect - Nature", Nature **446**, 167–171 (2007).

[11]P. Nozières and A. Blandin, "Kondo effect in real metals", J. Phys. **41**, 193–211 (1980).

[12]J. Koch, T. M. Yu, J. Gambetta, A. A. Houck, D. I. Schuster, J. Majer, A. Blais, M. H. Devoret, S. M. Girvin, and R. J. Schoelkopf, "Charge-insensitive qubit design derived from the Cooper pair box", Phys. Rev. A **76**, 042319 (2007).

[13]F. Arute et al., "Quantum supremacy using a programmable superconducting processor - Nature", Nature **574**, 505–510 (2019).

[14]L. Yu, "Bound State in Superconductors with Paramagnetic Impurities", Acta Phys. Sin. **21**, 75 (1965).

[15]H. Shiba, "Classical Spins in Superconductors", Prog. Theor. Phys. **40**, 435–451 (1968).

[16]A. I. Rusinov, "Superconductivity near a paramagnetic impurity", JETP Lett. **9**, [Zh. Eksp. Teor. Fiz. 9, 146 (1968)], 85–87 (1969).

[17]A. V. Balatsky, I. Vekhter, and J.-X. Zhu, "Impurity-induced states in conventional and unconventional superconductors", Rev. Mod. Phys. **78**, 373–433 (2006).

[18]H. Bruus and K. Flensberg, *Many-body quantum theory in condensed matter physics - an introduction* (Oxford University Press, Great Clarendon Street, Oxford, US, 2004).

[19]I. Affleck, J.-S. Caux, and A. M. Zagoskin, "Andreev scattering and Josephson current in a one-dimensional electron liquid", Phys. Rev. B **62**, 1433–1445 (2000).

[20]E. Vecino, A. Martín-Rodero, and A. L. Yeyati, "Josephson current through a correlated quantum level: Andreev states and π junction behavior", Phys. Rev. B **68**, 035105 (2003).

[21]G. O. Steffensen, "Yu-Shiba-Rusinov Bound States in Quantum Dots", MA thesis (Niels Bohr Institute, 2017).

[22]M. M. Salomaa, "Schrieffer-Wolff transformation for the Anderson Hamiltonian in a superconductor", Phys. Rev. B **37**, 9312–9317 (1988).

[23]V. Koerting, B. M. Andersen, K. Flensberg, and J. Paaske, "Nonequilibrium transport via spin-induced subgap states in superconductor/quantum dot/normal metal cotunnel junctions", Phys. Rev. B **82**, 245108 (2010).

[24]G. Kiršanskas, M. Goldstein, K. Flensberg, L. I. Glazman, and J. Paaske, "Yu-Shiba-Rusinov states in phase-biased superconductor-quantum dot-superconductor junctions", Phys. Rev. B **92**, 235422 (2015).

[25]K. Yosida, "Bound State Due to the s-d Exchange Interaction", Phys. Rev. **147**, 223–227 (1966).

[26]T. Soda, T. Matsuura, and Y. Nagaoka, "s-d Exchange Interaction in a Superconductor", Prog. Theor. Phys. **38**, 551–567 (1967).

[27]T. Yoshioka and Y. Ohashi, "Numerical Renormalization Group Studies on Single Impurity Anderson Model in Superconductivity: A Unified Treatment of Magnetic, Nonmagnetic Impurities, and Resonance Scattering", J. Phys. Soc. Jpn. **69**, 1812–1823 (2000).

[28]K. G. Wilson, "The renormalization group: Critical phenomena and the Kondo problem", Rev. Mod. Phys. **47**, 773–840 (1975).

[29]K. Satori, H. Shiba, O. Sakai, and Y. Shimizu, "Numerical Renormalization Group Study of Magnetic Impurities in Superconductors", J. Phys. Soc. Jpn. **61**, 3239–3254 (1992).

[30]J. Bauer, A. Oguri, and A. C. Hewson, "Spectral properties of locally correlated electrons in a Bardeen-Cooper-Schrieffer superconductor", J. Phys.: Condens. Matter **19**, 486211 (2007).

[31]R. Žitko, J. S. Lim, R. López, and R. Aguado, "Shiba states and zero-bias anomalies in the hybrid normal-superconductor Anderson model", Phys. Rev. B **91**, 045441 (2015).

[32]A. Martín-Rodero and A. L. Yeyati, "The Andreev states of a superconducting quantum dot: mean field versus exact numerical results", J. Phys.: Condens. Matter **24**, 385303 (2012).

[33]M. Žonda, V. Pokorný, V. Janiš, and T. Novotný, "Perturbation theory of a superconducting o - π impurity quantum phase transition", Sci. Rep. **5**, 1–6 (2015).

[34]A. Kadlecovaá, M. Žonda, V. Pokorný, and T. Novotný, "Practical Guide to Quantum Phase Transitions in Quantum-Dot-Based Tunable Josephson Junctions", Phys. Rev. Appl. **11**, 044094 (2019).

[35]C. Karrasch, A. Oguri, and V. Meden, "Josephson current through a single Anderson impurity coupled to BCS leads", Phys. Rev. B **77**, 024517 (2008).

[36]V. Meden, "The Anderson–Josephson quantum dot-a theory perspective", J. Phys.: Condens. Matter **31**, 163001 (2019).

[37]G. Sellier, T. Kopp, J. Kroha, and Y. S. Barash, "π junction behavior and Andreev bound states in Kondo quantum dots with superconducting leads", Phys. Rev. B **72**, 174502 (2005).

[38]T. Meng, S. Florens, and P. Simon, "Self-consistent description of Andreev bound states in Josephson quantum dot devices", Phys. Rev. B **79**, 224521 (2009).

[39]A. Martín-Rodero and A. L. Yeyati, "Josephson and Andreev transport through quantum dots", Adv. Phys. **60**, 899–958 (2011).

[40] A. Yazdani, B. A. Jones, C. P. Lutz, M. F. Crommie, and D. M. Eigler, "Probing the Local Effects of Magnetic Impurities on Superconductivity", Science **275**, 1767–1770 (1997).

[41] S.-H. Ji, T. Zhang, Y.-S. Fu, X. Chen, X.-C. Ma, J. Li, W.-H. Duan, J.-F. Jia, and Q.-K. Xue, "High-Resolution Scanning Tunneling Spectroscopy of Magnetic Impurity Induced Bound States in the Superconducting Gap of Pb Thin Films", Phys. Rev. Lett. **100**, 226801 (2008).

[42] G. C. Ménard et al., "Coherent long-range magnetic bound states in a superconductor - Nature Physics", Nat. Phys. **11**, 1013–1016 (2015).

[43] L. Cornils, A. Kamlapure, L. Zhou, S. Pradhan, A. A. Khajetoorians, J. Fransson, J. Wiebe, and R. Wiesendanger, "Spin-Resolved Spectroscopy of the Yu-Shiba-Rusinov States of Individual Atoms", Phys. Rev. Lett. **119**, 197002 (2017).

[44] L. Malavolti et al., "Tunable Spin–Superconductor Coupling of Spin 1/2 Vanadyl Phthalocyanine Molecules", Nano Lett. **18**, 7955–7961 (2018).

[45] K. J. Franke, G. Schulze, and J. I. Pascual, "Competition of Superconducting Phenomena and Kondo Screening at the Nanoscale", Science **332**, 940–944 (2011).

[46] M. Ruby, F. Pientka, Y. Peng, F. von Oppen, B. W. Heinrich, and K. J. Franke, "Tunneling Processes into Localized Subgap States in Superconductors", Phys. Rev. Lett. **115**, 087001 (2015).

[47] N. Hatter, B. W. Heinrich, M. Ruby, J. I. Pascual, and K. J. Franke, "Magnetic anisotropy in Shiba bound states across a quantum phase transition - Nature Communications", Nat. Commun. **6**, 1–6 (2015).

[48] M. T. Randeria, B. E. Feldman, I. K. Drozdov, and A. Yazdani, "Scanning Josephson spectroscopy on the atomic scale", Phys. Rev. B **93**, 161115 (2016).

[49] L. Farinacci, G. Ahmadi, G. Reecht, M. Ruby, N. Bogdanoff, O. Peters, B. W. Heinrich, F. von Oppen, and K. J. Franke, "Tuning the Coupling of an Individual Magnetic Impurity to a Superconductor: Quantum Phase Transition and Transport", Phys. Rev. Lett. **121**, 196803 (2018).

[50] H. Huang, R. Drost, J. Senkpiel, C. Padurariu, B. Kubala, A. L. Yeyati, J. C. Cuevas, J. Ankerhold, K. Kern, and C. R. Ast, "Quantum phase transitions and the role of impurity-substrate hybridization in Yu-Shiba-Rusinov states", Commun. Phys. **3**, 1–9 (2020).

[51] H. Huang, C. Padurariu, J. Senkpiel, R. Drost, A. L. Yeyati, J. C. Cuevas, B. Kubala, J. Ankerhold, K. Kern, and C. R. Ast, "Tunnelling dynamics between superconducting bound states at the atomic limit", Nat. Phys. **16**, 1227–1231 (2020).

[52]M. Ruby, Y. Peng, F. von Oppen, B. W. Heinrich, and K. J. Franke, "Orbital Picture of Yu-Shiba-Rusinov Multiplets", Phys. Rev. Lett. **117**, 186801 (2016).

[53]D.-J. Choi, C. Rubio-Verd'u, J. de Bruijckere, M. M. Ugeda, N. Lorente, and J. I. Pascual, "Mapping the orbital structure of impurity bound states in a superconductor - Nature Communications", Nat. Commun. **8**, 1–6 (2017).

[54]R. S. Deacon, Y. Tanaka, A. Oiwa, R. Sakano, K. Yoshida, K. Shibata, K. Hirakawa, and S. Tarucha, "Tunneling Spectroscopy of Andreev Energy Levels in a Quantum Dot Coupled to a Superconductor", Phys. Rev. Lett. **104**, 076805 (2010).

[55]J. O. Island et al., "Proximity-Induced Shiba States in a Molecular Junction", Phys. Rev. Lett. **118**, 117001 (2017).

[56]A. Garc'ia Corral, D. M. T. van Zanten, K. J. Franke, H. Courtois, S. Florens, and C. B. Winkelmann, "Magnetic-field-induced transition in a quantum dot coupled to a superconductor", Phys. Rev. Res. **2**, 012065 (2020).

[57]W. Chang, V. E. Manucharyan, T. S. Jespersen, J. Nygård, and C. M. Marcus, "Tunneling Spectroscopy of Quasiparticle Bound States in a Spinful Josephson Junction", Phys. Rev. Lett. **110**, 217005 (2013).

[58]E. J. H. Lee, X. Jiang, M. Houzet, R. Aguado, C. M. Lieber, and S. De Franceschi, "Spin-resolved Andreev levels and parity crossings in hybrid superconductor–semiconductor nanostructures", Nat. Nanotechnol. **9**, 79–84 (2014).

[59]J. Schindele, A. Baumgartner, R. Maurand, M. Weiss, and C. Schönenberger, "Nonlocal spectroscopy of Andreev bound states", Phys. Rev. B **89**, 045422 (2014).

[60]J. Gramich, A. Baumgartner, and C. Schönenberger, "Andreev bound states probed in three-terminal quantum dots", Phys. Rev. B **96**, 195418 (2017).

[61]E. J. H. Lee, X. Jiang, R. Žitko, R. Aguado, C. M. Lieber, and S. De Franceschi, "Scaling of subgap excitations in a superconductor-semiconductor nanowire quantum dot", Phys. Rev. B **95**, 180502 (2017).

[62]K. Grove-Rasmussen, G. Steffensen, A. Jellinggaard, M. H. Madsen, R. Žitko, J. Paaske, and J. Nygård, "Yu–Shiba–Rusinov screening of spins in double quantum dots", Nat. Commun. **9**, 1–6 (2018).

[63]J. C. Estrada Saldaña, A. Vekris, V. Sosnovtseva, T. Kanne, P. Krogstrup, K. Grove-Rasmussen, and J. Nygård, "Temperature induced shifts of Yu-Shiba-Rusinov resonances in nanowire-based hybrid quantum dots - Communications Physics", Commun. Phys. **3**, 1–11 (2020).

[64]T. Sand-Jespersen, J. Paaske, B. M. Andersen, K. Grove-Rasmussen, H. I. Jørgensen, M. Aagesen, C. B. Sørensen, P. E. Lindelof, K. Flensberg, and J. Nygård, "Kondo-Enhanced Andreev Tunneling in InAs Nanowire Quantum Dots", Phys. Rev. Lett. **99**, 126603 (2007).

[65]A. Eichler, M. Weiss, S. Oberholzer, C. Schönenberger, A. L. Yeyati, J. C. Cuevas, and A. Martín-Rodero, "Even-Odd Effect in Andreev Transport through a Carbon Nanotube Quantum Dot", Phys. Rev. Lett. **99**, 126602 (2007).

[66]K. Grove-Rasmussen, H. I. Jørgensen, B. M. Andersen, J. Paaske, T. S. Jespersen, J. Nygård, K. Flensberg, and P. E. Lindelof, "Superconductivity-enhanced bias spectroscopy in carbon nanotube quantum dots", Phys. Rev. B **79**, 134518 (2009).

[67]J.-D. Pillet, C. H. L. Quay, P. Morfin, C. Bena, A. L. Yeyati, and P. Joyez, "Andreev bound states in supercurrent-carrying carbon nanotubes revealed", Nat. Phys. **6**, 965–969 (2010).

[68]E. J. H. Lee, X. Jiang, R. Aguado, G. Katsaros, C. M. Lieber, and S. De Franceschi, "Zero-Bias Anomaly in a Nanowire Quantum Dot Coupled to Superconductors", Phys. Rev. Lett. **109**, 186802 (2012).

[69]J.-D. Pillet, P. Joyez, R. Žitko, and M. F. Goffman, "Tunneling spectroscopy of a single quantum dot coupled to a superconductor: From Kondo ridge to Andreev bound states", Phys. Rev. B **88**, 045101 (2013).

[70]B.-K. Kim, Y.-H. Ahn, J.-J. Kim, M.-S. Choi, M.-H. Bae, K. Kang, J. S. Lim, R. López, and N. Kim, "Transport Measurement of Andreev Bound States in a Kondo-Correlated Quantum Dot", Phys. Rev. Lett. **110**, 076803 (2013).

[71]A. Kumar, M. Gaim, D. Steininger, A. L. Yeyati, A. Martín-Rodero, A. K. Hüttel, and C. Strunk, "Temperature dependence of Andreev spectra in a superconducting carbon nanotube quantum dot", Phys. Rev. B **89**, 075428 (2014).

[72]S. Li, N. Kang, P. Caroff, and H. Q. Xu, "0-pi phase transition in hybrid superconductor–InSb nanowire quantum dot devices", Phys. Rev. B **95**, 014515 (2017).

[73]Z. Su et al., "Mirage Andreev Spectra Generated by Mesoscopic Leads in Nanowire Quantum Dots", Phys. Rev. Lett. **121**, 127705 (2018).

[74]J. He et al., "Nonequilibrium interplay between Andreev bound states and Kondo effect", Phys. Rev. B **102**, 075121 (2020).

[75]A. Jellinggaard, K. Grove-Rasmussen, M. H. Madsen, and J. Nygård, "Tuning Yu-Shiba-Rusinov states in a quantum dot", Phys. Rev. B **94**, 064520 (2016).

[76]J.-P. Cleuziou, W. Wernsdorfer, V. Bouchiat, T. Ondarçuhu, and M. Monthioux, "Carbon nanotube superconducting quantum interference device - Nature Nanotechnology", Nat. Nanotechnol. **1**, 53–59 (2006).

[77]J. A. van Dam, Y. V. Nazarov, E. P. A. M. Bakkers, S. De Franceschi, and L. P. Kouwenhoven, "Supercurrent reversal in quantum dots - Nature", Nature **442**, 667–670 (2006).

[78]R. Delagrange, D. J. Luitz, R. Weil, A. Kasumov, V. Meden, H. Bouchiat, and R. Deblock, "Manipulating the magnetic state of a carbon nanotube Josephson junction using the superconducting phase", Phys. Rev. B **91**, 241401 (2015).

[79]D. B. Szombati, S. Nadj-Perge, D. Car, S. R. Plissard, E. P. A. M. Bakkers, and L. P. Kouwenhoven, "Josephson ϕo-junction in nanowire quantum dots - Nature Physics", Nat. Phys. **12**, 568–572 (2016).

[80]W. Chang, S. M. Albrecht, T. S. Jespersen, F. Kuemmeth, P. Krogstrup, J. Nygård, and C. M. Marcus, "Hard gap in epitaxial semiconductor–superconductor nanowires - Nature Nanotechnology", Nat. Nanotechnol. **10**, 232–236 (2015).

[81]T. W. Larsen, K. D. Petersson, F. Kuemmeth, T. S. Jespersen, P. Krogstrup, J. Nygård, and C. M. Marcus, "Semiconductor-Nanowire-Based Superconducting Qubit", Phys. Rev. Lett. **115**, 127001 (2015).

[82]A. Kringhøj, B. van Heck, T. W. Larsen, O. Erlandsson, D. Sabonis, P. Krogstrup, L. Casparis, K. D. Petersson, and C. M. Marcus, "Suppressed Charge Dispersion via Resonant Tunneling in a Single-Channel Transmon", Phys. Rev. Lett. **124**, 246803 (2020).

[83]R. Aguado, "A perspective on semiconductor-based superconducting qubits", Appl. Phys. Lett. **117**, 240501 (2020).

[84]M. Hays et al., "Coherent manipulation of an Andreev spin qubit", Science **373**, 430–433 (2021).

[85]P. D. Kurilovich, V. D. Kurilovich, V. Fatemi, M. H. Devoret, and L. I. Glazman, "Microwave response of an Andreev bound state", arXiv (2021).

[86]C. Janvier et al., "Coherent manipulation of Andreev states in superconducting atomic contacts", Science **349**, 1199–1202 (2015).

[87]R. M. Lutchyn, E. P. A. M. Bakkers, L. P. Kouwenhoven, P. Krogstrup, C. M. Marcus, and Y. Oreg, "Majorana zero modes in superconductor–semiconductor heterostructures - Nature Reviews Materials", Nat. Rev. Mater. **3**, 52–68 (2018).

[88]E. Prada, P. San-Jose, M. W. A. de Moor, A. Geresdi, E. J. H. Lee, J. Klinovaja, D. Loss, J. Nygård, R. Aguado, and L. P. Kouwenhoven, "From Andreev to Majorana bound states in hybrid superconductor–semiconductor nanowires", Nat. Rev. Phys. **2**, 575–594 (2020).

[89]M. Valentini, F. Peñaranda, A. Hofmann, M. Brauns, R. Hauschild, P. Krogstrup, P. San-Jose, E. Prada, R. Aguado, and G. Katsaros, "Nontopological zero-bias peaks in full-shell nanowires induced by flux-tunable Andreev states", Science (2021).

[90]M. T. Deng, S. Vaitiekėnas, E. B. Hansen, J. Danon, M. Leijnse, K. Flensberg, J. Nygård, P. Krogstrup, and C. M. Marcus, "Majorana bound state in a coupled quantum-dot hybrid-nanowire system", Science (2016).

[91]B. A. Jones and C. M. Varma, "Study of two magnetic impurities in a Fermi gas", Phys. Rev. Lett. **58**, 843–846 (1987).

[92]S. Nadj-Perge, I. K. Drozdov, J. Li, H. Chen, S. Jeon, J. Seo, A. H. MacDonald, B. A. Bernevig, and A. Yazdani, "Observation of Majorana fermions in ferromagnetic atomic chains on a superconductor", Science (2014).

[93]M. Ruby, F. Pientka, Y. Peng, F. von Oppen, B. W. Heinrich, and K. J. Franke, "End States and Subgap Structure in Proximity-Coupled Chains of Magnetic Adatoms", Phys. Rev. Lett. **115**, 197204 (2015).

[94]B. E. Feldman, M. T. Randeria, J. Li, S. Jeon, Y. Xie, Z. Wang, I. K. Drozdov, B. Andrei Bernevig, and A. Yazdani, "High-resolution studies of the Majorana atomic chain platform - Nature Physics", Nat. Phys. **13**, 286–291 (2017).

[95]S. Nadj-Perge, I. K. Drozdov, B. A. Bernevig, and A. Yazdani, "Proposal for realizing Majorana fermions in chains of magnetic atoms on a superconductor", Phys. Rev. B **88**, 020407 (2013).

[96]F. Pientka, L. I. Glazman, and F. von Oppen, "Topological superconducting phase in helical Shiba chains", Phys. Rev. B **88**, 155420 (2013).

[97]A. Y. Kitaev, "Unpaired Majorana fermions in quantum", Phys.-Usp. **44**, 131–136 (2001).

[98]J. D. Sau and S. D. Sarma, "Realizing a robust practical Majorana chain in a quantum-dot-superconductor linear array - Nature Communications", Nat. Commun. **3**, 1–6 (2012).

[99]M. Leijnse and K. Flensberg, "Parity qubits and poor man's Majorana bound states in double quantum dots", Phys. Rev. B **86**, 134528 (2012).

[100]I. C. Fulga, A. Haim, A. R. Akhmerov, and Y. Oreg, "Adaptive tuning of Majorana fermions in a quantum dot chain", New J. Phys. **15**, 045020 (2013).

[101]Z. Su, A. B. Tacla, M. Hocevar, D. Car, S. R. Plissard, E. P. A. M. Bakkers, A. J. Daley, D. Pekker, and S. M. Frolov, "Andreev molecules in semiconductor nanowire double quantum dots", Nat. Commun. **8**, 1–6 (2017).

[102]P. Krogstrup, N. L. B. Ziino, W. Chang, S. M. Albrecht, M. H. Madsen, E. Johnson, J. Nygård, C. M. Marcus, and T. S. Jespersen, "Epitaxy of semiconductor–superconductor nanowires - Nature Materials", Nat. Mater. **14**, 400–406 (2015).

[103]A. Vekris, "Supercurrent and screening of spins in a double quantum dot josephson junction", MA thesis (Niels Bohr Institute, 2018).

[104]A. Chatterjee, P. Stevenson, S. De Franceschi, A. Morello, N. P. de Leon, and F. Kuemmeth, "Semiconductor qubits in practice - Nature Reviews Physics", Nat. Rev. Phys. **3**, 157–177 (2021).

[105]J. R. Petta, A. C. Johnson, J. M. Taylor, E. A. Laird, A. Yacoby, M. D. Lukin, C. M. Marcus, M. P. Hanson, and A. C. Gossard, "Coherent Manipulation of Coupled Electron Spins in Semiconductor Quantum Dots", Science (2005).

[106]W. G. van der Wiel, S. De Franceschi, J. M. Elzerman, T. Fujisawa, S. Tarucha, and L. P. Kouwenhoven, "Electron transport through double quantum dots", Rev. Mod. Phys. **75**, 1–22 (2002).

[107]J. Paaske, A. Andersen, and K. Flensberg, "Exchange cotunneling through quantum dots with spin-orbit coupling", Phys. Rev. B **82**, 081309 (2010).

[108]A. E. Antipov, A. Bargerbos, G. W. Winkler, B. Bauer, E. Rossi, and R. M. Lutchyn, "Effects of Gate-Induced Electric Fields on Semiconductor Majorana Nanowires", Phys. Rev. X **8**, 031041 (2018).

[109]D. Vion, M. Götz, P. Joyez, D. Esteve, and M. H. Devoret, "Thermal Activation above a Dissipation Barrier: Switching of a Small Josephson Junction", Phys. Rev. Lett. **77**, 3435–3438 (1996).

[110]P. Joyez, D. Vion, M. Götz, M. H. Devoret, and D. Esteve, "The Josephson Effect in Nanoscale Tunnel Junctions", J. Supercond. **12**, 757–766 (1999).

[111]A. Steinbach, P. Joyez, A. Cottet, D. Esteve, M. H. Devoret, M. E. Huber, and J. M. Martinis, "Direct Measurement of the Josephson Supercurrent in an Ultrasmall Josephson Junction", Phys. Rev. Lett. **87**, 137003 (2001).

[112]P. Jarillo-Herrero, J. A. van Dam, and L. P. Kouwenhoven, "Quantum supercurrent transistors in carbon nanotubes", Nature **439**, 953–956 (2006).

[113]K. Grove-Rasmussen, H. I. Jørgensen, and P. E. Lindelof, "Kondo resonance enhanced supercurrent in single wall carbon nanotube Josephson junctions", New J. Phys. **9**, 124 (2007).

[114]J. C. Estrada Saldaña, R. Žitko, J. P. Cleuziou, E. J. H. Lee, V. Zannier, D. Ercolani, L. Sorba, R. Aguado, and S. De Franceschi, "Charge localization and reentrant superconductivity in a quasi-ballistic InAs nanowire coupled to superconductors", Sci. Adv. **5**, eaav1235 (2019).

[115]H. I. Jørgensen, T. Novotný, K. Grove-Rasmussen, K. Flensberg, and P. E. Lindelof, "Critical Current o-π Transition in Designed Josephson Quantum Dot Junctions", Nano Lett. **7**, 2441–2445 (2007).

[116]A. Eichler, R. Deblock, M. Weiss, C. Karrasch, V. Meden, C. Schönenberger, and H. Bouchiat, "Tuning the Josephson current in carbon nanotubes with the Kondo effect", Phys. Rev. B **79**, 161407 (2009).

[117]M. Tinkham, *Introduction to Superconductivity: Second Edition*, 2nd ed. (Dover Publications, June 2004).

[118]Y. M. Ivanchenko and L. A. Zil'berman, "The Josephson effect in small tunnel contacts", JETP Lett. **28**, 1272 (1969).

[119]M. Toda, R. Kubo, and N. Saito, *Statistical Physics I* (Springer-Verlag, Berlin, Germany, 1983).

[120]I. van Weperen, S. R. Plissard, E. P. A. M. Bakkers, S. M. Frolov, and L. P. Kouwenhoven, "Quantized Conductance in an InSb Nanowire", Nano Lett. **13**, 387–391 (2013).

[121]G.-L. Ingold, H. Grabert, and U. Eberhardt, "Cooper-pair current through ultrasmall Josephson junctions", Phys. Rev. B **50**, 395–402 (1994).

[122]H. Grabert, G.-L. Ingold, and B. Paul, "Phase diffusion and charging effects in Josephson junctions", EPL **44**, 360–366 (1998).

[123]P. Joyez, "Self-Consistent Dynamics of a Josephson Junction in the Presence of an Arbitrary Environment", Phys. Rev. Lett. **110**, 217003 (2013).

[124]A. Murani, N. Bourlet, H. le Sueur, F. Portier, C. Altimiras, D. Esteve, H. Grabert, J. Stockburger, J. Ankerhold, and P. Joyez, "Absence of a Dissipative Quantum Phase Transition in Josephson Junctions", Phys. Rev. X **10**, 021003 (2020).

[125]G.-L. Ingold and Y. V. Nazarov, "Charge Tunneling Rates in Ultrasmall Junctions", arXiv (2005).

[126]B. Jäck, M. Eltschka, M. Assig, M. Etzkorn, C. R. Ast, and K. Kern, "Critical Josephson current in the dynamical Coulomb blockade regime", Phys. Rev. B **93**, 020504 (2016).

[127]C. R. Ast, B. Jäck, J. Senkpiel, M. Eltschka, M. Etzkorn, J. Ankerhold, and K. Kern, "Sensing the quantum limit in scanning tunnelling spectroscopy", Nat. Commun. **7**, 1–8 (2016).

[128]J. Ankerhold, "Overdamped quantum phase diffusion and charging effects", EPL **67**, 280–286 (2004).

[129]P. Joyez, "The single Cooper pair transistor: a macroscopic quantum system", Theses (Université Pierre et Marie Curie - Paris VI, Mar. 1995).

[130]L. I. Glazman and K. A. Matveev, "Resonant Josephson current through Kondo impurities in a tunnel barrier", JETP Lett. **43**, 659 (1991).

[131]B. I. Spivak and S. A. Kivelson, "Negative local superfluid densities: The difference between dirty superconductors and dirty Bose liquids", Phys. Rev. B **43**, 3740 (1991).

[132]T. Novotný, A. Rossini, and K. Flensberg, "Josephson current through a molecular transistor in a dissipative environment", Phys. Rev. B **72**, 224502 (2005).

[133]A. Brunetti, A. Zazunov, A. Kundu, and R. Egger, "Anomalous Josephson current, incipient time-reversal symmetry breaking, and Majorana bound states in interacting multilevel dots", Phys. Rev. B **88**, 144515 (2013).

[134]Y. Zhu, Q.-f. Sun, and T.-h. Lin, "Probing spin states of coupled quantum dots by a dc Josephson current", Phys. Rev. B **66**, 085306 (2002).

[135]R. Žitko, M. Lee, R. López, R. Aguado, and M.-S. Choi, "Josephson Current in Strongly Correlated Double Quantum Dots", Phys. Rev. Lett. **105**, 116803 (2010).

[136]C. Karrasch, S. Andergassen, and V. Meden, "Supercurrent through a multilevel quantum dot close to singlet-triplet degeneracy", Phys. Rev. B **84**, 134512 (2011).

[137]S. Droste, S. Andergassen, and J. Splettstoesser, "Josephson current through interacting double quantum dots with spin–orbit coupling", J. Phys.: Condens. Matter **24**, 415301 (2012).

[138]V. Pokorný, M. Žonda, G. Loukeris, and T. Novotný, "Second Order Perturbation Theory for a Superconducting Double Quantum Dot", in *Proceedings of the International Conference on Strongly Correlated Electron Systems (SCES2019)*, Vol. 30 (The Physical Society of Japan, Mar. 2020).

[139]F. S. Bergeret, A. L. Yeyati, and A. Martín-Rodero, "Interplay between Josephson effect and magnetic interactions in double quantum dots", Phys. Rev. B **74**, 132505 (2006).

[140]A. V. Rozhkov and D. P. Arovas, "Josephson Coupling through a Magnetic Impurity", Phys. Rev. Lett. **82**, 2788 (1999).

[141]D. J. Luitz and F. F. Assaad, "Weak-coupling continuous-time quantum Monte Carlo study of the single impurity and periodic Anderson models with s-wave superconducting baths", Phys. Rev. B **81**, 024509 (2010).

[142]R. Delagrange, R. Weil, A. Kasumov, M. Ferrier, H. Bouchiat, and R. Deblock, "0-pi quantum transition in a carbon nanotube Josephson junction: Universal phase dependence and orbital degeneracy", Phys. Rev. B **93**, 195437 (2016).

[143]H. v. Löhneysen, T. Pietrus, G. Portisch, H. G. Schlager, A. Schröder, M. Sieck, and T. Trappmann, "Non-Fermi-liquid behavior in a heavy-fermion alloy at a magnetic instability", Phys. Rev. Lett. **72**, 3262–3265 (1994).

[144]A. Georges, G. Kotliar, W. Krauth, and M. J. Rozenberg, "Dynamical mean-field theory of strongly correlated fermion systems and the limit of infinite dimensions", Rev. Mod. Phys. **68**, 13–125 (1996).

[145]A. Mishra, P. Simon, T. Hyart, and M. Trif, "A Yu-Shiba-Rusinov qubit", arXiv (2021).

[146]H. Haug and A.-P. Jauho, *Quantum Kinetics in Transport and Optics of Semiconductors* (Springer-Verlag, Berlin, Germany, 2008).

[147]A. Kamenev, *Field Theory of Non-Equilibrium Systems* (Cambridge University Press, Cambridge, England, UK, Sept. 2011).

[148]H. Aoki, N. Tsuji, M. Eckstein, M. Kollar, T. Oka, and P. Werner, "Nonequilibrium dynamical mean-field theory and its applications", Rev. Mod. Phys. **86**, 779–837 (2014).

[149]D. Averin and A. Bardas, "ac Josephson Effect in a Single Quantum Channel", Phys. Rev. Lett. **75**, 1831–1834 (1995).

[150]J. C. Cuevas, A. Martín-Rodero, and A. L. Yeyati, "Hamiltonian approach to the transport properties of superconducting quantum point contacts", Phys. Rev. B **54**, 7366–7379 (1996).

[151]E. Scheer, P. Joyez, D. Esteve, C. Urbina, and M. H. Devoret, "Conduction Channel Transmissions of Atomic-Size Aluminum Contacts", Phys. Rev. Lett. **78**, 3535 (1997).

[152]E. Scheer, N. Agraït, J. C. Cuevas, A. L. Yeyati, B. Ludoph, A. Martín-Rodero, G. R. Bollinger, J. M. van Ruitenbeek, and C. Urbina, "The signature of chemical valence in the electrical conduction through a single-atom contact", Nature **394**, 154–157 (1998).

[153]S. Behnel, R. Bradshaw, C. Citro, L. Dalcin, D. S. Seljebotn, and K. Smith, "Cython: the best of both worlds", Computing in Science & Engineering **13**, 31–39 (2011).

[154]R. Cron, M. F. Goffman, D. Esteve, and C. Urbina, "Multiple-Charge-Quanta Shot Noise in Superconducting Atomic Contacts", Phys. Rev. Lett. **86**, 4104–4107 (2001).

[155]A. Villas, R. L. Klees, H. Huang, C. R. Ast, G. Rastelli, W. Belzig, and J. C. Cuevas, "Interplay between Yu-Shiba-Rusinov states and multiple Andreev reflections", Phys. Rev. B **101**, 235445 (2020).

[156]H. Shiba, "A Hartree-Fock Theory of Transition-Metal Impurities in a Superconductor", Prog. Theor. Phys. **50**, 50–73 (1973).

[157]M. I. Salkola, A. V. Balatsky, and J. R. Schrieffer, "Spectral properties of quasiparticle excitations induced by magnetic moments in superconductors", Phys. Rev. B **55**, 12648–12661 (1997).

[158]A. Villas, R. L. Klees, G. Morrás, H. Huang, C. R. Ast, G. Rastelli, W. Belzig, and J. C. Cuevas, "Tunneling processes between Yu-Shiba-Rusinov bound states", Phys. Rev. B **103**, 155407 (2021).

[159]R. C. Dynes, V. Narayanamurti, and J. P. Garno, "Direct Measurement of Quasiparticle-Lifetime Broadening in a Strong-Coupled Superconductor", Phys. Rev. Lett. **41**, 1509–1512 (1978).

[160]P. Joyez, P. Lafarge, A. Filipe, D. Esteve, and M. H. Devoret, "Observation of parity-induced suppression of Josephson tunneling in the superconducting single electron transistor", Phys. Rev. Lett. **72**, 2458–2461 (1994).

[161]R. Lutchyn, L. Glazman, and A. Larkin, "Quasiparticle decay rate of Josephson charge qubit oscillations", Phys. Rev. B **72**, 014517 (2005).

[162]M. D. Shaw, R. M. Lutchyn, P. Delsing, and P. M. Echternach, "Kinetics of nonequilibrium quasiparticle tunneling in superconducting charge qubits", Phys. Rev. B **78**, 024503 (2008).

[163]M. Hays, G. de Lange, K. Serniak, D. J. van Woerkom, D. Bouman, P. Krogstrup, J. Nygård, A. Geresdi, and M. H. Devoret, "Direct Microwave Measurement of Andreev-Bound-State Dynamics in a Semiconductor-Nanowire Josephson Junction", Phys. Rev. Lett. **121**, 047001 (2018).

[164]L. Tosi, C. Metzger, M. F. Goffman, C. Urbina, H. Pothier, S. Park, A. L. Yeyati, J. Nygård, and P. Krogstrup, "Spin-Orbit Splitting of Andreev States Revealed by Microwave Spectroscopy", Phys. Rev. X **9**, 011010 (2019).

[165]M. Zgirski, L. Bretheau, Q. Le Masne, H. Pothier, D. Esteve, and C. Urbina, "Evidence for Long-Lived Quasiparticles Trapped in Superconducting Point Contacts", Phys. Rev. Lett. **106**, 257003 (2011).

[166]D. G. Olivares, A. L. Yeyati, L. Bretheau, Ç. Ö. Girit, H. Pothier, and C. Urbina, "Dynamics of quasiparticle trapping in Andreev levels", Phys. Rev. B **89**, 104504 (2014).

[167]A. Zazunov, A. Brunetti, A. L. Yeyati, and R. Egger, "Quasiparticle trapping, Andreev level population dynamics, and charge imbalance in superconducting weak links", Phys. Rev. B **90**, 104508 (2014).

[168]A. G. Kozorezov, A. A. Golubov, J. K. Wigmore, D. Martin, P. Verhoeve, R. A. Hijmering, and I. Jerjen, "Inelastic scattering of quasiparticles in a superconductor with magnetic impurities", Phys. Rev. B **78**, 174501 (2008).

[169]I. Martin and D. Mozyrsky, "Nonequilibrium theory of tunneling into a localized state in a superconductor", Phys. Rev. B **90**, 100508 (2014).

[170]B. M. Andersen, K. Flensberg, V. Koerting, and J. Paaske, "Nonequilibrium Transport through a Spinful Quantum Dot with Superconducting Leads", Phys. Rev. Lett. **107**, 256802 (2011).

[171]H.-P. Breuer and F. Petruccione, "The Theory of Open Quantum Systems", in *The Theory of Open Quantum Systems* (Oxford University Press, Oxford, England, UK, 2007).

[172]D. Manzano, "A short introduction to the Lindblad master equation", AIP Adv. **10**, 025106 (2020).

[173]V. V. Ryazanov, V. A. Oboznov, A. Y. Rusanov, A. V. Veretennikov, A. A. Golubov, and J. Aarts, "Coupling of Two Superconductors through a Ferromagnet: Evidence for a π Junction", Phys. Rev. Lett. **86**, 2427–2430 (2001).

[174]X. Wu, S. Qin, Y. Liang, H. Fan, and J. Hu, "Topological characters in Fe(Te1-xSex) thin films", Phys. Rev. B **93**, 115129 (2016).

[175]J. Danon and Y. V. Nazarov, "Pauli spin blockade in the presence of strong spin-orbit coupling", Phys. Rev. B **80**, 041301 (2009).

[176]K. F. Riley and M. P. Hobson, "Essential mathematical methods for the physical sciences", in (Cambridge University Press, 2011), p. 66.

[177]J. Schwinger, "Brownian Motion of a Quantum Oscillator", J. Math. Phys. **2**, 407–432 (1961).

[178]L. Kadanoff and G. Baym, *Quantum Statistical Mechanics* (W.A. Benjamin Inc., New York, 1962).

[179]L. V. Keldysh, "Diagram technique for nonequilibrium processes", Sov. Phys. JETP **20**, [Zh. Eksp. Theor. Fiz. 47, 1515 (1964)], 1018 (1965).